Lecture Notes in Mechanical Engineering

L. M. Das
Naveen Kumar
Rohit Singh Lather
Pramod Bhatia *Editors*

Emerging Trends in Mechanical Engineering

Select Proceedings of ICETMIE 2019

Springer

Lecture Notes in Mechanical Engineering

Lecture Notes in Mechanical Engineering (LNME) publishes the latest developments in Mechanical Engineering—quickly, informally and with high quality. Original research reported in proceedings and post-proceedings represents the core of LNME. Volumes published in LNME embrace all aspects, subfields and new challenges of mechanical engineering. Topics in the series include:

- Engineering Design
- Machinery and Machine Elements
- Mechanical Structures and Stress Analysis
- Automotive Engineering
- Engine Technology
- Aerospace Technology and Astronautics
- Nanotechnology and Microengineering
- Control, Robotics, Mechatronics
- MEMS
- Theoretical and Applied Mechanics
- Dynamical Systems, Control
- Fluid Mechanics
- Engineering Thermodynamics, Heat and Mass Transfer
- Manufacturing
- Precision Engineering, Instrumentation, Measurement
- Materials Engineering
- Tribology and Surface Technology

To submit a proposal or request further information, please contact the Springer Editor of your location:

China: Dr. Mengchu Huang at mengchu.huang@springer.com
India: Priya Vyas at priya.vyas@springer.com
Rest of Asia, Australia, New Zealand: Swati Meherishi at swati.meherishi@springer.com
All other countries: Dr. Leontina Di Cecco at Leontina.dicecco@springer.com

To submit a proposal for a monograph, please check our Springer Tracts in Mechanical Engineering at http://www.springer.com/series/11693 or contact Leontina.dicecco@springer.com

Indexed by SCOPUS. All books published in the series are submitted for consideration in Web of Science.

More information about this series at http://www.springer.com/series/11236

L. M. Das · Naveen Kumar · Rohit Singh Lather · Pramod Bhatia
Editors

Emerging Trends in Mechanical Engineering

Select Proceedings of ICETMIE 2019

Springer

Editors
L. M. Das
Department of Mechanical Engineering
Indian Institute of Technology Delhi
New Delhi, India

Naveen Kumar
Department of Mechanical Engineering
Delhi Technological University (DTU)
New Delhi, India

Rohit Singh Lather
Department of Mechanical Engineering
The NorthCap University
Gurugram, India

Pramod Bhatia
Department of Mechanical Engineering
The NorthCap University
Gurugram, India

ISSN 2195-4356 ISSN 2195-4364 (electronic)
Lecture Notes in Mechanical Engineering
ISBN 978-981-15-8303-2 ISBN 978-981-15-8304-9 (eBook)
https://doi.org/10.1007/978-981-15-8304-9

This Springer imprint is published by the registered company Springer Nature Singapore Pte Ltd.
The registered company address is: 152 Beach Road, #21-01/04 Gateway East, Singapore 189721, Singapore

Preface

It is our pleasure for the Mechanical Engineering Department, The NorthCap University, to organize the 4th edition of the International Conference on Emerging Trends in Mechanical Engineering (ICETMIE)—2019. For many years, the Mechanical Engineering Department has been organizing the ICETMIE conference series. ICETMIE —2019 capitalizes on our common strengths, built on our common commitment to carry out quality research, promoting technology and innovation. We are proud to have you all here at this important platform.

We, at the ME Department, School of Engineering and Technology, NorthCap University, are honoured and delighted to host the 4th ICETMIE —2019 and contribute towards the assimilation and generation of scientific knowledge.

The conference adopts a timely theme, sustainable technologies. As the sustainable approach has penetrated virtually all areas of our life, we talk about energy conservation, water conservation, responsible production, and consumption patterns. At present it is entwined with our research and development practices to develop technology, alternatives and substitute for existing systems. To effectively benefit from technology applications, researchers must set themselves ready for transforming their research and practices and keep identifying effective ways for transformations in their contexts.

We hope to learn new ideas from each other, which we could be adopted to further improve our work in the important areas of mechanical and industrial engineering. There have been many interesting and useful presentations during the conference, both in the plenary session and in the interactive technical sessions. Many good experiences have been shared and good lessons learned. Many people have commented that a lot of good work has been done and presented in the conference, and that the presentations demonstrated good practical activities and experience.

These proceedings provide a record of the good work presented during the conference and serve as a document for future reference.

Finally, I would like to thank everyone associated with the conference ensuring it ran so smoothly.

New Delhi, India — L. M. Das
New Delhi, India — Naveen Kumar
Gurugram, India — Rohit Singh Lather
Gurugram, India — Pramod Bhatia

Contents

About the Editors

Dr. L. M. Das is currently Professor at the Centre for Energy Studies, IIT Delhi. He took his Bachelor's degree in Mechanical Engineering from the Regional Engineering College, Rourkela in 1970 and M. Tech degree from the, Kharagpur in 1972. Dr. Das completed his doctorate from IIT, Delhi in field of Mechanical Engineering. His primary areas of research interest include the development of alternative-fuelled low emission engine/vehicles. He has published more than 80 research papers in various independently refereed international and national journals in the area of alternative fuels such as Hydrogen, CNG, Biodiesel and Hydrogen- CNG blend.

Dr. Naveen Kumar is working as Professor of Mechanical Engineering at Delhi Technological University (formerly Delhi College of Engineering. Prof. Naveen Kumar did his B.E. from Dayal Bagh Educational Institute, Agra, M.Tech. from IIT Delhi and Ph.D. from the University of Delhi. He is a Fellow of Institution of Mechanical Engineers (FIMechE), UK; Fellow of Institution of Engineers (FIE), India and Charted Engineer, Engineering Council, UK. His research interests include; alternative fuels with special emphasis on biofuels, decentralized energy systems, renewable energy, waste recycling and sustainable development. Prof. Kumar possesses 27 years of experience in academics, industry, and research. He has published more than 90 research papers in international journals of repute and more than 100 in Indian journals and conferences.

Dr. Rohit Singh Lather is currently Associate Professor at the Mechanical Engineering Department from The NorthCap University. He graduated in 2005 with a bachelor of mechanical engineering from Kurukshetra University. He post-graduated in Automotive Engineering from Vellore Institute of Technology (VIT) and Automotive Research Association of India (ARAI) in 2008. Dr. Rohit Singh Lather earned a PhD, in Energy Studies from Indian Institute of Technology (IIT) Delhi in 2014. His general area of research includes Energy and alternative energy, automotive engineering and thermal systems. In particular, his areas of specialization include engine development, alternative fuels (CNG, HCNG,

Hydrogen, and Biofuels), emission reduction, combustion diagnostics, and electric vehicles. He has several peer-reviewed international and national Journal publications and conference proceedings.

Dr. Pramod Bhatia who has completed his PhD (in Mechanical Engineering) from Purdue University, USA; Master's from the University of Illinois, USA and BTech from IIT Delhi, is currently working as Professor and Head, Department of Mechanical Engineering from The NorthCap University for last nine years. Prior to joining NCU, he worked as a consultant for two years in the USA. His areas of specialization are Computational Fluid Dynamics and Combustion. Apart from his administrative and research responsibilities, Dr. Bhatia is actively involved in teaching Combustion and Flames, Heat Transfer, Fluid Mechanics, Fluid Machines, Hydraulics and Pneumatics, Introduction to Mechanical and Production Engineering, Basics of Mechanical Engineering and Thermodynamics. He has 20 journal publications, 12 conference publications and one book to his credit. He is currently guiding two PhD scholars.

Engineering Design

Impact of Armor-Perforating Projectile on a Bullet-Resistant Silicon-Carbide-Graphene Composite Through Finite Element Method

Divashu Guleria, Harmesh Kumar, Shankar Sehgal, and Sarbjeet Singh

Abstract With the advancement in the defence technologies of the military sector of the world, the chances of encountering life threats have also increased. Police personnel and the armed forces deal with such situations regularly during their duty. The most common of such situations is injuries and life threats due to small arms and light weapons. Thus, there is an emerging need for advancement in the study and manufacturing of bullet-resistant or bullet-proof materials to avoid the harms created by ballistic impacts of a projectile. This paper studies the effect of Young's modulus of the material and thickness of the target plate on residual velocity of the projectile through finite filament modeling. Simulations were carried out to study the effect of adding graphene to silicon carbide matrix to the penetration of the projectile and to find out the minimum thickness of the composite plate required to resist the complete perforation of the projectile.

Keywords Finite element method · Bullet-resistant materials · Simulations · Armor-perforating projectile

1 Introduction

The study of problems related to impacts which involve a collision of two or more solids has become increasingly important to military, modern industries and society [1]. In history, all impact-related studies were limited to theoretical models and empirical models generated by experimental methods which were a lot of cost burdening and time-consuming. The complexity of the theoretical models made it quite difficult to achieve a closer accuracy in a short period of time. The advancement in the computer-based simulations has helped researchers in reducing the time as well as the cost of analysis. Software like ANSYS [2] provides explicit dynamics analysis

D. Guleria · H. Kumar · S. Sehgal (✉)
Mechanical Engineering, UIET, Panjab University, Chandigarh, India
e-mail: sehgals@pu.ac.in

S. Singh
Mechanical Engineering Department, GCET, Jammu, India

L. M. Das et al. (eds.), *Emerging Trends in Mechanical Engineering*, Lecture Notes in Mechanical Engineering, https://doi.org/10.1007/978-981-15-8304-9_1

Table 1 Summation of sub-fields of ballistics

S. No.	Type of impact/ballistics	Velocity range of projectile (v)	Industries/sectors associated
1	Low/moderate velocity impact	$v < 0.05$ km/s	Automobile industry
2	High-velocity impact	0.05 km/s $< v <$ 1.5 km/s	Aviation industry, military, department of defence
3	Hyper-velocity impact	$v > 1.5$ km/s	Aeronautics and astronautics

which is widely used to perform finite element modeling-based numerical simulations of high-velocity impacts. Since the cost and time involved in doing one single simulation are far less in comparison to actual experimental analysis, computer simulations are preferred over the latter. This also helps in developing new armors and ammunition/projectiles in a shorter time and allows enhancement and easy modifications as well [3]. Ballistics is the science which deals with the phenomenon related to the study of the firing of an object/projectile and its effects on the target from the time it is fired until effects on the target are completely observed. Ballistics can further be sub-classified into different sub-fields at various sectors of industries as shown in Table 1 [4].

The impact of bullet depends upon number of factors such as impact angle, nose profile of bullet, etc., Bhaurya [5] studied the effect of the impact angle of the projectile on perforation. Results concluded that the bullet perforated the plate at 0°, 15°, and 30° angle but got deflected back at a 45° angle. A hemispherical nose profile has lesser tendency of perforating the target than a conical nose profile [6].

The ANSYS Workbench is a finite element analysis utility software that is used in conjunction with other CAD programs or its own DesignModeler. ANSYS Workbench performs structural, thermal, electromagnetic and explicit dynamic analyses. ANSYS [7] is capable of solving a number of problems in the field of steady state and time-dependent problems. ANSYS can also work in the areas of static analysis where the effect of inertia is excluded and dynamic analysis where it is a must to consider inertial effects. It also allows performing nonlinear transient dynamic analysis (time-dependent response).

Graphene [8] is a 2D sheet of single carbon atom thickness with a honeycomb arrangement of carbon atoms. Graphene has a very high strength-to-weight ratio due to its very large value of Young's modulus. The density of graphene being 2267 kg/m^3 makes it super light material as well. Both these properties makes it a perfect choice for a bullet-resistant material.

2 Finite Element Modeling

The design of the composite-based bullet-resistant armor was done by using ANSYS-Explicit Dynamics 18.1. The simulations were carried out in three phases. To reduce the computational time per simulation, a smaller circular region of diameter 40 mm was taken for phase-1 simulations analysis. The bullet was considered to have a spherical nose with a diameter of 7.62 mm comparable to an AK-47 bullet. Initially, the simulation was done on a sample circular plate having 40 mm diameter and 2 mm thickness as shown in Fig. 1. The material of both plate and bullet was considered to be AISI 4340 Steel. Later, to study the effect of change in Young's modulus, the material properties of AISI 4340 Steel were changed. The Young's modulus was increased in steps to analyze its effect on residual velocity of the projectile while keeping all other material properties unchanged. For safety purpose, the impact velocity was taken a little higher from the actual AK-47 bullet velocity range of 720–750 m/s. The impact velocity for each simulation was considered to be 1000 m/s. In Phase-1, the thickness of the target plate was kept constant at 2 mm while Young's modulus was increased in steps starting from 2×10^{11} Pa in AISI 4340 Steel to 2.5×10^{12} Pa in Material 'G' as given in Table 2. The properties of AISI Steel 4340 steel and materials A–G used in ANSYS has been shown in Fig. 2.

The plate-projectile finite element model was made up of a total 11,840 nodes and 8863 elements in Phase-1 samples with an element size of 1 mm.

In Phase-2 simulations, Material G which had shown the best results in the Phase 1 simulations was taken and was divided into sub-cases with gradual increase in the thickness of the plate to get the threshold thickness which cannot be perforated. The thickness of Material G plate was varied from 2 to 6 mm. Later, similar simulations were done on silicon carbide (SiC) to find out the threshold plate thickness which cannot be penetrated by the projectile at 1000 m/s velocity. The simulations on SiC were done on sample plate of 60 mm diameter and thickness varying from 4 to 8 mm. The element size for the ceramic was taken as default so as to decrease the computational time to 7–8 h per simulation.

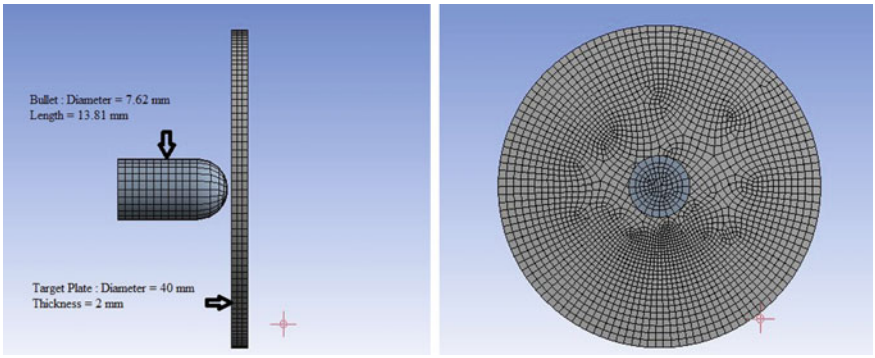

Fig. 1 Finite element model of target plate and projectile for Phase 1 analysis

Table 2 Young's modulus of materials used in simulations of phase 1

S. No.	Material	Young's modulus	Units
1	AISI Steel 4340	2.0×10^{11}	Pa
2	Material A	3.0×10^{11}	Pa
3	Material B	5.0×10^{11}	Pa
4	Material C	7.0×10^{11}	Pa
5	Material D	1.1×10^{12}	Pa
6	Material E	1.5×10^{12}	Pa
7	Material F	2.0×10^{12}	Pa
8	Material G	2.5×10^{12}	Pa

In Phase-3 simulation, a 0.5 mm graphene layer was added as a back plate to the silicon carbide matrix and the result was compared with the previous results of simple silicon carbide plate without any graphene layer. The target plate diameter for phase-3 simulations was taken same as phase-2 simulations, i.e., 60 mm, while thickness of SiC layer was taken 4 mm with 0.5 mm graphene layer as back plate in combination. The element size for phase-3 simulation was again taken as default for the similar reason. The residual velocity in 4 mm SiC case came out to be 531.54 m/s in phase-2 simulations which became the initial velocity or the impact velocity for the graphene layer.

3 Assumptions and Material Model

Assumptions made while performing the simulations are given below:

(i) The gravity effect on bullet has been neglected in every simulation.
(ii) There is no medium in between target plate and bullet; hence, air drag on the bullet has been neglected. This means that the velocity of projectile will remain same as the initial velocity till the point of impact.
(iii) The distance between bullet and target plate is kept small (0.5 mm) so that total simulation time can be reduced to 6–10 h per simulation.

The material model used in these simulations is Johnson–Cook model [9]. According to Johnson–Cook material model, the yield stress with respect to temperature and plastic strain is given by (1);

$$\sigma_y = \left[A + B\varepsilon^N\right][1 + C\ln(\varepsilon)]\left[1 - \theta^M\right] \tag{1}$$

where A, B, C, M and N are model parameters, ε is plastic strain, and θ is homologous temperature given by (2);

Properties of Outline Row 167: STEEL 4340

	A	B	C
1	Property	Value	Unit
2	Density	7830	kg m^-3
3	Specific Heat	477	J kg^-1 C^-1
4	Johnson Cook Strength		
5	Strain Rate Correction	First-O...	
6	Initial Yield Stress	7.92E+08	Pa
7	Hardening Constant	5.1E+08	Pa
8	Hardening Exponent	0.26	
9	Strain Rate Constant	0.014	
10	Thermal Softening Exponent	1.03	
11	Melting Temperature	1519.9	C
12	Reference Strain Rate (/sec)	1	
13	Bulk Modulus	1.59E+11	Pa
14	Shear Modulus	8.18E+10	Pa

(a) AISI Steel 4340

Properties of Outline Row 4: Material A

	A	B	C
1	Property	Value	Unit
2	Density	7830	kg m^-3
3	Isotropic Elasticity		
4	Derive from	Young's...	
5	Young's Modulus	3E+11	Pa
6	Poisson's Ratio	0.28	
7	Bulk Modulus	2.2727E+11	Pa
8	Shear Modulus	1.1719E+11	Pa
9	Specific Heat	477	J kg^-1 C^-1
10	Johnson Cook Strength		
11	Strain Rate Correction	First-O...	
12	Initial Yield Stress	7.92E+08	Pa
13	Hardening Constant	5.1E+08	Pa
14	Hardening Exponent	0.26	
15	Strain Rate Constant	0.014	
16	Thermal Softening Exponent	1.03	
17	Melting Temperature	1519.9	C
18	Reference Strain Rate (/sec)	1	

(b) Material A

Properties of Outline Row 4: Material B

	A	B	C
1	Property	Value	Unit
2	Density	7830	kg m^-3
3	Isotropic Elasticity		
4	Derive from	Young's...	
5	Young's Modulus	5E+11	Pa
6	Poisson's Ratio	0.28	
7	Bulk Modulus	3.7879E+11	Pa
8	Shear Modulus	1.9531E+11	Pa
9	Specific Heat	477	J kg^-1 C^-1
10	Johnson Cook Strength		
11	Strain Rate Correction	First-O...	
12	Initial Yield Stress	7.92E+08	Pa
13	Hardening Constant	5.1E+08	Pa
14	Hardening Exponent	0.26	
15	Strain Rate Constant	0.014	
16	Thermal Softening Exponent	1.03	
17	Melting Temperature	1519.9	C
18	Reference Strain Rate (/sec)	1	

(c) Material B

Properties of Outline Row 5: Material C

	A	B	C
1	Property	Value	Unit
2	Density	7830	kg m^-3
3	Isotropic Elasticity		
4	Derive from	Young's...	
5	Young's Modulus	7E+11	Pa
6	Poisson's Ratio	0.28	
7	Bulk Modulus	5.303E+11	Pa
8	Shear Modulus	2.7344E+11	Pa
9	Specific Heat	477	J kg^-1 C^-1
10	Johnson Cook Strength		
11	Strain Rate Correction	First-O...	
12	Initial Yield Stress	7.92E+08	Pa
13	Hardening Constant	5.1E+08	Pa
14	Hardening Exponent	0.26	
15	Strain Rate Constant	0.014	
16	Thermal Softening Exponent	1.03	
17	Melting Temperature	1519.9	C
18	Reference Strain Rate (/sec)	1	

(d) Material C

Properties of Outline Row 6: Material D

	A	B	C
1	Property	Value	Unit
2	Density	7830	kg m^-3
3	Isotropic Elasticity		
4	Derive from	Young's...	
5	Young's Modulus	1E+12	Pa
6	Poisson's Ratio	0.28	
7	Bulk Modulus	7.5758E+11	Pa
8	Shear Modulus	3.9063E+11	Pa
9	Specific Heat	477	J kg^-1 C^-1
10	Johnson Cook Strength		
11	Strain Rate Correction	First-O...	
12	Initial Yield Stress	7.92E+08	Pa
13	Hardening Constant	5.1E+08	Pa
14	Hardening Exponent	0.26	
15	Strain Rate Constant	0.014	
16	Thermal Softening Exponent	1.03	
17	Melting Temperature	1519.9	C
18	Reference Strain Rate (/sec)	1	

(e) Material D

Fig. 2 Properties of the materials used in phase 1 simulations (ANSYS 18.1 Engineering Data Sources)

Properties of Outline Row 7: Material E

	A	B	C
1	Property	Value	Unit
2	Density	7830	kg m^-3
3	Isotropic Elasticity		
4	Derive from	Young's...	
5	Young's Modulus	1.5E+12	Pa
6	Poisson's Ratio	0.28	
7	Bulk Modulus	1.1364E+12	Pa
8	Shear Modulus	5.8594E+11	Pa
9	Specific Heat	477	J kg^-1 C^-1
10	Johnson Cook Strength		
11	Strain Rate Correction	First-O...	
12	Initial Yield Stress	7.92E+08	Pa
13	Hardening Constant	5.1E+08	Pa
14	Hardening Exponent	0.26	
15	Strain Rate Constant	0.014	
16	Thermal Softening Exponent	1.03	
17	Melting Temperature	1519.9	C
18	Reference Strain Rate (/sec)	1	

(f) Material E

Properties of Outline Row 8: Material F

	A	B	C
1	Property	Value	Unit
2	Density	7830	kg m^-3
3	Isotropic Elasticity		
4	Derive from	Young's...	
5	Young's Modulus	2E+12	Pa
6	Poisson's Ratio	0.28	
7	Bulk Modulus	1.5152E+12	Pa
8	Shear Modulus	7.8125E+11	Pa
9	Specific Heat	477	J kg^-1 C^-1
10	Johnson Cook Strength		
11	Strain Rate Correction	First-O...	
12	Initial Yield Stress	7.92E+08	Pa
13	Hardening Constant	5.1E+08	Pa
14	Hardening Exponent	0.26	
15	Strain Rate Constant	0.014	
16	Thermal Softening Exponent	1.03	
17	Melting Temperature	1519.9	C
18	Reference Strain Rate (/sec)	1	

(g) MaterialF

Properties of Outline Row 9: Material G

	A	B	C
1	Property	Value	Unit
2	Density	7830	kg m^-3
3	Isotropic Elasticity		
4	Derive from	Young's...	
5	Young's Modulus	2.5E+12	Pa
6	Poisson's Ratio	0.28	
7	Bulk Modulus	1.8939E+12	Pa
8	Shear Modulus	9.7656E+11	Pa
9	Specific Heat	477	J kg^-1 C^-1
10	Johnson Cook Strength		
11	Strain Rate Correction	First-O...	
12	Initial Yield Stress	7.92E+08	Pa
13	Hardening Constant	5.1E+08	Pa
14	Hardening Exponent	0.26	
15	Strain Rate Constant	0.014	
16	Thermal Softening Exponent	1.03	
17	Melting Temperature	1519.9	C
18	Reference Strain Rate (/sec)	1	

(h) Material G

Fig. 2 (continued)

$$\theta = \frac{T - T_{\mathrm{r}}}{T_{\mathrm{M}} - T_{\mathrm{r}}} \tag{2}$$

where T is the material temperature, T_{r} is the room temperature and T_{M} is the melting temperature.

The damage (D) is bounded in between 0 and 1. The damage quantity is given as (3);

$$D = \frac{\varepsilon}{\varepsilon^f} \tag{3}$$

where ε^f is known as failure strain and is given as (4);

$$\varepsilon^f = \left\{\left[D_1 + D_2 e^{D_3\sigma^*}\right]\left[1 + D_4 \ln\left(\varepsilon^*\right)\right][1 + D_5\theta]\sigma^* < 1.5\right.$$
$$\varepsilon^f = \left\{\varepsilon^f_{\min}\sigma^* \geq 1.5\right. \tag{4}$$

where D_1, D_2, D_3, D_4, D_5 and $\varepsilon^f_{\min}$ are the parameters of the model and σ^* is known as tri-axial ratio and is given as (5);

$$\sigma^* = \frac{P}{\sigma} \tag{5}$$

where P is the hydrostatic pressure and σ is the von Mises stress. The quantity ε^* is known as dimensionless plastic strain.

Similarly, Johnson-Holmquist model [10] is used for ceramic material, i.e., SiC. According to this model, the relationship between fracture strength, volume and pressure is represented by (6);

$$\sigma^* = \left[A(1 - D) + B P^{*n}\right]\left[1 + C \ln \varepsilon^*\right] \tag{6}$$

where A, B, C and n are model constants, D is damage encountered to the target similar to damage given by Eq. 3, ε^* is dimensionless plastic strain, σ^* is normalized strength and $P^*$is normalized pressure given by (7) and (8) respectively;

$$\sigma^* = \frac{\sigma}{f'_c} \tag{7}$$

$$P^* = \frac{P}{f'_c} \tag{8}$$

where f'_c is uniaxial compressive strength, σ is von Mises flow stress and P is pressure.

4 Results and Discussion

4.1 Model Analysis

Finite element analysis was done using ANSYS 18.1 Explicit dynamics to simulate the effect of perforation. The simulations were done on an i5-HP PC with 4.00 GB RAM and 2.4 GHz processor for an analysis time period of 0.00035 s for each phase. The analysis time is taken small so as to decrease the simulation computational time of complete perforation. Each simulation was completed within time duration of 7–10 h.

4.2 Phase-1 Simulations

The first simulation was carried out with both bullet and plate material to be AISI Steel 4340 where plate thickness was 2 mm, diameter 40 mm and impact velocity of 1000 m/s. It was observed that the velocity goes on decreasing during perforation and becomes constant after complete penetration (neglecting the effect of air drag and gravity). Initially, the bullet-plate system had a total energy corresponding to the kinetic energy of the bullet only. During perforation of the plate, the kinetic energy of the bullet decreases and was utilized in increasing the internal energy, breaking and plastic deformation of the plate. The result of this simulation was compared with the experimental work of Kurtaran et al. [11]. It is important to compare the simulation and experimental results so that in case of large errors the simulation model can be improved by using some model updating techniques [12–17]. The residual velocity in this simulation came out to be 793.07 m/s which was in close proximity to the latter's results which was around 860 m/s. This simulation verifies the appreciable accuracy of this numerical material model with the realistic experiment, hence making it the base model for the next simulations. The graph generated by ANSYS between residual velocity and time for AISI 4340 Steel is shown in Fig. 3 and equivalent strain and deformation of the target plate is shown in Fig. 4.

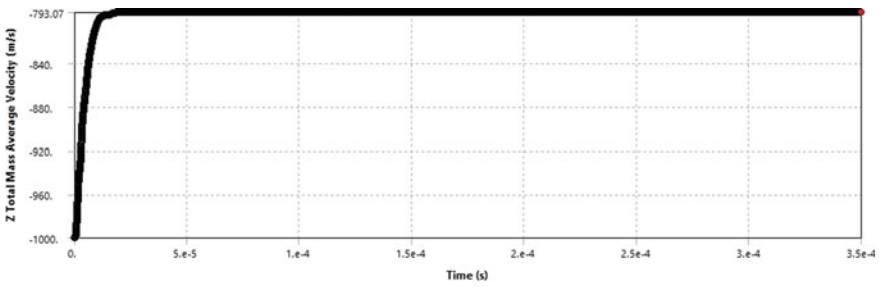

Fig. 3 Residual velocity versus time for AISI 4340 Steel

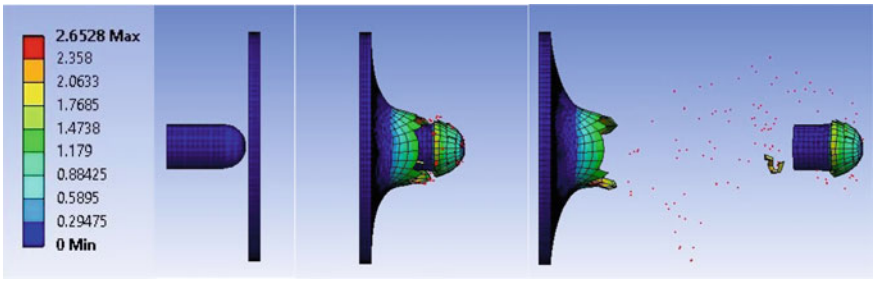

Fig. 4 Equivalent elastic strain of AISI Steel 4340 deformed target plate and bullet

Table 3 Residual velocities of the projectile after perforation of target plate of material A–G

S. No.	Material	Young's modulus (Pa)	Residual velocity of the bullet (m/s)
1	Material A	3.0×10^{11}	779.77
2	Material B	5.0×10^{11}	772.31
3	Material C	7.0×10^{11}	766.13
4	Material D	1.1×10^{12}	759.41
5	Material E	1.5×10^{12}	753.01
6	Material F	2.0×10^{12}	748.39
7	Material G	2.5×10^{12}	745.08

Next simulations in phase-1 were carried out on Material A, B, C, D, E, F and G with similar material properties to AISI Steel 4340 except for an increase in Young's modulus within these materials. It was observed that there is a significant decrease in the residual velocity of the bullet with the increase in Young's modulus of the material for the same 2 mm thickness. This is because of the fact that for the same deformation, more stress is required for the material having higher Young's modulus. The results of above materials are given in Table 3 and Fig. 5.

4.3 Phase-2 Simulations

Material G, which had shown the best result in terms of bullet-resistant ability, was considered for Phase-2 simulations and was sub-divided into different cases to find out the minimum thickness which cannot be perforated. The density of Material G is same as that of AISI Steel 4340. The residual velocities for Phase-2 simulations are shown in Fig. 6. It was observed that the minimum thickness required by Material G comes out to be close to 6 mm to avoid complete penetration as given in Fig. 7.

Similar simulations were done on SiC material alone, and the results were compared to the Material G. The simulations were done on a sample circular region of 60 mm diameter. The thickness was gradually increased from 4 mm to find out the minimum thickness of SiC required to resist the bullet without perforation. It was observed that the residual velocity drops down to zero in between 7 and 8 mm, i.e., at around 7.75 mm. Since the density of SiC is less than the half density of Material G or AISI Steel, SiC, being lighter for same conditions, would be a better choice than AISI Steel 4340 in terms of weight-to-strength ratio. Material properties of SiC are shown in Fig. 8.

The simulations result for SiC is given in Table 4, and graphs generated for SiC are shown in Fig. 9. The deformation of the target plate is shown in Fig. 10.

4.4 Phase-3 Simulations

Phase-3 simulations were similar to SiC Phase-2 simulations. A 0.5 mm layer of graphene was added as the back plate to the SiC matrix, and the composite was then simulated for 1000 m/s impact velocity of the projectile. The properties of graphene are given in Fig. 11. This simulation was carried out in two parts. Firstly, the residual velocity for 4 mm SiC plate came out to be 531.45 for 1000 m/s impact velocity. In the second stage of this simulation, the residual velocity from SiC layer becomes the impact velocity for the graphene layer. It was observed that adding graphene layer

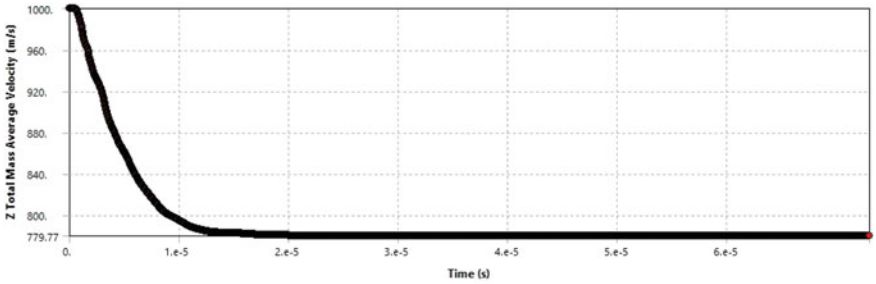

(a) Residual velocity of the bullet for Material A

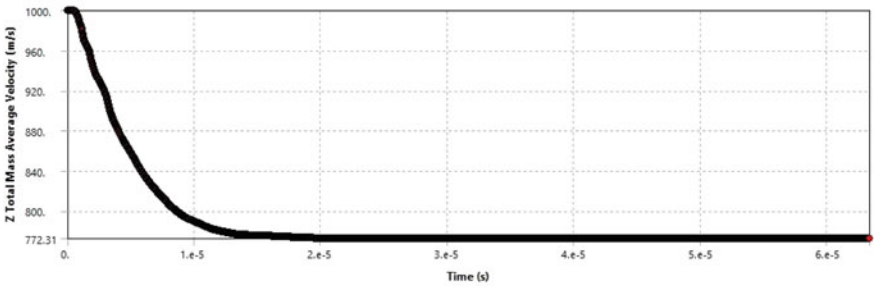

(b) Residual velocity of the bullet for Material B

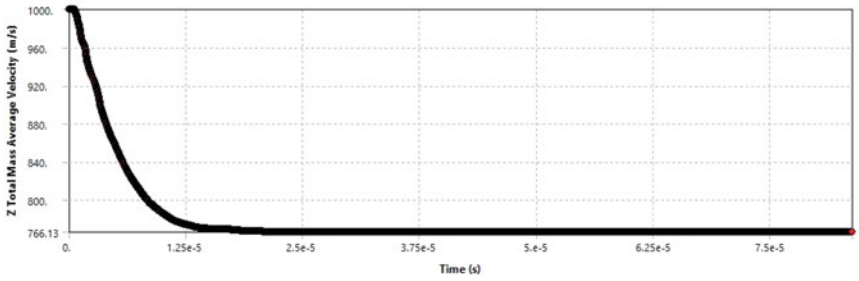

(c) Residual velocity of the bullet for Material C

Fig. 5 Residual velocities of projectile with time for different materials

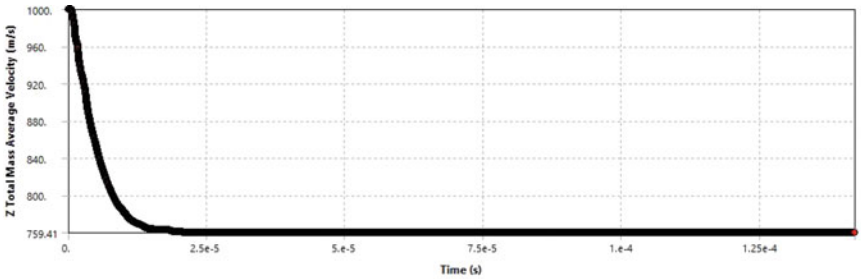

(d) Residual velocity of the bullet for Material D

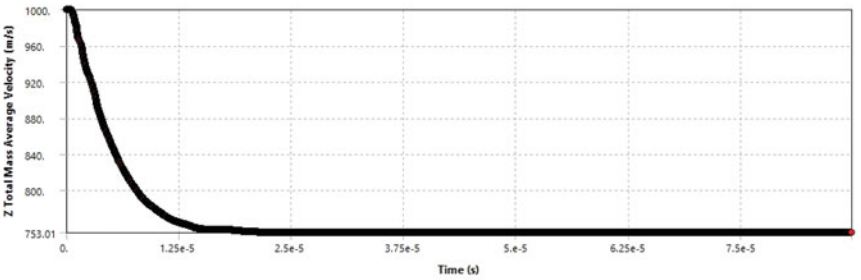

(e) Residual velocity of the bullet for Material E

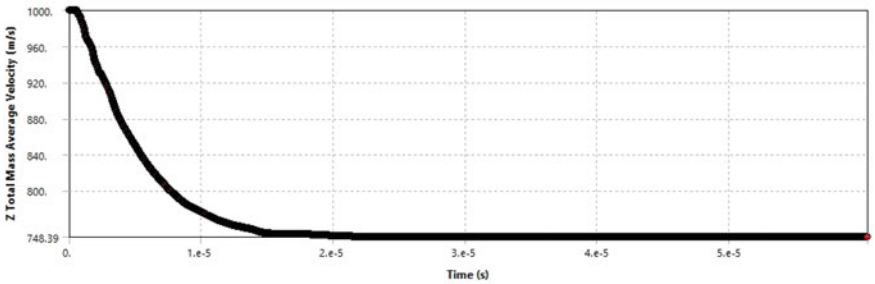

(f) Residual velocity of the bullet for Material F

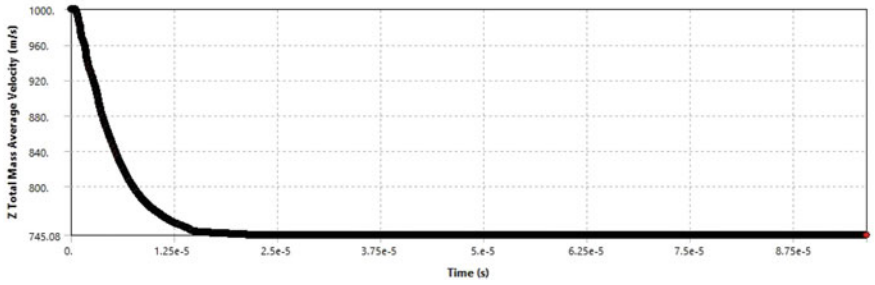

(g) Residual velocity of the bullet for Material G

Fig. 5 (continued)

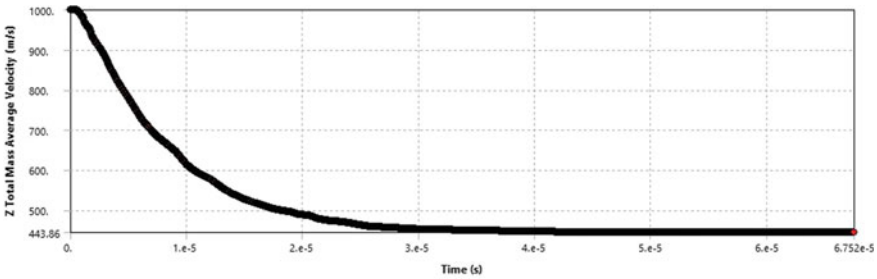

(a) Residual velocity of the bullet for Material G at 4 mm thickness

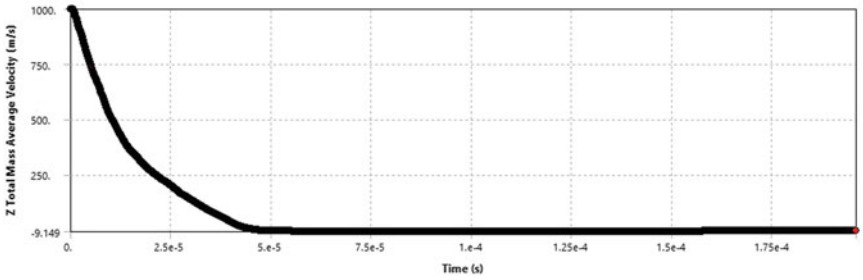

(b) Residual velocity of the bullet for Material G at 6 mm thickness

Fig. 6 Residual velocities of projectile with time for different thickness

in the SiC matrix increased the strength of the material and 0.5 mm graphene layer was enough to withstand the impact completely reducing down the residual velocity to zero as given by Fig. 12.

5 Conclusion

From the above simulations done in three phases, the following can be concluded:

(i) With the increase in Young's modulus of the material, it is resistance to projectile penetration increases. This is because of the reason that for the same deformation, more stress is required for the material having higher Young's modulus.

(ii) The minimum thickness to resist complete perforation required by Material G plate having density 7830 kg/m^3 comes out to be 5.9 mm while for SiC plate having density 3215 kg/m^3, it comes out to be 7.75 mm. Although the thickness required is more in case of SiC, the SiC plate would weigh almost half that of material G. Hence, SiC would be a better choice than the latter.

(iii) Addition of graphene layer to SiC matrix increases its strength by almost 45–50%. The minimum thickness required by this SiC-graphene composite comes

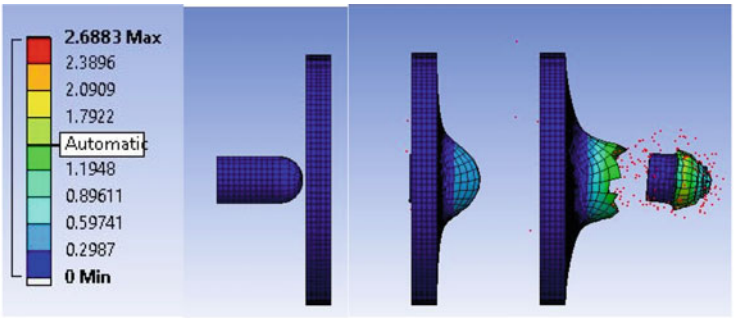

(a) Equivalent elastic strain of 4 mm thick Material G deformed target plate and bullet.

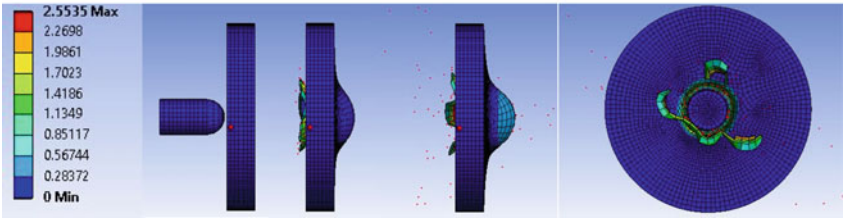

(b) Equivalent elastic strain of 6 mm thick Material G deformed target plate and bullet.

Fig. 7 Deformation in Material G

Properties of Outline Row 3: SiC

	A	B	C	D	E
1	Property	Value	Unit		
2	Material Field Variables	Table			
3	Density	3215	kg m^-3		
4	Johnson-Holmquist Strength Segmented				
17	~~Bulk Modulus~~	2.2E+11	Pa	☑	
18	Shear Modulus	1.935E+11	Pa		
19	Polynomial EOS				
20	Parameter A1	2.2E+11	Pa		
21	Parameter A2	3.61E+11	Pa		
22	Parameter A3	0	Pa		
23	Parameter B0	0			
24	Parameter B1	0			
25	Parameter T1	2.2E+11	Pa		
26	Parameter T2	0	Pa		

Fig. 8 Material properties of SiC

Table 4 Residual velocity of the projectile for SiC target plate of different thickness

S. No.	Thickness of the plate (mm)	Residual velocity of the bullet (m/s)
1	4	531.53
2	6	242.94
3	7.75	$-0.3153 \cong 0$

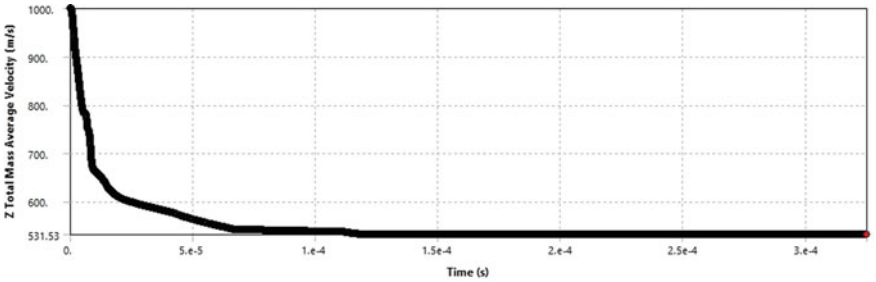

(a) Residual velocity of the bullet for SiC of 4 mm thickness

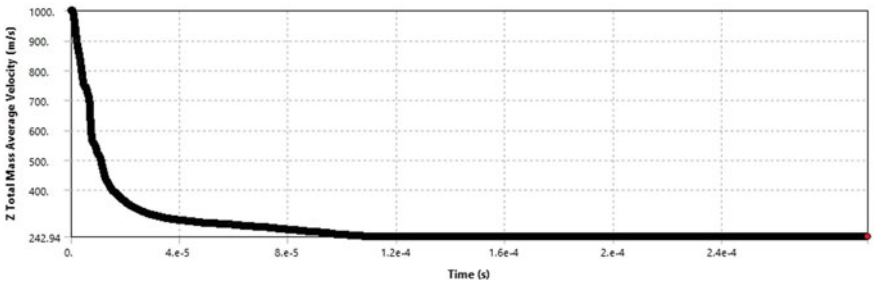

(b) Residual velocity of the bullet for SiC of 6 mm thickness

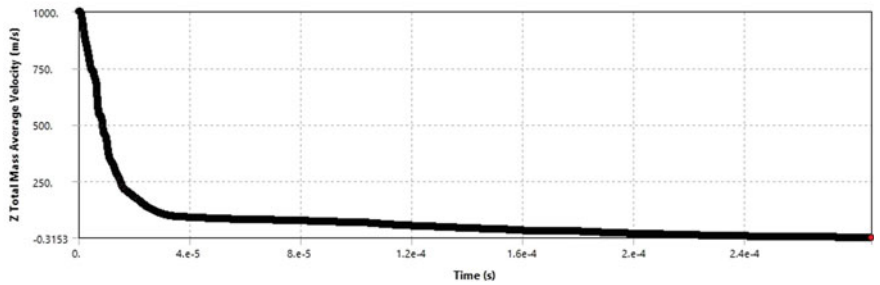

(c) Residual velocity of the bullet for SiC of 7.75 mm thickness

Fig. 9 Residual velocity of the bullet with time for SiC target

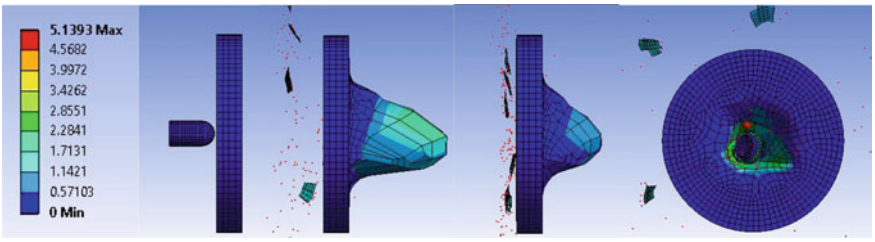

Fig. 10 Equivalent elastic strain in deformed 7.75 mm SiC plate and bullet

Properties of Outline Row 4: Graphene 2

	A	B	C	D	E
1	Property	Value	Unit		
2	Material Field Variables	Table			
3	Density	2267	kg m^-3		
4	Isotropic Elasticity				
5	Derive from	Youn...			
6	Young's Modulus	1.3E+11	Pa		
7	Poisson's Ratio	0.186			
8	Bulk Modulus	6.9002E+10	Pa		
9	Shear Modulus	5.4806E+10	Pa		

Fig. 11 Properties of graphene

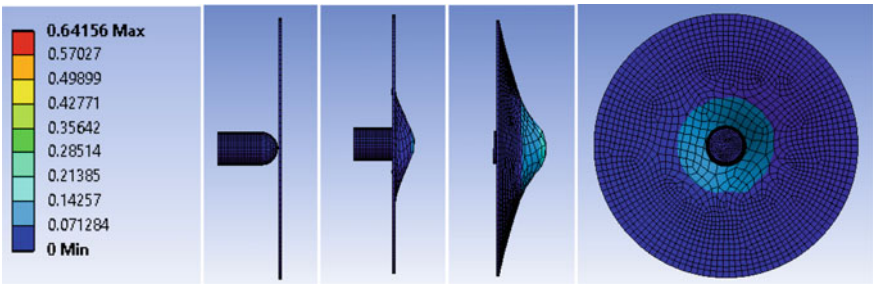

Fig. 12 Equivalent elastic strain in deformed 0.5 mm graphene back plate and bullet impacted with 531.54 m/s

out to be 4.5 mm with 4 mm SiC layer and 0.5 mm graphene layer, which is less than SiC alone. Hence, making it 40–50% more lighter material than SiC alone.

References

1. Børvik T (2001) Ballistic penetration and perforation of steel plates. Fakultet for ingeniørvitenskap og teknologi
2. ANSYS N (2013) ANSYS explicit dynamics in ANSYS workbench user's guide. ANSYS. Inc., 15
3. Narayanamurthy V, Rao CL, Rao BN (2014) Numerical simulation of ballistic impact on armour plate with a simple plasticity model. Def Sci J 64(1):55–61
4. Adams B, Geers MGD, van Dommelen JAW, Huizinga ATMJM (2006) Simulation of ballistic impacts on armored civil vehicles. Technische Universiteit Eindhoven
5. Bhuarya MK, Rajput MS, Gupta A (2017) Finite element simulation of impact on metal plate. Procedia Eng 173:259–263
6. Kpenyigba KM, Jankowiak T, Rusinek A, Pesci R, Wang B (2015) Effect of projectile nose shape on ballistic resistance of interstitial-free steel sheets. Int J Impact Eng 79:83–94
7. Thompson MK, Thompson JM (2017) ANSYS mechanical APDL for finite element analysis. Butterworth-Heinemann
8. Papageorgiou DG, Kinloch IA, Young RJ (2017) Mechanical properties of graphene and graphene-based nanocomposites. Prog Mater Sci 90:75–127
9. Sanchez JJ (2018) The finite strain johnson cook plasticity and damage constitutive model in ALEGRA (No. SAND-2018-1392). Sandia National Lab.(SNL-NM), Albuquerque, NM (United States)
10. Johnson GR (2011) Numerical algorithms and material models for high-velocity impact computations. Int J Impact Eng 38(6):456–472
11. Kurtaran H, Buyuk M, Eskandarian A (2003) Ballistic impact simulation of GT model vehicle door using finite element method. Theor Appl Fract Mech 40:113–121
12. Sehgal S, Kumar H (2020) Damage and damping identification in a structure through novel damped updating method. Iran J Sci Technol Trans Civ Eng
13. Sehgal S, Kumar H (2019) Experimental damage identification by applying structural dynamic model updating. J Theor Appl Mech (Bulgaria) 49:51–61
14. Sehgal S, Kumar H (2017) Novel dynamic model updating technique for damped mechanical system. J Theor Appl Mech 47(4):75–85
15. Sehgal S, Kumar H (2014) Damage detection using Derringer's function based weighted model updating method. In: Wicks A (ed) Structural health monitoring, vol 5. Springer, New York, pp 241–253
16. Sehgal S, Kumar H (2014) Development of efficient model updating technique using multi-stage response surfaces and derringer's function. In: Proceedings of the first international conference on recent advances in engineering and computational sciences, IEEE Xplore, pp 1–6
17. Sehgal S, Kumar H (2016) Structural dynamic model updating techniques: a state of the art review. Arch Comput Methods Eng 23:515–533

Artificial Neural Network Model Development for the Analysis of Maximum Pressure of Hole Entry Journal Bearing Using SciLab

Sunil Kumar, Vijay Kumar, and Anoop Kumar Singh

Abstract Artificial neural network (ANN) is used as an advanced technology for the prediction of the behaviour of mechanical systems. ANN research is focused on developing computational approaches to analyse the complex and time-consuming problems. The present paper shows the ANN predictions for maximum pressure of hole entry hybrid journal bearing for different values of non-dimensional load and speed parameters. The present ANN model is trained and tested in SciLab using literature data and found capable to show more accurate results. Feed forward back propagation algorithm is used in this ANN model to minimize the error and to update the weights. Sigmoid activation function is used for hidden layer neurons and output layer neuron. ANN is found as best predictor for journal bearing analysis.

Keywords ANN · Journal bearing · Finite element methods · SciLab

1 Introduction

Journal bearings is used for heavy load and high speed moving mechanical assemblies in industrial and vacuum applications. Hydrostatic, hydrodynamic and hybrid journal bearings are used depending upon the application. In hydrostatic bearing, the continuous supply of lubricant is required with the help of pump. It works on hydrostatic law of fluid statics. In hydrodynamic bearings, the lubricant flow takes place by the hydrodynamic action. No external pressure is required for lubricant flow. Hybrid journal bearings combine the advantages of both hydrostatic and hydrodynamic journal bearings.

The generally used configurations of journal bearings are circular, elliptical, conical, 2-lobes, 3-lobes and four lobes [1–3]. The lubricant entry in the clearance space may be hole entry or slot entry. In hole entry journal bearings, the flow of lubricant is controlled by restrictors such as orifice, capillary compensated or constant flow valve restrictor [4]. The schematic diagram of hole entry journal bearing is shown

S. Kumar (✉) · V. Kumar · A. K. Singh
Chitkara Institute of Engineering and Technology, Chitkara University, Punjab, India
e-mail: sunil.sharma@chitkara.edu.in

L. M. Das et al. (eds.), *Emerging Trends in Mechanical Engineering*, Lecture Notes in Mechanical Engineering, https://doi.org/10.1007/978-981-15-8304-9_2

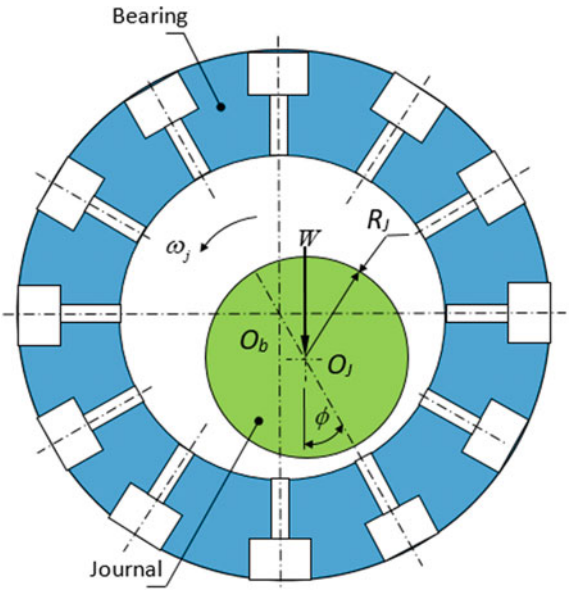

Fig. 1 Schematic diagram of hole entry journal bearing

in Fig. 1. In this figure, (W), (R_J), (O_b), (O_J), (ϕ) and (ω_J) represent external applied load, journal radius, bearing centre, journal centre, attitude angle and journal angular velocity. Ram and Sharma [5] analysed the performance of micropolar lubricated journal bearing and Khakse et al. [6] analysed the performance of conical journal bearing. The results of these two research papers are considered here for the ANN model validation.

Artificial neural network (ANN) is considered as the best predictor for many mechanical problems, particularly for the journal bearing analysis [7–9]. The principle of ANN is similar to the functioning of the human brain neurons. The signal from one neuron is fed to the another neuron. When the threshold value is achieved, the neurons fire and this process is continuous till the signal arrived at the final neuron. ANN simplifies the complex journal bearing problems by using computer programs. In the present work, SciLab is used for program development. Sinanoğlu et al. [10] analysed the pressure variations at circumferential positions experimentally and developed the ANN model to predict the behaviour. A close agreement for experimental values and ANN model values was obtained. ANN was also used for bearing fault detection and diagnosis [11, 12].

2 Analysis of Journal Bearing

Journal bearings can be analysed theoretically and experimentally to determine their performance characteristics. Finite element method (FEM) is widely used for theoretical analysis. The governing Reynolds equation in non-dimensional form for flow field in journal bearing is shown as Eq. (1) [13–15];

$$\frac{\partial}{\partial\alpha}\left(\overline{h}^3\overline{F}_2\frac{\partial\overline{p}}{\partial\alpha}\right)+\frac{\partial}{\partial\beta}\left(\overline{h}^3\overline{F}_2\frac{\partial\overline{p}}{\partial\beta}\right)=\Omega\left[\frac{\partial}{\partial\alpha}\left\{\left(1-\frac{\overline{F_1}}{\overline{F_0}}\right)\overline{h}\right\}\right]+\frac{\partial\overline{h}}{\partial\overline{t}} \tag{1}$$

In this equation, α and β shows circumferential and longitudinal coordinates. $\overline{F}_1, \overline{F}_2$ and $\overline{F}_3$ are the viscosity functions. $\overline{p}, \Omega$ and $\overline{h}$ are the pressure, speed parameter and film thickness, respectively. This governing equation can be modified depending upon the lubricant model used. Finally, the performance characteristics can be determined by using the appropriate equation.

The pressure calculation in FEM is given by the Eq. (2);

$$\overline{p}=\sum_{j=1}^{n_l^e}\overline{p}_j N_j \tag{2}$$

Pressure variation in journal bearing is the static performance characteristic which varies at each point during rotation of the journal. In this document, the variation of maximum pressure value with respect to load is presented and discussed.

3 Artificial Neural Network

Feed forward network is multilayer neural network (MLN) which contains hidden layers. Total number of hidden layers and neurons in hidden layer can be decided heuristically whereas the number of neurons in input layer and output layer are fixed depending upon the concerned problem. Feed forward neural network adopts trial-and-error approach to solve complex problems associated with complex relationship between input and output data set. Back propagation algorithm is employed for learning of feed forward neural network because of its simple implementation in journal bearing performance analysis. Feed forward back propagation algorithm uses the gradient decent approach for the adjustment of connected weights and finally to minimize the error. Using this approach, best possible results can be predicted.

Sigmoid activation function is mostly used in ANN. It is used to get the nonlinear output from the hidden layers and output layer. This function gives the output value in the range 0–1. If desired output in not in this range, then some normalization or standardization methods should be used to convert the data in the range of 0–1.

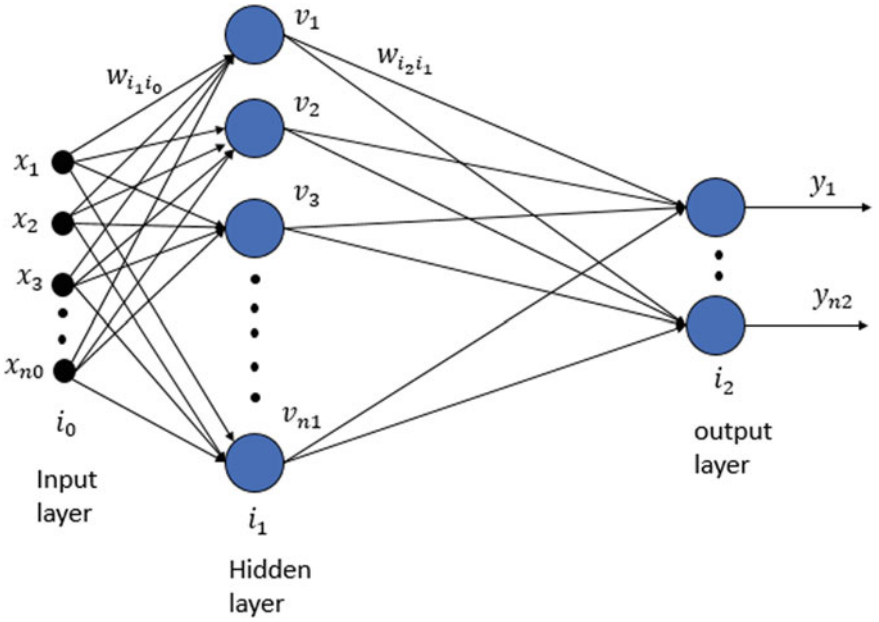

Fig. 2 Schematic diagram of feed forward neural network

A single hidden-layered feed forward neural network with neuron connectivity is Shown in Fig. 2.

Input to the hidden layer $\left(h_{i_1}\right)$ is given by Eq. (3) where x_{i_0} represents the data for input layer

$$h_{i_1} = \sum_{i_0=1}^{n_0} w_{i_1 i_0} x_{i_0} \tag{3}$$

The response of the hidden layer $\left(v_{i_1}\right)$ is shown in Eq. (4) by sigmoid activation function;

$$v_{i_1} = \frac{1}{1 + e^{-h_{i_1}}} \tag{4}$$

where h_{i_2} is the input to the output layer and given as Eq. (5);

$$h_{i_2} = \sum_{i_1=1}^{n_1} w_{i_2 i_1} v_{i_1} \tag{5}$$

The response of the output layer y_{i_2} is shown as Eq. (6) by sigmoid activation function;

$$y_{i_2} = \frac{1}{1 + e^{-h_{i_2}}} \tag{6}$$

These weights should be updated to minimize the error. Mean square error is calculated by using given relation as Eq. (7);

$$\text{Error} = \frac{1}{2} \sum_{i_2=1}^{n_2} \left(y_{i_2}^d - y_{i_2}\right)^2 \tag{7}$$

where $y_{i_2}^d$ is desired output and y_{i_2} is ANN model output. The equation to get updated weight is given by standard gradient descent approach as Eq. (8);

$$w_{i_2 i_1}(\text{new}) = w_{i_2 i_1}(\text{old}) - \eta \frac{\partial E}{\partial w_{i_2 i_1}} \tag{8}$$

where $w_{i_2 i_1}$ are weights associated between output layer neurons and hidden layer neurons, η is the learning rate and E is the mean square error. This equation can also be written as Eq. (9);

$$w_{i_2 i_1}(\text{new}) = w_{i_2 i_1}(\text{old}) + \eta \delta_{i_2} v_{i_1} \tag{9}$$

where $\delta_{i_2} = \left(y_{i_2}^d - y_{i_2}\right) y_{i_2} \left(1 - y_{i_2}\right)$ called error back propagated through weights from output layer neurons to hidden layer neurons. Response of hidden layer neurons is written as v_{i_1}. Same procedure is followed to update the weights between hidden layer neurons and input layer neurons. Associated gradient descent approach is shown as Eq. (10);

$$w_{i_1 i_0}(\text{new}) = w_{i_1 i_0}(\text{old}) - \eta \frac{\partial E}{\partial w_{i_1 i_0}} \tag{10}$$

where $w_{i_1 i_0}$ are weights associated between hidden layer neurons and input layer neurons. This equation can also be written as Eq. (11);

$$w_{i_1 i_0}(\text{new}) = w_{i_1 i_0}(\text{old}) + \eta \delta_{i_1} x_{i_0} \tag{11}$$

where $\delta_{i_1} = v_{i_1} \left(1 - v_{i_1}\right) \sum_{i_2=1}^{n_2} \delta_{i_2} w_{i_2 i_1}$ called error back propagated through weights from hidden layer neurons to input layer neurons.

If a situation occurs when the input becomes zero during iteration process, it will give no value when multiply by weights. Hence, to get the non-zero value, a bias is introduced. The value of bias should not be zero.

4 Algorithm Development

The present work is to develop the ANN model to get the maximum pressure values for the journal bearing. These values are compared with the literature data to validate the program. The non-dimensional pressure variations with respect to non-dimensional load is considered for study and shown in Fig. 3.

Two number of neurons are considered in input layer (first for the non-dimensional load values and second for the bias). Bias value is considered as 1. One neuron for output layer and ten neurons for hidden layers are considered. Sigmoid activation function is used for hidden layer and output layer in SciLab program (Fig. 4). The behaviour of neurons in this SciLab program is linear for input layer and nonlinear for hidden and output layer. The nonlinearity is achieved by using activation function.

SciLab is an open-source software used for programming and proved as better alternate to MATLAB. In the present work, the ANN coding is done using SciLab. Epocs are the number of iterations performed in the program to achieve the convergence criteria. The initial weights are chosen randomly. Hence, the number of iterations vary each time when running the program. The average value of iterations is considered. The error is minimized by using the above-mentioned equations in the sciLab program and the weights are updated. The parameters for the ANN predictor

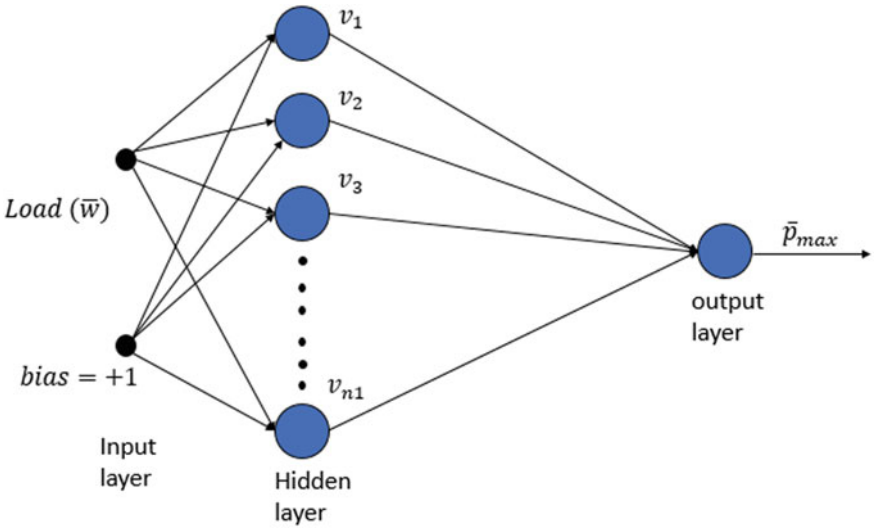

Fig. 3 ANN for maximum bearing pressure w.r.t. applied radial load

```
function[y,h,v,yl]=nn_sigy_fwd(NN,x)
    h=NN.whi*x;          //input to hidden layer
    v=1./(1+exp(-h));    //response of hidden layer
    yl=NN.woh*v;         //input to output layer
    y=1./(1+exp(-yl));   //response of output layer
endfunction
```

Fig. 4 Sigmoid activation function in SciLab

Table 1 Parameters for the ANN predictor

ANN	η	n_i	n_h	n_o	N	Activation function
	1	2	10	1	100,000	Sigmoid

are shown in Table 1. In this table, the learning rate is represented by (η) which shows the speed of learning for the convergence. (n_i), (n_h) and (n_o) shows the number of neurons in input layer, hidden layer and output layer, respectively. (N) shows the number of iterations performed to achieve most accurate predictions.

5 Results and Discussion

The result obtained from ANN model is compared with the literature data. Ram and Sharma [5] analysed the performance characteristics for hole entry hybrid journal bearing under micropolar lubrication. Micropolar lubricants are the non-Newtonian lubricants whose performance in journal bearing depends upon the characteristic length of lubricant and coupling number. The effect of coupling number (n^2) and characteristic length of lubricant (l_m) on the maximum pressure $\left(\overline{p}_{max}\right)$ for different values of load ($\overline{w}$) has been studied. The $\overline{p}_{max}$ values of ANN model were compared with Ref. [5] results and shown in Fig. 5 (for $n^2 = 0.5$ and $l_m = 30$) and Fig. 6 (for $n^2 = 0.9$ and $l_m = 10$).

It is observed that maximum pressure values increase with increase in load. The range for non-dimensional values of load ($\overline{w}$) is considered as 0.25–1.25. The ANN predictions for both these cases are found to be very close to the desired results. The values of $\overline{p}_{max}$ are found to be large for all values of $\overline{w}$ when n^2 is considered as 0.9 and l_m as 10 compared to n^2 as 0.5 and l_m as 30.

Khakse et al. [6] analysed the performance of conical hole entry journal bearing and shows the effects of semi-cone angle on the hydrostatic and hybrid journal bearings. It was observed that the maximum pressure values increase with the increase in semi-cone angle (γ). For hybrid journal bearing, the speed parameter (Ω) is taken as 1, whereas it is 0 for hydrostatic journal bearing. The literature data is considered

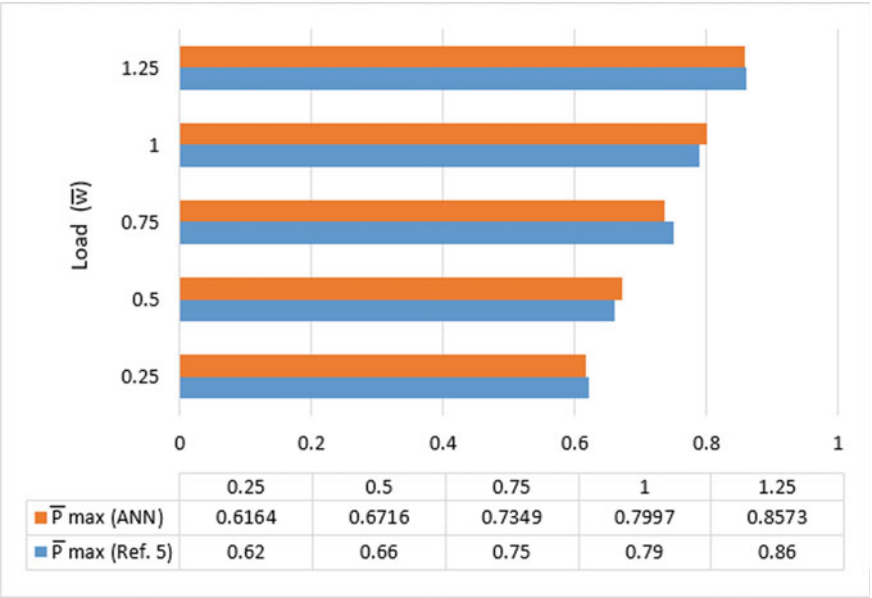

	0.25	0.5	0.75	1	1.25
$\overline{P}$ max (ANN)	0.6164	0.6716	0.7349	0.7997	0.8573
$\overline{P}$ max (Ref. 5)	0.62	0.66	0.75	0.79	0.86

Fig. 5 $\overline{p}_{\max}$ versus load ($\overline{w}$) for $n^2 = 0.5$ and $l_m = 30$

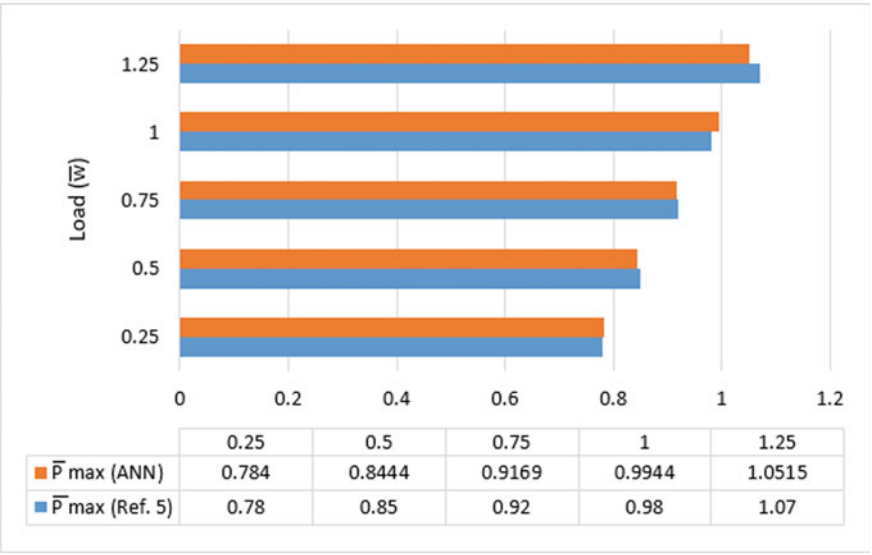

	0.25	0.5	0.75	1	1.25
$\overline{P}$ max (ANN)	0.784	0.8444	0.9169	0.9944	1.0515
$\overline{P}$ max (Ref. 5)	0.78	0.85	0.92	0.98	1.07

Fig. 6 $\overline{p}_{\max}$ versus load ($\overline{w}$) for $n^2 = 0.9$ and $l_m = 10$

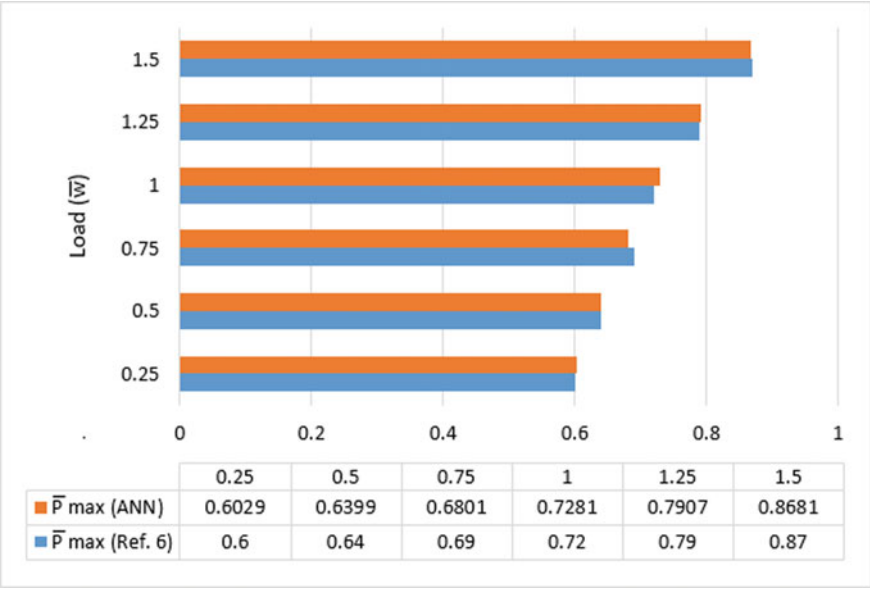

	0.25	0.5	0.75	1	1.25	1.5
$\overline{P}$ max (ANN)	0.6029	0.6399	0.6801	0.7281	0.7907	0.8681
$\overline{P}$ max (Ref. 6)	0.6	0.64	0.69	0.72	0.79	0.87

Fig. 7 $\overline{p}_{\max}$ versus load ($\overline{w}$) for speed parameter (Ω) = 1 and semi-cone angle (γ) = 10°

here for the validation of the ANN model. Figures 7 and 8 show the $\overline{p}_{\max}$ comparison with respect to load for different values of speed parameter (Ω) and semi-cone angle (γ).

The range for non-dimensional values of load ($\overline{w}$) is considered as 0.25–1.5. The ANN model gives the very close predictions for conical hole entry journal bearings. The values of $\overline{p}_{\max}$ are found to be large for all values of $\overline{w}$ in hydrostatic journal bearing (for $\gamma = 30°$) compared to hybrid journal bearing(for $\gamma = 10°$).

6 Conclusion

The present work shows that the ANN model can give best predictions for journal bearing analysis. The ANN model results and desired results are very close. The pressure variations are considered as desired output and radial load as input. This model is tested on hybrid and hydrostatic journal bearings of cylindrical and conical configuration. The increase in pressure is observed for the externally applied radial load for both cylindrical and conical journal bearing configurations. It is concluded that the present ANN model is best suited for both hydrostatic and hybrid journal bearings. The convergence speed of this ANN model is very fast. Both experimental and theoretical results can be mapped with high accuracy by using ANN. SciLab is the best software to develop the neural network models. The computation involved makes the journal bearing performance predictions more easy and less time consuming.

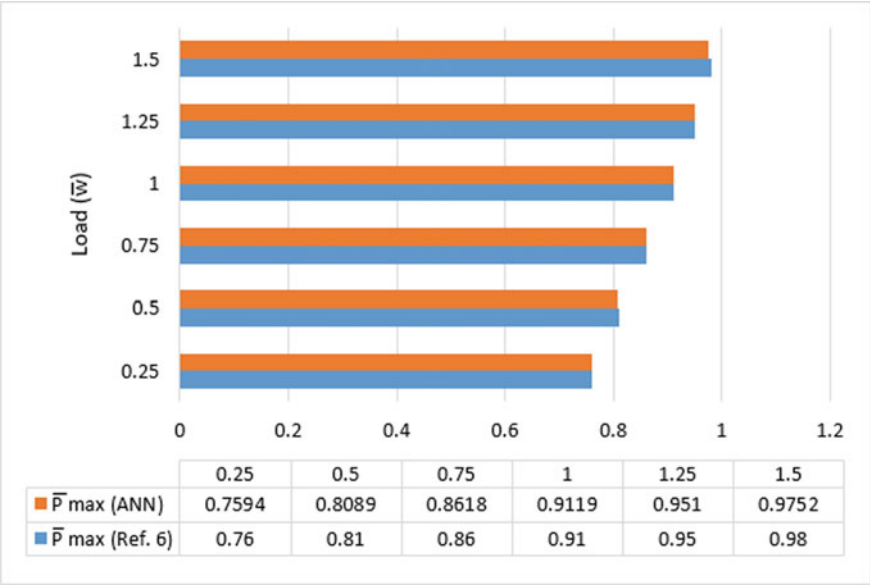

	0.25	0.5	0.75	1	1.25	1.5
$\overline{P}$ max (ANN)	0.7594	0.8089	0.8618	0.9119	0.951	0.9752
$\overline{P}$ max (Ref. 6)	0.76	0.81	0.86	0.91	0.95	0.98

Fig. 8 $\overline{p}_{\max}$ versus load ($\overline{w}$) for speed parameter (Ω) = 0 and semi cone angle (γ) = 30°

References

1. Garg HC, Kumar V, Sharda HB (2009) Thermohydrostatic analysis of capillary compensated symmetric hole-entry hybrid journal bearing operating with non-Newtonian lubricant. Ind Lubr Tribol 61(1):11–21
2. Rahmatabadi AD, Nekoeimehr M, Rashidi R (2010) Micropolar lubricant effects on the performance of noncircular lobed bearings. Tribol Int 43(1/2):404–413
3. Pawar SR, Phalle VM (2019) Influence of wear on the performance of capillary compensated hole entry hybrid conical journal bearing. Ind Lubr Tribol 71(2):333–340
4. Ram N (2017) Effect of couple stress lubrication on symmetric hole-entry hybrid journal bearing. Tribol Online 12(2):58–66
5. Ram N, Sharma SC (2012) Analysis of orifice compensated non-recessed hole-entry hybrid journal bearing operating with micropolar lubricants. Tribol Int 52:132–143
6. Khakse PG, Phalle VM, Mantha SS (2017) Orifice compensated performance characteristics of hybrid hole-entry conical journal bearing. Proc Inst Mech Eng Part J J Eng Tribol 231(3):316–331
7. Sinanoğlu C (2006) A neural predictor to analyse the effects of metal matrix composite structure (6063 Al/SiCp MMC) on journal bearing. Ind Lubr Tribol 58(2):95–109
8. Sinanoğlu C (2009) Design of neural model for analysing journal bearings considering effects of transverse and longitudinal profile. Ind Lubr Tribol 61(3):132–139
9. Patel PM, Prajapati JM (2011) A review on artificial intelligent system for bearing condition monitoring. Int J Eng Sci Technol 3(2):1520–1525
10. Sinanoğlu C, Kurban AO, Yildirim Ş (2004) Analysis of pressure variations on journal bearing system using artificial neural network. Ind Lubr Tribol 56(2):74–87
11. Samanta B, Al-Balushi KR, Al-Araimi SA (2003) Artificial neural networks and support vector machines with genetic algorithm for bearing fault detection. Eng Appl Artif Intell 16(7–8):657–665

12. Liu R, Yang B, Zio E, Chen X (2018) Artificial intelligence for fault diagnosis of rotating machinery: A review. Mech Syst Sig Process 108:33–47
13. Dowson D (1962) A generalized Reynolds equation for fluid-film lubrication. Int J Mech Sci 4(2):159–170
14. Fowles PE (1970) A simpler form of the general Reynolds equation. J Lubr Technol 92(4):661–662
15. Kucinschi BR, Fillon M, Fre J, Pascovici MD (2000) A transient thermoelastohydrodynamic study of steadily loaded plain journal bearings using finite element method analysis. J Tribol 122(1):219–226

Design and Simulation of Wind Tunnel Using CFD Analysis

Ganpati Chandrakant Arjune and Shivaji Vithal Bhivsane

Abstract The wind tunnel is proper functioning platform for accurate aerodynamic research which helps to provides adequate environment condition around scaled model to the compatible dimension. Wind tunnel data is part of design process that used to design their model. For correcting wind tunnel data of wall and mounting effects very careful techniques are used. But it shows limitation for linear flow approximation. This research paper proposed first part of the project i.e. design calculation and simulation i.e. flow in wind tunnel and checking incompressible flow in test section over an airfoil using CFD software. Test section design in rectangular shape for proposed wind tunnel. Contraction cone has contraction ratios 7 and cross section in rectangular shape. Diffuser design in conical shape with 5° diffusion angle and area ratio 1.33. The design philosophy is discussed along method for wind tunnel calculation is outlined. Using Computational fluid dynamics (CFD), design and simulation of flow parameter are investigated with systematic way in open loop wind tunnel. It shows good quality flow in test section as well as in entire wind tunnel. The proposed wind tunnel is conformed to design and can be used for different test in the field of aerodynamics. Wind tunnel design to achieve 40 m/s speed of air with expected low intensity turbulence level. Analysis of airfoil shows that good flow quality in test section. Lift and drag coefficient plotted against angle of attack.

Keywords Subsonic wind tunnel · Aerodynamics · Fluid dynamics · CFD simulation · Airfoil analysis

1 Introduction

To study the effect of air moving past solid object, wind tunnel is used as a significant research apparatus in aerodynamic investigation such as aerodynamic forces and pressure distribution to simulate with actual condition [1]. For aerodynamic research;

G. C. Arjune (✉) · S. V. Bhivsane
Assistant Professor, Department of Mechanical Engineering, Maharashtra Institute of Technology, Aurangabad, Maharashtra 431010, India
e-mail: arjungc163@gmail.com

L. M. Das et al. (eds.), *Emerging Trends in Mechanical Engineering*, Lecture Notes in Mechanical Engineering, https://doi.org/10.1007/978-981-15-8304-9_3

fast, economical and correct way offer by wind tunnel the most important aspect of wind tunnel is their ability to accurate recreate the full complexity of full fluid flow. For solving aerodynamic problems experimental information required which obtain in different way like water tunnel test, wind tunnel test, drop test, flight test, shock tube test, flying scale model, ballistic range, whirling arms rocket sleds etc. Each way is best in its sphere of superiority. Among them wind tunnel seems absolute to solve aerodynamic problems, but still basis and complex aerodynamic problem need to solve using wind tunnel even though society use computer and high technology in wind tunnel testing [2].

Flow visualisation in wind tunnel is unique which can find critical problem and solution not seen in the pure numbers but computer provides mostly quantitative data [3]. Essential lift, drag and efficiency can calculate using complex equation. One of the important parts of the aerodynamic research is versatility and tangibility which help to continue to promote wind tunnel testing. All aerodynamic problem could not solve in one single wind tunnel hence wind tunnel needs to classified as: (a) on the basic of circuit i.e. open and closed circuit wind tunnel (b) based on structure (c) based on structure material (d) based on shape of inlet section (d) based on location (4) based on speed of air velocity i.e. subsonic, supersonic, transonic and hypersonic wind tunnel (6) based on anemometer placement [2].

An Apparatus needed to calculate lift and drag forces when first begins to study bird and primitive flying machines based on aviation structure because conventional apparatus failed again and again. Benjamin Robins (1707–1751), used whirling arm who conclude that different shapes produces different air resistance irrespective of Model frontal area to the air stream that means model shape and drag existed a complex relationship hence end of the nineteenth century, the whirling arm was considered to be the best systematic source for the aerodynamic experimentation.

Osborne Reynolds (1842–1912) define a Reynold Number. He specified that behaviour of air is same for scale model and original Model has same Reynold Number as long it passes i.e. wind tunnel established as the appropriate apparatus for air flow experimentation. Then (1840–1960) Sir Hiram Maxim constructed a wind tunnel which was 12 ft long and 3 ft $\times$ 3 ft test section used for cambered aerofoil. Wright Brothers (1903) compared different model and found out ideal design variable for their Air Craft using own designed wind tunnel. World War II was golden era for developing variable Wind tunnels such as sub sonic, supersonic and Hypersonic Wind Tunnel.

Primary purpose of Wind tunnel is changed when air craft was invented. Initially calculated forces being used to verify CFD algorithms, hybrid Flow Study and examine different material. In 2016, Bert Edis and Harm H. Ubbens designed a wind tunnel which is used to study the resistance offered by the wind to a cyclist. In 2015 T. H. Young and S. S. Dol constructed a low cost wind tunnel for small scale experiment and education purposes. Both wind tunnels based on R. D. Mehta and P. Bradshaw design guidelines specifications which provides certain guidelines for variety of requirements for designing a main component of a wind tunnel [4]. A very small wind tunnel i.e. 5 cm * 5 cm test section design for UAV, MAV and MWT which

are edge on research on aerodynamics. These vehicles have low Reynold number and low dimension [5].

Major parts of wind tunnel are test section, diffuser, contraction, settling chamber and driving unit say electric motor. Uniform flow within the test section is the main goal of wind tunnel. Test section dimension design based on size of model and type of test to be performed and defined rest of wind tunnel dimension. Test section is key factor in construction and running cost of wind tunnel. Overall length of the construction can be controlled by optimization the design. The optimum length is achieved CR only then is the dynamic load and boundary layer growth at their minimum list value [6]. The power of computing machines and the computer languages necessary to program the foundational mathematics started increasing exponentially. To develop such system was decrease in an equally trend. The condition was met for an economical study of fluid flow prediction to evolve into the field known as computational fluid dynamics. With the help of CFD software and its complimentary CAD graphic interface one can accurately design and evaluate the flow regimes of a highly capable wind tunnel device [1, 3].

2 Design of Wind Tunnel

Wind tunnel design starts with test section on the basis of accessibility and installation of test model as well as instrumentation. Test section length should be in range of 0.5–3 times of its hydraulic diameter and keep small as possible as for low pressure loss coefficient. Blockage has negligible effect on test result when it about 10%. Test section (cross-Sect. 0.3 * 0.3 m^2) set 0.5 m length i.e. 1.67 of its hydraulic diameters [1, 3].

Flow accelerates into the test section by contraction. Design criterion of contraction for desired application that separation is avoided and the exit non uniformity is equal to or less than the maximum tolerable level in shortest possible length. Contraction cones design starts with selection of contraction ratio. Which should be in range of 6–9 for small wind tunnel also length of contraction should be 0.15–1 times of its inlet section hydraulic diameter. Flow separation avoid if contraction is too large i.e. pressure drop coefficient decreasing with increase in contraction ratio. 1.05 m contraction length takes to avoid flow separation. Straight contraction shape uses for easier and cheaper contraction. Internal section of nozzle is identical to the test section [1, 2, 6].

Diffuser is used to decrease velocity flow in shortest distance which help to reduce load on drive system [1]. Area ratio, diffuser angle wall contour and diffuser cross-section shapes are key factor of diffuser flow. For controlling flow separation, area ratio should be less than 2.5 and diffuser angle 5°–7°. Here, diffusion angle considers as 5°. Calculated length found as 1.15 m, but here considering length is 1.5 m for better flow quality and area ratio 1.78 [2].

Settling chamber used to place honeycomb and screen which help to reduce flow turbulence before move into the contraction. Settling chamber cross section is same

as contraction and length took as 0.5 times of the hydraulic diameter of inlet of settling chamber area i.e. 0.35 [2, 3].

Primary purpose of honeycomb is to reduce swirl and produce well conditional flow which means reduce in variation in mean and transverse velocity without losing its flexural rigidity under forces during operation. Ratio of length to cell hydraulic diameter (L/D) and porosity (flow area/total area) is the primary design parameter for honeycomb. L/d took as 6–8 and porosity as 0.97. Square cross section has edge 5 mm, 0.075 mm thickness and length 12 mm [1].

Screen locate inside settling chamber which help to reduce upcoming air turbulence level i.e. breaks large eddies into small scale turbulent eddies. Porosity above 0.8 has no control on turbulence and below 0.58 lead to flow instability. Hence, it should be in range of 0.58–8 [2]. Finest screen shows better control over turbulence. Clearance between screens should be 0.2 times of settling chamber hydraulic diameter. Screen dimensions considered as 2 mm thick wire, cell height 8.9 mm hence 0.6 porosity and 0.14 m distance from contraction inlet. Another one is 3 mm thick wire and cell width 10.5 mm, porosity 0.65 placed from first screen. The drive system chooses which has optimum efficiency, RPM, and required power to produce 25 m/s mass flow [1] (Fig. 1 and Table 1).

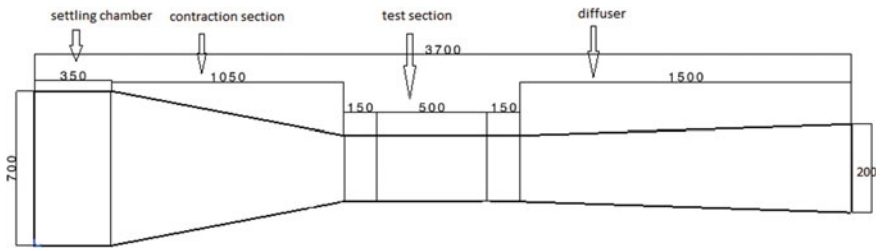

Fig. 1 Wind tunnel design (all dimension in mm)

Table 1 Wind tunnel component dimension

Component of wind tunnel	Cross-section area (m^2)	Length (m)
Test section	0.3 * 0.3	$L_{ts} = D_{ts} * 1.5 = 0.5$
Contraction cone	0.7 * 0.7	$L_{cs} = D_{cs} * 1.5 = 1.05$
Diffuser	0.4 * 0.4	$D_{D0} = D_{ts} + \left[2 * \left(L_d * \tan \frac{\theta}{2}\right)\right] = 1.5$
Settling chamber	0.7 * 0.7	$L_{sc} = \frac{D_{sc}}{2} = 0.35$
Honeycomb	0.003 * 0.003	= 0.012 (inside settling chamber)

3 Pressure Losses in Wind Tunnel

At any point in the wind tunnel, the energy loss depends on the cubic velocity at that point. In diffuser, velocity decrease with minimum loss and higher back pressure without boundary layer separation. The total losses occurring in the flow through wind tunnel is equal to the power required to maintain steady flow through the wind tunnel. Pressure loss for each component of wind tunnel determined to conducting numerical simulation in order to comprehends the functionality of the circuit [7]. The total pressure loss coefficient (k_i) which is sum of each section and head losses (h_1) are calculated for upstream and downstream wind tunnel section. Such total pressure loss is then subtracted from the pressure at the exit of the diffuser, establishing the pressure at the exit recovery required by the fluid pump. The pressure recovery required by the fluid pump is calculated on the total pressure loss. The pressure drops co-efficient represent as dimensionless form of the energy loss of each section.

Head loss calculated as:

$$h_1 = k\frac{V^2}{2g} = \frac{\Delta p}{\rho g} \tag{1}$$

where V, ρ and k are average fluid velocity in working section, density of fluid, loss coefficient respectively.

3.1 Test Section

Design of test section purpose is to maintain approximately constant static pressure with list change in Mach number throughout the test section. Test section has constant height. Its upper and lower wall are deflected to prevent boundary layer growth. The design provides good view to user. Only friction losses find inside test section and k is function of fraction factor which is calculated as [8].

$$k_{\text{ts}} = \frac{L_{\text{ts}}}{D_{\text{ts}}} f_{\text{ts}} \tag{2}$$

where k_{ts}, L_{ts}, D_{ts} and f_{ts} are loss coefficient, length, hydraulic diameter and friction factor of the test section i.e. working section. The friction factor calculated as following Colebrook equation:

$$\frac{1}{\sqrt{f_{\text{ts}}}} = -2\log_{10}\left[\frac{\varepsilon/D_{\text{ts}}}{3 \cdot 7} + \frac{2.51}{\text{Re}\sqrt{f_{\text{ts}}}}\right] \tag{3}$$

ε is roughness and consider as zero in working section.

3.2 Diffuser

The purpose of diffuser is to reduce the power losses due to high flow velocity i.e. decrease in velocity with distance without separation of boundary layer at walls. Vibration of fan which causes change in velocity at test section hence separation may occur. Divergence is important aspect for design of diffuser keep small as possible to ensure separation of boundary layer at wall of diffuser. It means long diffuser for high aspect ratio and may be costly inefficient [8]. The pressure losses in diffuser due to skin friction and expansion loss. Equivalent conical expansion angle (θ) and area ratio i.e. ratio of outlet and inlet cross sectional area of diffuser are main parameter. Loss coefficient for diffuser (k_d) is sum of these two-loss factor [1].

$$k_d = k_f + k_{ex} \tag{4}$$

wherek_f and k_{ex} are skin friction and expansion lass factors. They are calculated as:

$$k_f = \left(1 + \frac{1}{AR^2}\right)\frac{f_{ws}}{8\sin\theta} \tag{5}$$

Expansion angle (θ) may calculated as: -

$$\theta = \tan^{-1}\left(\frac{R_2 - R_1}{L}\right) = \tan^{-1}\left(\frac{1}{2}\frac{\sqrt{AR} - 1}{\frac{L_n}{D_{ws}}}\right) \tag{6}$$

$$k_{ex} = k_e(\theta)\left(\frac{AR - 1}{AR}\right)^2 \tag{7}$$

For an expansion angle $1.5° \leq \theta \leq 5°$ $k_e(\theta)$ calculated as:

$$\begin{aligned} k_e(\theta) = {} & 0.1709 - 0.1170(\theta) + 0.03260(\theta)^2 + 0.001078(\theta)^3 \\ & - 0.00090760(\theta)^4 - 0.00001331(\theta)^5 + 0.000001345(\theta)^6 \end{aligned} \tag{8}$$

3.3 Contraction Cone

Only, skin friction loss considers in a contraction cone and it may be calculated as follows [1, 3]:

$$k_{cs} = \frac{f}{4}\frac{L_{CS}}{D_{CS} - D_{TS}}\left(1 - \frac{D_{TS}^4}{D_{CS}^4}\right) \tag{9}$$

where L_{CS}, D_{CS}, D_{TS} and f are length of cc, inlet hydraulic diameter of cc, test section hydraulic diameter and skin friction coefficient respectively [1].

3.4 Settling Chamber

Honey comb and screen are two section which used to decrease the turbulence in flow and make it straight. To decrease the pressure loss in wind tunnel, velocity at honeycomb and screen section must be low as possible. Screen and honeycomb reduce axial and lateral turbulence respectively. Screen have a relatively large pressure drop in the flow direction but honeycomb have small pressure drop. Loss in honeycomb calculated as [1]:

$$k_h = \lambda_h \left(\frac{L_h}{D_h} + 3\right)\left(\frac{1}{\beta_n}\right)^2 + \left(\frac{1}{\beta_n} - 1\right)^2 \tag{10}$$

where

$$\lambda_h = 0.375\left(\frac{\Delta}{D_h}\right)^{0.4} R_{e\Delta}^{-0.1} \quad \text{Re} < 275 \tag{11}$$

$$\lambda_h = 0.214\left(\frac{\Delta}{D_h}\right)^{0.4} \quad \text{Re} > 275 \tag{12}$$

Screen loss coefficient can be calculated as:

$$k_m = k_{mesh} k_{Rn} \sigma_S + \left(\frac{\sigma_S^2}{\beta_S^2}\right) \tag{13}$$

where σ_S and β_S are screen solidity and screen porosity. k_{mesh} is mesh factor, 1 for new metal wire, 1.3 for average circular metal wire, k_{Rn} is calculated as [1] (Table 2):

$$k_{Rn} = 0.785 + \left(1 - \frac{\text{Re}_{ws}}{354}\right) + 1.010 \leq \text{Re}_{ws} \leq 400 \tag{14}$$

$$k_{Rn} = 1 \quad \text{Re}_{ws} \geq 400 \tag{15}$$

Total pressure loss calculated as power loss in each section of wind tunnel and fan:

$$\Delta P_t = \frac{1}{2}\rho V^2 \sum k_i + \frac{1}{2}\rho V_{fan}^2 \tag{16}$$

Table 2 Loss coefficient in wind tunnel section

Wind tunnel component	Loss coefficient
Test section	0.0188
Contraction cone	0.0048
Diffuser	0.04271
Honeycomb	0.00049
Screen 1	0.6399
Screen 2	0.7787
Straight section	0.0111
Total	$\sum k_i = 1.4965$

Take 25% safety factor i.e. $\sum k_i = 1.4854 + 0.37135 = 1.871$.

Dimension of fan is same as diffuser outer diameter. Hence, velocity of fan is calculated as:

$$A_{\text{fan}} V_{\text{fan}} = A_{\text{ts}} V_{\text{ts}} \tag{17}$$

where $A_{\text{fan}} = A_{\text{ds}} = 0.16$, $A_{\text{ts}} = 0.09$, $V_{\text{ts}} = 25$ m/s, hence. $V_{\text{fan}} = 14.0625$ m/s therefore;

$$\Delta P_{\text{t}} = 806.47 \text{ Pa}$$

3.5 Power Requirement

To maintain steady flow inside test section power is required that power is equal to losses by kinetic energy dissipated phenomenon i.e. vortices and turbulence [1]. Design of fan may be on the basis of required velocity at test section and to resist the decrease in pressure along the wind tunnel. Sum of the pressure drop coefficient (K_i) in each section of wind tunnel equal to required power for given section size and flow condition [8].

$$\eta P = \frac{1}{2} \rho A V^2 \sum k_i \tag{18}$$

Power required is sum of total pressure loss in all section of wind tunnel and fan:

$$P_{\text{req}} = Q = A_{\text{fan}} V_{\text{fan}} \Delta P_{\text{t}} = 1814.55 \text{ W} \tag{19}$$

Power in Hp is 2.42.

For BHP (brake horse power) = 60% approximately;

Table 3 CFD model boundary condition summary

Parameter	Input values
Discretization scheme	Second order upwind
Algorithm	SIMPLEC
Inlet velocity	4.76 m/s
Pressure outlet	105,779.4035 Pa
Air density (at 25 °C)	1.18 kg/m^3
Gas constant	287 J/kg K
Kinematic viscosity	1.51 * 10^{-5} kg/m s
Time	Steady state

Then,

$$\text{EFF} = \frac{\text{Power in Hp}}{\text{BHP}} = \frac{P(\text{Hp})}{\text{BHP}} = 4.03(\text{hp}) \tag{20}$$

Calculated power is more than required power reason is that for future work when increase in velocity at test section around 40 m/s.

4 CFD Simulation

4.1 Wind Tunnel Simulation

To visualize flow in side wind tunnel or any complex configuration to find a mechanical and flow properties, Ansys use like a tool to represent it. First step is to model wind tunnel and apply proper boundary condition which are calculated using design [8]. Steps involve in Ansys are Preprocessing i.e. modeling, boundary condition (Table 3) and meshing, solution i.e. fluent as a solver and for post-processing CFX may use.

Total element and node use to simulate wind tunnel are 391,368 and 381,808 respectively. Ansys solution (fluent) shows steady, incompressible viscous flow of ideal gas with constant velocity (25 m/s) along test section that means good result which indicates prepared design has no separation at all and no thickening of boundary layer at that region which may face an error in measurement.

4.2 Airfoil Simulation in Test Section

Wind tunnel test section provides good result which may clarify to simulate flow over airfoil in the test section 2D model use for it because 3D model and mesh provide

same result as per study and less time and matrix may have needed. To analyze the aerodynamic characteristics (lift and drag) of 2d airfoil use input variable such as experimental measurement (wind tunnel test data) result and airfoil coordinate. The understanding problem statement that is flow is external aerodynamic flow so we need to fix the outer airflow boundary i.e. airflow. Airfoil and stream condition (flight speed/air speed) are required to carry out the analysis. NACA 2412 airfoil coordinates take from UIUC airfoil database.

4.2.1 Flow Consideration

Flow is incompressible and turbulent i.e. density and viscosity are constant. Only mass and momentum equation need to be solved. Appropriate pressure velocity coupling scheme and turbulence model need to be selected. Here only steady state analysis is sufficient [7]. Flow is external, as per industry practice, fluid domain around airfoil can be taken as 15–20 times the chord length. Modeling of boundary layer is challenging task for flow around airfoil because of severe stalling effect in the stalling region. Analysis can be fine turned with multiple modeling approaches by comparing the CFD analysis results with experimental results (wind tunnel test data). The flow is incompressible and compressibility effects are negligible therefore there will not a shock wave [9].

4.2.2 CFD Analysis Procedure

The first step is to scale the mesh to SI (length in meter) units after importing the mesh to CFD analysis software which include structured mesh with 45,888 quad elements and 46,440 nodes. In this problem there is need to scale mesh, because airfoil coordinates are normalized to one-unit chord length for test section analysis model scale as 1:10. Pressure based CFD solver i.e. ANSYS fluent is used as solver, since there are no severe compressible effects like shock waves. Energy equation and model density as a function of pressure, temperature and viscosity selected for analysis. Reference pressure is as sea level 101,325 pa which needs to consider for environmental flow. We fix the far field boundary condition, wall boundary condition and solver setting. For test section model inlet velocity is sufficient. For far field boundary condition, we need provide gauge pressure, flow Mach number i.e. flow is turbulent say velocity as 40 m/s and flow direction cosine along with turbulence boundary condition. X-direction of flow is given by $\cos(\alpha)$ and Y-direction flow is $\sin(\alpha)$. Wall boundary condition assign with no slip, adiabatic boundary condition. Need to create fluid properties like density, viscosity, thermal conductivity, specific heat as an air fluid property to all 2D volume elements (quad element). Solver setting depends on governing equation discretization scheme i.e. second order upwind scheme which was selected. SIMPLE algorithm is used for pressure–velocity coupling algorithms. Under relaxation factor can set solution control. We take residual value like $1e-10$ or $1e-20$. Because we know that getting converged solution up to this value is

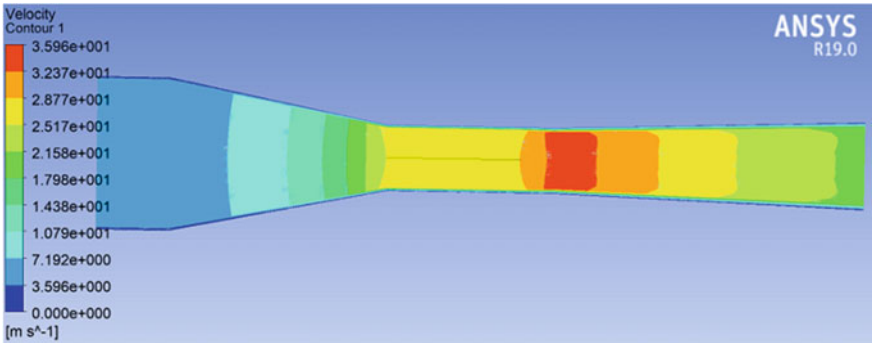

Fig. 2 Velocity profile in complete wind tunnel

impossible, but it is a technique to keep the analysis running till we stop based on our technical judgment. One the fluctuation stops; we can declare that solution is converged. Monitor lift and drag coefficient on the curve of airfoil. *Y* plus (30–300 i.e. inertia dominant region) value use for fine mesh in turbulence flow to clarify viscous and inertia effect i.e. boundary layer thickness, Repeat the analysis by changing the number of element both core flow region and near wall regions till solution becomes grid independent.

4.3 Post Processing Result

Velocity profile inside test section need to constant when solving mass conservation equation. Such Fig. 2 shows more accurate profile for design data for the mass conservation and momentum equation. Boundary layer growth in test section is very much smaller hence effect of boundary layer on overall flow field in test section is negligible Fig. 3 [10].

Stalling Angle of attack of NACA2412 is nearly equal to all result with constant mach number and Reynolds number. It shows that all flow properties at test section i.e. wind tunnel are accurately design.

Airfoil theory i.e. lift, drag and angle of attack curves Figs. 4, 5, 6 and 7 obtained in simulation are more satisfied result as standard wind tunnel data i.e. NACA2412 is cambered airfoil which has lift at zero angle. Slope means lift verses angle of attack, increase in angle of attack there is increase in lift in roughly linear way as shown in Figs. 4 and 5. But, lift fall when airfoil falls about 14° angle of attack know as stall point or stall angle of attack. Upper surface boundary layer is reason for lift falls which separates and thicken over upper surface at and past of stall angle. Airfoil effective chamber i.e. shape of airfoil changes by this thicken boundary layer displacement thickness which modifies overall flow field i.e. reduce circulation and

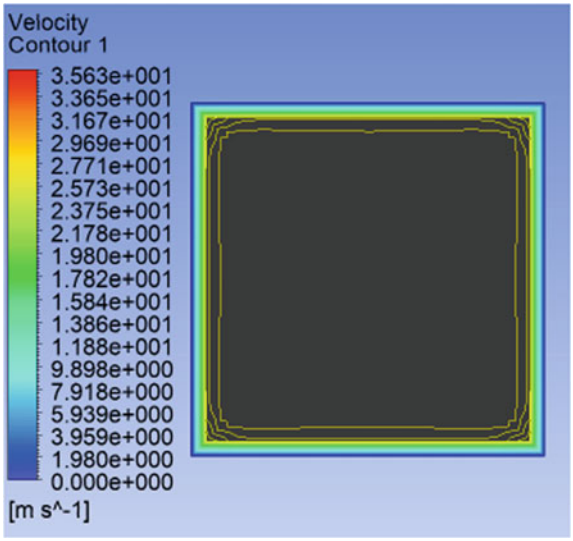

Fig. 3 Velocity profile in test section

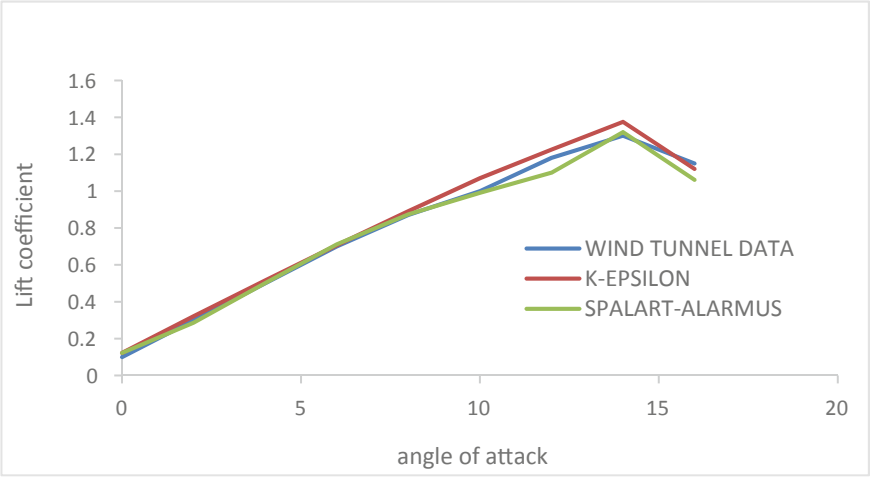

Fig. 4 Lift coefficient versus angle of attack at different model of simulation compare with wind tunnel data

lift. Pressure drag increase dramatically is another cause of boundary layer that means overall drag produce near and past the stall point Fig. 8. This all data clarify with good flow simulation into the design wind tunnel [11].

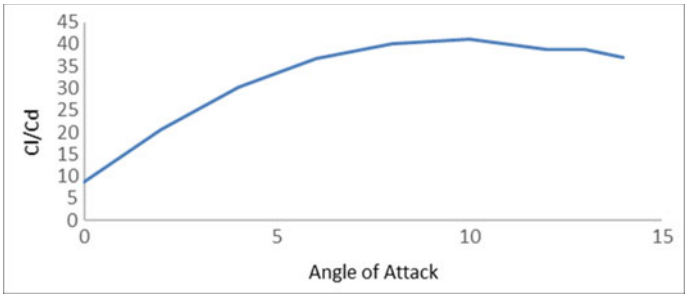

Fig. 5 C_l/C_d versus angle of attack at constant Reynolds number (Re $= 10^5$)

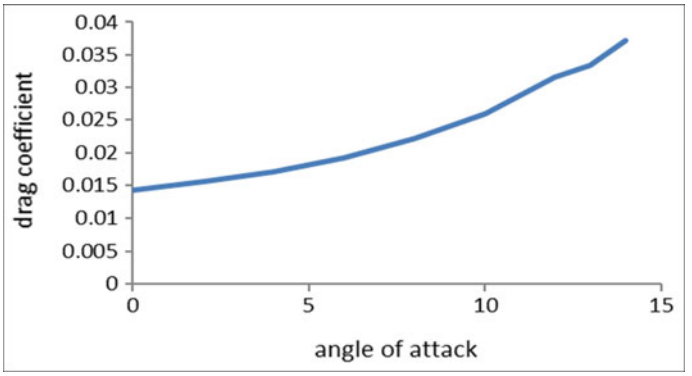

Fig. 6 Drag coefficient versus angle of attack at constant Reynolds number (Re $= 10^5$)

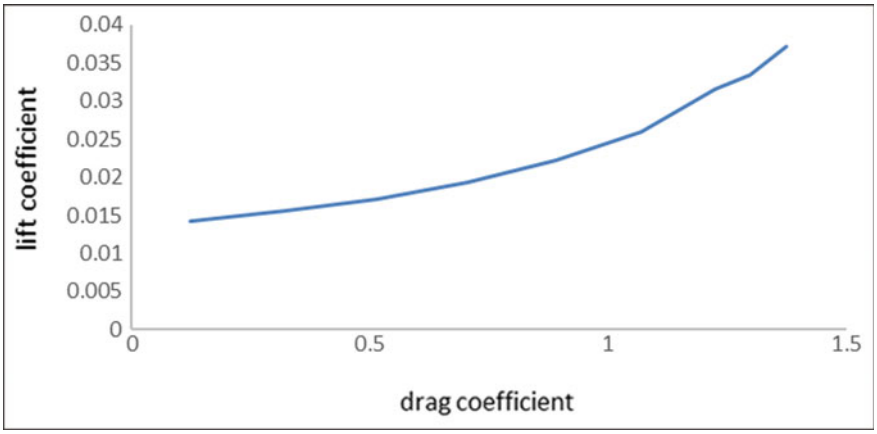

Fig. 7 Lift coefficient versus drag coefficient at different angle of attack

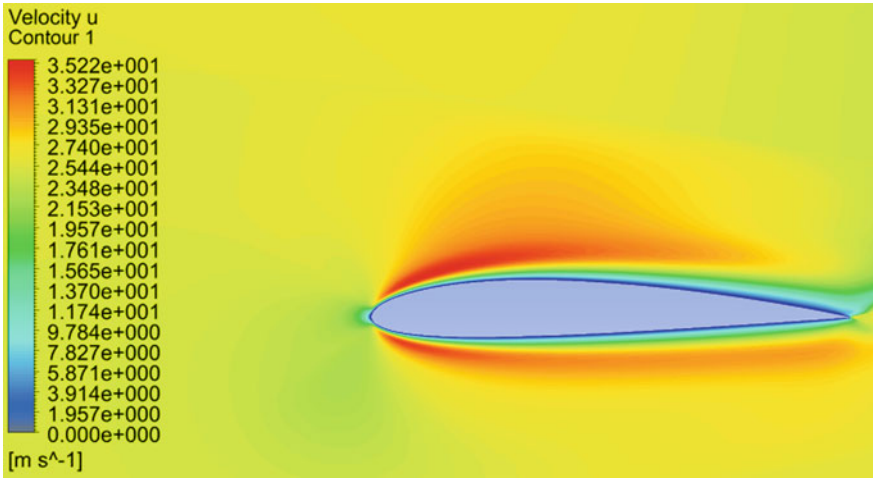

Fig. 8 Flow visualisation over airfoil (naca 2412)

5 Conclusion

- To obtain velocity up to 40 m/s at test section (0.3 * 0.3) m^2, an open circuit wind tunnel has been designed and simulated. Power loss coefficient in wind tunnel is nearly 1.871 with respect to dynamic pressure at test section and 2 Hp motor may sufficient to produce 25 m/s velocity at test section. Construction, test work and calibration will be done in next paper.
- The wind tunnel (Fig. 1) length is 3.7 m and free stream velocity about 25 m/s which is very much smaller and probably not found anywhere.
- CFD using FLUENT to predict flow around airfoil has been achieved it is clear from the result that lift coefficient on airfoil is increase due to angle of attack increase (Fig. 3) as well as it is notice that lift and drag coefficient in CFD simulation comparably accurate as wind tunnel data. The 1:10 scaled model of NACA2412 airfoil show good result in CFD simulation for flow pattern and force coefficient. On the basis of CFD and wind tunnel data result validate.
- To avoid traditional approach of wind tunnel experiment which costly and time consuming, Pre-Experimental CFD study help to reduce repetitive experiment.
- Critical study like turbulence intensities where it is important to resort to wind tunnel experiment.

References

1. Panda MK, Samanta AK (2016) Design of low cost open circuit wind tunnel-a case study. Indian J Sci Technol 9(30). https://doi.org/10.17484/ijst/2016/v9i30/99195
2. Arifuzzaman M, Mashud M Design construction and performance test of a low cost subsonic wind tunnel. Wind Tunn IOSR J Eng (IOSRJEN). e-ISSN:2250-3021, p-ISSN: 2278-8719

3. Singh M, Singh N, Yadav SK, Ramswaroop S (2013) Review of design and construction of an open circuit low speed wind tunnel. Glob J Res 13(5) version 1.0
4. Mangrulkar AL, Bagade S, Chavan S, Babani J, Bhagat S (2019) Design and fabrication of an open circuit subsonic wind tunnel for educational purposes. Int Res J Eng Technol (IRJET) 06(04). e-ISSN: 2395-0056, p-ISSN: 2395-0072
5. Mauro SA, Brusca SB, Lanzafame RA, Famoso FA, Galvagno AB, Messina MA (2017) Small-scale open-circuit wind tunnel: design criteria, construction and calibration. Int J Appl Eng Res 12(23):13649–13662. ISSN 0973-4562. © Research India Publications. https://www.ripublication.com
6. Bell JH, Mehata RD (1988) Contraction design for small low speed wind tunnel. JIAA report TR-84. Department of Aeronautics, Standard University, NASA CR-177488
7. Pop, Harper JJ (1986) Low speed wind tunnel testing. McGraw-Hill
8. Hussain IY, Mjeed MH, Ali AH, Saesam WS (2011) Design, construction and testing of LSWT with its measurement and inspection and inspection devices. J Eng 17(6)
9. Joglekar B, Mourya RM (2014) Design, construction and testing open circuit low speed wind tunnel. Int J Eng Res Rev. ISSN 2348-697X (Online) 2(4):1–9, Available at: www.researchpublish.com
10. Libbi JN (2011) Wind tunnel in engineering education. Wind tunnel and experimental fluid dynamics research. In: Lerner JC (ed). ISBN: 978-953-307-6232. InTech. https://www.intechopen.com/books/windtunnel-and-experimental-fluid-dyanamics-research/wind-tunnels-in-engineering-education
11. Anderson JD Jr (2011) Fundamental of aerodynamics, 5th edn. McGraw-Hill. New York, NY

Evaluation of Seat to Head Transmissibility at Different Backrest Conditions During Whole Body Vibration Using Fem

Harkirat Singh, Arvinder Singh, Ishbir Singh, and Sachin Kalsi

Abstract In this study, finite element technique has been used to evaluate vertical and fore–aft seat to head transmissibility of human subject representing 95th percentile anthropometric data of Indian male population when exposed to whole body vibration. Human model has been subjected to three different back support postures (without back support, vertical back support and inclined back support) at acceleration magnitudes of 0.25, 0.5 and 1.0 m/s^2 rms. This study is focused in frequency range of 0.5–15 Hz as in this range many human organs such as heart, shoulder natural frequency lies, which causes general feeling of discomfort and motion sickness. Maximum transmissibility in vertical and fore–aft direction has been evaluated in frequency range between 4–7 Hz at acceleration of 0.25 m/s^2. Study shows that backrest support has more influence on fore-and-aft transmissibility than vertical transmissibility.

Keywords Whole-body vibration · Transmissibility · 3D CAD model · Agriculture tractor seat · Backrest support

1 Introduction

Human body is exposed to whole body vibration while traveling or operating vehicles on road, by air and sea, exposure to vibration may cause motion sickness, back pain and other health-related issues. To reduce the effect of vibration on human body, it is necessary to analyze the various factors which act as a medium between the source of

H. Singh · A. Singh · I. Singh (✉) · S. Kalsi
Chandigarh University, Mohali 140413, India
e-mail: ishbir@rediffmail.com

H. Singh
e-mail: harkiratsinghdhadhly@gmail.com

A. Singh
e-mail: arvindernagra2@gmail.com

S. Kalsi
e-mail: phd.sachinkalsi@gmail.com

L. M. Das et al. (eds.), *Emerging Trends in Mechanical Engineering*, Lecture Notes in Mechanical Engineering, https://doi.org/10.1007/978-981-15-8304-9_4

vibration and human body. Lot of research has been reported on suspension system and cushion material to isolate human subject from the source of excitations. Seating posture is strongly linked to comfort of seat occupant; it is necessary to study various sitting parameters to enhance the occupant comfort.

Wu et al. [1] developed a coupled model of human–seat-suspension with three degrees of freedom biodynamic model of the occupant; evaluation of suspension has been done under continuous and shock excitation assessed in form of vibration dose value and seat effective amplitude transmissibility. Tiwari and Prasad [2] developed a three degree of freedom model to study transmissibility of tractor seat for Indian subject; results show that seat suspension having stiffness between 10.726 and 18.957 KN/m was found suited for Indian tractor seats. Rakheja and Stiharu [3] experiments had been conducted on 24 human subjects seated under various automotive sitting representing posture to analyze the biodynamic apparent mass response. Study concluded that position of hand and body mass have most significant influence on the apparent mass response.

Holmlund and Lundstorm [4] measured mechanical impedance of human body in sitting posture in vertical direction while performing experimental condition, such as acceleration level of 0.5 to 1.4 m/s^2 and frequency range of 2–100 Hz. Outcomes show that impedance increases with frequency up to a peak at about 5 Hz after which it keeps on decreasing; heavy person shows higher impedance at lower frequency as compared to subjects having less weight.

Deboli et al. [5] conducted experimental study to evaluate the response of human subject during agricultural conditions when exposed to whole body vibrations in vertical and horizontal direction. Dewagan et al. [6] three different cushion materials (flat and contoured polyurethane foam and air cushion) has been evaluated for apparent mass response of human body with and without back rest support at three levels of vertical acceleration (0.23, 0.50 and 0.75 m/s^2) with in frequency range of 0.5 to 20 Hz. Results show that apparent mass is highly effected by contouring visco-elastic properties of seat material, results of this study show that primary peak for air cushion occurs in frequency range of 3.94 to 5.25 Hz, for flat PUV foam, peak occurs in frequency range of 3.94 to 5.13 Hz and for contoured foam, peak occurs in range of 3.81 to 5.63 Hz.

Singh et al. [7] study investigates the effects of tractor ride circumstance such as pulling force, tillage depth and forward speed. Rotary tillage operation is performed by using three-point hinge mounted rotavator using L-, C- and J-shaped blades. Study shows that forward speeds have contributed 76.24%, pulling force 21.74% and tillage depth 1.79%, respectively. Duke and Goss [8] study conducted to reduce seat transmissibility by using nonlinear stiffness and on–off damper. Mathematical and experimental study shows that combination of nonlinear and switching damper has 40% reduction in transmissibility than conventional seat model. Lianig and Chaing [9] conducted research on two multi-body models representative of automotive postures one with back support and other without back support. Fourteen-degrees-of-freedom

modal proposed in this study was found to be fitted to the test results, so this model has been recommended for studying the biodynamic responses of a seated human body exposed to vertical vibrations.

Harsha et al. [10] conducted experiments on twelve healthy male subjects to measure vertical vibration transmissibility from seat to head in three different postures (erect, vertical back on and forward lean on table) in frequency range of 1 to 20 Hz; peak transmissibility comes in frequency between 2–6 Hz in all three sitting postures. Mansfield and Griffin [11] exposed twelve human subjects to acceleration magnitude between 0.25 to 2.5 rms in frequency range of 0.2 -20 Hz. Apparent mass resonance frequency reduced from 5.4 to 2 Hz as excitation magnitude increases from 0.25 to 2.5 m/s^2. Nawayseh and Griffin [12] conducted experiments on 12 male human subjects with in frequency of 0.25 to 20 Hz at four different magnitudes (0.125, 0.25, 0.625 and 1.25) m/s^2. Results show the presence of second resonance peak of relatively small magnitude in 10–15 Hz frequency.

From existing literature, it has been found that most of work has been performed experimentally on European subjects as compared to Indian subjects using finite element method. Taking this into consideration, current study has been conducted on Indian human subject's model using finite element method.

2 Methodology

While designing a vehicle, occupant comfort has been considered as important parameter. Human body under seated posture is sensitive to low frequency vibration; this distribution of vibration is dependent on extrinsic, intrinsic variable and interface between the human body and vibration object. In this study, seat to head transmissibility has been evaluated in three different sitting postures and three different magnitudes of acceleration using FEM approach in ANSYS 18.5.

Proposed study is based on Indian human model representing 95th percentile of Indian male population. A 3D CAD model of human subject has been modeled in Solid Works 2016 by considering anthropometric data from chakarbarti [13]. Human model in sitting posture with lower arms has been parallel to floor and hands on steering wheel representing the position of a tractor operator. Weight of human subject is 76 kg considering density of bone, muscle soft tissues and skin are 1850, 1062 and 1000 kg/m^3, respectively; Table 1 shows material properties considered in this study.

Table 1 Bio-mechanical properties of human subject [14]

Sr. No.	Bio-mechanical material	Density (kg/m^3)	Young's modulus(MPa)	Poisson's ratio
1	Bone	1700	10,000	0.3
2	Muscle	1060	0.1	0.49
3	Skin	1100	0.15	0.46

Human subject has been exposed to three magnitudes of excitation, i.e., 0.25, 0.5 and 1.0 m/s^2 rms in frequency range of 0.5 to 15 Hz in three different sitting postures as shown in Fig. 1, i.e., without backrest, vertical backrest and inclined backrest at an angle of 12°.

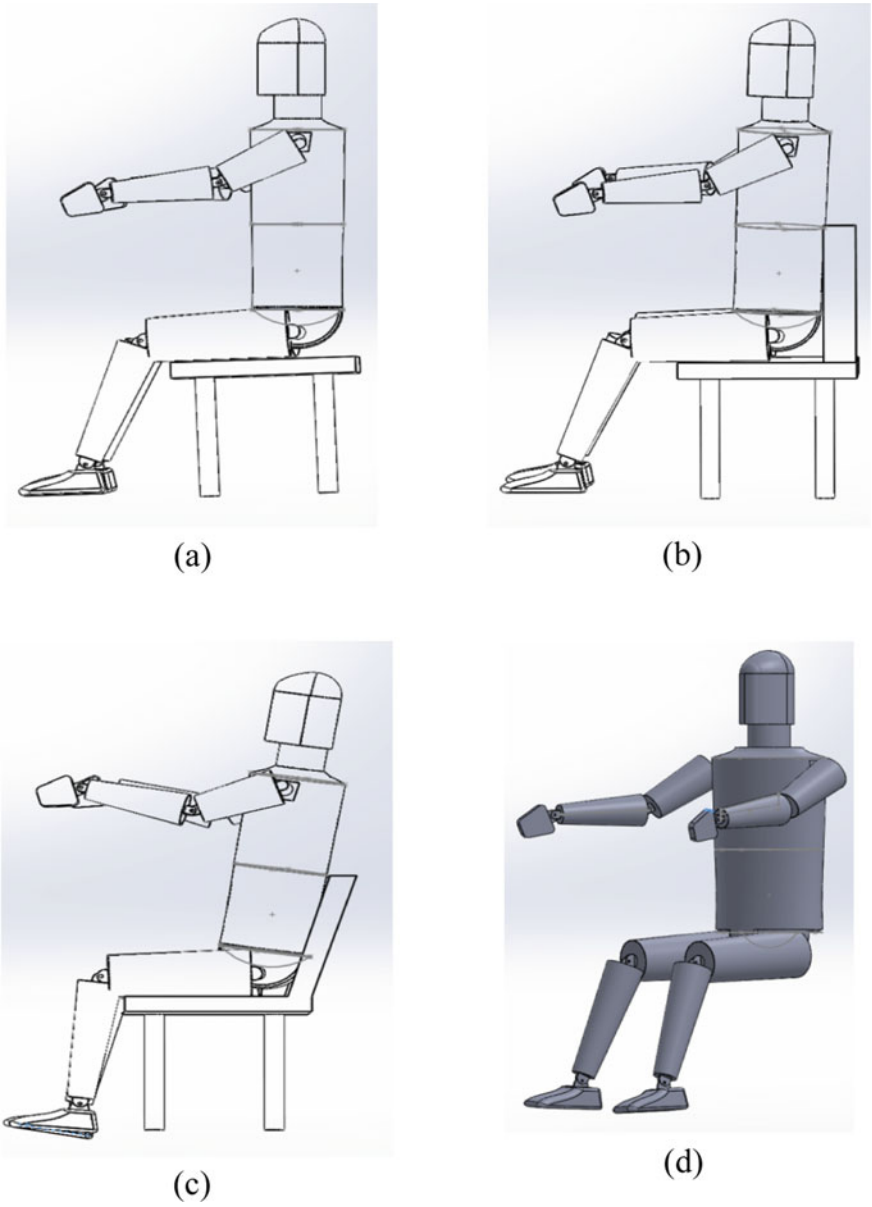

Fig. 1 **a** Without back rest, **b** vertical back rest,**c** inclined back rest (12°),**d** CAD human model

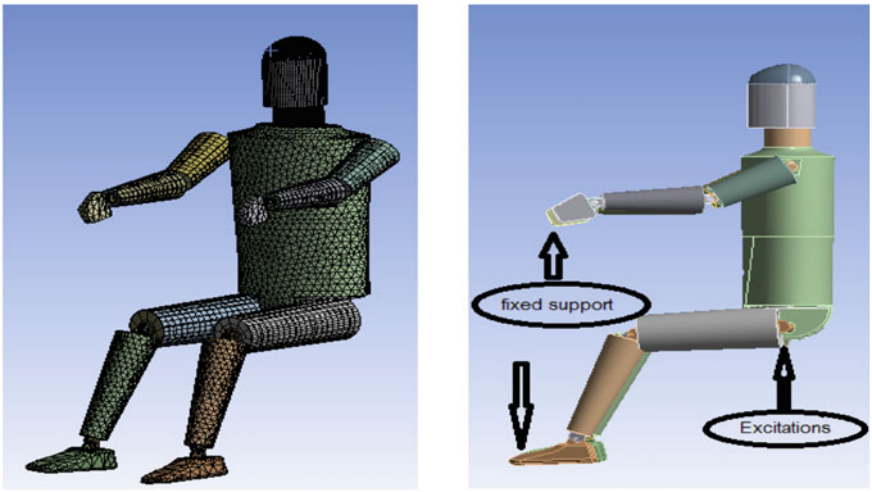

Fig. 2 **a** Meshing of human CAD model,**b** fixed support

Due to variation in dimensions of different body segments of human body, it has slight variation in stiffness and damping characteristics of human body. Meshing of human CAD model Fig. 2a has been done using different size and element type, depending on shape and size of body section. Body sections having complex geometry are meshed with tetrahedral elements and parts having less complex shape are meshed with hexahedral elements. As hexahedral elements have less distortion at edges and have less calculation time as compared to tetrahedral elements [15]. Number of tetrahedral elements and nodes are 4,563 and 7,845, respectively, by keeping element size 10 mm. Sum of hexahedral elements and nodes 5,467 and 9,876, respectively, by keeping element size same as tetrahedral.

Boundary condition shown in Fig. 2b has been given to human model depict real environment conditions in FEM software while evaluating the results. Human subject is to be in sitting posture with hand are considered to be in contact with steering wheel and feet are fixed with floor. Excitations have been provided from seat at three magnitudes, i.e., 0.25,0.5 and 1.0 m/s^2 in frequency range of 0.5 to 15 Hz. Using these boundary conditions, analysis has been performed in FEM software to evaluate seat to head transmissibility in vertical and fore–aft direction.

3 Results and Discussion

A CAD model of human subject has been meshed with different elements according to their shape and stiffness. Human subject is supposed to be in seated posture for

three different back rest conditions, i.e., (without backrest, vertical backrest and inclined backrest at 12°).

Transmissibility evaluated in vertical direction at different back rest condition considered in this study has been shown in Fig. 3. In without back rest condition in Fig. 3, transmissibility evaluated at all three acceleration has been above 1.75, at acceleration of 0.25 m/s^2, maximum transmissibility of 1.99 has been observed at frequency of 6.2 Hz, as we increase the acceleration magnitude to 0.5 m/s^2, transmissibility value decreases to 1.9 at frequency of 4.9 Hz. When acceleration magnitude has been further increased to 1.0 m/s^2, highest value of transmissibility, i.e., 1.75, has been observed in frequency range of 3–4 Hz. With change in sitting posture to vertical back support as shown in Fig. 3, transmissibility shows slight increase but peak shift toward left, i.e., low frequency.

At acceleration of 1.0 m/s^2, highest transmissibility of 1.95 has been observed at frequency of 5.2 Hz; at acceleration of 0.5 m/s^2, frequency of 4.7 Hz shows highest transmissibility of 1.98. With decrease in acceleration up to 0.25 m/s^2, study shows transmissibility of 2.05 at frequency of 4.4 Hz. For further study, human subject is considered to be in inclined back rest support at an angle of 12^0 from vertical as shown in Fig. 3. Evaluating this condition for acceleration of 0.25 m/s^2, it has been found that maximum transmissibility of 1.99 is in range of 6–7 Hz. For evaluating inclined back support condition at acceleration of 0.5 m/s^2, it has been found peak transmissibility of 1.92 arrive at frequency of 5.4 Hz. For excitation of 1.0 m/s^2 in case of inclined vertical support, highest transmissibility is 1.85 at rate of reoccurrence of 3.8 Hz.

4 Evaluation of Transmissibility in Fore-And-Aft Direction

Evaluation of transmissibility in fore-and-aft direction at three different sitting postures considered in this study has been done by applying excitation from base in vertical direction. In without back rest sitting condition, maximum transmissibility of 4.1 has been evaluated at frequency of 5.2 Hz when acceleration of 0.25 m/s^2 has been applied. At acceleration of 0.5 m/s^2, maximum transmissibility 3.5 has been evaluated in frequency between 4–5 Hz. Minimum transmissibility, i.e., 3.0, of no back rest condition has been evaluated at 4 Hz when acceleration 1.0 m/s^2 has been applied. Transmissibility in fore–and–aft direction for no back rest condition is shown in Fig. 4a.

In case of vertical back rest support as shown in Fig. 4b, maximum transmissibility of 3.1 has been evaluated at frequency of 6.1 Hz when acceleration of 0.25 m/s^2 is provided from base. For acceleration of 0.5 m/s^2, peak transmissibility of 2.8 has come at frequency of 5.3 Hz. As the excitation further increases to 1.0 m/s^2, transmissibility decreases to 2.5 at frequency of 4.6 Hz. After the resonant frequencies, transmissibility decreases to 0.5 for all the acceleration values considered in this study. For third sitting condition, i.e., inclined back rest support as shown in Fig. 4c, transmissibility of head in fore-and-aft has been observed least among all three sitting

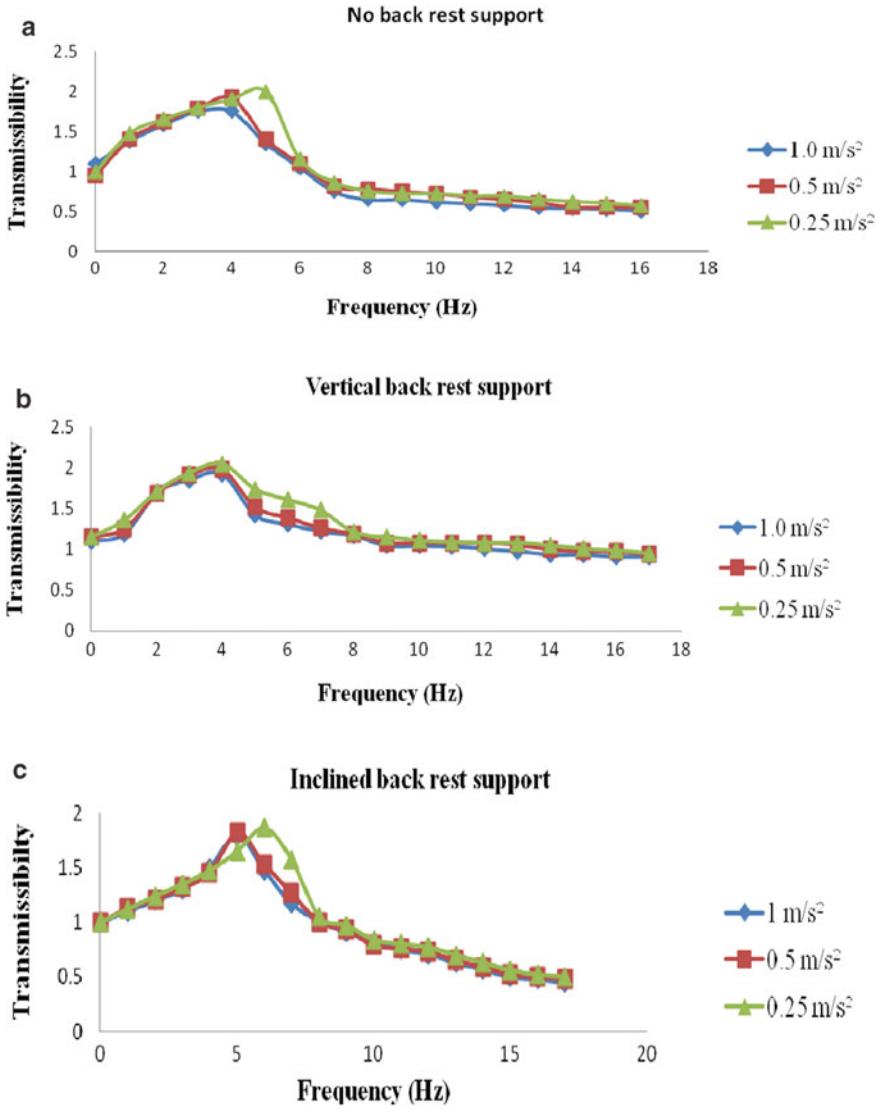

Fig. 3 **a** Transmissibility in vertical direction without backrest support **b** transmissibility in vertical direction with vertical backrest support **c** transmissibility in vertical direction with inclined backrest support

conditions. Maximum transmissibility of 2.8 in this sitting position has been evaluated at frequency of 6.3 Hz when excitation of 0.25 m/s^2 provided from base. Further increase of acceleration magnitude to 0.5 m/s^2 transmissibility decreases to 2.6 at frequency of 5.7 Hz. Minimum transmissibility of 2.4 has been evaluated at 4.8 Hz when acceleration of 1.0 m/s^2 has been applied.

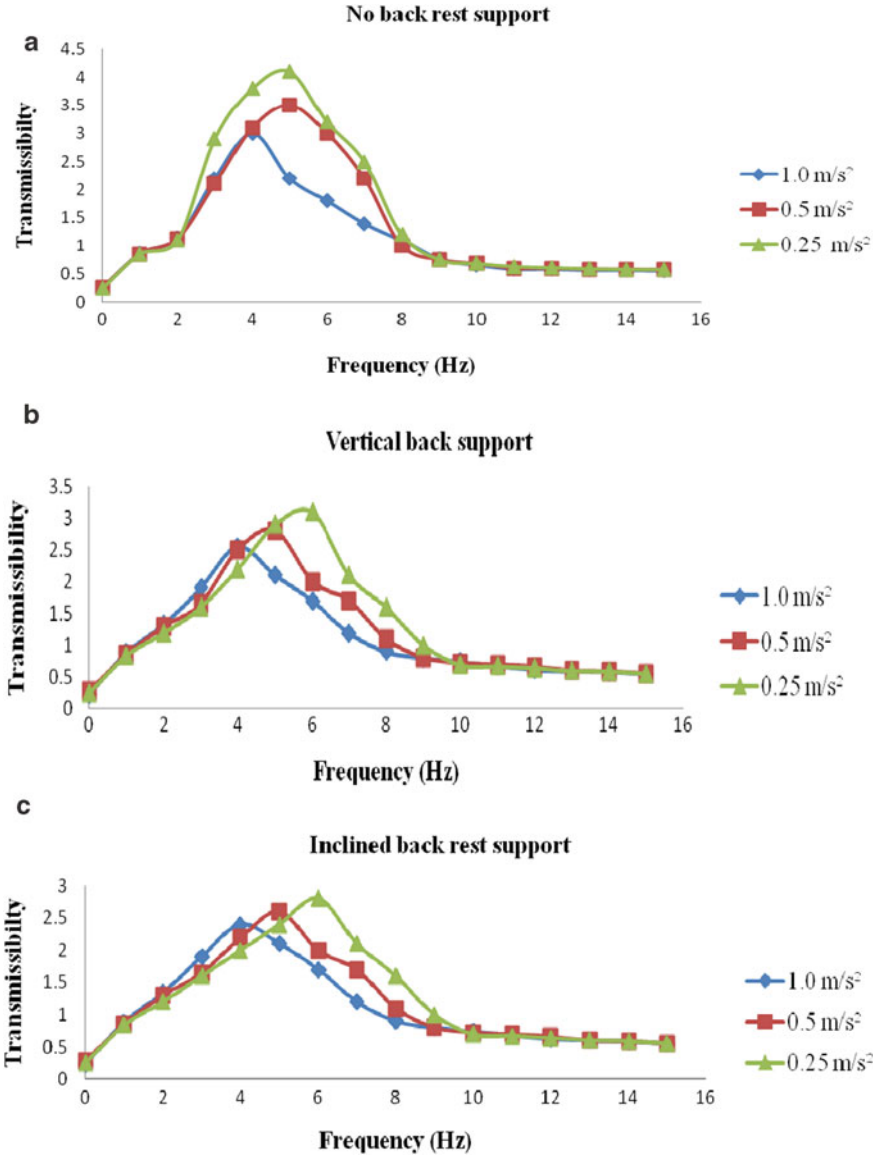

Fig. 4 **a** Transmissibility seat to head in fore-and-aft direction without back rest support, **b** Transmissibility seat to head in fore-and-aft direction with vertical back support, **c** Transmissibility seat to head in fore-and-aft direction with inclined back rest support

A study has been performed on an Indian human subject of mass 76 kg that corresponds to 95th percentile anthropometric data of Indian male population to evaluate the effect of whole body vibration for Indian conditions at different back rest positions. An acceleration of 0.25 m/s^2, 0.5 m/s^2 and 1.0 m/s^2 has been applied in both fore-and-aft direction and vertical direction. A three different back rest positions have also been considered while evaluating a ride comfort, i.e., transmissibility of a human subject. It has been found from the results, when an acceleration of 0.25 m/s^2 has been applied in vertical direction, effect of whole body vibration found to be more dominated and has a maximum value as compared to other accelerations. As there is no support for the damping of vibrations, a condition with no backrest support found to be with maximum transmissibility. In the case of inclined backrest support, a sufficient damping has been provided by a seat to constraint the flow of vibrations at head. Therefore, a value of transmissibility in case of inclined back rest support found to be less as compared to other conditions for vertical direction.

It has been found from the existing literature, low frequency range is more prominent to give an effect of whole body vibrations to cause ride discomfort. It has been found from the results, when a human subject has been exposed to whole body vibrations in fore-and-aft direction, 0.25 m/s^2 found to be more effective with maximum transmissibility. In case of without back rest, maximum transmissibility has been obtained that may due to a reason of non-availability of any damping material (backrest support) that may constraint the flow of vibrations to head. In case of vertical and inclined backrest support, value of transmissibility found to be low due to availability of back rest for the damping of vibrations as it increases the area of contact with human subject that constraints the flow of vibrations to head.

Fore-and-aft vibration direction found to be more dominant for the cause of discomfort as compared to vertical vibration direction. Also, it has been found low acceleration values are more prominent for the cause of ride discomfort as compared to higher value of accelerations.

5 Validation of Results

Results evaluated from current study have been compared with the experimental work conducted by wang et al. [16]. In experimental study, wang et al. [16] find out seat to head transmissibility on 12 human subjects in three different sitting postures, i.e., without back rest support, vertical back rest support, inclined back rest support at vertical excitation of (0.25, 0.5 and 1.0 m/s^2 rms). A helmet-strap-mounted accelerometer has been used to measure the excitation in all three axes.

In present study, i.e., evaluation of seat to head transmissibility at different back rest conditions using FEM shows that inclined back rest support has lowest fore-and-aft transmissibility among all three back rest conditions considered in current study. Current study reveals that back rest conditions have no such effect on vertical transmissibility, but have high effect on fore-and-aft transmissibility.

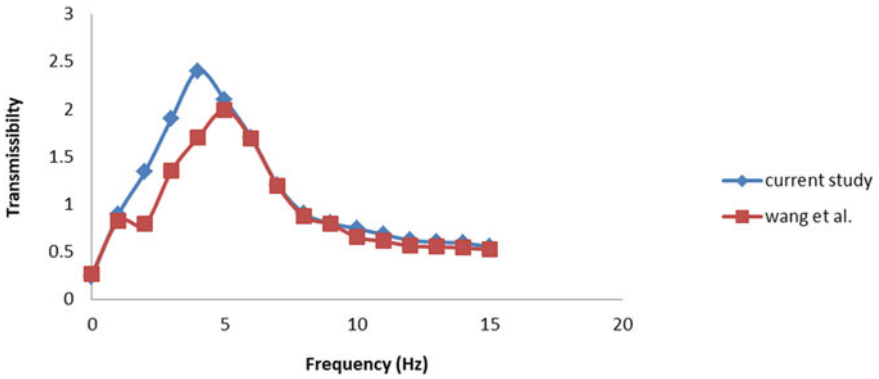

Fig. 5 validation of current study with available literature

While comparing current study results with experimental study conducted by wang et al., it has been shown in Fig. 5 that FEM study shows maximum transmissibility of 2.4 at frequency of 4.8 Hz when acceleration of 1.0 m/s^2 has been applied. While in experimental study conducted by wang et al. [16] shows maximum transmissibility, i.e., 1.9 at frequency of 5.2 Hz. After primary peak, transmissibility in both studies (current and wang et al.) decreases to 0.65 at frequency of 10 Hz, then after value of transmissibility has been between range of 0.65-0.55 for the next frequency up to 15 Hz.

It has been found that results obtained using this study found to be in good relation with existing literature. Inclined back rest posture shows least transmissibility on head in both studies (Current and Wang et al. [16]) for vertical as well as fore-and-aft direction when excitation applied from base with in frequency range of 0.5 to 15 Hz.

6 Conclusion

In this study, seat to head transmissibility has been evaluated in vertical as well as fore-and aft direction on three different sitting conditions, i.e., no back rest sitting, vertical back rest and inclined back rest. It has been found that maximum transmissibility evaluated in vertical direction at vertical back support condition, which is 2.05 at acceleration of 0.25 m/s^2 at frequency of 4.4 Hz. Current study shows that back support has no effect on reduction in transmissibility in vertical direction. While evaluating transmissibility in fore-and-aft direction, it has been found sitting conditions have vital role in reduction of transmissibility. Study shows that transmissibility decreases from no back rest condition to inclined back rest condition. For no back rest condition, maximum transmissibility is 4.1 at acceleration of 0.25 m/s^2, while in inclined back rest condition, maximum transmissibility is 2.8 at same level of excitations.

References

1. Wu X, Rakheja S, Boileau P-E (2018) Dynamic performance of suspension seats under vehicular vibration and shock excitation, SAE technical paper pp 1–15
2. Tiwari VK, Prasad N (1999) Three –DOF modeling of tractor seat–operator system. J Terrramech 36:207–219
3. Rakheja S, Stiharu I (2002) Seated occupant apparent mass characteristics under automotive postures and vertical vibration. J Sound Vib 253(1):57–75
4. Holmlund P, Lundstorm R (2001) Mechanical impedance of the sitting human body in single-axis compared to multi-axis whole body vibration exposure. Clin Biomech 16(1):101–110
5. Deboli R, Calvo A, Preti C (2017) Whole-body vibration: measurement of horizontal and verticaltransmissibility of an agricultural tractor seat. Int J Ind Ergon 58:69–78
6. Dewangan KN, Rakheja S, Marcotte P, Shahmir A (2015) Effects of elastic seats on seated body apparent mass responses to vertical whole body vibration. Ergonomics 58(7):1175–1190
7. Singh A, Singh LP, Singh S, Singh H, Chhuneja NK, Singh M (2018) Evaluation and analysis of occupational ride comfort in rotary soil tillage operation. Measurement 131:19–27
8. Duke M, Gross G (2007) Investigation of tractor driver seat performance with nonlinear stiffness and on-off damper. Biosys Eng 96(4):477–486
9. Laing CC, Chaing CF (2008) Modeling of a seated human body exposed to vertical vibrations in various automotive postures. Ind Health 46:125–137
10. Harsha SP, Desta M, Prashanth AS, Saran VH (2014) Measurement and bio-dynamic model development of seated human subject exposed to low frequency vibration environment. Int J Veh Noise Vib 10(1–2):1–24
11. Mansfield NJ, Griffin MJ (2000) Non-linearities in apparent mass and transmissibility during exposure to whole-body vertical vibration. J Biomech 33:931–944
12. Nawayseh N, Griffin MJ (2004) Tri-axial forces at the seat and backrest during whole-body vertical vibration. J Sound Vib 277(1–2):109–129
13. Chakarbarti D (1997) Indian anthropometric dimensions: For ergonomic design practice. National institute of design, Ahmendabad, pp 30–93
14. Dong RC, He L, Du W, Cao Z-K, Haung Z-L (2018) Effect of sitting posture and seat on biodynamic responses of internal human body simulated by finite element modeling of body-seat system. J Sound Vib 438:543–554
15. Gokhale NS, Deshpande SS, Bedakar SV, Thite AN (2008) Practical element analysis. Finite to infinite, India
16. Wang W, Rakheja S, Boileau P-E (2006) Effect of back support condition on seat to head transmissibilities of seated occupants under vertical vibrations. Journal of Low Frequency Noise, Vibration and Active Control 25(4):239–259

Developments in Three-Dimensional Scanning Techniques and Scanners

Varun Batra and Vijay Kumar

Abstract Three-dimensional scanning is increasingly used in numerous domains such as medicine, computer graphics, and architecture. The first three-dimensional scanning technology was evolved in the 1960s. There are an immense variety of methods to scan objects and their assortment depends primarily on the type of the object and its location. The objective of this study is to provide an overview of three-dimensional scanning technologies and methodologies which were projected in the existing industrial as well as scientific literature. All through the paper, basic physics of surface reflectivity and a variety of related techniques are reviewed, which consist, mainly, of laser scanning and photogrammetry, as well as the three-dimensional scanners, augmented with combinational and comparative studies. These studies are helpful for intending to make a clearer distinction on the relevance and reliability of the possible preferences.

Keywords 3D scanning · Triangulation · Time of flight

1 Introduction

Three-dimensional scanning technology evolutes during the latter half of the twentieth century in an endeavor for accurately recreation of the surfaces for various places and objects. The technology has copious applications and entailing various magnitudes of object scale. These embrace reverse engineering [1, 2], validation of product quality [3], digitally preserving historical artifacts [4, 5], medical applications [6–9], assessing the bearing capacity of slab concrete [10], turbine blades [11], etc. Fundamentally, three-dimensional scanning is the act of confining the data from factual world and bringing that same into the digital conduit which in result gives the cloud of points. Several images or scans, depending on the technique, are brought

V. Batra (✉) · V. Kumar
Chitkara University Institute of Engineering and Technology, Chitkara University, Punjab, India
e-mail: varun.batra.research@gmail.com

V. Kumar
e-mail: vijay.jadon@chitkara.edu.in

L. M. Das et al. (eds.), *Emerging Trends in Mechanical Engineering*, Lecture Notes in Mechanical Engineering, https://doi.org/10.1007/978-981-15-8304-9_5

into a common reference system where they are merged to form a comprehensive model known as alignment [12]. Cameras and three-dimensional scanners are very akin to each other. Similar to cameras, three-dimensional scanners also have a conical field of view and are only able to gather information about the surfaces which are not veiled. Whereas the camera gathers the color information and three-dimensional scanner gathers the information of distance, regarding the surfaces of subjects within its field of view.

The first three-dimensional scanning technology was established in the 1960s. The advent of computers makes it feasible to build up a vastly complex model, but there is a hitch in creation of that model. Subjects having complex surfaces defied the tape measure, so in 1980s, the tool-making industry built up a contact probe which allowed the creation of precise model, although it was quite slow. The endeavor was to develop a technology, which gathers the equal amount of information but at higher speed, resulting in a more valuable application. These lead professionals to initiate the development of optical technology, because the use of light was much faster than a physical probe. This will enable the scanning of soft objects, which would be susceptible to prodding. After 1985, the contact ones were replaced with three-dimensional scanners that could use the optical technology which involves lasers and white light to capture a given subject surface [13].

This paper will first discuss the different techniques involved in three-dimensional scanning of the object. This will be augmented by an overview of basic physics of surface reflectivity and different range measurement principles implicated in laser scanning. The third section briefly outlines the three-dimensional scanners of different types operating on different principles. The fourth section constitutes the comparative study of various techniques and instruments involved in three-dimensional scanning. The fifth section will describe the diverse applications of three-dimensional scanning.

2 Three-Dimensional Scanning Techniques

For digitally attaining the profile of a three-dimensional subject, there are copious techniques. A well-established categorization [14] categorizes them into two categories: contact and non-contact three-dimensional scanning techniques [15]. As well there are numerous techniques which are fall underneath these techniques.

2.1 Contact Technique

Contact three-dimensional scanning techniques are those which will probe the subject by making a physical contact with the subject itself. The probing of the subject is done

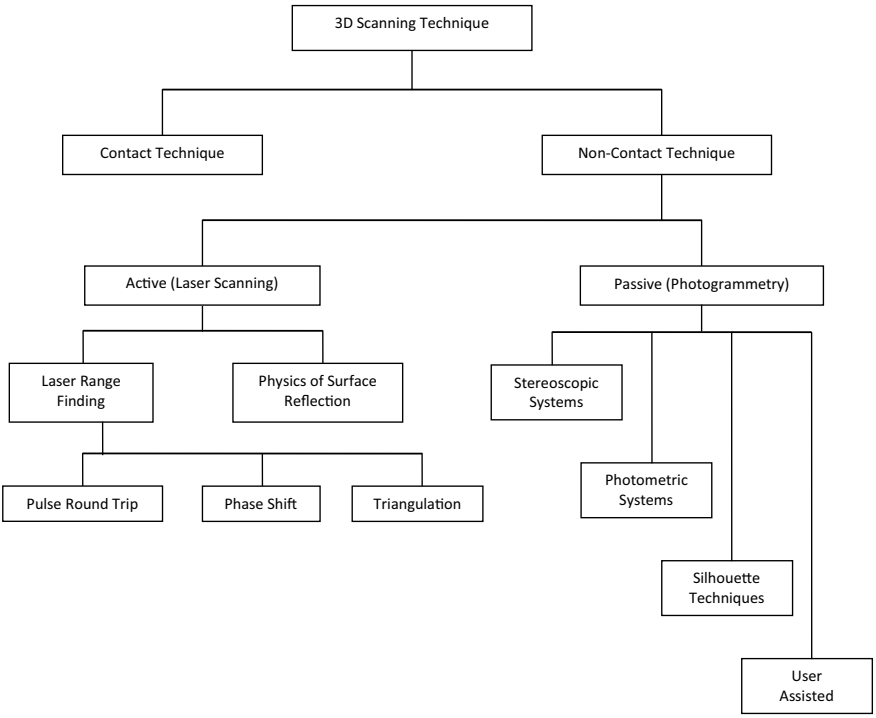

Fig. 1 Categorization of three-dimensional scanning techniques

with the help of robotic arm or manual arm at end of which the probe is available. As the probe touches the surface of the subject, position of the probe recorded and system gets the information of subject (Fig. 1).

2.2 Non-Contact Technique

In this technique, the three-dimensional scanning of the subject is done by without making any physical contact with subject; more appropriately will say the use of an optical technology to probe the subject. In this, the probing is done either by the white light or a beam of laser or ambient light which are projected against the subject's surface. Non-contact three-dimensional scanning technique is further classified [16] into two techniques, i.e., active and passive.

Non-contact active technique. Active non-contact three-dimensional technique radiates the subject with energy and detects the change in behavior of radiated energy in order to probe the subject. In today's era, the most actively using technique to probe the subject is the three-dimensional laser scanning technique which falls under the category of non-contact active technique.

Laser scanning is the technique that gathers three-dimensional coordinates of a subject in a given region at a high rate without human intervention with a systematic pattern and achieving the results in factual instance by using laser device. Laser range finding is the term that involves the aspect of distance measurement, which relies on laser light for performing that particular measurement. The complete technique entails the surface reflectivity physics [17] and some principles involved in laser range finding [18] are discussed in the sections below.

Physics of surface reflection. Electromagnetic radiation involving laser and light demonstrates the properties of both particles and waves. The characterization of electromagnetic radiations is done by a frequency, amplitude and wavelength. The nature of radiation is examined with the help of their relationship between frequency and wavelength of electromagnetic radiation. The electromagnetic waves have a property that all electromagnetic waves have same speed in the vacuum. As described in Eq. 1, the speed of wave is dependent upon frequency and wavelength, clearly helps in characterization of wave:

$$c = f\lambda \tag{1}$$

where c = speed of light, f = frequency of radiation, λ = wavelength of radiation.

Equation 2 describes that light is prepared by photons that possess no mass and also shows that energy (E) is relative to the wavelength (λ) of electromagnetic radiation:

$$E = \frac{hc}{\lambda} \tag{2}$$

where h = Plank's constant.

The standard categorization of electromagnetic radiations specifically based on wavelength as shown in Fig. 2. From the figure, we observe that the range of lasers falls into both the ultraviolet and infrared parts of the spectrum as well as some lasers exhibit in visible region of spectrum. The different wavelength lasers are developed and used for various applications. Lasers are categorized into semiconductor diode, solid state, gas, and dye lasers. Each laser has different mode of operation that is continuous and pulsed, some of them exhibit only pulsed mode and some exhibit both. Some of the lasers are shown on the electromagnetic spectrum with their respective wavelengths in micrometers (μm).

Natural light comprises of an abundant wavelengths. When this light with random emission paths strikes the surface of a subject, amount of an electromagnetic radiation gets reflected by it. The fraction of radiation reflected to the quantity formerly received at the subject surface is practically defined as reflection. A subject surface exhibits various properties in contrast with incident radiation; surface may reflect, transmit, or absorb the incident radiation. There are varieties of surfaces that we deal in our daily life; all those will show the different reflection behavior depending on their surface roughness. When the roughness of surface is lesser than the incident radiation wavelength, this surface will perform the specular reflection where the

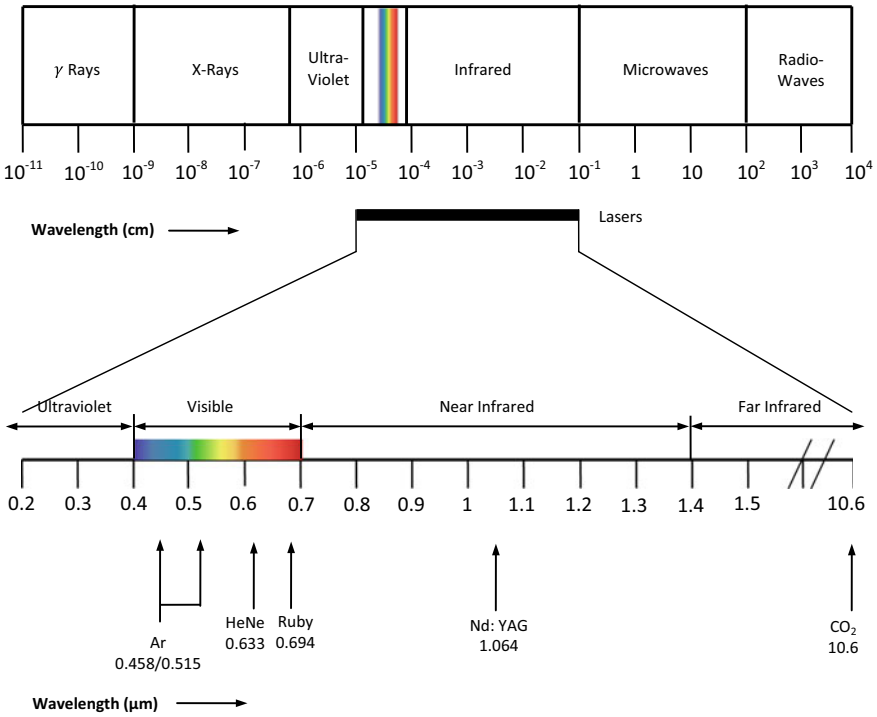

Fig. 2 Wavelength-based classification of electromagnetic radiations

angle of incidence is equal to angle reflection as shown in Fig. 3a. Similarly, when the roughness of surface is greater than the incident radiation wavelength that surface will perform the diffuse reflection as shown in Fig. 3b. Most of the surfaces in the natural atmosphere demonstrate the combination of specular and diffuse reflection known as a mixed reflection as shown in Fig. 3c.

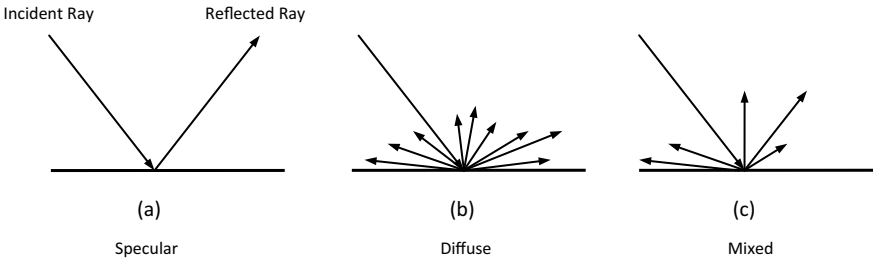

Fig. 3 Reflection types:**a** Specular,**b** diffuse, and**c** mixed

Laser range finding. There are different ranging principles that can be used to compute the distance amid sensing device and subject. These different ranging principles are based on the optical time of flight technique and triangulation technique. These principles have different precision and range perimeter. Optical time of flight is the round trip estimation of a light wave emitted from the emitter to the targeted subject, and then reflected from the subject back to the receiver. It is classified into two types: direct and indirect time of flight. The probing of longer ranges can be done by using the measurement principle of direct time of flight also known as pulse round trip time obtaining the centimeter accuracy. The more precise system of measurement which is fast and accurate than the former but limit to shorter distances of hundred meters is indirect time of flight or phase shift measurement technique. The higher precision and accuracy from the latter technique is also developed known as triangulation which is constrained to smaller distances. These ranging principles detailed below.

Pulse round trip time (Direct time of flight). It is a measure of the time delay between the light pulse sent and received using a time-to-digital converter. The light pulses are typically very short and high intensity. In pulse round trip measurement, a laser pulse is emitted by using a semiconductor or solid-state laser as shown in Fig. 4. The emitted pulse is allowed to pass through the environment, and while traveling through it, laser pulse interacts with surface of subject that comes in its path. The incident laser pulse has energy package associated with it, which can be absorbed or reflected depending on the surface of subject. If laser pulse is reflected, then it will follow the law of reflectivity which we are already discussed. The reflected laser pulse from the surface will then be captivated by receiver. The influence of subject surface on the laser pulse character is shown in Fig. 5. Upon emission of the laser

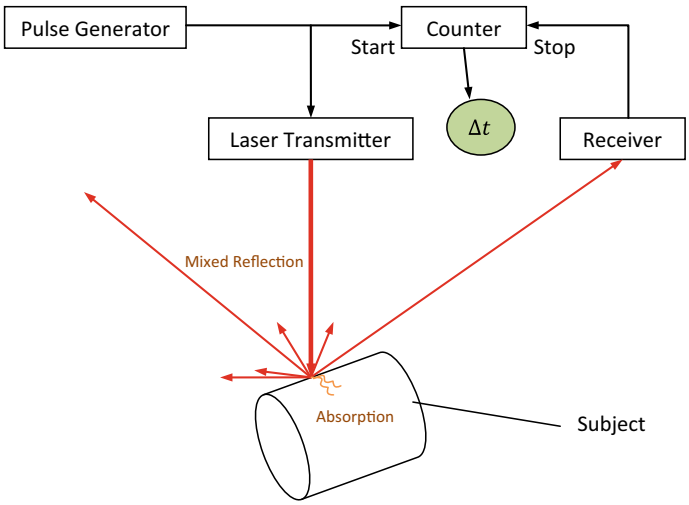

Fig. 4 Pulse round trip measurement principle

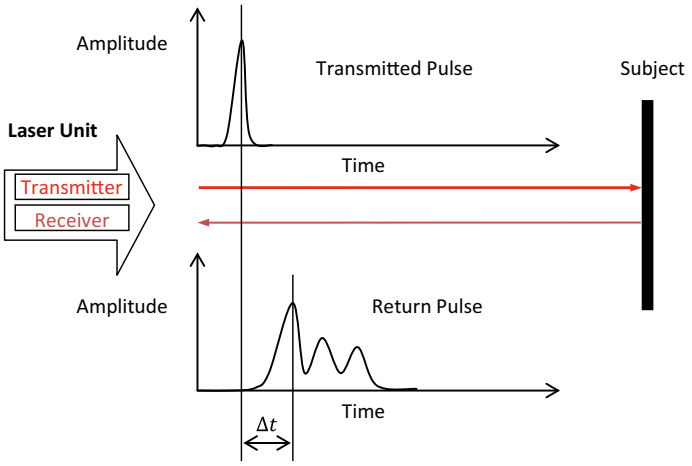

Fig. 5 Subject's surface influence on laser pulse

pulse, a time counter begins and ends after receiving the reflected pulse. If the interval of time is Δt, and c is the velocity of the light amid pulse emitter and subject, the range (r)

$$r = \frac{c\Delta t}{2}$$

Phase shift (Indirect time of flight). This technique uses periodic, low intensity, modulated light pulses. The periodicity of the pulses is determined by the modulation frequency. The phase delay among the transmitted light and the reflected light represents the round trip distance to the subject which is measured by the signal processing pipeline as shown in Fig. 6. Since the signal processing is done in the frequency domain, several cycles of that low intensity periodic pulses are required to complete a single measurement. The measurements which can be done by high frequency modulation will result in precise distances but will constraint to smaller distances. If phase shift among the signal emitted and received is φ, and c is the velocity of the light between the path from emitter to subject and the modulated frequency f_m, the range (r)

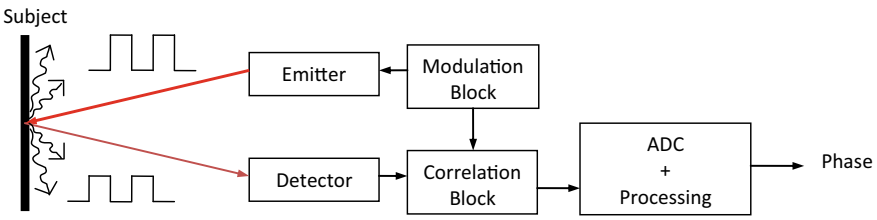

Fig. 6 Indirect time of flight principle

$$r = \frac{c\varphi}{4\pi f_m}$$

When using indirect time of flight, there is a distance, where the phase shift among the signal emitted and the signal received is greater than or equal to the emitter period. This is referred to as aliasing as the two different signals become indistinguishable. To find the maximum range or maximum distance before aliasing occurs as shown in Fig. 7, the formula is:

$$\text{Max Range} = \frac{c}{2f_m}$$

If the target is further than the max range, steps must be taken in order to de-aliasing their signals. If de-aliasing of signals is not performed, ambiguity in distance measurement can be attained due to periodic variation in phase as the distance is increased above the max range [19]. The removal of vagueness can be easily attained by measuring through two dissimilar modulation frequencies. The approach

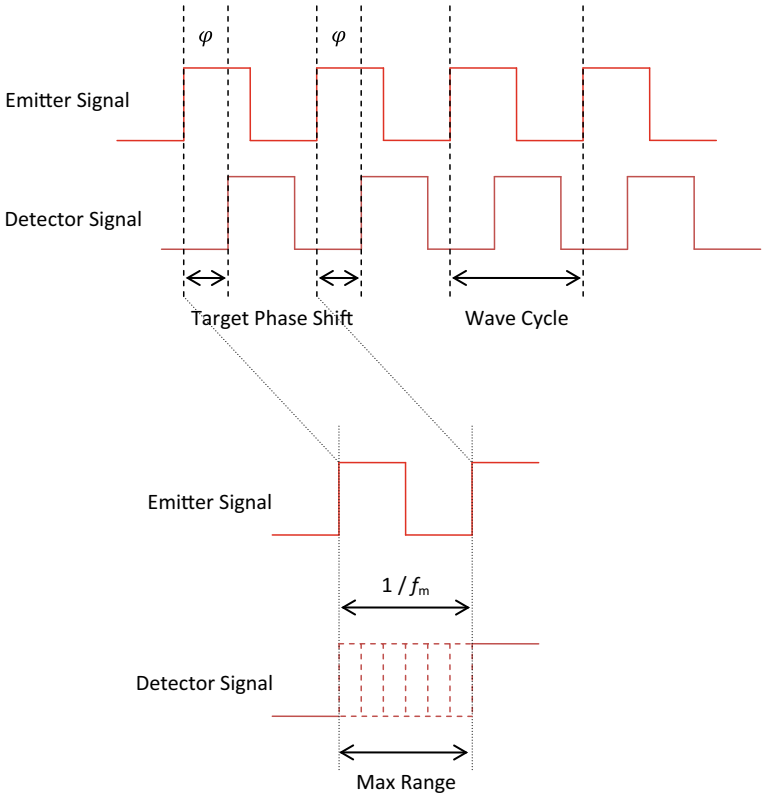

Fig. 7 Showing maximum range before aliasing

of frequency discriminatory computation of the phase variations among emitter and receiver helps to determine the precise measurements [20]. The scanning rate, using indirect time of flight technique, is much quicker than using the direct time of flight technique. The output or point of cloud attained from the indirect time of flight is noisier than the direct time of flight technique [21].

Triangulation. The optical methods which include triangulation technique are the methods based on contactless light reflected from the object and determine its geometry by means of a light-sensitive detector. Active optical methods rely on the projections, so to study the reflected light observations. The active optical method is based upon laser triangulation beam projection. Triangulation-based laser scanning technique was initially developed at National Research Council of Canada in 1978 [22].

For probing subject, the measuring system using method of laser triangulation comprises the laser light as a source (in the form of point or line), and the subject measuring light-sensitive receiver, most commonly uses a camera [23]. The laser beam projected on the surface of subject and by making use of a light-sensitive receiver to seem for the position of dot of the laser. Depending upon the distance from which the laser beam is striking on the subject's surface, dot of the laser emerges at dissimilar positions in the receiver's field of view. The technique named as laser triangulation for the reason that the laser emitter, the camera, and the dot of laser collectively stature a triangle as shown in Fig. 8. The measurement system consists of a laser line and the camera mounted on stand. The distance between the camera and laser beam projector provides one of the length dimensions of triangle. The angle between the plane of the laser beam and the plane perpendicular to the camera image is known. With these pieces of information, distance of dot of laser (measuring point) from the receiver (camera lens) is determined. A stripe of laser is more desired over the dot of laser, as it would sweep around the subject for probing and helps in speeding up the data acquirement process.

Non-contact passive technique. Passive non-contact three-dimensional technique does not radiates the subject with energy; instead rely on detecting ambient

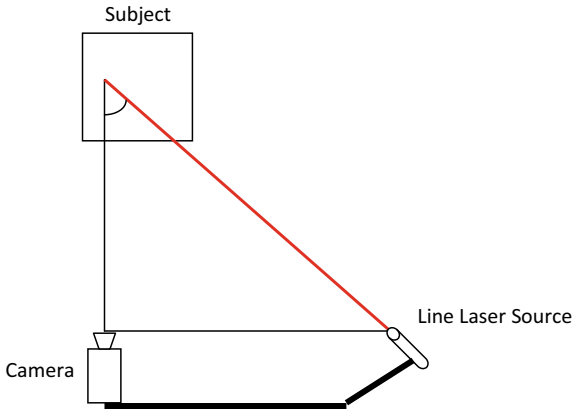

Fig. 8 Principle of a laser triangulation

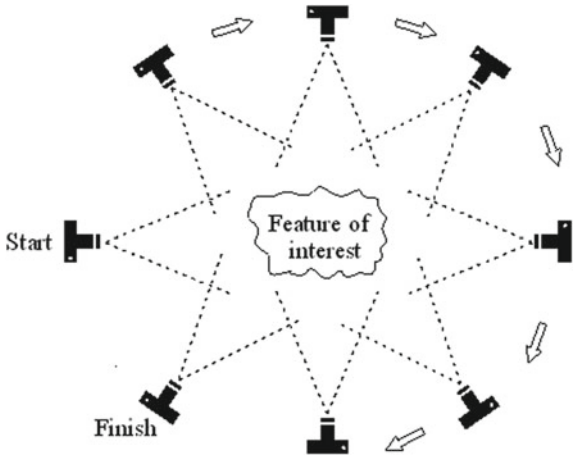

Fig. 9 Principle of photogrammetry

radiation in order to probe the subject. This technique uses the visible light for probing as it is an eagerly existing ambient radiation. This involves the technique of photogrammetry to replicate the subject.

Photogrammetry technique. Photogrammetry is the science of making measurements from photographs [24]. Photogrammetry technique is defined as the technology of gaining the useful information about the substantial subjects and surroundings during the procedure of interpreting photographic images, measuring and recording. This technique uses methods from different disciplines, mainly projective geometry and optics. The principle behind photogrammetry is capturing the numerous images of the subject from different sights and importantly having a common point of reference in each photograph as shown in Fig. 9. The subject which needs to be developed is placed at a well luminosity position. The set of images are then put up into any photogrammetry application software to develop a three-dimensional model of the subject as an end product. There are some systems and techniques which are using the photogrammetry principle are discussed in section below.

Stereoscopic systems. These systems are generally using the two video cameras which are faintly spaced out from each other and both looking at the same scenario. Examining the trivial difference among the digital images perceived by both the cameras makes it feasible for determining the distance at every point in the images.

Photometric systems. These systems are typically using a single camera, apart from numerous shots of digital images are taken underneath the changeable lighting situations. In an attempt to recuperate the orientation of surface at each pixel, these techniques capsize the image formation model.

Silhouette techniques. These techniques are using outlines produced by the series of photographs about a three-dimensional subject which is contiguous to a contrasted surrounding. The visual hull approximation of subject is attained by the intersection

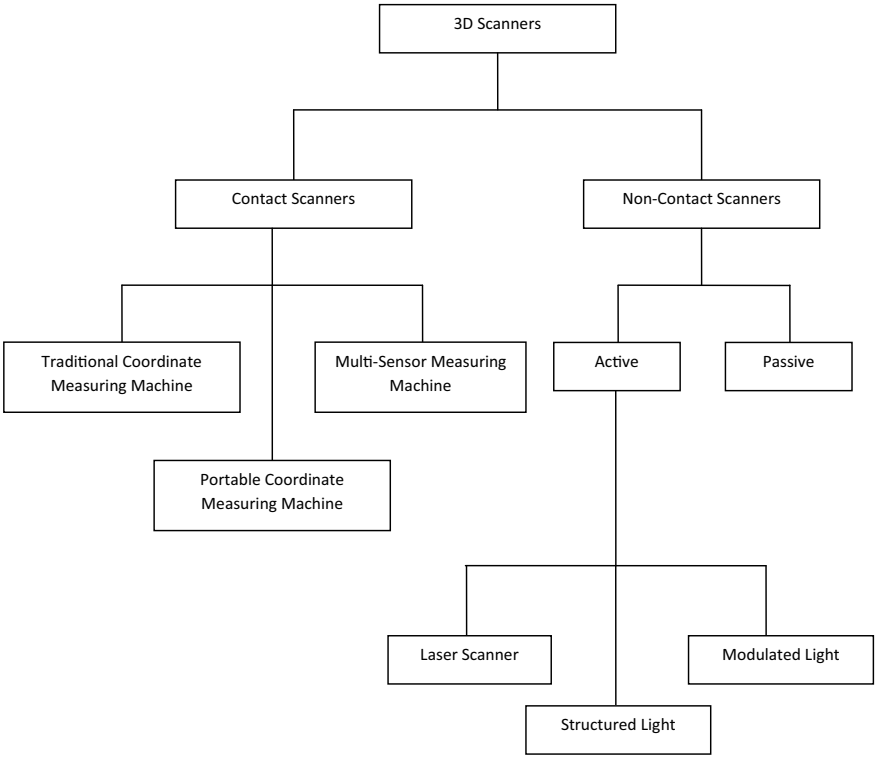

Fig. 10 Categorization of three-dimensional scanners

of those extruded silhouettes. The drawback of using this approach is, sometimes the concavities of the subject are unable to detect.

User assisted (Image-based modeling). These are the methods which are based on the assistance of user for the purpose of identifying and detecting some of the features as well as shapes from a set of various digital pictures of a subject. Then the resulting assistance would help in building the approximated model of the subject itself. Building a quick approximation of simple-shaped subjects is the useful perspective of this technique.

3 Three-Dimensional Scanners

Three-dimensional scanners are the devices which are used to capture the physical objects from factual world as well as surroundings in some scenarios, so that the captured object can be remodeled or analyzed digitally along with getting the complete or partial 3D measurement of subject. The majority of these devices

generate an output of highly dense point cloud. There are numerous scanning equipments for digitally attaining the profile of a three-dimensional subject. A well-established categorization [25] categorizes them into two types: contact and non-contact three-dimensional scanners. Non-contact three-dimensional scanners are further categorizing into two main categories, active three-dimensional scanners and passive three-dimensional scanners. There are varieties of scanning equipments that fall underneath these categories (Fig. 10).

3.1 Contact Three-Dimensional Scanner

Contact three-dimensional scanners are normally attuned to operate on the rigid podium which consists of an articulated mechanical arm at the end of which the probe is attached. This articulated arm can be manipulated over the surface of subject either robotically or manually. The moment probe makes a contact with the surface of subject; there is some position of the arm from which the probing point is determined and the same recorded by scanner. The recorded positions at different points of a subject form a point cloud. The highly accurate contact three-dimensional scanners called coordinate measuring machines (CMM's). These kinds of contact three-dimensional scanners are often used by the manufacturing industry for inspection rationale. Contact three-dimensional scanners are not a suitable choice for the delicate subjects because the probing may deform or else damage the surface of subject as well as these scanners undergoes very slow scanning speed. The various scanners are fall under this category are discussed in section below.

Traditional coordinate measuring machine (CMM). A traditional coordinate measuring machine (CMM) is a three-dimensional contact scanner for assessing the physical geometrical characteristics of the subject. The scanner can be operated manually or controlled through application software installed on system software. Probes are the tools which consist of a shaft at the end of which a small ball of known radius is attached as well as the dimensions are defined by attaching the same to scanner. The coordinate measuring machine is subsequently programmed to probe the subject. The positional measurements are recorded by the scanner after the scanner senses the contact of probe on the surface of subject.

The most common type of traditional coordinate measuring machine is a viaduct type which consists of three axis x, y, and z. The probing system of scanner endows with six degrees of freedom. When the accuracy and precision is the primary perimeter to attained in the output, these coordinate measuring machines are separately deployed in a control room which consists of reinforced floor, vibration isolated system, controlled environmental conditions and must not have forces which affect the accuracy. Moreover, most coordinate measuring machines have a rigid and perfectly leveled granite base at which the subject is fixed so to constrain the movement of the subject (Fig. 11).

Portable coordinate measuring machines. Portable coordinate measuring machines are quite analogous to traditional coordinate measuring machines in the

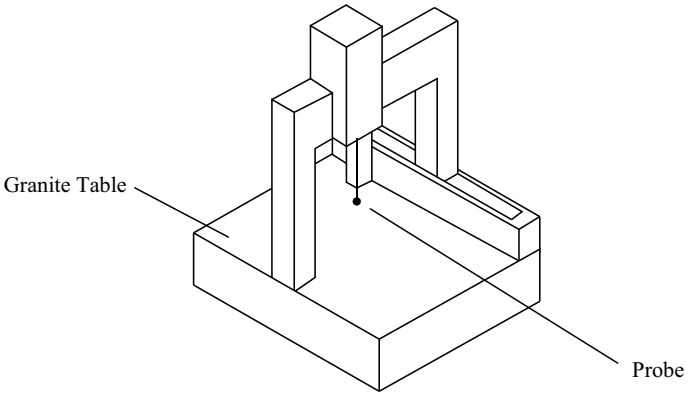

Fig. 11 Traditional coordinate measuring machine

verity that it also uses the touch probe to digitally acquire a subject. The portable coordinate measuring machines are using a ball or point probe on an articulating arm, allowing the users to collect individual three-dimensional data points from the physical object. These articulating arms have several rotary axis with rotary encoders, instead of linear axis. The advantages of these portable arms are that these are light in weight and can be carried and used anywhere. These scanners are always requiring a human for its use, and the overall efficiency is less accurate than the traditional coordinate measuring machines. These measuring machines are required to be fixed on a rigid surface, subsequently to make the arrangement prone to vibrations and other surrounding constraints which will affect the quality and performance of the machine. These machines also lack in flexibility in terms of the shape of the subject to probe as well as the location where the arm is fixed (Fig. 12).

Fig. 12 Portable coordinate measuring machine

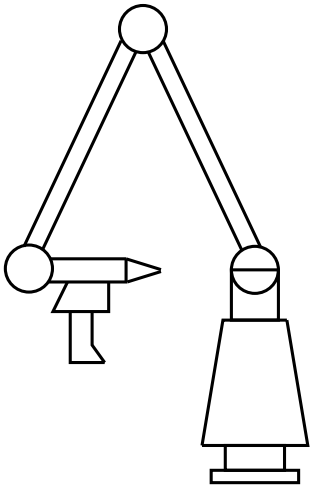

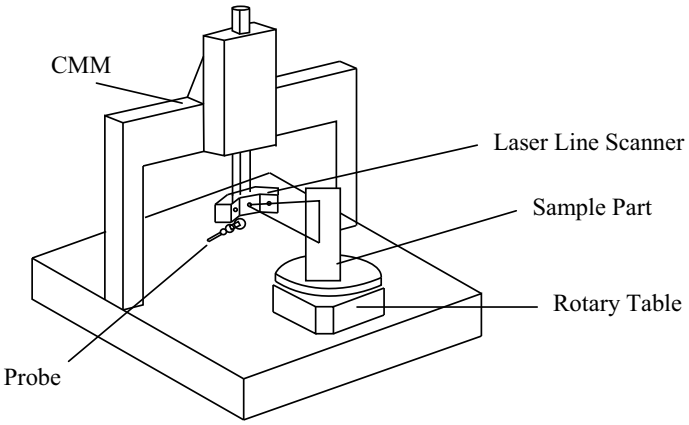

Fig. 13 Multi-sensor measuring machine

Multi-sensor measuring machines. The technology of traditional coordinate measuring machines is making use of the touch probes for the measurement. The same setup evolutes with other measurement technology or we can say optical technology. This combined arrangement of touch probe and optical technology which constitutes laser and white light sensors develops a machine known as multi-sensor measurement machines (Fig. 13).

3.2 Non-Contact Three-Dimensional Scanner

Non-contact three-dimensional scanners justified by its name itself that an arrangement does not make any physical contact with the subject's surface to digitally acquire the same. Non-contact three-dimensional scanners are further categorizing into two techniques, i.e., active and passive techniques to digitally acquire the subject. The ultimate outcomes of these scanners are the highly accurate and dense cloud of points which can be further used for numerous applications like rapid prototyping and feature or surface inspection.

Non-contact active scanners. Non-contact three-dimensional active scanners radiate the subject with energy and detect the change in the behavior of radiated energy in desire to digitally acquire the subject or environment. The possible radiations which employs on the subject for probing are electromagnetic radiations, from which ultrasound, x-ray, light, and laser are the most predominantly using nowadays. The frequently used non-contact three-dimensional active scanners embraces three-dimensional laser scanners, structured light scanners and modulated light scanners as well as some volumetric techniques that are computed tomography scanners and magnetic resonance imaging scanners. Several existing non-contact active scanners are discussed in the sections below.

Three-dimensional laser scanners. Three-dimensional laser scanners, as the name implies, do make use of the laser for scanning or probing the subject's surface. The basic principles behind the laser scanners are that they emanate and entertain their own electromagnetic radiation for probing the surface of subject. The term laser scanner encloses a variety of instruments that functions on different principles as well as in different surroundings along with different levels of accuracy and precision. Most of the laser scanners functions on any of three laser ranging principles: pulse round trip time (direct time of flight), phase shift (indirect time of flight), or triangulation. The data referred to as a collection of points converted from angular and range measurements into a universal Cartesian coordinate system that delineates the subject's surface in immense detail. This data collection can be done with different laser scanners, importantly classifies into four types on the basis of their orientation that are: terrestrial scanners, airborne scanners, mobile scanners, handheld scanners. The laser scanning systems with typical accuracies and ranges with the usage are detailed in the table given in [24].

Structured light scanners. Structured light three-dimensional scanners emanate a pattern of electromagnetic radiation, usually light is used, onto a subject and look at the distorted pattern of light after hitting the subject. The three-dimensional models can be built by altering the light patterns and view angles. Either a sweeping laser or the LCD projector is used for projection of one-dimensional light onto the subject. The pattern projector and camera are aligned, angled, and calibrated to one another. A camera seems the character of the distorted light pattern and uses a range finding technique of triangulation or any other algorithm for calculating the distance of each point on the distorted pattern or in line as shown in Fig. 14. The pattern of emitted light is categorized into one-dimensional pattern and two-dimensional pattern. The arrangement in which line is probing the subject is one-dimensional light pattern scanning, and on the other hand, if it is probed with the grid or line stripe, pattern is the two-dimensional pattern scanning. The laser stripe ambiguity comes to scenario

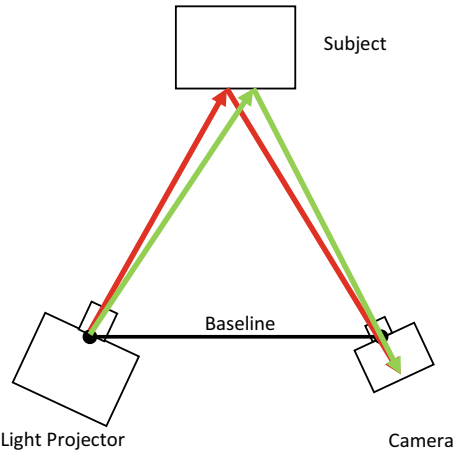

Fig. 14 Working of structured light scanner (Top down view)

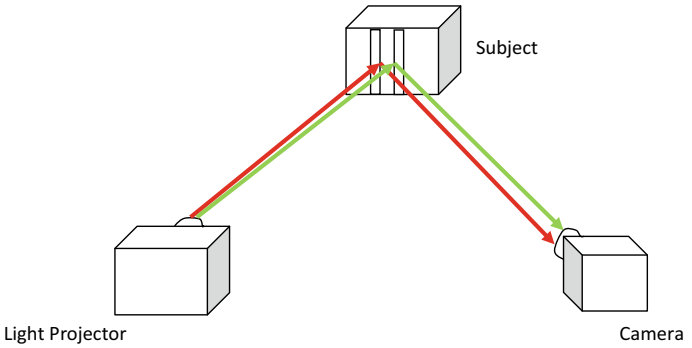

Fig. 15 Working of structured light scanner (Angled view)

in the cases where the subjects profile is containing holes, rapid change in depths and occlusions; these parameters either break down the stripe sequencing or may hide the stripe. This ambiguity can be resolved using multi-stripe laser triangulation algorithms.

The advantages of structured light scanners deliver an admirable resolution and good quality data, which enables it to capture the smallest detail or feature available on the subject's surface. The limitation as we know these scanners can acquire a good quality data in addition to that they also acquire the good quantity data in one scan. The subject replica development requires a multiple scans that are very time consuming, which denotes that the scanning speed is not enhanced by this methodology (Fig. 15).

Modulated light scanners. The modulated light three-dimensional scanners illuminate a persistently altering light on the subject. Generally, the light source has a cycle whose amplitude portrays a sinusoidal pattern. The reflected light is detected by the camera which measures the importance of light variation and find out the distance traveled by light. The modulated light moreover allocates the three-dimensional scanner arrangement to disregard the light from other sources except laser, so to avoid any obstruction.

Non-Contact Passive Scanners. Non-contact passive scanners cannot emanate any sort of radiations on subject for probing, but instead dependent on perceiving reflected ambient radiation. Most of the passive scanners perceive visible light because it is an eagerly presented ambient radiation. The other type of radiations possibly will use infrared radiations. Passive scanning methods are quite economical due to no need of particular hardware requirement, only required is digital camera. Some non-contact three-dimensional scanners include stereoscopic scanners, silhouette scanners, etc.

4 Discussion

The three-dimensional scanning techniques and instruments compose an extensively broad range; due to this fact, several studies have performed to contrast them from diverse perspectives.

4.1 A Comparison of Active and Passive Scanning Technique

In [26], the comparison for data attainment and processing from three-dimensional scanning techniques, i.e., passive and active, were discussed. In this overview, majorly the laser scanning in active technique and photogrammetry in passive technique are reviewed. Initially for data acquisition, the laser scanning senses through point sensors with polar geometry, whereas photogrammetry senses with linear or framed sensors with perspective geometry. As the subject is radiated with laser directly, it is a direct acquisition in active technique, whereas there is neither any direct contact with subject surface nor by any optical technology so it is an indirect acquisition in passive technique. The active technique is founded to be lesser in flexibility and variability and vice versa in case of passive techniques. Active technique would efficient at lower flying speed and height, whereas passive technique gives efficient outcome at higher flying speed and height. Last but not the least, the active technique is proved somewhat automatic and passive technique requires a manual intervention.

4.2 Three-Dimensional Scanning Instrument

The various three-dimensional scanners are studied in the third section, from where we conclude that each scanner has advantages and disadvantages in perspective of range, accuracy, and precision. So, it is not feasible that each scanner will able to perform in all scanning situations. The scanning devices are broadly categorized into three categories on the basis of range [27] that are 10 to 100 cm, 100 to 1000 cm, and 1000 to 10,000 cm. More importantly, when rate of scanning or point acquisition speed taken into the account for looking into the practical use of three-dimensional instrument, this parameter can increase or decrease the operational time for digitally acquiring the subject or surroundings. Usually, the scanning resolutions of higher resolution are desirable. Every three-dimensional scanner has its own limited field of view. Larger is the field of view of scanner, larger is the data collected by scanner in the single scan. Portability factor is to be present in every scanner for the ease of transportation as well as their use.

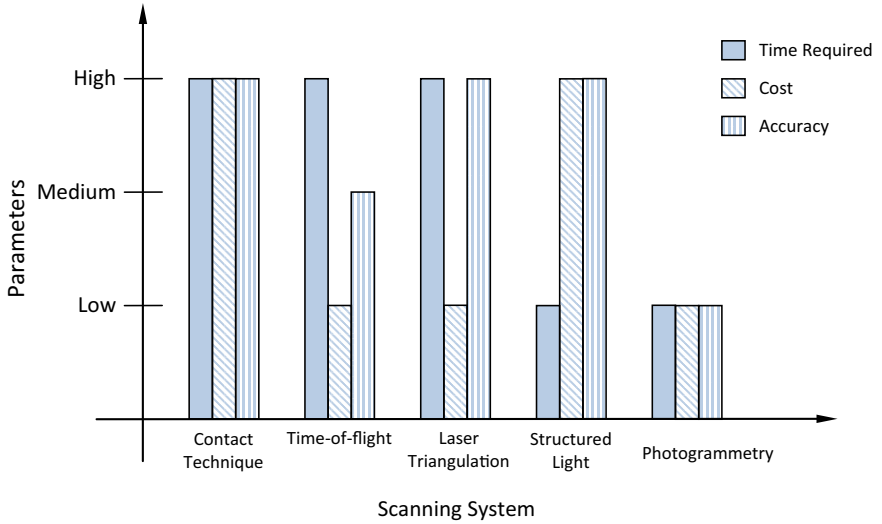

Fig. 16 Parameter-based comparison

4.3 Metric Survey

In terms of size and complexity, Fig. 16 attempts to differentiate between the available techniques to guide the user toward an appropriate decision [28]. Hand measurements are able to provide the dimensions of the small objects at finite number of points and become uneconomic for larger size objects. Total station theodolites (TSTs) are the instruments used in data collection as well as for survey of site control network. A global navigation satellite system (GNSS) is generally used for geographic information system (GIS) data collection and topographic task. GNSS is also used to measure control networks, especially when connecting to a national grid. Photogrammetry and laser scanning are the techniques which are collecting the data from the object in abundance and are found appropriate techniques for scanning the compound subjects over a variety of scales (Figs. 17, 18, 19 and 20).

4.4 A Comparison of Laser Range Finders

The various three-dimensional scanning techniques are studied in the second section, from where we conclude that each technique has associated benefits and limitations which make them apposite for diverse situations. Here, we discuss some of them for laser range finders that are time of flight and triangulation range finders. The time-of-flight range finders have an advantage that this technique allows to use for amazingly long distances, about thousands of meters [29]. This principle is therefore suitable for

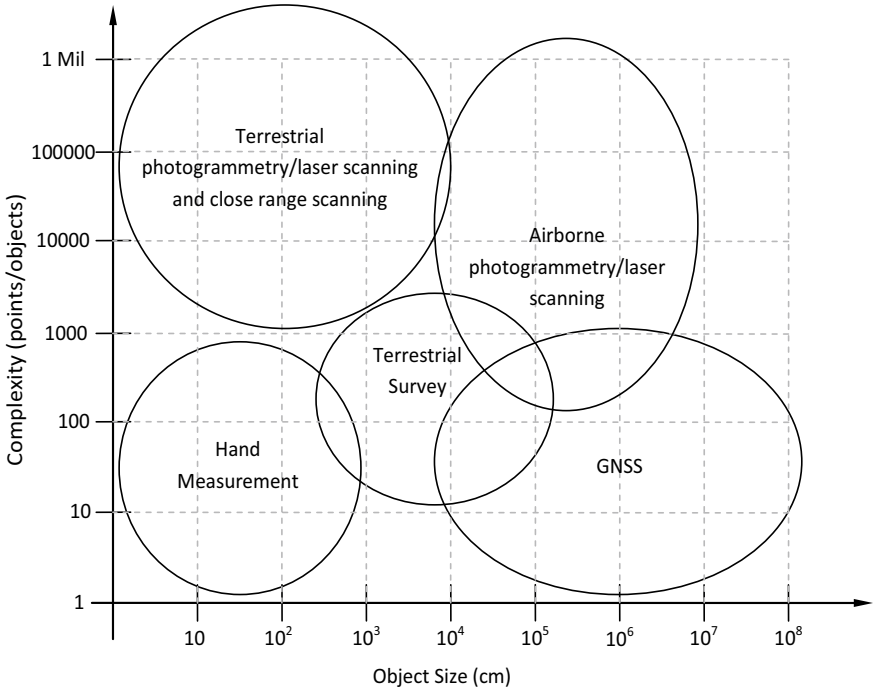

Fig. 17 Appropriate technique selection through size and complexity

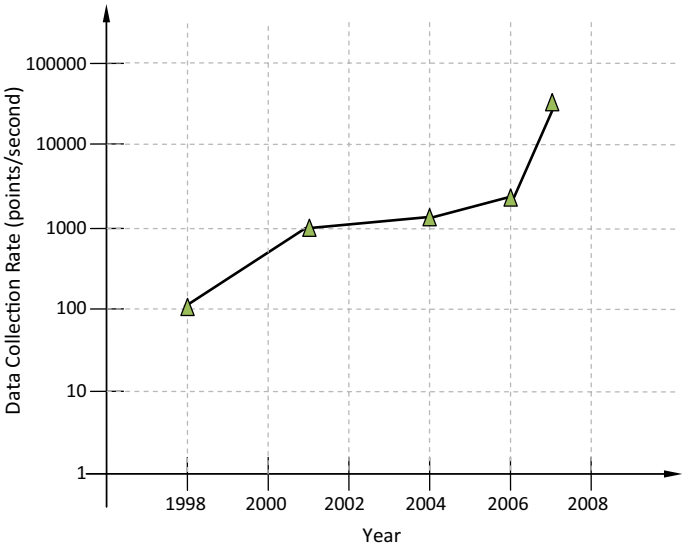

Fig. 18 Showing evolution of terrestrial pulsed laser scanning technology

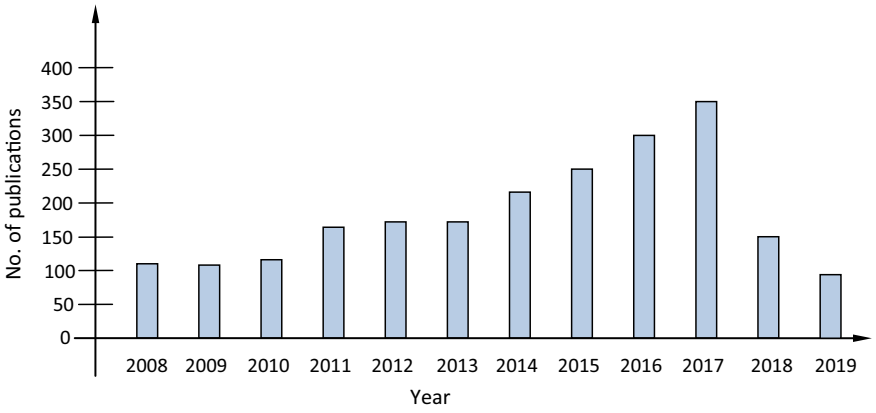

Fig. 19 Year-wise publication of 3D scanning. *Source* Scopus

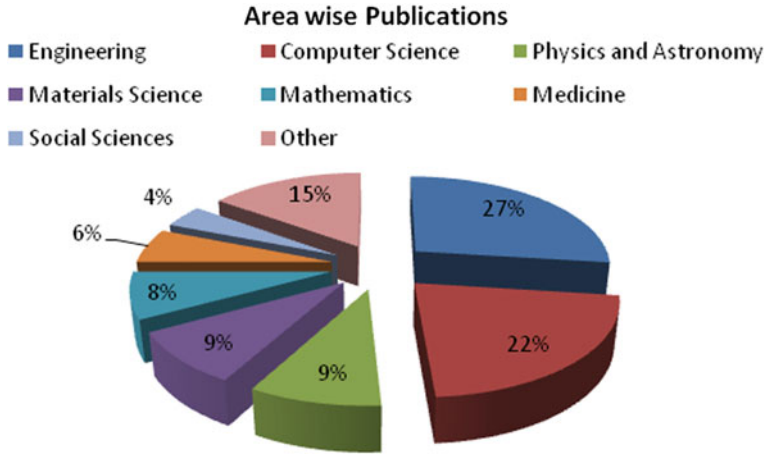

Fig. 20 Area-wise contributions of 3D scanning. *Source* Scopus

digitally acquiring the large structures like building exteriors or interiors and large site prospecting as well as mapping. It is difficult to compute the round trip time because of high light speed which leads to low accuracy that is near millimeters. The triangulation range finders are entirely converse to the time-of-flight range finders. These range finders have weakness for some constrained range of several meters, but equally have strength of higher level of accuracy near to tens of micrometers [30].

4.5 Comparison Table

See Table 1.

5 Application

The evolutions of non-contact scanning techniques would be useful in diverse applications. A few general examples which utilize one of the non-contact scanning techniques that are active and passive scanning techniques are cited and presented in Table 2.

6 Conclusion

The comprehensive study reveals that instead of threat by prodding of subject, the major concern is precision and accuracy for a three-dimensional scanning. In solution to this, contact scanner appears to be a suitable approach. On the other hand, non-contact scanners are best choice where subjects are affected by prodding and require high digital data acquisition speed. Further, non-contact scanner has been classified as active and passive three-dimensional scanners which functions for different surroundings and with their own level of accuracy and precision.

While categorizing the active laser scanners, it was found that active laser scanners work on three different principles; direct time of flight(first), indirect time of flight(second), triangulation(third). Where the first principle is suitable for very long range scans, the second principle is found to be suitable for short range scans while very short range scans are possible by third principle. The precision and accuracy of the above active laser scanners was found to be decreasing with increase in the ranges of laser scanners. Besides this, they also need enough time to digitally acquire the subject. Later for improved accuracy and fast time response, the structured light scanners were developed using triangulation principle. But, these structured light scanners require large initial investment. In order to obtain low cost and high speed, photogrammetry technique can be used while compromising the precision and accuracy. This type of approach comes under passive scanning technique.

Therefore, the selection of appropriate scanning instrument according to the application plays an important role to generate the accurate replica of the subject. The reported work will be helpful for suggesting the best scanning system for performing the chore of three-dimensional scanning.

Table 1 Evaluation of numerous three-dimensional scanning techniques

Sr. No	Scanning system	Time required	Cost	Accuracy	Usage
1	Contact technique	▲	▲	▲	Shiny, mirroring or transparent objects
2	Time of flight	▲	▽	■	Streetscapes, highways, buildings
3	Laser triangulation	▲	▽	▲	Replica production of small objects
4	Structured light (Triangulation)	▽	▲	▲	Reverse engineering
5	Photogrammetry	▽	▽	▽	Planimetric mapping, topographic mapping

Note Respective symbol represents the status.

▲ High ■ Medium ▽ Low

Table 2 General examples utilizing active and passive techniques

Technique	Scanning System	Application(s)		Citation(s)
Non-Contact Active Scanning	Laser Scanning	Heritage Monitoring	Statues of Michelangelo	[31]
			The Guyue Bridge	[32]
		Mining		[33, 34]
		Configuration Modeling for a Constrained Elastica Cable		[35]
	Mobile Laser Scanning	Extracting Road Information	3D Local Feature BKD	[36]
			Semiautomated Delineation	[37]
			Detecting Road Boundaries	[38]
		Street Object Recognition	Feature Matching	[39]
			Detecting Street Lighting Poles	[40]
	Terrestrial Laser Scanning	Archaeological Site Documentation	Byzantine Land Walls of Istanbul	[41]
			The Temple of the Sacred Tooth Relic at Kandy, Sri Lanka	[42]
			Geoarchaeological Sites in Jordan, Egypt and Spain	[43]
		Data Acquisition for Indoor Assets		[44]
		Urban Environment Modeling		[45]
	Airborne Laser Scanning	Landslide Activity Analysis		[26, 46]
		Forest Canopy Analysis	Quantification	[47]
			Estimating the LAI	[48]
	Time of flight, Structured Light and Phase Comparison	Motion Compensation		[49]
		A Tool-free Calibration Method		[50]
		Improved Coverage through Online Structured Light Calibration		[51]

(continued)

Table 2 (continued)

Technique	Scanning System	Application(s)			Citation(s)
		3D Shape Scanning with TOF Sensors			[52]
		Low-cost Hand-held 3D Scanning of Architectural Elements			[53]
		The Kinect Sensor	Objects		[54, 55]
			Persons		[56]
		Polarization and Phase shifting	Translucent Objects		[57]
			A Wideband Antenna		[58]
		An Infrared System for Metallic Surfaces			[59]
Non-Contact Passive Scanning	Photogrammetry	Fast Implementation of a Radial Symmetry Measure			[60, 61]
		Survey of Natural Areas of Special Protection			[62]
		Relative Pose Measurement of Satellite and Rocket			[63–65]
	Close-Range Photogrammetry	Automatic Camera Calibration			[41, 66, 67]
		Line Detection and Matching			[68]
		Forest Analysis	Plant Diversity and Surface Fuel Structure		[69]
			Mapping Eroded Areas on Mountain Grassland		[70]
		A Simulation Tool for the SRT			[71]
		River Surface Water Topography Mapping at Sub-mm Resolution and Precision			[72]
		City Modeling			[73]
	Aerial Photogrammetry	The ISPRS Benchmark			[74–76]
		Feature Extraction and Matching			[77, 78]
		Accurate Optical Target Pose Determination			[79]
		Survey of Historical Heritage		Pre-Hispanic Wall Painting	[80]

(continued)

Table 2 (continued)

Technique	Scanning System	Application(s)		Citation(s)
			Historical Buildings of the City of Strasbourg	[81]
		Street-level Modeling	Steep Surfaces	[82]
			Building Abstraction	[83]
			Effects of Image Orientation and Ground Control Point Distributions	[84]
		Topographic Monitoring		[85–87]
		Determining Fault Planes		[88, 89]
		Improving Height Accuracy Using a Multi-class System		[90]
	Terrestrial Photogrammetry	Coastal Projectors		[91]
		Landslides		[92]

References

1. Javed MA, Won SHP, Khamesee MB, Melek WW, Owen W (2013) A laser scanning based reverse engineering system for 3D model generation. IECON Proc Indus Electron Conf 4334–4339. https://doi.org/10.1109/IECON.2013.6699832
2. Peterka J, Morovič L, Pokorný P, Kováč M, Hornák F (2013) Optical 3D Scanning of Cutting Tools. Appl Mech Mater 421:663–667. https://doi.org/10.4028/www.scientific.net/amm.421.663
3. Voicu AC, Gheorghe GI (2013) Complex 3D measuring by multiple laser scanning of automotive parts. Adv Mater Res 837:511–516. https://doi.org/10.4028/www.scientific.net/amr.837.511
4. Todorov Y, Todorova G, Nikolay B, Bogdanova G, Todorov T, Noev N (2013) Digitization and 3D scanning of historical artifacts. Digit Present Preserv Cult Sci Herit 3:133–138
5. Kumar S, Snyder D, Duncan D, Cohen J, Cooper J (2003) Digital preservation of ancient cuneiform tablets using 3D-scanning. Proc Int Conf 3-D Digit Imaging Model 3DIM 326–333. https://doi.org/10.1109/IM.2003.1240266
6. Ares M, Royo S, Vidal J, Campderrós L, Panyella D, Pérez F, Vera S, González Ballester MA (2014) 3D Scanning System for In-Vivo Imaging of Human Body. In: Fringe 2013. pp 899–902. Springer Berlin Heidelberg, Berlin, Heidelberg
7. Berryman F, Pynsent P, Fairbank J, Disney S (2008) A new system for measuring three-dimensional back shape in scoliosis. Eur Spine J 17:663–672. https://doi.org/10.1007/s00586-007-0581-x
8. Glinkowski W, Sitnik R, Witkowski M, Kocoń H, Bolewicki P, Górecki A (2009) Method of pectus excavatum measurement based on structured light technique. J. Biomed. Opt. 14:044041. https://doi.org/10.1117/1.3210782
9. Jaspers S, Hopermann H, Sauermann G, Hoppe U, Lunderstädt R, Ennen J (1999) Rapid in vivo measurement of the topography of human skin by active image triangulation using a digital micromirror device. Ski. Res. Technol. 5:195–207. https://doi.org/10.1111/j.1600-0846.1999.tb00131.x
10. Bindean I-A, Stoian V (2013) Determination of the remaining bearing capacity of an existing slab using 3D scanning technology. Recent Adv Civ Min Eng 136–140
11. Brozović M, Avsec A, Tevcic M (2013) Dimensional control of complex geometry objects using 3d scanning technology. In: Proceedings of the 14th International Scientific Conference on Production Engineering–Cim 2013, Biograd, Hrvatska
12. Bernardini F, Rushmeier H (2002) The 3D model acquisition pipeline. Comput. Graph. Forum. 21:149–172. https://doi.org/10.1111/1467-8659.00574
13. History of 3D scanners, https://www.modena.co.za/history-of-3d-scanners/
14. Curless B (2000) From Range Scans to 3D Models. ACM SIGGRAPH Comput. Graph. 33:38–41
15. Chougule VN, Gosavi HS, Dharwadkar MM, Gaind AA (2018) Review of Different 3D Scanners and Scanning Techniques. IOSR J Eng 41–44
16. Abdel-Bary EBRAHIM M (2013) 3D Laser Scanners' Techniques Overview. Int J Sci Res 4:2319–7064
17. Heritage GL, Large ARG (2009) Laser Scanning for the Environmental Sciences. Wiley-Blackwell, Oxford, UK
18. Pfeifer N, Briese C (2014) Laser scanning—principles and applications. GeoSiberia 2007.Int Exhib Sci Congr 1–20. https://doi.org/10.3997/2214-4609.201403279
19. Moussa W (2014) Integration of Digital Photogrammetry and Terrestrial Laser Scanning
20. Fröhlich C, Mettenleiter M, Härtl F, Dalton G, Hines D (2000) Imaging laser radar for 3-D modelling of real world environments. Sens. Rev. 20:273–282. https://doi.org/10.1108/02602280010351019
21. Mechelke K, Kersten TP, Lindstaedt M (2007) Comparative Investigation into the Accuarcy Behaviour of the New Generation of Terrestrial Laser Scanning Systems. Opt. 3-D Meas. Tech. VIII I:319–327

22. Mayer R (1999) Scientific Canadian : invention and innovation from Canada's National Research Council. Vancouver : Raincoast Books
23. Mikulski, S.: Laser triangulation in three-dimension al scanners. 485–491
24. Photogrammetry, https://en.wikipedia.org/wiki/Photogrammetry
25. 3D scanning, https://en.wikipedia.org/wiki/3D_scanning
26. Baltsavias EP (1999) A comparison between photogrammetry and laser scanning. ISPRS J. Photogramm. Remote Sens. 54:83–94. https://doi.org/10.1016/S0924-2716(99)00014-3
27. Daneshmand M, Helmi A, Avots E, Noroozi F, Alisinanoglu F, Arslan HS, Gorbova J, Haamer RE, Ozcinar C, Anbarjafari G (2018) 3D Scanning: A Comprehensive Survey
28. England H (2018) 3D Laser Scanning for Heritage: Advice and Guidance on the Use of Laser Scanning in Archaeology and Architecture
29. Valanis A, Georgopoulos A, Sofronidou M (2009) Scanning for microns. Technology
30. Naughton TJ, Falldorf C, Onural L, Ferraro P, Depeursinge C, Krueger S, Emery Y, Hennelly BM, Kujawifiska M (2010) Capture, processing, and display of real-world 3D objects using digital holography. 2010 9th Euro-American Work. Inf. Opt. WIO 2010. 3–5. https://doi.org/10.1109/WIO.2010.5582528
31. Levoy M (1999) The digital Michelangelo project. Proc 2nd Int Conf 3-D Digit Imaging Model. 3DIM 1999. 2–11. https://doi.org/10.1109/IM.1999.805329
32. Lu N, Wang Q, Wang S, Zhang R (2015) The application of 3d laser scanning in the survey and measuring of guyue bridge of song dynasty in Yiwu City. ISPRS Ann Photogramm Remote Sens Spat Inf Sci 2:185–190. https://doi.org/10.5194/isprsannals-II-5-W3-185-2015
33. Fengyun G, Hongquan X (2013) Status and development trend of 3D laser scanning technology in the mining field. In: Proceedings of the 2013 International Conference on Remote Sensing,Environment and Transportation Engineering. pp 407–410. Atlantis Press, Paris, France
34. Guo J, Jiang J, Wu L, Zhou W, Wei L (2016) 3D modeling for mine roadway from laser scanning point cloud. In: 2016 IEEE International Geoscience and Remote Sensing Symposium (IGARSS). pp 4452–4455. IEEE
35. Du H, Xiong W, Wang H, Yuan B, Wang Z (2014) Configuration Modeling and Experimental Verification with 3D Laser Scanning Technology for a Constrained Elastica Cable. Int J Signal Process. Image Process. Pattern Recognit. 7:363–370. https://doi.org/10.14257/ijsip.2014.7.4.34
36. Yang B, Liu Y, Dong Z, Liang F, Li B, Peng X (2017) 3D local feature BKD to extract road information from mobile laser scanning point clouds. ISPRS J. Photogramm. Remote Sens. 130:329–343. https://doi.org/10.1016/j.isprsjprs.2017.06.007
37. Yang B, Fang L, Li J (2013) Semi-automated extraction and delineation of 3D roads of street scene from mobile laser scanning point clouds. ISPRS J. Photogramm. Remote Sens. 79:80–93. https://doi.org/10.1016/j.isprsjprs.2013.01.016
38. Zai D, Guo Y, Li J, Luo H, Lin Y, Sun Y, Huang P, Wang C (2016) 3D road surface extraction from mobile laser scanning point clouds. In: 2016 IEEE International Geoscience and Remote Sensing Symposium (IGARSS). pp 1595–1598. IEEE
39. Wang J, Lindenbergh R, Menenti M (2017) SigVox – A 3D feature matching algorithm for automatic street object recognition in mobile laser scanning point clouds. ISPRS J. Photogramm. Remote Sens. 128:111–129. https://doi.org/10.1016/j.isprsjprs.2017.03.012
40. Guan H, Li J, Yu Y, Wang C, Chapman M, Yang B (2014) Using mobile laser scanning data for automated extraction of road markings. ISPRS J. Photogramm. Remote Sens. 87:93–107. https://doi.org/10.1016/j.isprsjprs.2013.11.005
41. Kim D-M, Kim H (2013) Digital Single Lens Reflex (DSLR) Camera
42. Rahrig M, Luib A (2017) Sri Dalada Maligawa - 3D-Scanning and Documentation of the Temple of the Sacred Tooth Relic at Kandy, Sri Lanka. ISPRS Ann. Photogramm. Remote Sens Spat Inf Sci 4:229–236. https://doi.org/10.5194/isprs-annals-IV-2-W2-229-2017
43. Hoffmeister D, Zellmann S, Kindermann K, Pastoors A, Lang U, Bubenzer O, Weniger GC, Bareth G (2014) Geoarchaeological site documentation and analysis of 3D data derived by terrestrial laser scanning. ISPRS Ann Photogramm Remote Sens Spat Inf Sci 2:173–179. https://doi.org/10.5194/isprsannals-II-5-173-2014

44. Lee SY, Majid Z, Setan H (2013) 3D data acquisition for indoor assets using terrestrial laser scanning. ISPRS Ann Photogramm Remote Sens Spat Inf Sci 2:221–226. https://doi.org/10.5194/isprsannals-II-2-W1-221-2013
45. Babahajiani P, Fan L, Kamarainen JK, Gabbouj M (2016) Comprehensive automated 3D urban environment modelling using terrestrial laser scanning point cloud. IEEE Comput. Soc. Conf. Comput. Vis. Pattern Recognit. Work. 652–660 (2016). doi:https://doi.org/10.1109/CVPRW.2016.87
46. Fey C, Rutzinger M, Wichmann V, Prager C, Bremer M, Zangerl C (2015) Deriving 3D displacement vectors from multi-temporal airborne laser scanning data for landslide activity analyses. GIScience Remote Sens. 52:437–461. https://doi.org/10.1080/15481603.2015.1045278
47. Vauhkonen J (2015) Reconstruction, quantification, and visualization of forest canopy based on 3d triangulations of airborne laser scanning point data. ISPRS Ann Photogramm. Remote Sens Spat Inf Sci 2:255–261. https://doi.org/10.5194/isprsannals-II-3-W4-255-2015
48. Majasalmi T, Korhonen L, Korpela I, Vauhkonen J (2017) Application of 3D triangulations of airborne laser scanning data to estimate boreal forest leaf area index. Int. J. Appl. Earth Obs. Geoinf. 59:53–62. https://doi.org/10.1016/j.jag.2017.02.022
49. Weise T, Leibe B, Van Gool L (2007) Fast 3D scanning with automatic motion compensation. Proc IEEE Comput Soc Conf Comput Vis Pattern Recognit. https://doi.org/10.1109/CVPR.2007.383291
50. Pang X, Lau RWH, Song Z, Li Y, He S (2016) A Tool-Free Calibration Method for Turntable-Based 3D Scanning Systems. IEEE Comput. Graph. Appl. 36:52–61. https://doi.org/10.1109/MCG.2014.83
51. Albarelli A, Cosmo L, Bergamasco F, Torsello A (2014) High-coverage 3D scanning through online structured light calibration. Proc Int Conf Pattern Recognit 4080–4085. https://doi.org/10.1109/ICPR.2014.699
52. Cui Y, Schuon S, Thrun S, Stricker D, Theobalt C (2013) Algorithms for 3D shape scanning with a depth camera. IEEE Trans. Pattern Anal. Mach. Intell. 35:1039–1050. https://doi.org/10.1109/TPAMI.2012.190
53. Allegra D, Gallo G, Inzerillo L, Lombardo M, Milotta FLM, Santagati C, Stanco F (2016) Low Cost Handheld 3D Scanning for Architectural Elements Acquisition. 10–15. https://doi.org/10.2312/stag.20161372
54. Daneshmand M, Helmi A, Avots E, Noroozi F, Alisinanoglu F, Arslan HS, Gorbova J, Haamer RE, Ozcinar C, Anbarjafari G (2018) 3D Scanning: A Comprehensive Survey. 1–18
55. Dou M, Taylor J, Fuchs H, Fitzgibbon A, Izadi S (2015) 3D scanning deformable objects with a single RGBD sensor. In: 2015 IEEE Conference on Computer Vision and Pattern Recognition (CVPR). pp 493–501. IEEE
56. Bylow E, Sturm J, Kerl C, Kahl F, Cremers D (2016) Real-Time Camera Tracking and 3D Reconstruction Using Signed Distance Functions. https://doi.org/10.15607/rss.2013.ix.035
57. Chen T, Lensch HPA, Fuchs C, Seidel HP (2007) Polarization and phase-shifting for 3D scanning of translucent objects. Proc IEEE Comput Soc Conf Comput Vis Pattern Recognit. https://doi.org/10.1109/CVPR.2007.383209
58. Ma H, Wang D, Shi J, Tian J (2017) A wideband 45 degree polarized electrical scanning antenna array manufactured by 3D printing with metals. 2016 CIE Int Conf Radar, RADAR 2016. 3:4–6 (2017). https://doi.org/10.1109/RADAR.2016.8059418
59. Aubreton O, Bajard A, Verney B, Truchetet F (2013) Infrared system for 3D scanning of metallic surfaces. Mach. Vis. Appl. 24:1513–1524. https://doi.org/10.1007/s00138-013-0487-z
60. Fuciños M, López J, Pardo XM, Fdez-Vidal XR (2013) Fast Implementation of a New Radial Symmetry Measure for Photogrammetry. Presented at the (2013)
61. OpenMP https://www.openmp.org/
62. Drosos V, Fidani S, Manesis C (2013) Use of photogrammetry and GIS in the survey of natural areas of special protection: case study of aesthetic forest Kouri Almyrou Magnisias. Presented at the August 5 2013
63. Jie Wang, Xiaohu Zhang, Hao Chen, Shaowen Ding: Relative pose measurement of Satellite and rocket based on photogrammetry. In: 2017 2nd International Conference on Image, Vision and Computing (ICIVC). pp. 1117–1122. IEEE (2017)

64. Dong, X., Zhang, Y., Liu, J., Hu, G.: A fisheye image barrel distortion correction method of the straight slope constraint. In: 2015 8th International Congress on Image and Signal Processing (CISP). pp. 173–177. IEEE (2015)
65. Lu C-P, Hager GD, Mjolsness E (2000) Fast and globally convergent pose estimation from video images. IEEE Trans. Pattern Anal. Mach. Intell. 22:610–622. https://doi.org/10.1109/34.862199
66. Luhmann T, Fraser C, Maas HG (2016) Sensor modelling and camera calibration for close-range photogrammetry. ISPRS J. Photogramm. Remote Sens. 115:37–46. https://doi.org/10.1016/j.isprsjprs.2015.10.006
67. Fraser CS (2013) Automatic Camera Calibration in Close Range Photogrammetry. Photogramm Eng Remote Sens 79:381–388. https://doi.org/10.14358/PERS.79.4.381
68. López J, Fuciños M, Fdez-Vidal XR, Pardo XM (2013) Detection and matching of lines for close-range photogrammetry. Lect Notes Comput Sci (including Subser. Lect. Notes Artif. Intell. Lect. Notes Bioinformatics). 7887 LNCS, 732–739. https://doi.org/10.1007/978-3-642-38628-2_87
69. Bright BC, Loudermilk EL, Pokswinski SM, Hudak AT, O'Brien JJ (2016) Introducing Close-Range Photogrammetry for Characterizing Forest Understory Plant Diversity and Surface Fuel Structure at Fine Scales. Can. J Remote Sens 42:460–472. https://doi.org/10.1080/07038992.2016.1229598
70. Mayr A, Rutzinger M, Bremer M, Geitner C (2016) Mappping eroded areas on mountain grassland with terrestrial photogrammetry and objext-based image analysis. ISPRS Ann Photogramm Remote Sens Spat Inf Sci 3:137–144. https://doi.org/10.5194/isprs-annals-III-5-137-2016
71. Buffa, F., Pinna, A., Sanna, G (2016) A simulation tool assisting the design of a close range photogrammetry system for the sardinia radio telescope. ISPRS Ann Photogramm Remote Sens Spat Inf Sci 3:113–120. https://doi.org/10.5194/isprs-annals-III-5-113-2016
72. Han B, Endreny TA (2014) River surface water topography mapping at sub-millimeter resolution and precision with close range photogrammetry: Laboratory scale application. IEEE J Sel Top Appl Earth Obs Remote Sens 7:602–608. https://doi.org/10.1109/JSTARS.2014.2298452
73. Singh SP, Jain K, Ravibabu Mandla V (2014) A newapproach towards image based virtual 3D city modeling by using close range photogrammetry. ISPRS Ann Photogramm Remote Sens Spat Inf Sci 2:329–337. https://doi.org/10.5194/isprsannals-II-5-329-2014
74. Rottensteiner F, Sohn G, Gerke M, Wegner JD, Breitkopf U, Jung J (2014) Results of the ISPRS benchmark on urban object detection and 3D building reconstruction. ISPRS J Photogramm. Remote Sens. 93:256–271. https://doi.org/10.1016/j.isprsjprs.2013.10.004
75. Nex F, Gerke M, Remondino F, Przybilla HJ, Bäumker M, Zurhorst A (2015) Isprs benchmark for multi-platform photogrammetry. ISPRS Ann Photogramm Remote Sens Spat Inf Sci 2:135–142. https://doi.org/10.5194/isprsannals-II-3-W4-135-2015
76. Blomley R, Weinmann M (2017) Using Multi-scale features for the 3D semantic labeling of airborne laser scanning data. ISPRS Ann Photogramm Remote Sens Spat Inf Sci 4:43–50 (2017). https://doi.org/10.5194/isprs-annals-IV-2-W4-43-2017
77. Sun Y, Zhao L, Huang S, Yan L, Dissanayake G (2014) L2-SIFT: SIFT feature extraction and matching for large images in large-scale aerial photogrammetry. ISPRS J. Photogramm. Remote Sens. 91:1–16. https://doi.org/10.1016/j.isprsjprs.2014.02.001
78. Herlihy M, Luchangco V, Moir M, Scherer WN (2003) Software transactional memory for dynamic-sized data structures. In: Proceedings of the twenty-second annual symposium on Principles of distributed computing - PODC '03. pp 92–101. ACM Press, New York, New York, USA
79. Cucci DA (2016) Accurate optical target pose determination for applications in aerial photogrammetry. ISPRS Ann Photogramm Remote Sens Spat Inf Sci 3:257–262. https://doi.org/10.5194/isprs-annals-III-3-257-2016
80. Lucet G (2013) 3D survey of pre-hispanic wall painting with high resolution photogrammetry. ISPRS Ann Photogramm Remote Sens Spat Inf Sci 2:191–196 (2013). https://doi.org/10.5194/isprsannals-II-5-W1-191-2013

81. Murtiyoso A, Koehl M, Grussenmeyer P, Freville T (2017) Acquistion and processing protocols for UAV images: 3D Modelling of historical buildings using photogrammetry. ISPRS Ann Photogramm Remote Sens Spat Inf Sci 4:163–170. https://doi.org/10.5194/isprs-annals-IV-2-W2-163-2017
82. Casella V, Franzini M (2016) Modelling steep surfaces by various configurations nadir and oblique photogrammetry. ISPRS Ann Photogramm Remote Sens Spat Inf Sci 3:175–182. https://doi.org/10.5194/isprs-annals-III-1-175-2016
83. Ley A, Hänsch R, Hellwich O (2017) Automatic building abstraction from aerial photogrammetry. ISPRS Ann Photogramm Remote Sens Spat Inf Sci 4:243–250. https://doi.org/10.5194/isprs-annals-IV-2-W4-243-2017
84. Carvajal-Ramírez F, Agüera-Vega F, Martínez-Carricondo PJ (2016) Effects of image orientation and ground control points distribution on unmanned aerial vehicle photogrammetry projects on a road cut slope. J Appl Remote Sens 10:034004. https://doi.org/10.1117/1.JRS.10.034004
85. Barlow J, Gilham J, Ibarra Cofrã I (2017) Kinematic analysis of sea cliff stability using UAV photogrammetry. Int J Remote Sens 38:2464–2479. https://doi.org/10.1080/01431161.2016.1275061
86. Gonçalves JA, Henriques R (2015) UAV photogrammetry for topographic monitoring of coastal areas. ISPRS J Photogramm Remote Sens 104:101–111. https://doi.org/10.1016/j.isprsjprs.2015.02.009
87. Scarelli FM, Sistilli F, Fabbri S, Cantelli L, Barboza EG, Gabbianelli G (2017) Seasonal dune and beach monitoring using photogrammetry from UAV surveys to apply in the ICZM on the Ravenna coast (Emilia-Romagna, Italy). Remote Sens. Appl. Soc. Environ. 7:27–39. https://doi.org/10.1016/j.rsase.2017.06.003
88. Amrullah C, Suwardhi D, Meilano I (2016) Product accuracy effect of oblique and vertical non-metric digital camera utilization in UAV-Photogrammetry to determine fault plane. ISPRS Ann Photogramm Remote Sens Spat Inf Sci 3:41–48 (2016). https://doi.org/10.5194/isprs-annals-III-6-41-2016
89. Zhang J, Wang X (2013) Digital photogrammetry of Chinese early aerial photo and application in morphotectonics mapping of Tanlu active fault zone. Int Geosci Remote Sens Symp 2924–2926 (2013). https://doi.org/10.1109/IGARSS.2013.6723437
90. Duan Y, Yan L, Zhong Y, Yao J (2014) A new method of improving height accuracy of airborne photogrammetry using a multi-camera system. Int. Geosci. Remote Sens. Symp. 1:2019–2022. https://doi.org/10.1109/IGARSS.2014.6946859
91. Sánchez-García E, Balaguer-Beser A, Pardo-Pascual JE (2017) C-Pro: A coastal projector monitoring system using terrestrial photogrammetry with a geometric horizon constraint. ISPRS J Photogramm Remote Sens 128:255–273. https://doi.org/10.1016/j.isprsjprs.2017.03.023
92. Roncella R, Forlani G, Fornari M, Diotri F (2014) Landslide monitoring by fixed-base terrestrial stereo-photogrammetry. ISPRS Ann Photogramm Remote Sens Spat Inf Sci 2:297–304. https://doi.org/10.5194/isprsannals-II-5-297-2014

Damping Behaviour of Bias Flow Perforated Acoustic Liners: A Parametric Study

N. K. Jha, Ashutosh Tripathi, and R. N. Hota

Abstract Perforated bias flow liners are widely applied to mitigate combustion instabilities in afterburner of a jet engine. Combustion instabilities are the product of pressure pulsations caused due to thermoacoustic feedback between the heat release and acoustic waves inside a combustor, which may result in excessive wearing or even cracking of exposed components within the combustor. There is a grazing flow, which grazes the perforations while another is cooling or bias flow, which passes through the perforations of the liner. Damping of sound is a result of the interaction between sound wave and the joint grazing-bias flow. There are a number of parameters that affect the acoustic damping response of these liners. The variable parameters include porosity, diameter, bias flow, grazing flow and thickness. This study is concerned with the analytical predictions for the variable parameters. The analytical model used to predict the behaviour of the perforated liner is first validated with the experimental measurements. The experimental measurement used standard two-load method for the acoustic characterization of liners. The measurements and predictions are conducted in the environments with and without mean flow. Results of the parametric study provide a basis to design such liners and also provide insights into the effects of parameters on the absorption.

Keywords Bias flow · Grazing flow · Liner · Absorption coefficient

1 Introduction

Acoustic liners have wide applications in interrupting the instability causing feedback loop between sound waves and the heat release oscillations. In an afterburning turbofan engine, grazing (tangential) flow and bias flow (cooling flow) through the liner interact with the acoustic waves, which leads to the damping of the sound wave. Sound absorption by sound–flow interaction was first analytically and experimentally demonstrated by Bechert [1]. Howe [2] presented an analytical impedance

N. K. Jha (✉) · A. Tripathi · R. N. Hota
Indian Institute of Technology (Indian School of Mines), Dhanbad, Jharkhand 826004, India
e-mail: nandanjha922@gmail.com

L. M. Das et al. (eds.), *Emerging Trends in Mechanical Engineering*, Lecture Notes in Mechanical Engineering, https://doi.org/10.1007/978-981-15-8304-9_6

model and supported the mechanism of sound absorption by establishing the transfer of acoustic energy into vorticity before being dissipated into heat. All of the incident sound energy was shown to get absorbed at a particular frequency by Hughes and Dowling [3]. The liners offer impedance to the acoustic waves, whose model was given by Howe [2], Bauer [4] and Betts et al. [5]. Bauer [4] presented empirical impedance model accounting both the grazing flow and bias flow. Eldredge and Dowling [6] derived conservation equations with respect to the control volumes considered for cavity and the liner section.

They were able to predict the acoustic damping behaviour of liners through the solution of governing equations for combined grazing–bias flow case. Lawn [7] conducted an extensive survey of all the existing approaches and correlated them. Lahiri and Bake [8] reviewed all the relevant literature on bias flow liners and thus explored the abilities of different models that points out the shortcomings associated with them. The present study conducts a parametric study to conclude the effect of various parameters on the absorption in a range of frequency. In Sect. 2, the analytical model of a lined duct is presented. The experimental technique is mentioned in Sect. 3. Finally, Sect. 4 presents the results of parametric analytical predictions.

2 Analytical Model

The present analytical model considers a lined cavity section in the middle of an impedance tube, attached with the upstream and downstream ducts as shown in Fig. 2. In the lined cavity section, two separate control volumes are considered and governing conservation equations are obtained with respect to them. The analytical model is the same as presented by Eldredge and Dowling [6] only with the difference in impedance model chosen to get the absorption coefficient. They used Howe impedance model [2] in their absorption estimation, which includes only the effect of bias flow. The realistic configuration of bias flow liners in an afterburning turbofan engine includes both bias flow and grazing flow (Fig. 1), the terms of which are included in the Bauer impedance model and chosen in the present study after validation with the experimental results. The governing equations are first converted into an initial value problem using a simplex search method and then solved using MATLAB function ode45. The applied boundary conditions can be found in Eldredge and Dowling [6].

Absorption coefficient (α) [6] is given by,

$$a = 1\frac{\left|B_u^-\right|^2 + \left|B_d^+\right|^2}{\left|B_u^+\right|^2 + \left|B_d^-\right|^2} \tag{1}$$

Where B is the fluctuating stagnation enthalpy. ± stands for forward and backward travelling waves, u and d stands for forward and backward travelling wave directions, respectively.

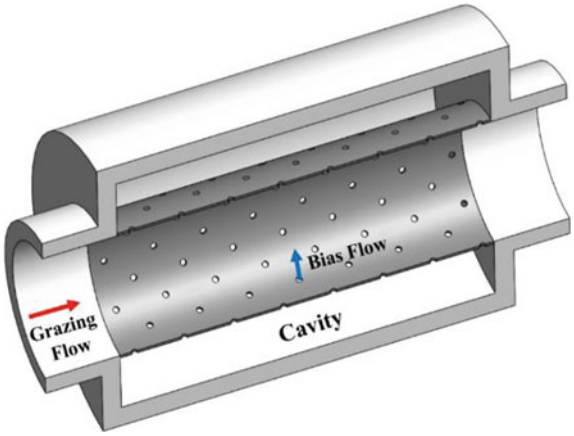

Fig. 1 Schematic of acoustic liner backed by a cavity with grazing and bias flow

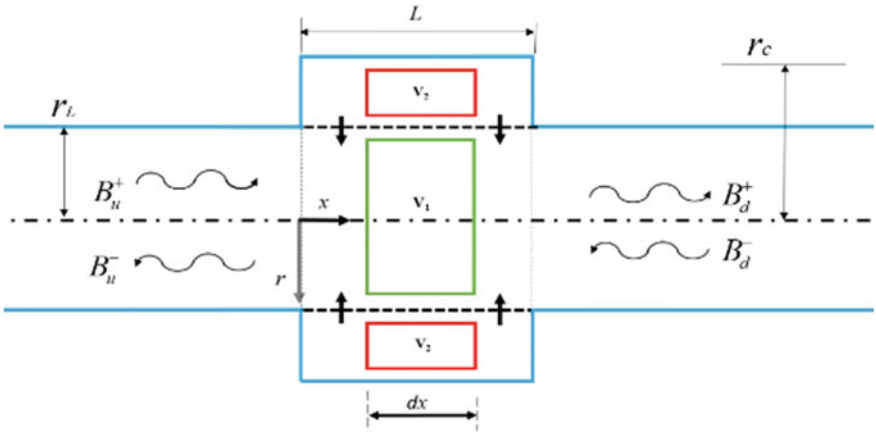

Fig. 2 Schematic of control volumes in the impedance tube [6]

3 Experimental Measurements

Figure 3 shows the schematic of a bias flow liner backed by a cavity, in between the upstream and downstream part of the impedance tube, with microphones mounted on either side of the lined section. The grazing flow and bias flow are imposed through the upstream tube and the cavity, respectively. The calculation of the absorption coefficient is done by processing microphone measured data using the standard ASTM Two Load Method.

The absorption coefficient (α) [9] can be written as

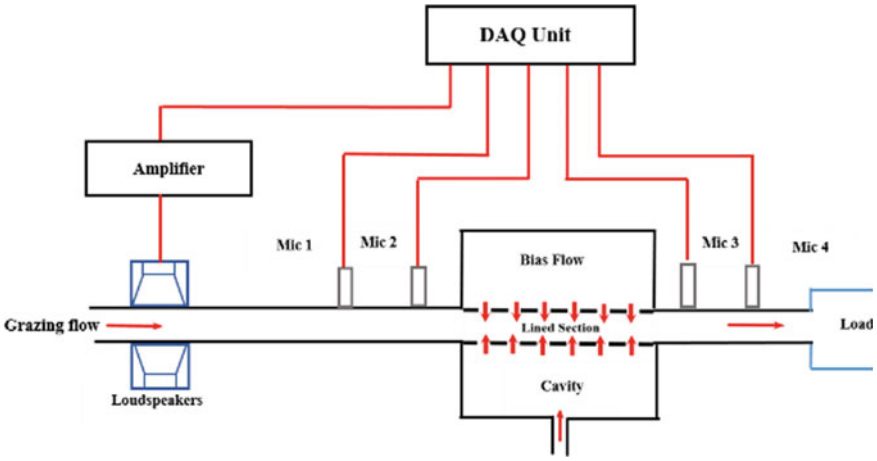

Fig. 3 Schematic of the experimental set-up

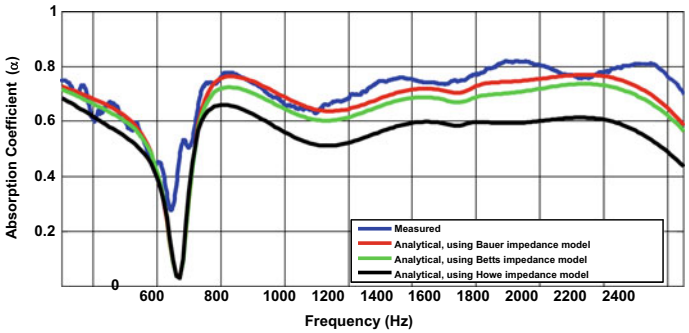

Fig. 4 Absorption coefficient of liner of porosity (σ)= 2.4%, orifice diameter (d) = 3.2 mm, thickness(t) = 1.6 mm at grazing and bias flow Mach number $M_G = 0.05$ and $M_B = 0.1$, respectively

$$a = 1 - \frac{|R_n(1 - M_u)|^2 + |T_n(1 + M_d)|^2}{|(1 + M_u)|^2 + |T_n R_d(1 - M_d)|^2} \tag{2}$$

where M_u and M_d are upstream (grazing) and downstream flow Mach numbers, R_n. and $T_n$are the normal incidence transmission and reflection coefficient, and R_d is the downstream reflection coefficient.

4 Results and Discussions

4.1 Validation

The calculation of absorption coefficient requires impedance of orifices. Three such available impedance models of Howe [2], Bauer [4] and Betts et al. [5] are used to get the analytically predicted absorption coefficient. Bauer impedance model is used in the present study as it shows the closest agreement of analytical prediction with the measured results using this model, as shown in Fig. 4.

4.2 Bias Flow

Figure 5 presents the results of absorption coefficient plotted over frequency for varying bias flow in the absence of grazing flow. Without bias flow, there is a distinct maximum around 1600 Hz, which corresponds to the Helmholtz resonance frequency. The introduction of bias flow shifts the absorption maximum to a higher frequency. The most striking feature of this figure is that it reveals the contribution of bias flow regarding the broadband absorption of sound in the entire frequency range of investigation except in the range of frequency containing the trough. The bias flow helps to achieve maximum and broadband absorption. There is an optimum bias flow corresponding to the maximum absorption. A deviation in the optimum bias flow results in the lowering of absorption curve. The present analytical findings are in compliance with those reported by Lahiri [8] and Eldredge and Dowling [6]. In the case of without grazing flow, the addition of bias flow results in a broadband shoot up in the amount of absorption in the higher frequency range for bias flow

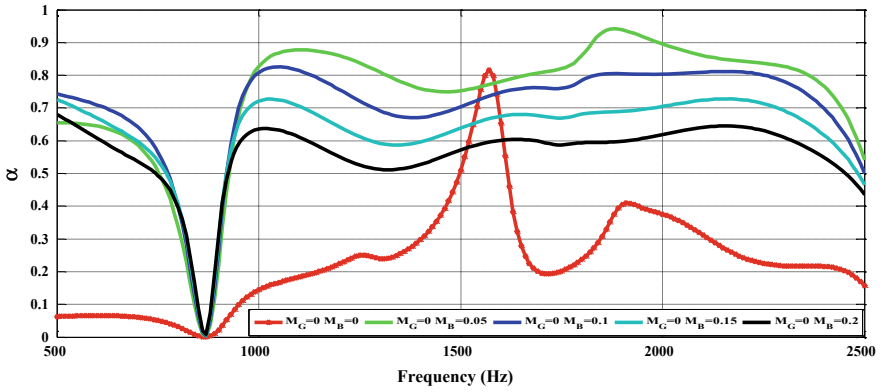

Fig. 5 Predicted absorption coefficient of liner of $\sigma = 2.4\%$, $d = 3.2$ mm, $t = 1.6$ mm for $M_G = 0$ at different bias flow

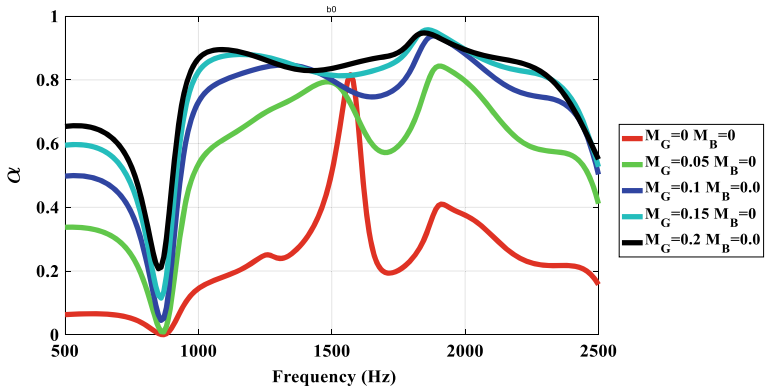

Fig. 6 Predicted absorption coefficient of liner of $\sigma = 2.4\%$, $d = 3.2$ mm, $t = 1.6$ mm for $M_B = 0$ at different grazing flow

Mach number 0.05. A further increase in the bias flow causes absorption to decrease linearly. The effect is same in the lower frequency range with the difference in the amount of absorption.

4.3 Grazing Flow

In the absence of bias flow, the addition and further increase in grazing flow results in a broadband absorption as shown in Fig. 6. The grazing flow lifts the absorption curve in the entire range of frequency with the amount being higher in the lower frequency range.

4.4 Combined Bias-Grazing Flow

Figure 7 shows the absorption coefficient curves in order to observe the effect of varying bias flow in the presence of a fixed grazing flow. At zero bias flow velocity, there are only two absorption maxima and with the increase in bias flow, absorption achieves its higher value as well as the broadband nature. However, the absorption starts decreasing from bias flow Mach number 0.1.

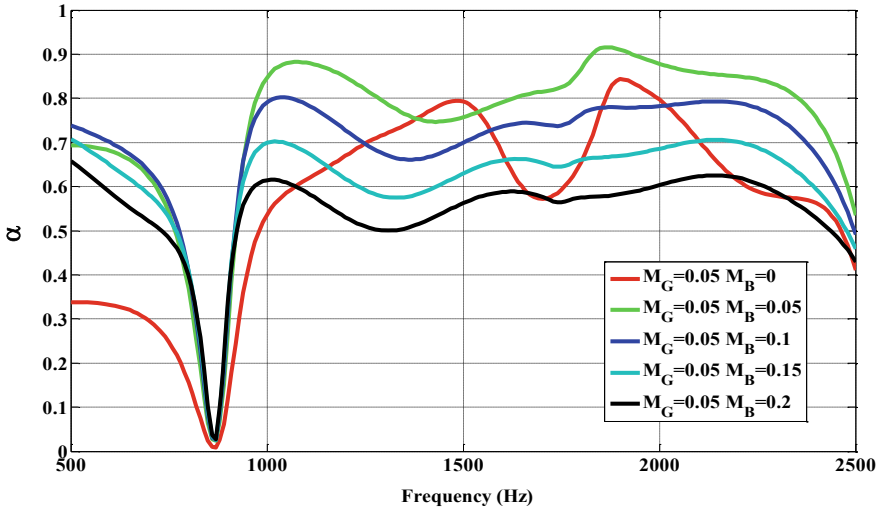

Fig. 7 Predicted absorption coefficient of liner of $\sigma = 2.4\%$, $d = 3.2$ mm, $t = 1.6$ mm for $M_G = 0.05$ at different bias flow

4.5 Thickness

For thickness from 0.5 mm to 2 mm, there is not much variation in the amount of absorption as shown in Fig. 8. After this range of thickness, the increase in thickness results in the decrease in the absorption after 1000 Hz. This increase in thickness has no effects on absorption in the lower frequency range below around 1000 Hz. There can be same porosity corresponding to different orifice diameter and vice-versa.

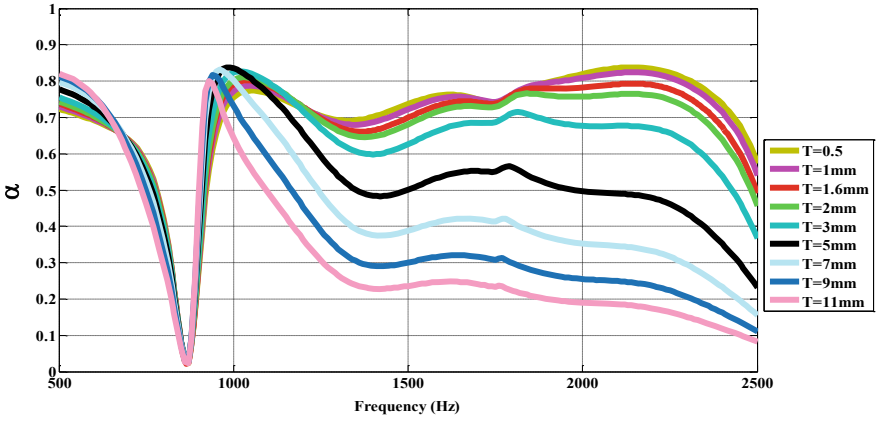

Fig. 8 Predicted absorption coefficient of liner of $\sigma = 2.4\%$, $d = 3.2$ mm, $M_G = 0.05$, and $M_B = 0.1$ at different liner thickness

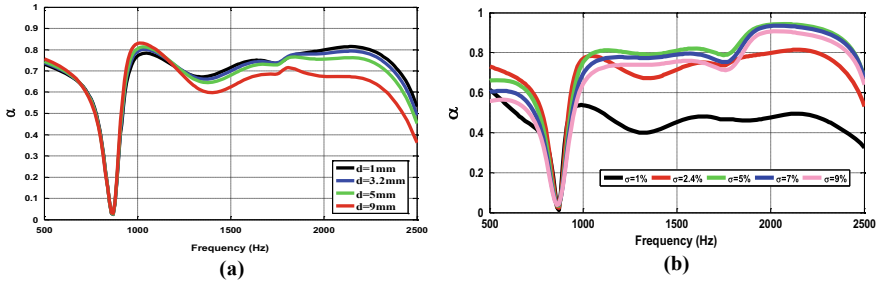

Fig. 9 Predicted absorption coefficient of liner configuration at $M_B = 0.1$ and $M_G = 0.05$ **a** porosity = 2.4%, varying hole diameter **b** diameter = 3.2 mm, varying porosity

4.6 Porosity

For a fixed value of porosity, absorption curves are obtained for different orifice diameters as shown in Fig. 9a. With the increase in diameter, there is decrease in absorption in the higher frequency range. In the lower frequency range, the curves are almost in match with each other for all the thickness values considered. Now, Fig. 9b is plotted considering different porosities keeping orifice diameter fixed at 3.2 mm. For the porosity value of 1%, the absorption is much low and with its increase, the absorption curves are observed to get shifted to higher magnitude appreciably. However, it starts decreasing after attaining the maximum absorption.

4.7 Equal Absorption Curves

For the condition corresponding to $M_B M_{G>}$ 0.3, the grazing flow effect can be neglected. This limit also refers to the condition $M_G = 3.5\,MB$. Following this limiting condition, different sets of grazing–bias flow combination are considered and the results are presented in Fig. 10. Authors in the past stated that the similarity is due to the grazing flow velocities, which induce fluctuations of boundary layer, further leading to airflows through the liner. The frequencies associated with these fluctuations are believed to be low enough so that the resulting through flows affect the acoustic characteristics of the liner in a way similar to steady through flows'.

5 Conclusions

This paper presents an analytical parametric study of a cavity-backed bias flow liner regarding its geometric and flow parameters. The analytical model is first validated with the experimental results before using it for predictions. The significant features

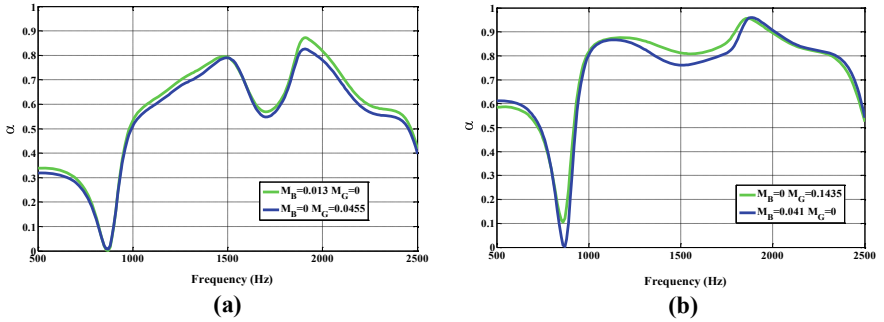

Fig. 10 Predicted equal absorption coefficient curves of liner of $\sigma = 2.4\%$, $d = 3.2$ mm, $t = 1.6$ mm at (a) $M_B = 0.013$, $M_G = 0.0455$, (b) $M_B = 0.041$, $M_B = 0.1435$

of each parameter are discussed. The parametric study reveals that corresponding to each parameter, there is a certain limit beyond which absorption of liner starts decreasing. The bias flow shifts the absorption maximum to a higher frequency with broadband absorption over the entire frequency range. When there is no bias flow, the increase in grazing flow results in broadband absorption and also it lifts the absorption curve with an appreciable amount especially in the lower frequency range. After a certain thickness value, the absorption decreases in the higher frequency range. The equal absorption curve shows an equal amount of absorption in the presence of either grazing or bias flow, following the limiting condition. The increase in porosity results in first increase and then decrease in the absorption.

References

1. Bechert DW (1980) Sound absorption caused by vorticity shedding, demonstrated with a jet flow. J Sound Vib 70(3):389–405
2. Howe MS (1979) On the theory of unsteady high Reynolds number flow through a circular aperture. Proc R Soc Lond A Math Phys Sci 366:205–223
3. Hughes IJ, Dowling AP (1990) The absorption of sound by perforated linings. J Fluid Mech 218:299–335
4. Bauer AB (1977) Impedance theory and measurements on porous acoustic liners. J Aircr 14(8):720–728
5. Betts J, Follet J, Kelly J, Thomas R (2000) Evaluation of an impedance model for perforates including the effect of bias flow
6. Eldredge JD, Dowling AP (2003) The absorption of axial acoustic waves by a perforated liner with bias flow. J Fluid Mech 485:307–335
7. Lawn C (2016) The acoustic impedance of perforated plates under various flow conditions relating to combustion chamber liners. Appl Acoust 106:144–154
8. Lahiri C, Bake F (2017) A review of bias flow liners for acoustic damping in gas turbine combustors. J Sound Vib 400:564–605
9. Jha NK, Das D, Tripathi A, Hota RN (2019) Acoustic damping: analytical prediction with experimental validation of mixed porosity liners and analytical investigation of conical liners. Appl. Acoust. 150:179–189

Design and Fabrication of a Socket Jockey and Its Use in Home Automation

Rajat Jain, Vishal Garg, Abhaas Nayyar, Deepinder Sethi, Abhinav Ray, Vishal Gupta, and Sachin Singh

Abstract In today's fast-paced generation, the need of the hour is to develop a technology that can make day-to-day mundane activities obsolete and replace them with a much more convenient and versatile solution. One of such mundane activities is the operation of household switchboards. This project provides the luxury of comfort while "jockeying the sockets of one's household." The world is facing the problem of overcharging, wherein a lot of phone companies are investing billions to solve it by modernizing phones/chargers, while our solution is to modernize the sockets instead. In the current work, basic networking and communication have been used. Base framework for developing technology that can solve many of our day-to-day problems is developed. One of the primary aims of the current work is to eliminate the physical requirement of the user at the time of switching on or off devices plugged on to switchboards. This will not only be a luxury for the buyers but also to the world as it cuts on electronic waste and saves electricity. Finally, a product is designed and developed to be used remotely to switch on or off (timer enabled) the power supply of devices at the convenience of the user.

Keywords Internet of things · Rectifier circuit · Wireless sensor networks · Short message service · Arduino Uno

1 Introduction

Home automation involves automating the household environment. This has been made possible because of the vast usage of smartphones and the Internet in the current time. In this work, we have developed a device called "socket jockey." It is an Internet of things (IoT) device which works as an intermediary between the user and the electronic product needed to be controlled remotely. As shown in Fig. 1, the "socket jockey" plugs on to any conventional switchboard, like a multiplug, and any device can be plugged into this jockey, very much like a multiplug. The user can

R. Jain · V. Garg · A. Nayyar · D. Sethi · A. Ray · V. Gupta (✉) · S. Singh
Mechanical Engineering Department, Thapar Institute of Engineering and Technology, Patiala 147004, India
e-mail: vishal.gupta@thapar.edu

L. M. Das et al. (eds.), *Emerging Trends in Mechanical Engineering*, Lecture Notes in Mechanical Engineering, https://doi.org/10.1007/978-981-15-8304-9_7

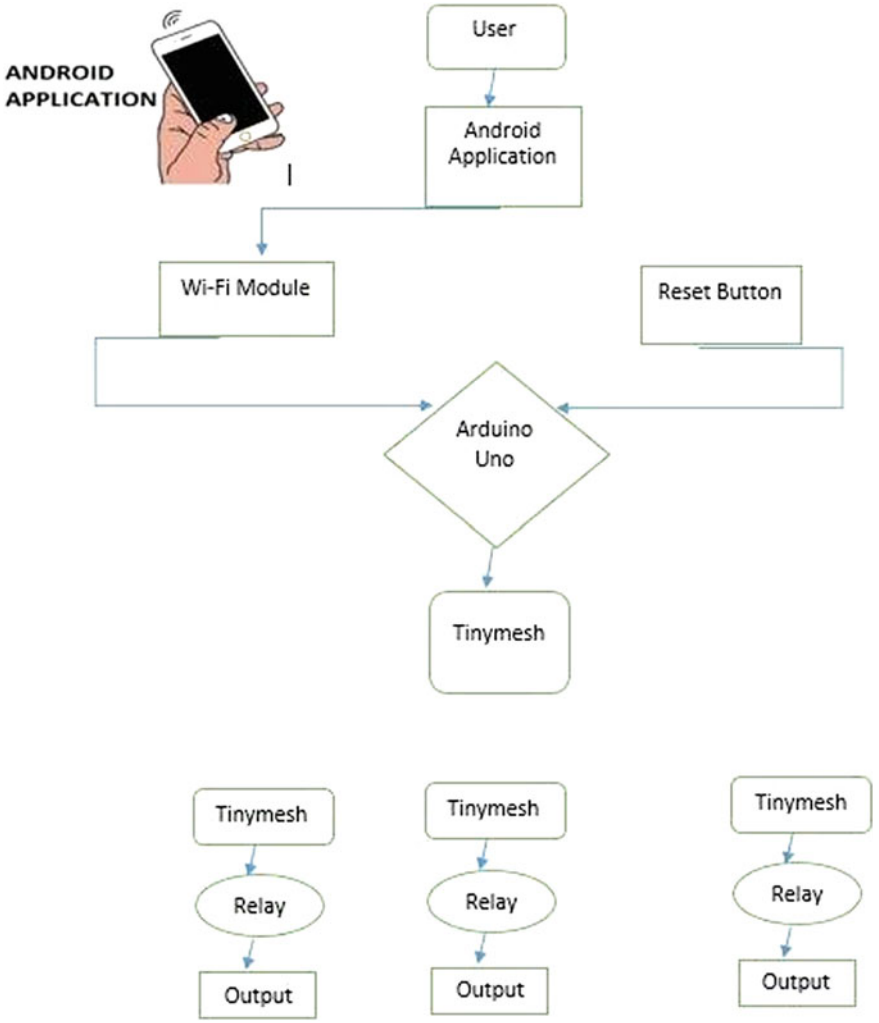

Fig. 1 Flowchart explaining the functioning of the project

then use an app provided in their phone to control the switching (on or off) of their electronic device and set a timer to do so according to their needs. Once the user has set the timer, he/she can rest assured and need not worry about being physically present to switch off their device.

IoT is changing the landscape of our households by offering more fidelity and interconnectivity with our everyday electrical and/or electronics items, thus solving day-to-day problems. IoT device solves the physical requirement of the user to switch

on or off devices at specific times throughout the day some of the common examples include:

- In certain areas of cities like Delhi, water availability is limited to a few, often odd, hours of the day. The electric motor that draws water needs to be switched on/off accordingly.
- Overcharging your electronic devices can damage their battery life. They need to be switched off at an appropriate time.
- Refrigerators need to be switched off for a few hours to facilitate defrosting. Once the refrigerator has defrosted, the power supply needs to be restored as food may get spoilt if kept unrefrigerated for long hours.
- Electric geysers and heaters need to be switched off after use.

The physical requirement of the user for switching makes the task cumbersome, wastes energy, and may also decrease the life of the appliance. No physical requirement of the user is the need analysis. A versatile switching system needs to be in a place that can not only be controlled remotely but also at one's own convenience.

The device proposed in the current work provides a simple yet innovative solution to above-described problems. The developed device acts as an independent and semi-autonomous intermediary that can timely switch on or off devices plugged into an electrical socket according to the needs of the user. Multiple devices can be in use at the same time at separate switchboard locations all controlled by an Android app in the user's phone. Any number of persons in the house can control the device provided that they have the app installed on their phones. Advantages of this device include its flexibility, i.e., it can be used to operate any electronic component. Secondly, it is a cost-effective alternative to the commercially available variants. An outcome of the work user will be able to manage their devices that are plugged on to their switchboards remotely.

The novelty of the work is that this device will employ the TinyMesh module by radiocrafts. It is a compact, surface-mounted, high-performance modules for wireless mesh networking that will allow us more flexibility and the power of extension of the workable environment as much as we need. The low cost, maintenance, and usability are a promise that no other device has been able to fulfill in the market.

2 Literature Review

There are many systems or many approaches available that can easily control home appliances with the help of a mobile application or using a Web server. In recent years, a new approach named IoT is used, for completing our tasks by the use of Internet wirelessly. Each system available in the market has its unique features, having its pros and cons, respectively. At present, there are many companies available that are officially registered and many research scholars are working hard to provide better home automation features. As home automation being a wide field and having a wide scope available to proceed with, following are the models and research papers

available that describe the work performed by the others. Storme systems have developed an automatic power-cutoff socket for universal type D sockets. When charging your smartphone, once when the battery has attained 100%, and the device is still plugged to its charger, some "trip-current" flows periodically to the device in order to maintain a 100% charge.

The Storme socket has been designed primarily to provide a safety system for such scenarios. Built-in surge protection circuits prevent damage against over voltages and/or spikes. Piyare and Tazil [1] explained the model of home automation system using a smartphone, Arduino board, and Bluetooth technology, and it is observed as a secured and low-cost system. The design is based on a stand-alone Arduino Bluetooth board, and the home automation is achieved when the devices are connected to the input/output ports of this microcontroller via relays. The communication between the cell phone and the Arduino BT board is achieved wirelessly. This system is designed to be of low cost, and its scalability allows a variety of devices to be controlled with minimum changes to its core platform. Password protection is also being used to only allow authorized users knowing the password from accessing the devices at home.

Asadullah and Raza [2] explained the home automation system model by explaining the various approaches for doing with various communication techniques such as Bluetooth, GSM, ZigBee, and Wi-Fi. In the research made, some of the common features are device controls, thermostat control, remote control lighting, live video surveillance, monitoring security cameras, etc. Kunal and Tushar [3] explained the working used IoT in their work. Authors described the approach of controlling home appliances by using a Web server. In this, a sensor senses the status of appliances and updates to the Web server by sending a signal. If the user is far away from home, he also can access and change the status of appliances, i.e., switches it on/off. This thing happens through the use of a global server so that our network is connected globally.

ZigBee protocol IEEE 802.15.4 wireless standard can be used to set up a network for some specific application purpose. ZigBee-based home automation wireless sensor network can be implemented with small initial cost and can be useful to control fans, lights, and other home appliances in which operation can be controlled with the help of a microcontroller. Kate and Rana [4] have presented a paper on the development of a Web-based controller for control electrical device. The prototype is developed using Microsoft Visual Studio. NET and Circuit design. The methodology used in this project consists of three main phases which are analysis, design, and implementation.

Ramli et al. [5] implemented home automation based on IoT using Node MCU, to not only for convenience purpose but also for energy conservation. The controlling tasks were done through Arduino, which enables the communication and upon receiving some commands, the system controls the different systems in the house. Finally, the commands to control the appliances in the house are sent by a central control unit such as a computer and remote controller smartphone. Tan et al. [6] studied on Internet-based monitoring of a DCS. This paper describes the hardware and software design considerations which allow the users to access the sensors and possibly activate actuators linked on the DCS, remotely and effectively, using a

commonly available Web browser. The author had done the work by server–client application using LabVIEW networking VI protocol. Developed models had a very small range or were economically infeasible to most of the people. Mainetti et al. [7] discussed the various types of WSNs and their implementation in the future world of home automation. The paper also discussed the use of WSNs in environmental monitoring, agriculture, multimedia, health care, and smart home applications.

Dey et al. [8] discussed home automation with the help of a smartphone and a computer. The devices are connected through a cloud server and are controlled by a single administrator. Various electrical and mechanical systems of the buildings are connected using IoT. Das et al. [9] discussed controlling of the household appliances using the cellphone by global system for mobile communication (GSM) technology in which controller sends the commands from a distance via short message service (SMS). Sriskanthan et al. [10] in their work discussed the application of Bluetooth technology and its application in home automation. It proposes a network, which contains a remote, mobile host controller and several client modules i.e. home appliances. The home appliances communicate with the host controller through Bluetooth devices.

Mandula et al. [11] in his paper described the two prototype models, namely home automation using Bluetooth and home automation using Ethernet. Whenever mobile app was used and launched, Arduino board got paired to a smartphone using Bluetooth connectivity using the serial communication protocol. This Bluetooth-based solution cannot be used from a distant location, as it uses short-range wireless communication technology which can work up to l0–20 m only, therefore Ethernet-based technology eas used.

Vikram et al. [12] illustrated a methodology to provide a low-cost home automation system using Wi-Fi which crystallizes the concept of Internetworking of smart devices. A Wi-Fi-based wireless sensor network (WSN) was designed for monitoring and controlling environmental, safety and electrical parameters of smart homes. Through the use of an application on a smartphone, the user can exercise seamless control over the devices in a smart home.

Vishwakarma et al. [13] proposed a smart energy-efficient home automation system that can access and control the home equipment from every corner of the world. Internet connectivity module is attached to the main supply unit of this home. For wireless connectivity, a static IP address is used.

This system is based on multimodal application that can be operated using voice recognition command of the user using the Google Assistant or through a Web-based application. Thus, main objective of this work is to make our home automation system more secure and intelligent.

Each of the aforesaid systems and models has its own unique features and on comparison with one another system, each lacks some advancement. Therefore, in the current work, a system that is economic as well as fulfills requirement of high ranges is proposed. The developed model reduces the cost by 85% in comparison to the already existing products. Our designed model works on the principles of the Internet of things, Android application and uses Google STT module for speech to text conversions. A local server was made to connect our system on a network. The

use of hardware modules like Node MCU, relay module, and Android application helps in reducing the cost of the model and also increases its efficiency.

3 Materials and Methods

Model is developed based on certain technical standards such as:

- **IEEE 802.11** is the collection of standards set up for wireless networking. Probably familiar with the three popular standards: 802.11a, 802.11b, 802.11 g and latest one is 802.11n. Each standard uses a frequency to connect to the network and has a defined upper limit for data transfer speeds.
- **IEEE C37.90–2005**—is the standard specified standard service conditions, standard ratings, performance requirements, and testing requirements for relays and relay systems that are used to protect and control power apparatus. The purpose of this standard is to establish a common reproducible basis for designing and evaluating relays.
- **ISO/IEC 15,067–3:2012** is a standard defined for information technology that is implemented on home electronic system application model.

3.1 Methodology

Present work requires considerable development of hardware that constitutes major part of the work. Management and execution of this work have several steps:

- Designing of the circuit
- Simulation in a software
- Test circuit fabrication
- Final fabrication of the circuit
- Encasing and outer body design
- Coding for the smartphone application
- Debugging.

3.2 Components Used

After thorough research, exploration, discussions, and analysis, three major components identified that are needed to be developed for proposed model are:

3.2.1 A Plugging Component: A Peripheral that Can Plug into the Switvhboard Safely

(a) It should receive and transmit data to an intermediate device using wireless communication regarding the status of the device.
(b) It should not exceed in size such that it covers or restricts access to the switches.
(c) It should provide 220 V of electricity to the user's device to be attached.
(d) It should function without a power source of its own.
(e) The power it receives must be stepped down to the specifications of the ICs and microcontrollers being used. (3.3 or 5 V).
(f) It should be compact and easy to use.

The peripheral circuit used is shown in Fig. 2.

Components used in plugin circuit:

(a) **Transformer**: The transformer converts 220 V AC supply to 5 V AC. This is, as discussed earlier, in accordance with the voltage specifications of the TinyMesh module.
(b) **Diodes (rectifier circuit)**: A full-wave bridge rectifier is necessary to convert the alternating current to fluctuating DC. The rectifier circuit is explained below briefly.
During the positive half-cycle of the AC, the electron flow will occur as shown Fig. 3. The blurred-out diodes in the diagram are effectively an open circuit.

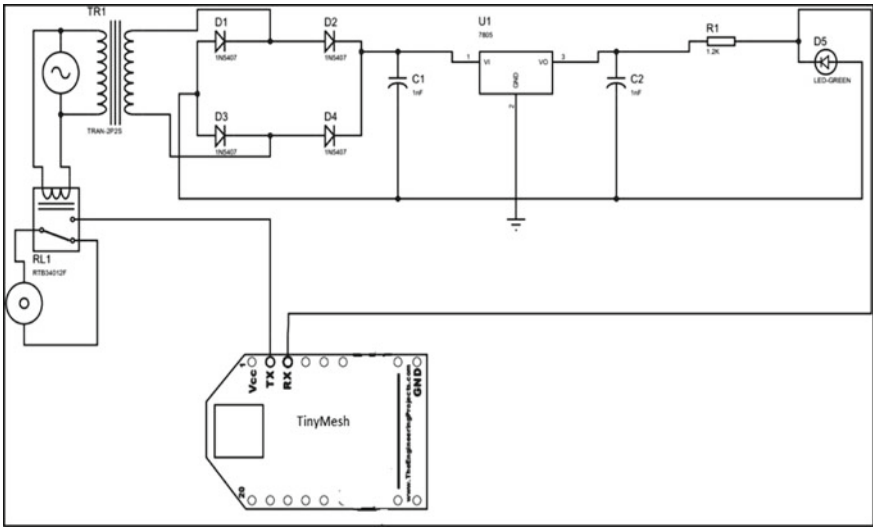

Fig. 2 Plugin circuit

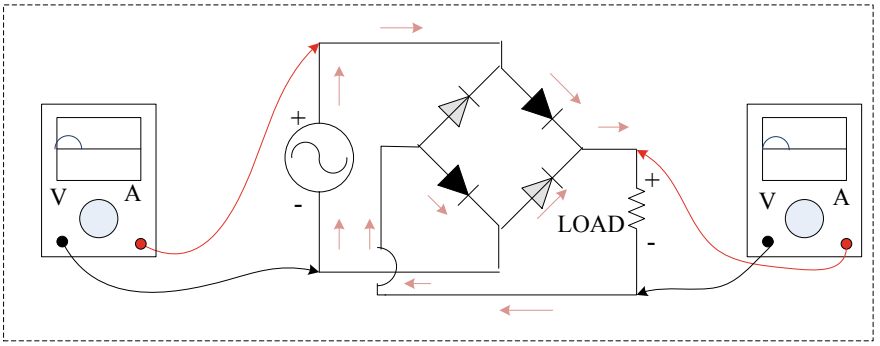

Fig. 3 Electron flow in the positive half-cycle

During the negative half-cycle, the electron flow is as shown in Fig. 4. The time-dependent output of the complete circuit will have the nature of fluctuating dc as shown in Fig. 5.

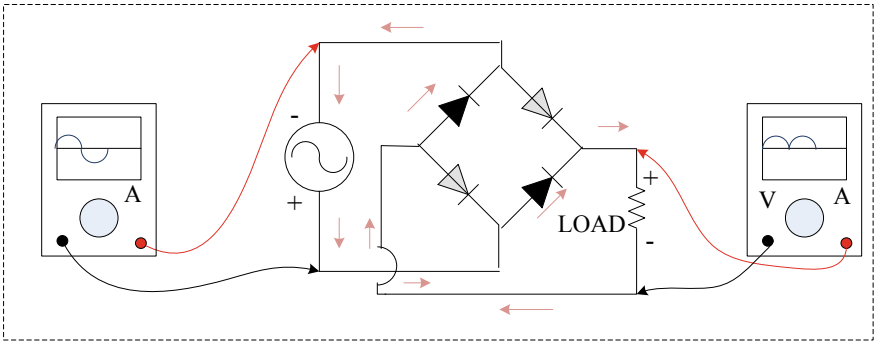

Fig. 4 Electron flow in negative half-cycle

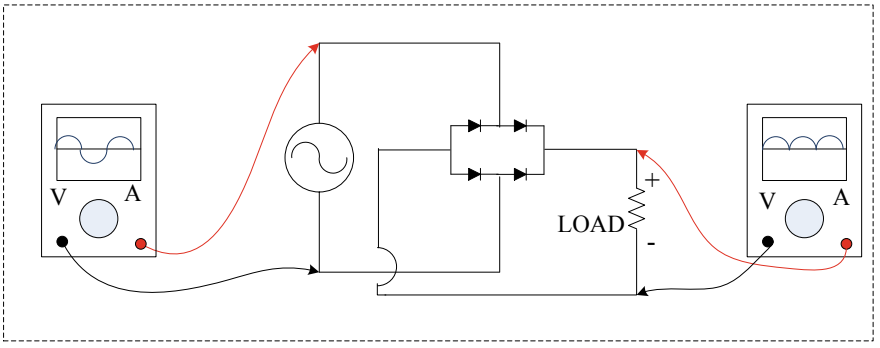

Fig. 5 Output of full-bridge rectifier

(c) **Filter circuit**: The purpose of the capacitor filter circuit is to "straighten" the fluctuating DC that it is receiving from the rectifier circuit. During the positive half-cycle of the input AC voltage, the capacitor starts charging to the maximum value of the supply voltage V_{sm}. When the capacitor is fully charged, it holds the charge until the input AC supply to the rectifier reaches the negative half-cycle. As soon as the negative half supply is reached, the diode gets reverse biased and thus stops conducting. During the non-conducting period, the capacitor discharges all the stored charges through the output load resistance, R_{Load}. As the voltage across R_{Load} and the voltage across the capacitor are the same ($V_{Load} = V_c$), they decrease exponentially with a time constant ($C * R_{Load}$) along the curve of the non-conducting period. This is shown in Fig. 6.

(d) **Relay**: 5 V-1 channel relay has been employed to do the actual switching. The circuiting is done in such a way that the whole circuit receives power by default.

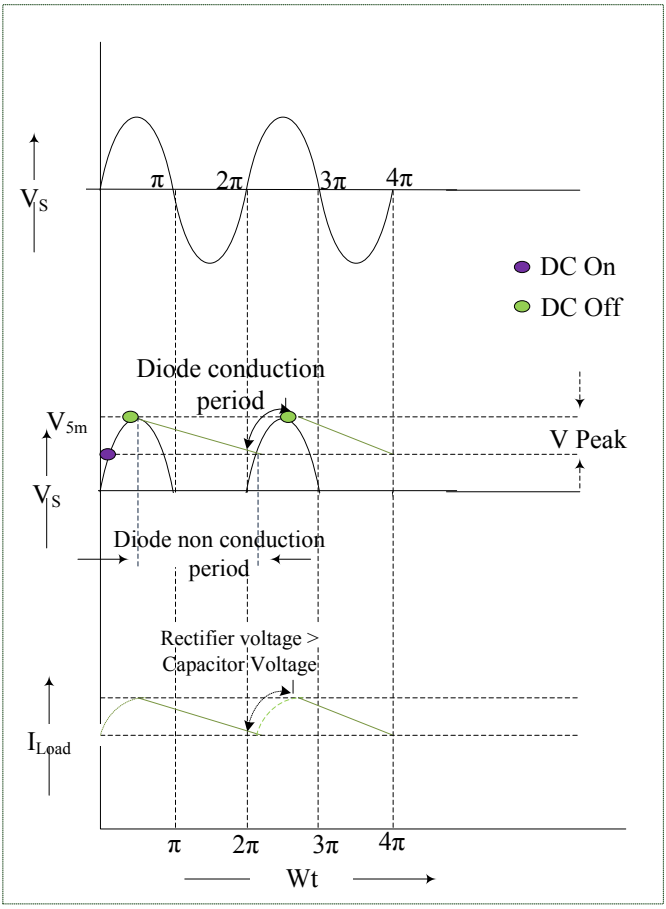

Fig. 6 Waveform of the filtered rectifier circuit

When the signal is received to the TinyMesh, current flows from the TX pin and breaks the circuit by switching the relay.

(e) **TinyMesh module**: Each TinyMesh module has a unique ID of its own. However, two or more modules can have the same system ID. The module in this circuit is the receiver module that receives 1 byte of instruction that will trigger a pulse from PWM pin 6 to switch the relay switch to "off" mode. The PWM has a peak value of 3.3 V, whereas the relay is designed for 5 V. To make the voltage jump necessary, a logic level controller is used in the circuit.

3.2.2 A HUB

A peripheral that connects all plugging components to the user's phone.

(a) It should sort, receive, and transmit data to and from the plugging devices and read instructions sent over local Wi-Fi from the user's application on their phone.
(b) It should be easily portable.
(c) May/may not have a separate power source (Fig. 7).

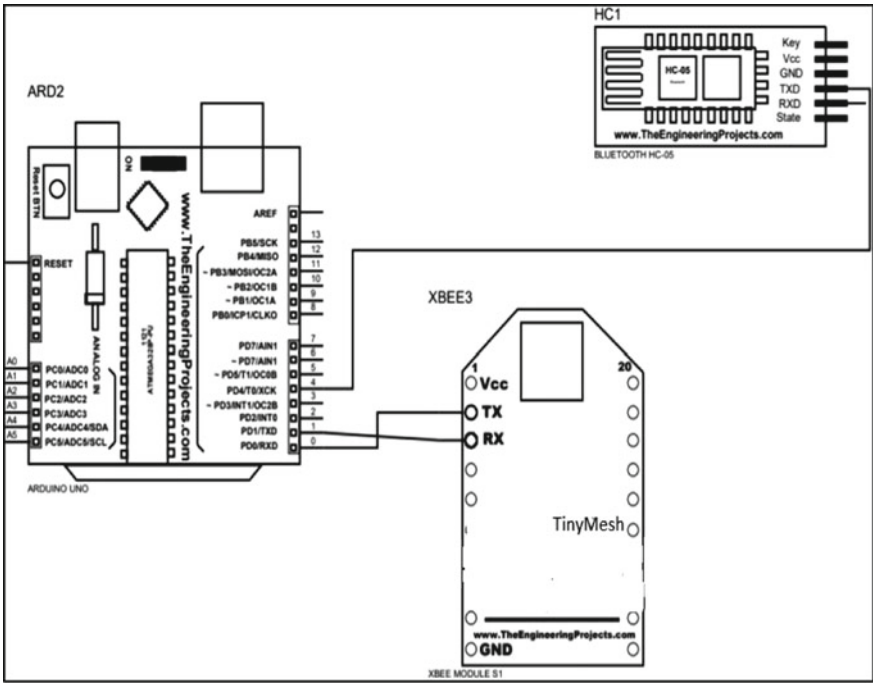

Fig. 7 Gateway circuit for hub

Table 1 Summary list of various components [15]

Components	Specification	Quantity
Microcontroller	ESP 8266	1
Relay Module	GURU JQC\3FF-S-Z	1
Transformer	GURU 220v	1
TinyMesh	AS RC2500HP-TM	2
controller	Logic-level controller Sparkfun 3.3–5 V	1
Jumper wires	Standard	–
LEDs	Standard	–
Encasing	Acrylic-2 mm thickness	1
plugs	Female and male plugs	2

Components used in hub:

(a) **TinyMesh module**: This module works as the transmitter module. It will have the same system ID as the receiver module. It will send a byte of data addressed to the unique ID of the receiver TM module.
(b) **ESP8266**: The ESP8266 creates a local server that houses the IP address where the Arduino IDE coding necessary to send the byte of instruction to the TinyMesh has been written.

Table 1 shows the specification of some of the important components used to develop model.

3.2.3 Mobile Application

A simple Android app that can be installed in any smartphone or tablet is developed. Some of the important features of the app are:

(a) The application should be able to access Wi-Fi and/or settings of the phone.
(b) It should have widgets to set a timer.
(c) It should have an easy-to-use UI.

MIT app inventor [14] was used to develop the Android application. The final look of the interface of the application is shown in Fig. 8a, b.

The summary and list of various components are provided in Table 1 and Fig. 9.

Fig. 8 a Application icon. **b** Interface

4 Results and Discussions

4.1 Testing of Plugin and Hub Circuit

To check if the TinyMesh modules were functioning correctly, a simulator was used to bounce signal between them. Each TinyMesh module has its own Unique ID but two or more TinyMesh modules can have a common Cluster ID. The idea here is to perform a "handshake." An 8-bit code is bounced from one module (transmitter) to another (receiver) (Fig. 10).

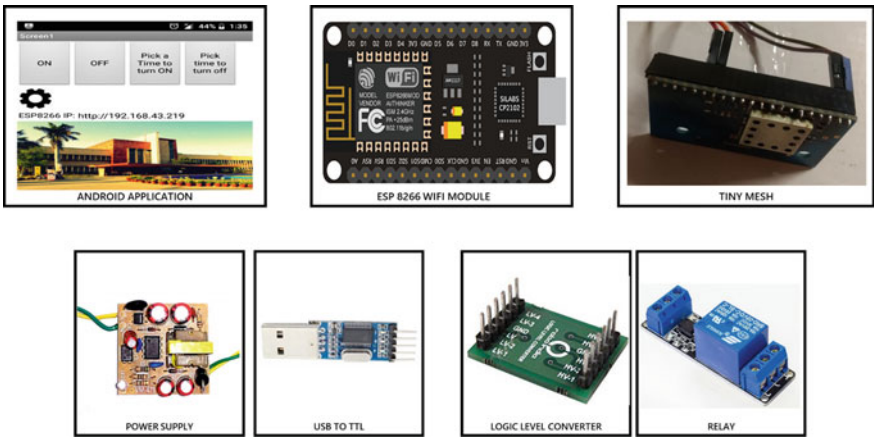

Fig. 9 Android application and Components used in the assembly of Socket Jockey

4.2 Application Testing

App developed adjusts itself with the phone's current time as shown in Fig. 11.

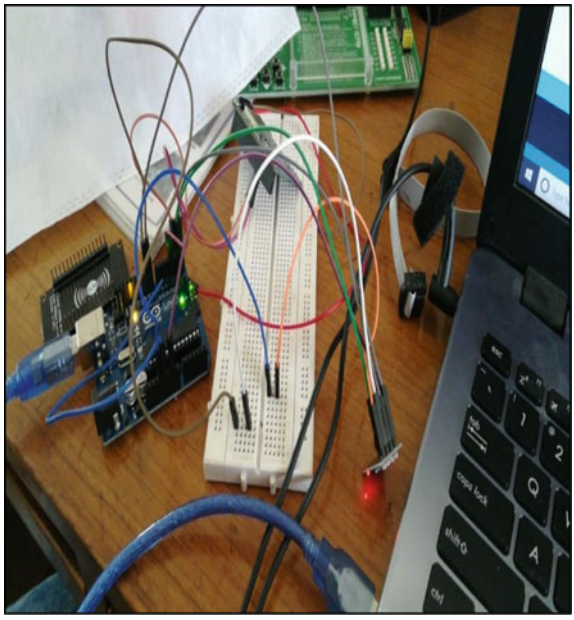

Fig. 10 Hub testing using Arduino

Fig. 11 Timer adjusts to the current time on the phone

4.3 Final Assembly

After the final assembly of the circuit, it is put into a box made of acrylic sheet. The complete model is shown in Fig. 12.

5 Conclusion

Our product concluded with the achievement of each of our goals as discussed earlier. We were able to design, analyze, and fabricate a product that does the following:

(1) It is able to plug into any electrical switchboard like a multiplug onto which any pluggable device can be added and
(2) It could be remotely be switched on or off as and when required by an app on the phone at the user's convenience.

All this was achieved while keeping the total cost of manufacturing minimal. Further observations were made as follows:

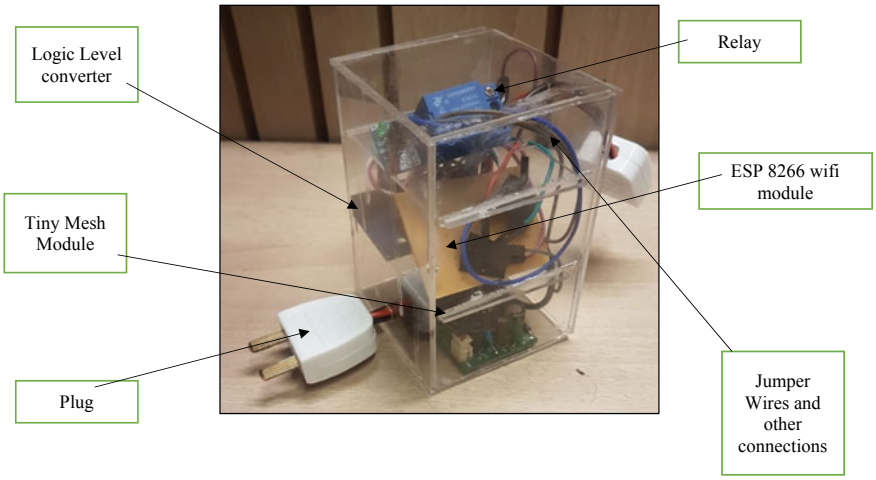

Fig. 12 Final assembly of the product

- ESP8266 equipped with its developer kit was able to replace the bulky Arduino Uno board and also eliminate the requirement of circuiting a separate Wi-Fi module. The main benefit of this is that a lot of dead space was freed up which could mean either more special adjustability for the remaining components or less bulky product or both.
- The hub can make use of USB inlet for powering. This means that it can make use of any female USB port like that of a power bank or a laptop.

References

1. Piyare R, Tazil M (2011) Bluetooth based home automation system using cell phone. In: 2011 IEEE 15th international symposium on consumer electronics (ISCE). IEEE, pp. 192–195
2. Asadullah M, Raza A (2016) An overview of home automation systems. In: 2016 2nd international conference on robotics and artificial intelligence (ICRAI). IEEE, pp. 27–31
3. Kunal D, Tushar D (2017) A survey on IoT based smart home. Int J Eng Sci Res Technol (IJESRT), Nashik, pp. 176–178. Doi: https://doi.org/10.5281/zenodo.376550
4. Kate PG, Rana JR (2015) ZIGBEE based monitoring theft detection and automatic electricity meter reading. In: 2015 international conference on energy systems and applications. IEEE, pp. 258–262
5. Ramli MI, Wahab MHA, Ahmad NN (2006) Towards smart home: control electrical devices online. In: International conference on science and technology: application in industry and education, vol 2
6. Tan KK, Voon EP, Chen Z, Chen S, Lee TH (2018) Teaching of automation and control engineering practice—a case study. In: 2018 IEEE 14th international conference on control and automation (ICCA), pp 324–329

7. Mainetti L, Patrono L, Vilei A (2011) Evolution of wireless sensor networks towards the Internet of Things: a survey. In: SoftCOM 2011, 19th international conference on software, telecommunications and computer networks. IEEE, pp 1–6
8. Dey S, Roy A, Das S (2016) Home automation using internet of thing. In: 2016 IEEE 7th annual ubiquitous computing, electronics & mobile communication conference (UEMCON). IEEE, pp 1–6
9. Das S, Debabhuti N, Das R, Dutta S, Ghosh A (2014) Embedded system for home automation using SMS. In: 2014 first international conference on automation, control, energy and systems (ACES). IEEE, pp 1–6
10. Sriskanthan N, Tan F, Karande A (2002) Bluetooth based home automation system. Microprocess Microsyst 26(6):281–289
11. Mandula K, Parupalli R, Murty CA, Magesh E, Lunagariya R (2015) Mobile based home automation using Internet of Things (IoT). In: 2015 International conference on control, instrumentation, communication and computational technologies (ICCICCT). IEEE, pp 340–343
12. Vikram N, Harish KS, Nihaal MS, Umesh R, Shetty A, Kumar A (2017) A low cost home automation system using wi-fi based wireless sensor network incorporating Internet of Things (IoT). In: 2017 IEEE 7th international advance computing conference (IACC). IEEE, pp 174–178
13. Vishwakarma SK, Upadhyaya P, Kumari B, Mishra AK (2019) Smart energy efficient home automation system using IoT. In: 2019 4th international conference on internet of things: smart innovation and usages (IoT-SIU). IEEE, pp 1–4
14. Sittón-Candanedo I, Alonso RS, García Ó, Muñoz L, Rodríguez-González S (2019) Edge computing, IoT and social computing in smart energy scenarios. Sensors 19(15):3353
15. Singh MD (2008) Power electronics. Tata McGraw-Hill Education

Algorithm for Translation and Rotation Motions of Gantry Robot

M. M. Abhinanth, Abhilash K. Raj, and R. Ramesh Kumar

Abstract A scaled version of a gantry robot to cover an envelope of 300 × 300 × 150 mm is designed to establish the accuracy of end positions prior to the manufacturing of any industrial gantry robot. A desk top 3D printer is suitably modified for the fabrication of robot, and measured translational motions are compared with prediction following well-known D-H parameter. A good agreement on the end positions between the test and prediction are illustrated. Arduino code employed to control the real-time execution of the gantry robot movement in a semi-automatic mode is provided for the designer.

Keywords DH parameter · Gantry robot · Pose · End effector

1 Introduction

Over couple of decades, industrial robots are worldwide implemented in various hazardous and non-hazardous applications. Mostly these are being used for material handling, welding, painting, assembling of parts, packaging, handling hazardous materials, and undersea operations. In order to access the proven technology on forward kinematics for large industrial manipulator gantry robots, it is necessary to produce robots of scaled geometry and compare with test data on its end position vectors. Well-known DH approach developed in the year 1955 at North Western University to predict the end position of robot within a coordinate frame space is availed in the present study to predict the end positions analytically [1]. The Denavit-Hartenberg analysis (DH) is presented to build the homogeneous transformations matrices between the robot joint axes.

M. M. Abhinanth (✉) · R. Ramesh Kumar
SreeChitra Thirunal College of Engineering, Thiruvananthapuram, India
e-mail: abhinanthmm@gmail.com

A. K. Raj
Digi Robotics, International Media Production Zone, Dubai, UAE
e-mail: abhilashkraj3@gmail.com

L. M. Das et al. (eds.), *Emerging Trends in Mechanical Engineering*, Lecture Notes in Mechanical Engineering, https://doi.org/10.1007/978-981-15-8304-9_8

Table 1 D-H parameters of gantry robot

Joint	a (Link length)	d (Joint offset)	α (Twist angle)	θ (Joint angle)
1 (X-axis)	$a1 = 0$	300 (JV)	90	0
2 (Y-axis)	$a2 = 0$	300 (JV)	90	0
3 (Z-axis)	$a3 = 0$	150 (JV)	90	0
4 (Guide block)	$a4 = 0$	0	0	180 (JV)
5 (Gripper)	$a5 = 0$	0	0	60 (JV)

The various commanding methods can be employed such as through PC with Arduino or Bluetooth control for remote application and accelerometer based on gesture control method [2–5]. It is well known that there are two types of kinematic analyses; forward and inverse kinematic analysis, forward kinematic analysis is concerned with the relationship between the joint angle of the robot manipulator and the position and orientation of the end effector [6]. The forward kinematic analysis of any robot configuration is simple to do but greater challenge is to analyze the inverse kinematics solution of the robot configuration using the final position of the robot [7]. To perform like a human being, these robots normally are designed with a high center of mass, which makes it challenging to maintain stability while achieving high performance on complex and unpredictable terrain [8]. Execution of the motion of robot is carried out by Arduino hardware and associated software. It provides readily available examples to execute a motor individually and by combination. Stepper motors and servo motors are commonly used for the motions. Stepper motor used in the present study works on 12 V DC and servo motor works on 5 V DC. So, SMPS unit with a RAMPS board to supply the power to motors is availed. Once a controlling command for a definite movement achieves an intermediate end location, it is necessary to ascertain the accuracy following an error correction feedback system. However, in this study, after each movement, intermediate location is made as a new reference location for the subsequent movement. The specification of motors is given in Appendix 3.

In this study, a new gantry robot is fabricated and kinematic analyses of that consist of three translations degrees of freedom that are carried out following DH parameter. In order to compare the prediction on end position, gantry robot is commanded with the serial monitor available in Arduino software, and end positions are arrived at a set up step by linear movement of the stepper motor. A good agreement is observed between predictions following DH parameter as well as Robo analyzer with present test results on end positions.

1.1 Methodology

D-H parameter table for gantry robot is defined first and then using these values transformation matrix for each link is established (Table 1). The end effecter matrix is obtained as post-multiplication product of these matrices.

1.2 Fabrication of Gantry Robot

While the drive technologies, work envelope geometries, and motion control methods provide convenient ways to broadly classify robots, there are a number of additional characteristics that allow the user to further specify robotic manipulators. Some of the common characteristics are listed below. The gantry robot is designed to provide a work space of 300 × 300 × 150 (vertical) mm (Fig. 1). The translation movements

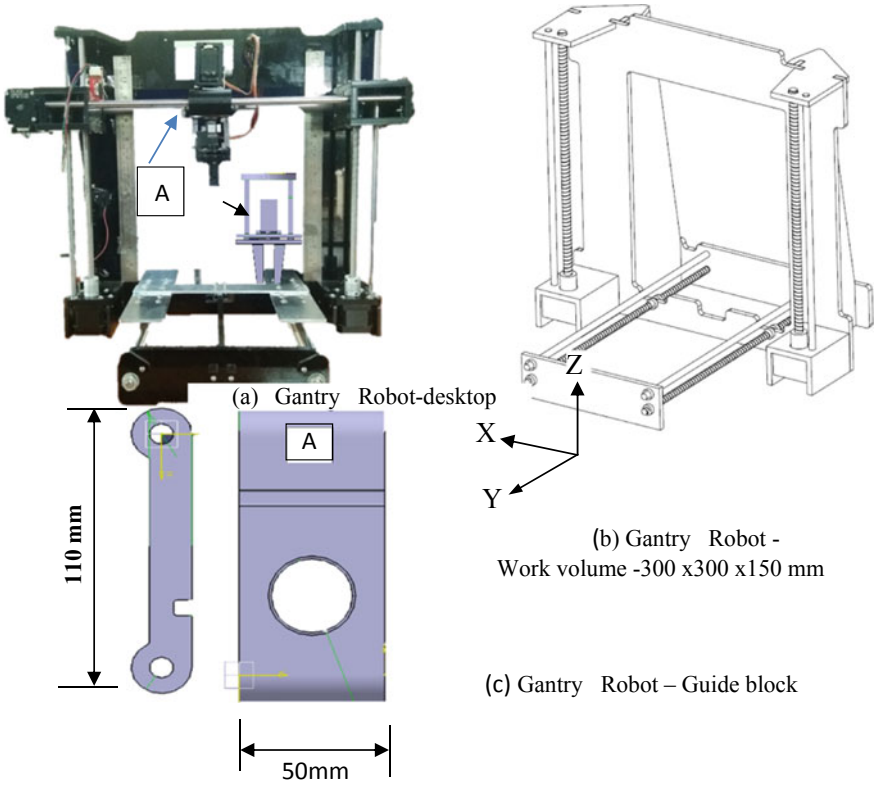

Fig. 1 Gantry robot

for 10 mm is aimed with a speed of 0.06 s. Maximum speed of servo motor used for the gripper is 0.09 s for 60° rotation. The expected accuracy of the unit is 0.012 mm.

The guide block is designed to move in X-direction which holds two servo motors for one rotation and one picking (Fig. 1a). This guide block unit will pick the object from the bed and place the object in another place. The load carrying capacity of the robot is around 200 g. The guide block is modeled in software and then its fabricated using 3D printing technology. The fabricated guide block is fixed in the place of the extruder unit in the Anet a6 printer to obtain the gantry robot setup. The modeled part is shown in Fig. 1c.

1.3 Design of Gripper Block

The gripper is designed for the point-to-point motion control in order to pick and place object from one space to another in the work volume. For the large-scale operation, loading and unloading are also done by the point-to-point motion control method. The gripper unit is also fabricated like guide block after that which is fitted with the robot. A 9 g servo motor powers up the gripper to pick and drop object from the work space. Gripper is totally rotatable in nature by fixing it on the servo.

1.4 Program Code

The interface between PC and robot is activated using Arduino code which enables the function of actuators. In other words, both stepper and servo motors are given commands. The specification of these motors is given below. All movement command along *x*, *y*, *z* axes also by guide block and gripper are given in Appendix 1.

Mega code for the working of gantry robot is follows

```
#define FAN_PIN          9
#define P_SERVO_PIN     11
#define R_SERVO_PIN     4
//Servo pins 11 6 5 4
Servo plucker,rotate;
int C = 0, d = 0, x = 0, y = 0, z = 0, p = 120, r = 90;
void setup() {
  //plucker.attach(P_SERVO_PIN);
  //rotate.attach(R_SERVO_PIN);
Serial.print("Ready to work");// Tells program is ready
delay(50);}
void loop (){
while (!Serial.available())
  {    C = Serial.parseInt();
Serial.println(C);
```

```
switch (C){
case 1 : C1(); break;
case 2 : C2(); break;
case 3 : C3(); break;
case 4 : C4(); break;
case 5 : C5(); break;
case 6 : C6(); break;   }
    //Serial.print('F');
Serial.flush();
while (Serial.read() != 'L')
{delay(50);
Serial.print('F');
      }*/  }}
```

1.5 Robot Gripper Block End Position Prediction [1]

Transformation matrix for first link with respect to base frame is given below

$$
{}_{0}T_{1}(\theta, d, a, \alpha) = \begin{bmatrix} \cos\theta_1 & -\sin\theta_1\cos\alpha_1 & \sin\theta_1\sin\alpha_1 & a_1\cos\theta_1 \\ \sin\theta_1 & \cos\theta_1\cos\alpha_1 & -\cos\theta_1\sin\alpha_1 & a_1\sin\theta_1 \\ 0 & \sin\alpha_1 & \cos\alpha_1 & d_1 \\ 0 & 0 & 0 & 1 \end{bmatrix}
$$

$$
= \begin{bmatrix} 0 & 0 & 1 & 0 \\ 1 & 0 & 0 & 0 \\ 0 & 1 & 0 & d_1 \\ 0 & 0 & 0 & 1 \end{bmatrix}
$$

Transformation matrix for second link with respect to first frame is given below

$$
T_2(\theta, d, a, \alpha) = \begin{bmatrix} \cos\theta_2 & -\sin\theta_2\cos\alpha_2 & \sin\theta_2\sin\alpha_2 & a_2\cos\theta_2 \\ \sin\theta_2 & \cos\theta_2\cos\alpha_2 & -\cos\theta_2\sin\alpha_2 & a_2\sin\theta_2 \\ 0 & \sin\alpha_2 & \cos\alpha_2 & d_2 \\ 0 & 0 & 0 & 1 \end{bmatrix}
$$

$$
= \begin{bmatrix} 0 & 0 & 1 & 0 \\ 1 & 0 & 0 & 0 \\ 0 & 1 & 0 & d_2 \\ 0 & 0 & 0 & 1 \end{bmatrix}
$$

Transformation matrix for third link with respect to second frame is given below

$$
{}_{2}T_{3}(\theta, d, a, \alpha) = \begin{bmatrix} \cos\theta_3 & -\sin\theta_3\cos\alpha_3 & \sin\theta_3\sin\alpha_3 & a_3\cos\theta_3 \\ \sin\theta_3 & \cos\theta_3\cos\alpha_3 & -\cos\theta_3\sin\alpha_3 & a_3\sin\theta_3 \\ 0 & \sin\alpha_3 & \cos\alpha_3 & d_3 \\ 0 & 0 & 0 & 1 \end{bmatrix}
$$

$$
= \begin{bmatrix} 0 & 0 & 1 & 0 \\ 1 & 0 & 0 & 0 \\ 0 & 1 & 0 & d_3 \\ 0 & 0 & 0 & 1 \end{bmatrix}
$$

The homogenous transformation matrix of the end effector frame with respect to base frame, i.e., transformation matrix T is now obtained by the post-multiplication of the above individual homogenous transformations.

$$
{}_{0}T_{3}(\theta, d, a, \alpha) = \begin{bmatrix} 0 & 0 & 1 & 0 \\ 1 & 0 & 0 & 0 \\ 0 & 1 & 0 & d_1 + d_2 + d_3 \\ 0 & 0 & 0 & 1 \end{bmatrix}
$$

2 Results and Discussion

Synthesis of gantry robot by suitably modifying an existing Anet a6 three—D printer is given in Fig. 1. The DH parameter method available in literature is used to predict the end positions of gantry robot of small size for specified motions along the three mutually perpendicular directions and given Table 2a–d. Same tables also compare the predicted values with measured data with a resolution of 0.012 mm. Code for real-time execution is generated such that after each command for movement, the new position is set as a reference point for the next operation. The code is provided in the Appendix 1.

It may be noted from Table 2a that for 1 mm displacement in X-direction from an initial position of 44.05 mm of the gripper block of the robot shown in Fig. 1a is expected to move to 45.05 mm by a command "C1X10". However, from actual measurement, it is found to be only at 45.03 mm with 2% error. Further, the commands are given for four more times from each intermediate final position along X-axis. The variation in error is within 1%. Similar comparison between the prediction and test for a movement of 10 mm displacement is observed within 0.6%. It may be noted that the maximum absolute deviation is 0.06 mm. Test is repeated along Y-axis and the maximum absolute deviation is found to be 0.03 mm and percentage deviation with respect to prediction is 2%. The study was not carried out along Z-axis movement due to test setup constraint for measurements.

It is concluded that even with stepwise command to set the intermediate local end locations as reference position for subsequent movement instead of error correction

Table 2 Comparison of translator motions predicted with measured data

Trial No.	Command	Initial value	Final value	Error (%)
(a) Along X-axis for 1 mm *movement*				
1	C1X10	44.05	45.03	2
2	C1X10	45.03	46.04	1
3	C1X10	46.04	47.04	0
4	C1X10	47.04	48.03	1
5	C1X10	48.03	49.02	1
(b) Along X-axis for 10 mm *movement*				
1	C1X100	27.40	37.38	0.2
2	C1X100	37.38	47.36	0.2
3	C1X100	47.36	57.32	0.4
4	C1X100	57.32	67.37	0.5
5	C1X100	67.37	77.31	0.6
(c) Along Y-axis for 1 mm *movement*				
1	C1X0Y10	44.05	45.03	2
2	C1X0Y10	45.03	46.06	3
3	C1X0Y10	46.06	47.04	2
4	C1X0Y10	47.04	48.02	2
5	C1X0Y10	48.02	49.04	2
(d) Along Y-axis 10 mm *movement*				
1	C1X0Y100	27.40	37.38	0.2
2	C1X0Y100	37.38	47.37	0.1
3	C1X0Y100	47.37	57.36	0.1
4	C1X0Y100	57.38	67.36	0.2
5	C1X0Y100	67.36	77.34	0.2

C1X10—Command for 1 mm displacement in *X*-direction with zero movement in *Y*-direction from any initial or intermediate position
C1X100—Command for 10 mm displacement in *X*-direction with zero movement in *Y*-direction from any initial or intermediate position
C1X0Y10—Command for 1 mm displacement in *Y*-direction with zero movement in *X*-direction from any initial or intermediate position
C1X0Y100—Command for 100 mm displacement in *Y*-direction with zero movement in *X*-direction from any intermediate position

by feedback system, it is possible to achieve the final end position accurately. The *x* command is implemented through program as shown below (vide Appendix 1).

```
1.1   Case 1
void C1()
{x = Serial.parseInt();
Y = Serial.parseInt()}
```

When value of *X* is assigned to X62 (6.2 mm movement along *X*-direction), then "parseInt" accepts only numerical value. Similarly C1X10 means, 10 mm movement along *X*-direction. Similarly, when value of *Y* is assigned to Y62 (6.2 mm movement along *Y*-direction), then "parseInt" accepts only numerical value. Similarly, C1X0Y10 means, 10 mm movement along *Y*-direction.

3 Conclusions

A well-established technique of DH parameter has been availed for the prediction of end position of scaled gantry robot required for the implementation of industrial manipulator. Details on fabrication of the robot are given for a ready reference. Comparison with measured data on end position with the prediction has shown good agreement within a resolution of 0.012 mm. For the real-time execution after each command for movement, the new position has been set as a reference point for the next operation for end positions along three mutually perpendicular axes. A generated code is provided in annexure. Synthesize of small-scale robot presented will be useful so that large-sized robot end positions can be confidently envisaged.

4 Appendix 1

1.Mega_code

```
#include <Servo.h>
#define X_STEP_PIN         54
#define dirPinx            55
#define X_DIR_PIN          55
#define stepPinx           54
#define X_ENABLE_PIN       38
#define X_MIN_PIN           3
#define ex                  3
#define X_MAX_PIN           2
#define Y_STEP_PIN         A6
#define dirPiny            A7
#define Y_DIR_PIN          A7
#define stepPiny           A6
#define Y_ENABLE_PIN       56
#define Y_MIN_PIN          14
#define ey                 14
#define Y_MAX_PIN          15
#define Z_STEP_PIN         46
```

```
#define dirPinz            48
#define stepPinz           46
#define Z_DIR_PIN          48
#define Z_ENABLE_PIN       48
#define Z_MIN_PIN          18
#define ez                 18
#define Z_MAX_PIN          19
#define FAN_PIN             9
#define P_SERVO_PIN        11
#define R_SERVO_PIN         4
//Servo pins 11 6 5 4
Servo plucker,rotate;
int C = 0, x = 0, y = 0, z = 0, p = 120, r = 90;
void setup() {
//plucker.attach(P_SERVO_PIN);
//rotate.attach(R_SERVO_PIN);
pinMode(X_STEP_PIN  , OUTPUT);
pinMode(X_DIR_PIN    , OUTPUT);
pinMode(X_ENABLE_PIN    , OUTPUT);
pinMode(Y_STEP_PIN  , OUTPUT);
pinMode(Y_DIR_PIN    , OUTPUT);
pinMode(Y_ENABLE_PIN    , OUTPUT);
pinMode(Z_STEP_PIN  , OUTPUT);
pinMode(Z_DIR_PIN    , OUTPUT);
pinMode(Z_ENABLE_PIN    , OUTPUT);
digitalWrite(X_ENABLE_PIN    , LOW);
digitalWrite(Y_ENABLE_PIN    , LOW);
digitalWrite(Z_ENABLE_PIN    , LOW);
pinMode(X_MIN_PIN, INPUT);
pinMode(ex, INPUT);
pinMode(ey, INPUT);
pinMode(ez, INPUT);
pinMode(X_MAX_PIN, INPUT); //X
EndstoppinMode(Y_MIN_PIN, INPUT);
pinMode(Y_MAX_PIN, INPUT); //Y
EndstoppinMode(Z_MIN_PIN, INPUT);
pinMode(Z_MAX_PIN, INPUT); //Z
Endstop
Serial.begin(9600);
//plucker.write(p);
// rotate.write(r);
Serial.print("Ready to work");//
Tells program is is ready
delay(50);}
void loop ()
{  while (!Serial.available())
  {    C = Serial.parseInt();
//Serial.println(C);
switch (C)
    {case 1 : C1(); break;
case 2 : C2(); break;
case 3 : C3(); break;
case 4 : C4(); break;
case 5 : C5(); break;
case 6 : C6(); break;
```

```
}//Serial.print('F');
Serial.flush();
/* while (Serial.read() != 'L')
{ delay(50);
Serial.print('F');
      }*/  }}
1.2 Case 1
void C1()
{x = Serial.parseInt();
y = Serial.parseInt();
z = Serial.parseInt();
xaxis(x);
delay(10);
yaxis(y);
delay(10);
zaxis(z);
delay(10);}
1.3 case 2
voidendstop()
{ //Serial.println("endstopx");
digitalWrite(dirPinx,LOW);
while(digitalRead(ex)==HIGH)
{   digitalWrite(stepPinx,HIGH);
delayMicroseconds(1500);
digitalWrite(stepPinx,LOW);
delayMicroseconds(1500); }
digitalWrite(dirPinx,HIGH);
while(digitalRead(ex)==LOW)
{digitalWrite(stepPinx,HIGH);
delayMicroseconds(1500);
digitalWrite(stepPinx,LOW);
delayMicroseconds(1500); }}
1.4 Case 3
voidendstopy()
{ digitalWrite(dirPiny,HIGH);
while(digitalRead(ey)==HIGH)
{digitalWrite(stepPiny,HIGH);
delayMicroseconds(1500);
digitalWrite(stepPiny,LOW);
delayMicroseconds(1500);
}digitalWrite(dirPiny,LOW);
while(digitalRead(ey)==LOW)
{ digitalWrite(stepPiny,HIGH);
delayMicroseconds(1500);
digitalWrite(stepPiny,LOW);
delayMicroseconds(1500); } }
1.5 Case 4
voidendstopz()
{digitalWrite(dirPinz,LOW);
while(digitalRead(ez)==LOW)
{ digitalWrite(stepPinz,HIGH);
delayMicroseconds(1500);
```

```
digitalWrite(stepPinz,LOW);
delayMicroseconds(1500);}
int n=0;
digitalWrite(dirPinz,HIGH);
while(n<=500)
{ digitalWrite(stepPinz,HIGH);
delayMicroseconds(1500);
digitalWrite(stepPinz,LOW);
delayMicroseconds(1500);
n++;}}
1.6 Case 5
void C5()
{delay(10);
r = Serial.parseInt();
rotate.attach(R_SERVO_PIN);
delay(10);
rotate.write(r);
delay(1000);
rotate.detach();}
1.7 Case 6
void C6()
{delay(10);
p = Serial.parseInt();
delay(50);
plucker.attach(P_SERVO_PIN);
delay(10);
plucker.write(p);
delay(1000);
plucker.detach();
}
```

5 Appendix 2

```
2.1 Programme for X stepper motor
voidxaxis(intxs)
{  if (xs> 0)
digitalWrite(X_DIR_PIN    , HIGH);
else
digitalWrite(X_DIR_PIN    , LOW);
for (inti = 0; i< abs(xs); i++)
{ digitalWrite(X_STEP_PIN    , LOW);
delayMicroseconds(1000);
digitalWrite(X_STEP_PIN    , HIGH);
delayMicroseconds(1000);} }
2.2 Programme for Y stepper motor
voidyaxis(intys)
{  if (ys> 0) digitalWrite(Y_DIR_PIN    , HIGH);
else
```

```
digitalWrite(Y_DIR_PIN    , LOW);
for (inti = 0; i< abs(ys); i++)
{ digitalWrite(Y_STEP_PIN    , LOW);
delayMicroseconds(1000);
digitalWrite(Y_STEP_PIN    , HIGH);
delayMicroseconds(1000);}}
2.3 Programme for Z stepper
voidzaxis(intzs)
{  if (zs> 0) digitalWrite(Z_DIR_PIN    , HIGH);
else {
digitalWrite(Z_DIR_PIN    , LOW);}
if (abs(zs) < 501)
  {for (inti = 0; i< abs(zs); i++)
{digitalWrite(Z_STEP_PIN    , LOW);
delayMicroseconds(1500);
digitalWrite(Z_STEP_PIN    , HIGH);
delayMicroseconds(1500);}}
else
  {for (inti = 0; i< 250; i++)
{digitalWrite(Z_STEP_PIN    , LOW);
delayMicroseconds(1500 -  (i * 2));
digitalWrite(Z_STEP_PIN    , HIGH);
delayMicroseconds(1500 -  (i * 2));}
for (inti = 0; i< (abs(zs) -  500); i++)
    {digitalWrite(Z_STEP_PIN    , LOW);
delayMicroseconds(1000);
digitalWrite(Z_STEP_PIN    , HIGH);
delayMicroseconds(1000);}
for (inti = 0; i< 250; i++)
    {digitalWrite(Z_STEP_PIN    , LOW);
delayMicroseconds(1000 + (i * 2));
digitalWrite(Z_STEP_PIN    , HIGH);
delayMicroseconds(1000 + (i * 2));}}
2.4 Programme for XY combination
voidxycomb(intxs, intys)
{if (xs> 0) digitalWrite(X_DIR_PIN    , HIGH);
Else
{ digitalWrite(X_DIR_PIN    , LOW);}
if (ys> 0) digitalWrite(Y_DIR_PIN    , HIGH);
else
{ digitalWrite(Y_DIR_PIN    , LOW);}
int extra = abs(xs -  ys), rest = 0;
if (abs(xs) == abs(ys)) rest = abs(xs);
if (abs(xs) > abs(ys))
{ rest = abs(xs) -  extra;
```

```
if (abs(extra) < 501)
{for (inti = 0; i< abs(extra); i++)
{digitalWrite(X_STEP_PIN    , LOW);
delayMicroseconds(1000);
digitalWrite(X_STEP_PIN    , HIGH);
delayMicroseconds(1000);}}
else
{ for (inti = 0; i< 250; i++)
{ digitalWrite(X_STEP_PIN    , LOW);
delayMicroseconds(1000 -  (i * 3));
digitalWrite(X_STEP_PIN    , HIGH);
delayMicroseconds(1000 -  (i * 3));}
for (inti = 0; i< (abs(extra) -  500); i++)
{ digitalWrite(X_STEP_PIN    , LOW);
delayMicroseconds(250);
digitalWrite(X_STEP_PIN    , HIGH);
delayMicroseconds(250);}
for (inti = 0; i< 250; i++)
      {digitalWrite(X_STEP_PIN    , LOW);
delayMicroseconds(250 + (i * 3));
digitalWrite(X_STEP_PIN    , HIGH);
delayMicroseconds(250 + (i *  3));}}}
else
  {rest = abs(ys) -  extra;
if (abs(extra) < 501)
    {for (inti = 0; i< abs(extra); i++)
{ digitalWrite(Y_STEP_PIN    , LOW);
delayMicroseconds(1000);
digitalWrite(Y_STEP_PIN    , HIGH);
delayMicroseconds(1000); }}
else
    {for (inti = 0; i<  250; i++)
{ digitalWrite(Y_STEP_PIN    , LOW);
delayMicroseconds(1000 -  (i * 3));
digitalWrite(Y_STEP_PIN    , HIGH);
delayMicroseconds(1000 -  (i * 3));}
for (inti = 0; i< (abs(extra) -  500); i++)
{ digitalWrite(Y_STEP_PIN    , LOW);
delayMicroseconds(250);
digitalWrite(Y_STEP_PIN    , HIGH);
delayMicroseconds(250); }
for (inti = 0; i< 250; i++)
{  digitalWrite(Y_STEP_PIN    , LOW);
delayMicroseconds(250 + (i * 3));
digitalWrite(Y_STEP_PIN    , HIGH);
delayMicroseconds(250 + (i * 3));}}}
```

```
if (rest < 501)
  {digitalWrite(X_STEP_PIN    , LOW);
digitalWrite(Y_STEP_PIN    , LOW);
delayMicroseconds(1000);
digitalWrite(X_STEP_PIN    , HIGH);
digitalWrite(Y_STEP_PIN    , HIGH);
delayMicroseconds(1000);}
else
{ for (inti = 0; i< 250; i++)
{ digitalWrite(X_STEP_PIN    , LOW);
digitalWrite(Y_STEP_PIN    , LOW);
delayMicroseconds(1000 -  (i * 2));
digitalWrite(X_STEP_PIN    , HIGH);
digitalWrite(Y_STEP_PIN    , HIGH);
delayMicroseconds(1000 -  (i * 2)); }
for (inti = 0; i< (abs(rest) -  500); i++)
{ digitalWrite(X_STEP_PIN    , LOW);
digitalWrite(Y_STEP_PIN    , LOW);
delayMicroseconds(500);
digitalWrite(X_STEP_PIN    , HIGH);
digitalWrite(Y_STEP_PIN    , HIGH);
delayMicroseconds(500);}
for (inti = 0; i< 250; i++)
{ digitalWrite(X_STEP_PIN    , LOW);
digitalWrite(Y_STEP_PIN    , LOW);
delayMicroseconds(500 + (i * 3));
digitalWrite(X_STEP_PIN    , HIGH);
digitalWrite(Y_STEP_PIN    , HIGH);
delayMicroseconds(500 + (i * 3));
}}}
```

6 Appendix 3

1. 12 g servo motor specification

   Operating voltage: 4.5–6.0 v
   Operating current: 50–180 mA
   Operating speed: 0.09 s for 60°
   Torque: 1.6 kg.cm
   Weight: 12 g
   Limit angle: 180°

2. 9 g servo motor specification

   Operating voltage: 4.5–6.0 v
   Operating current: 50–180 mA

Operating speed: 0.12 s for 60°
Torque: 1.6 kg.cm
Weight: 9 g
Limit angle: 180°.

References

1. Denavit J, Hartenberg RS (1955) A kinematic analysis notation for lower pair mechanisms based on matrices. Trans ASME J Appl Mech 23:215–221
2. Marvroids C, Lee E (2004) Geometric design of 3r robot manipulators for reaching four end effector spatial poses, Int J Robot Res 23(3):247–254
3. Xu D, Acosat CA, Gan JQ, Hu H (2005) Analysis of the inverse kinematics for a 5 DOF manipulator. Int J Autom Comput 2:114–124
4. Constantin D, Lupose M, Bachu C, Bulgia D (2013) Forward kinematics analysis of an industrial robot. New Dev Mech Mech Eng 03:90–95
5. Elot E, Deepak BB, Parhi DR, Srinivas J et al (2013) Design & kinematic analysis of an articulated robotic manipulator. Int J Mech Indus Eng 3:105–108
6. Khatamin A (2015) Solving kinematics problems of a 6 DOF robot manipulator. In: International conference scientific computing, vol 2
7. Game RU, Davkhare AA, Pakhale SS, Shinde VB (2017) Kinematic analysis of various robot configurations. Int Res J Eng Technol 4:921–933
8. Rojas S, Shen H, Griffths H, Li N, Zhang L (2017) Motion and gesture compliance control for high performance of a wheeled humanoid robot. In: International mechanical engineering and exposition, IMECE2017–72337
9. https://www.arduino.cc/
10. https://www.roboanalyser.com/helpFiles/en/tutorials.htm
11. https://www.ri.cmu.edu

Optimal Selection of Circular Interpolation for CNC Turning Centers

Yaser Hadi

Abstract A circular interpolation algorithm used to determine the parameters of separate circular paths was used to generate round shapes on a computer-controlled numeric (CNC) turning machine. It is suggested that this calculation should be included in the CNC lathes' resident software program. This would decrease the amount of blocks of data required for part of the program. In a single block, a complete circular interpolation cycle for the number of passes could be specified. The suggested algorithm is optimized for minimal machining time and enhanced surface roughness. The programming of the new interpolation scheme, using circular and linear segments, must be applied to the specific part.

Keywords Circular interpolation · CNC · Turning machine · Surface roughness

1 Introduction

PC has superseded machine tools that are once installed and powered by hand-driven models. The product for programming these machines has enabled specialists to create high-quality components [1]. Reference has been made to the fact that contemporary machine tool ideas, sophisticated machining procedures, and techniques are essential to achieving general quality and productivity objectives in order to satisfy future market demands [2]. It is referred to the reality that CNC tool path capabilities are prevalent in CAD/CAM systems, but STEP-CNC and Super Model Standards are the basis of technology for programming and monitoring CNC. This standard will permit software providers to revolutionize computer programming. The error compensation software system structure that can offset software errors by recreating CNC programs has been investigated [3]. Error compensation has proven to be a cost-effective method for improving machine tools precision.

The use of both spiral archimetrium segments and circulatory segments must be applied to accurate part programming on tri-axis lathes [4]. Where the polar

Y. Hadi (✉)
Yanbu Industrial College, Yanbu, Saudi Arabia
e-mail: hadiy@rcyci.edu.sa

L. M. Das et al. (eds.), *Emerging Trends in Mechanical Engineering*, Lecture Notes in Mechanical Engineering, https://doi.org/10.1007/978-981-15-8304-9_9

coordinate system is more effective than the cartesian coordination for rotating axes [5]. For the rotated component with steady forms, an optimization model has been formulated [6]. To study the work carried out on CNC machine devices to minimize surveillance and contour errors [7]. Experiments are performed in the automatic five-axis CNC machine for contouring error detection [8]. The recommended vision and cross-grid encoder are used to evaluate three kinds of paths contouring errors at distinct feed rates [9] included an assessment of machined pockets surface roughness after machining and an enhanced pocket surface finish with real spiral tool path was achieved compared to the other tool paths under examination.

This suggests that CNC code-driven energy demand software which includes feed axis, vices, and workpieces, the energy demand of the feeding unit for cutting is used to properly estimate the entire working time of the processing process by means of energy-efficient machining [10]. Reporting of the establishment, directly from its representation, of an efficient tool path schedule method, designed and used for 3-axis CNC machining, for machining free-form surfaces without temporary surface fitting. The finished cylindrical bar sections are generated by CNC machines. The completed profiles consist of straight, facial, and circular workmanship [11]. The programming of circular profiles requires a number of circular passes.

An algorithm was introduced to improve the precision of interpolation in turning activities [12]. The parts considered shall be formed by the rotation of the free-form profile, which shall be carried out in terms of the formulation around the center linear axis. Each pass is linked to a fast cross, an approach, an indirect presentation, and lastly, a fast exploration. Each of these is shown by a unique piece of data in the program portion. The program is given these features by free selection. Planning for such an amount of data squares is particularly annoying. These progressions can be submitted through the software as a process. The software includes post-processors with altered CNC lathe. The most important prerequisites for effective concurrent engineering are integrated design and production procedures [13]. This means that complex goods like formed rolls, rotating blades, prostheses, etc., are much better quality.

2 Circular Profile Models

Three models for circular profile machining have been implemented in this paper as shown in Fig. 1. In the first model, I, the remnant material is expelled through N passes. Each pass makes the machine bring the tool around the oa-ab-ba linear route. The leg from the fundamental position to the “a” is made at a fast cross-rate to generate a depth per pass. For each pass, this depth is held steady. The “a-b” leg is made at feed rate using the appropriate methodology. Create a lingering material expulsion for a particular pass. The tool is withdrawn back to “a” at that stage. Each of these three movements is stated by a separate information block in the CNC program. The value of *Xi* and *Zi* is required for the pass amount in the block:

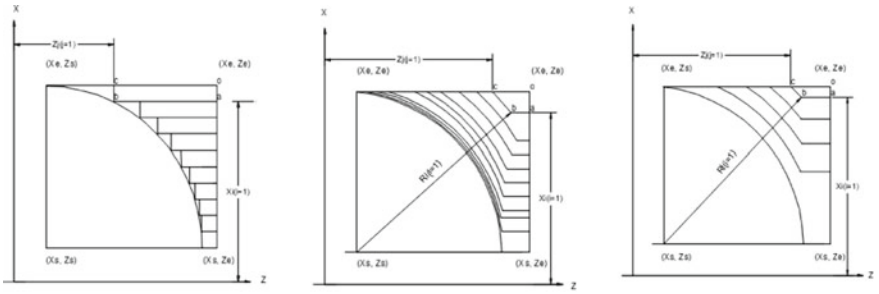

Fig. 1 Different models of machining methods used for circular interpolation

$$X_i = X_F + \frac{X_E - X_F}{N}(N-1) \tag{1}$$

$$Z_i = Z_E + \sqrt{\left[R_2 - (X_i - X_F)^2\right] + \mathrm{d}Z} \tag{2}$$

Total machining time can be calculated as below:

$$T_m = \frac{R_\theta}{F_C} + \sum_{i=1}^{N} \frac{Z_S - Z_i}{F_a} + \sum_{i=1}^{N} \frac{Z_S - Z_i}{F_c} + \frac{X_E - X_F}{F_a} \tag{3}$$

In Model II, the tool path is produced of direct and roundabout passes. The route cycle of the tool is depicted as in Fig. 1, oa-ab-bc-co. The leg from the fundamental position "o" to "a" is performed at a speed of rapid navigation. This leg reflects a sideways depth of cut per pass, which has remained the equivalent for all passes. This constant horizontal depth will generate a beginning with the deepest outs. The resulting cuts are produced systematically shallower in radial cuts. This keeps the rate of expulsion of the inventory continually decreasing as the tool is more deeply engaged in the job. The a-b leg is the method at the correct feed rate. At that stage, a round interjection of b-c is used to expel the lingering material for a particular pass. The tool is withdrawn back to place o at that stage. Each of the four movements shall be determined by a separate data block in the CNC program as follows:

$$\begin{matrix} G00\ X_i\ Z_S \\ G01\ X_i\ Z_F \\ G02\ X_E\ Z_i \\ G03\ X_E\ Z_S \end{matrix} \quad I(X_F - X_i), K(Z_E - Z_F) \tag{4}$$

where:

$$X_i = X_E - i\frac{X_E - X_F}{N}$$

$$Z_i = Z_E + \sqrt{\left[R_i^2 - (X_E - X_F)^2\right]}$$
$$R_i = Z_E + \sqrt{[(Z_F - Z_E) + (X_i - X_F)]^2}$$

Total machining time can be calculated as:

$$T_m = \sum_{i=1}^{N} \frac{X_E - X_i}{F_a} + N\frac{Z_S - Z_F}{F_c} + \sum_{i=1}^{N} \frac{Z_S - Z_i}{F_a} + \sum_{i=1}^{N} \frac{R_{1i}\theta_i}{F_c} \tag{5}$$

where:

$$\theta_i = \theta_{1i} - \theta_{2i} \quad \sin\theta_{1i} = \frac{X_E - X_F}{R_i} \quad \sin\theta_{2i} = \frac{X_i - X_F}{R_i}$$

In the third model, Model III, the lingering material is evacuated in an example such as Model II, with a distinction in the depth of the cut. The leg from the bottom position "0" to "a" is selected to produce a coherent radial cut. As needed, this will generate a start with the shallowest lateral depth. The resulting cuts are produced gradually in parallel depth. This is the reason for a bit-by-bit increase in the rate of inventory eviction as the tool is more deeply engaged in the job. Movements require a lonely cycle for this model, which is similar to Model II. The price of X_i and Z_i for the pass that I need in the blocks is:

$$X_i = X_F + \sqrt{\left[R_i^2 - (Z_F - Z_E)^2\right]} \text{ and } Z_i = Z_E + \sqrt{\left[R_i^2 - (X_E - X_F)^2\right]} \tag{6}$$

where

$$R_i = R_o - i + \frac{R_o - R}{N} \text{ and } R_o = \sqrt{\left[(X_E - X_F)^2 + (Z_s - Z_E)\right]^2}$$

3 Experimental Work

In order to make any statistical inference concerning the distinct patterns, a sample size of "n" is required from each technique. To study the qualitative reaction resulting from the three patterns of circular machining, an assessment of variance can be of excellent assistance. Testing the surface roughness factor resulting from three distinct round machining patterns is a single three-level variance analysis. Five runs per machining model were used as a sample size. Aluminum compound material was used for the samples where Table 1 used two groups with three sets for each.

Table 1 Machining conditions for various machining patterns

	Group I			Group II		
Machining method	A	B	C	D	E	F
Machining model	I	II	III	I	II	III
Feed (mm/min)	100	100	100	100	200	100
Cutting speed (rpm)	900	900	900	1800	900	900
Max. depth of cut (mm)	1.35	1.35	1.35	1.35	1.35	2.8
Machining time (sec.)	82	148	102	82	82	82

Fig. 2 A round sample performed on the CNC machine

Machining assignments have been finished with the Emco Concept Turn 155, PC-controlled CNC-Lath. A 35 mm round, powerful bar was used to machine round radius $R = 17$ mm, as shown in Fig. 2. A program [14] was drawn up for each suggested machining sample using the Xi and Zi characteristics to meet this need.

The technique and the suggested cutting conditions for each proposed machining sample are shown in Table 1 for the two groups.

The machining time is determined and shown in Table 1. Each of the samples was machined under the predefined machining and machining circumstances. The surface roughness was taken using the square root of the arithmetic mean of the squares of the set of values (RMS). The RMS of the machined surface was estimated using the Mitutoyo Surftest 301 [15]. Four measurements were done in regions halfway along the circular surface and 90 degrees were divided. Test printouts for the three specific group-1 methodologies are shown in Fig. 3. The least significant difference (LSD) technique [16] was used to compare these measurements for important contrasts in their impacts. LSD is determined using the mean square error (0.0052) in Table 3. Such test for the LSD was determined to have a value of 0.1.

Therefore, any set of techniques for any machining instance has a flat comparison in techniques of more than 0.1 value, which would suggest that the comparison of pairs of mean populations is fundamentally unique. The difference in techniques for different sets is as follows:

Unmistakably, the main pair of implies that does not vary essentially is for machining design “A”, and “C”. At the interim, machining with example “B” demonstrates bigger critical contrasts with either design “A” or “C”. These demonstrate

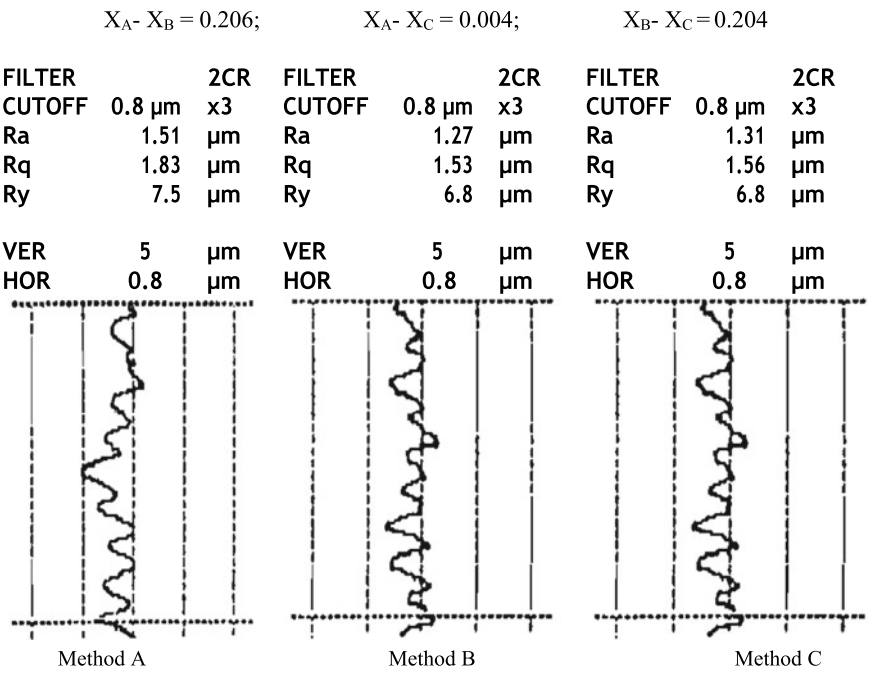

Fig. 3 Samples printouts of the surface roughness for the three methods "A", "B", and "C"

that both of machining designs "A", and "C" are factually proportional, and these watched varieties in the nature of the machined surfaces by these patterns are because of ordinary test errors as opposed with the impact of the utilized machining strategy itself. In addition, it is inferred that technique "B" gives a superior surface roughness contrasted with the other two machining technique "A", and "C".

Unmistakably, the primary pair of means that does not differ is mainly "A" and "C" for machining. In the interim, "B" machining shows greater critical contrasts with either "A" or "C" design. These show that both the machining design "A" and "C" are factually proportional, and these observed varieties, in the nature of the machined surfaces, are due to ordinary test errors, as opposed to the impact of the machining strategy itself. In fact, it is inferred that the "B" method provides a superior surface roughness compared to the other two "A" and "C" machining techniques.

In order to increase the additional requirements for the upgrade of these three suggested machining models, machining time may be used. Examination of the machining time is determined by the machining time circumstances for each machining model. It is very clear from Table 1 that the machining cycle using the "B" method is very much greater by almost 76 and 45% over the "A" and "C" patterns, respectively.

The above findings indicate that the predominant quality for surface roughness is achieved by the round machining of technique "B" which has a progressively drawn machining time. The author has tried to cope with this problem of either how to use

Table 2 Statistical results of surface roughness (RMS) for Group I

Method	A	B	C
Average (microns)	1.81	1.61	1.81
Variance (microns)2	0.00088	0.007	0.008

"B" design with a shorter machining time that is ideal with the machining time of "A" or "C". Dealing with this problem can give rise to the common quality of the machined surface in a shorter moment, which is the ideal reaction for any technique of machining when using CNC machines.

Another set of studies was suggested to enhance the machining method by using the round interpolation calculation of pattern "B" and the fresh features for cutting circumstances as shown in Group 2 of Table 1. These fresh features for cutting speeds, feeds, and cutting depth guarantee a basic machining time of 82 s. A summary of the verifiable outcomes for the preliminary information obtained to consider the impact of the modified cutting circumstances is shown in Table 2. Test printouts for the fresh balanced group 2 method are shown in Fig. 4.

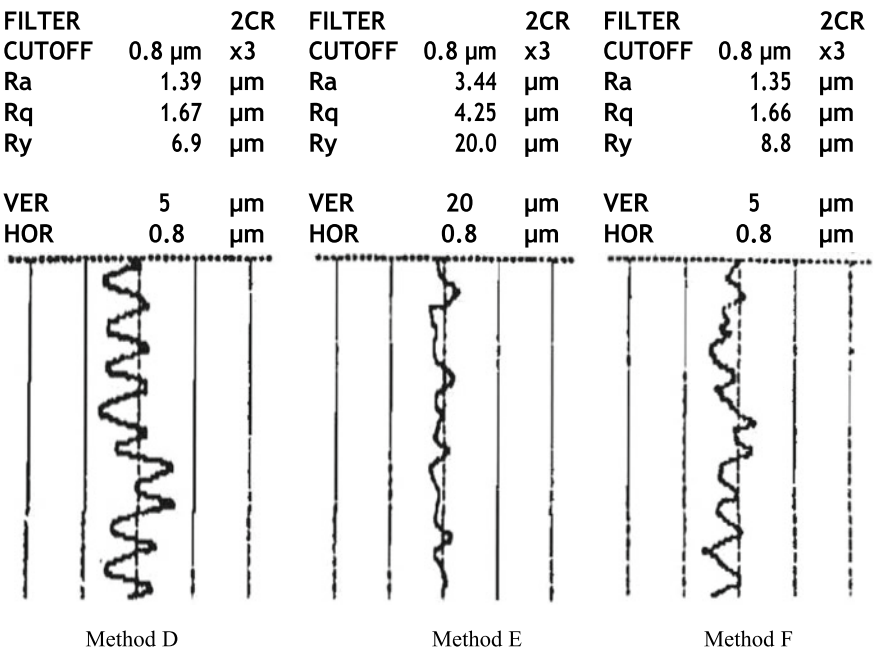

Fig. 4 Sample printouts of the surface roughness for the three methods "D", "E", and "F"

4 Results and Discussion

Table 2 shows measurable test outcomes A, B, and C of group I of Table 1 for surface roughness, showing that the circular interpolation algorithm can obviously improve the movement accuracy of a heavy-duty CNC floor-type instrument by reconstructing CNC programs. In this system, the circular algorithm for interpolation, reconstruction of the CNC program, simulation of the tool path, etc., can be carried out.

Comparing the average for each method, the "B" technique obviously provides the surface roughness of the machine a superior value than the other two techniques. Meanwhile, it appears that the "A" technique causes fewer disparities in output compared to the "B" and "C" methods. Before a powerful choice for machining design can be made by "B" method over "A" and "C" techniques, the assessment is advised. Table 3 shows the delayed implications of the assessment applied to the information collected from each machining technique. The findings of this inquiry show that the mean square between the techniques is numerous times greater than the mean square within the policy. This almost definitely shows that the means of the multiple methods have not been raised.

From the view of Table 4, the mean of the three methods is unique and has a critical impact in the delivery of different surface roughness features due to the use of distinctive circular insertion machining models for the CNC machine. This is a factual assumption regarding the mean and difference of "A", "B", and "C" machining patterns. In comparison to each other, sets of machining models such as "A-B," "A-C," and "B-C" are used. Return to Table 2, Measurements for the comparison of mean and variance for Group II methods "D", "E", and "F" and Group 1 methods "B" may suppose that sample "B" forces the largest value for machined surface roughness with the shortest machining time compared to separate samples from separate techniques.

Table 3 Investigation of the surface roughness from three machining techniques

Source of variation	Sum of squares	Degree of freedom	Mean square
Between method	0.141	2	0.0705
Within method	0.063	12	0.0052

Table 4 Group II results for surface roughness

Method	D	E	F
Average (microns)	1.83	3.7	1.67
Variance (microns)2	0.03	0.158	0.0005

5 Conclusions

The technology is used by a CNC turner and is based on various models of circular passes. The algorithm described uses a CNC interpolator in real time, in order to provide the highest precision possible for the rotating machine. The entire working process can be programmed as a sidelong cycle cutting depth that increases the generation capacity of the current fixed cycles G02/G03 CNC rotation. Three lineal algorithms of interpolation, liner passes, direct and circular passes, and lingering of different cutting depths were proposed and applied in the machination of hemispheric geometry by CNC machines.

Pattern "II" was discovered to give a superior surface roughness to the machined surface. This conclusion relied on the measurable derivation of the analysis examination and the right selection of the LSD method was made. In addition, upgrade the machining operation as stated by the moment of machining. Pattern II was redesigned with the aim of streamlining its machining time, yielding cutting speed, feed rate, and cutting depth. It was inferred that pattern II with increased depth of cutting forces was of the highest quality for machined surface roughness with base machining time. The calculation of this model is specified as necessary as an optimal round addition calculation that is appropriate for CNC turning points.

Nomenclature

XE, ZE	X- and Z-coordinates of arc end point
XF, ZF	X- and Z-coordinates of arc start point
dZ	Allowance for final finish pass
Fa	Accelerated feed rate
N	Number of passes
R	Arc radius
θ	Arc angle
Zs	ZF + approach (dz)
F_c	Cutting feed rate.

References

1. Kappmeyer G, Hubig C, Hardy M, Witty M, Busch M (2005) Modern machining of advanced aerospace alloys—enabler for quality and performance. Proc CIRP 1:28–43
2. Newman ST, Allen RD, Rosso Jr RSU (2010) CAD/CAM solutions for STEP-compliant CNC manufacture. Int J Comput Integrated Manuf 16:590–597
3. Cui G, Lu Y, Li J, Gao D, Yao Y (2012) Geometric error compensation software system for CNC machine tools based on NC program reconstructing. Int J Adv Manuf Technol 63(1–4):169–180

4. Zietarski S (2001) System integrated product design, CNC programming and post processing for three-axis lathes. J Mater Process Technol 109(3):294–299
5. Zhang DL, Chen XS, Du R (2013) A CNC program module based on polar coordinate system. Int J Adv Manuf Technol 68(5–8):1767–1773
6. Chao-Ton Su, Chen M-C (1999) Computer-aided optimization of multi-pass turning operations for continuous forms on CNC lathes. IIE Trans 31(7):583–596
7. Ramesh R, Mannan MA, Poo AN (2005) Tracking and contour error control in CNC servo systems. Int J Mach Tools Manuf 45(3):301–326
8. Li X, Liu W, Pan Y, Ma J, Wang F (2019) Binocular vision-based 3D method for detecting high dynamic and wide-range contouring error of CNC machine tools. Meas Sci Technol
9. Edem IF, Balogun VA, Nkanang BD, Mativenga PT (2019) Software analyses of optimum toolpath strategies from computer numerical control (CNC) codes. Int J Adv Manuf Technol 1–11
10. Dhanda M, Pande SS (2019) Adaptive tool path planning strategy for freeform surface machining using point cloud. Comput Aided Des Appl 16(2):289–307
11. Ganesan H, Mohankumar G, Ganesan K, Ramesh Kumar K (2011) Optimization of machining parameters in turning process using genetic algorithm and particle swarm optimization with experimental verification. Int J Eng Sci Technol (IJEST) 3(2)
12. Omirou SL, Rossides S, Lontos A (2012) A new CNC turning canned cycle for revolved parts with free-form profile. Int J Adv Manuf Technol 60(1–4):201–209
13. Hambali A, Sapuan SM, Ismail N, Nukman Y, Abdul Karim MS (2009) The important role of concurrent engineering in product development process. Pertanika J Sci Technol 17(1):9–20
14. EMCO WinNC SINUMERIK 810D/840D turning, software description/software version from 15.46, Ref. No. EN 1815 Edition E2003–5
15. Mitutoyo Surftest 301 Surface Roughness, User's Manual
16. Montgomery DC (2017) Design and analysis of experiments, 9th edn. Wiley

Classification of Motorcycles and Prediction of Indian Motorcyclist's Posture at the Conceptual Design Stage

Arunachalam Muthiah and Sougata Karmakar

Abstract It is challenging for a designer/engineer to presume the adopted posture of a rider on a motorcycle during the 2D sketching at the conceptual phase of the design. Current techniques followed for predicting rider's posture include superimposing 2D manikin on the sketch of the motorcycle. To facilitate the designer/engineer, apart from demonstrating a method for classifying motorcycles, the current research proposes 'rider triangle' (connecting three points located at the handlebar, seat, and footrest) based alternative posture determination technique for a standard motorcycle without the direct involvement of 2D manikin. The proposed method deploys regression models to predict absolute angles of six body joints, namely trunk, thigh, leg, foot, arm, and forearm. The regression models were validated with negligible (below 10%) errors compared with the posture of real human rider from 2D image analyses. Although there are various limitations of this technique, it is capable of giving rough estimates of aforesaid six body joint angles for the rider of average body dimensions.

Keywords Two-wheeler · Motorbike · Ergonomics · Posture · Biomechanics · Comfort

1 Introduction

A motorcycle is a standard mode of transportation in India. The Indian motorcycle industry is reporting a phenomenal growth over the past few years. Studies by Indices Analytics (2015) showed a double-digit growth rate with the sale of 10 million motorcycles during 2009–2010. Their prediction showed a trend towards the demand of a more powerful motorcycle with 72% in the 125 cc category, 27% in 125–250 cc category, and 1% in the premium segment. The motorcycle usage includes daily

A. Muthiah (✉) · S. Karmakar
Department of Design, Indian Institute of Technology (IIT) Guwahati, Guwahati, Assam 781039, India
e-mail: arunmuthiah8@gmail.com

S. Karmakar
e-mail: karmakar.sougata@gmail.com

L. M. Das et al. (eds.), *Emerging Trends in Mechanical Engineering*, Lecture Notes in Mechanical Engineering, https://doi.org/10.1007/978-981-15-8304-9_10

commuting on the long way for office going and other works that involve speed and have time constraints like fast food delivery, speed post, and police patrols [1].

The classification of motorcycles based on 'put to use' and 'intent to design' includes cruiser, scooters, sports/racer, and standard motorcycles. Generally, the classifications are based on motorcyclist's posture, engine capacity, context of use, and style. These classifications or nomenclature of the motorcycles are not standardized across the world [2]. Moreover, there are many approaches to classify motorcycles. Hale [2] reported the commonality and differences among different types of motorcycles. However, the Society of Automotive Engineers [3] provides a classification method with symbols. These recommended practices offer uniform definitions for the classification of motorcycles. There are three major classifications: (1) on-road (designed to ride on a paved surface or public road), (2) off-road (not intended to ride on the concrete surface or open road), and (3) competition motorcycle (designed for competitive events). These classification techniques are based on few criteria which include (1) steering means (handlebar-H, wheel-W, other-O), (2) operator seat configuration (straddle seat-S, bench or bucket seat-B), (3) engine capacity (less than 50—A, 50 to 169.9—B, 170 to 279.9—C, above 280—D, electric—E), (4) maximum speed (less than 50 km/h–L, 50 km/h, and higher—H). For example, an on-road motorcycle with two wheels, handlebar mean of steering, designed for two riders, 125 cc engine capacity, and speed more than 50 km/h, is classified as R1HS2BH. This symbolic representation-based classification method does not provide any particular name or term. Thus, it is not suitable or easily understandable for the common man. To avoid, the name evolved like cruisers, sport, touring, standard, street, naked motorcycles, etc.

In the USA, the motorcycles are grouped based on intended use, riding posture, engine capacity, comfort, and price [4]. Thus, 12 groups, namely cruiser, standard, touring, sport-touring, sport, unclad sport, supersport, chopper, dual-purpose, scooter, all-terrain vehicle, and off-road, are found. In these groups, many of them are found to be with minimal differences [5]. In the UK, the motorcycles are grouped like naked road motorcycle, faired road motorcycle, super sports, tourer, sport-tourer, endure (large and small), and cruiser, based on intended uses riding posture, aesthetical style, and aerodynamic architecture.

Among various techniques, the rider's posture-based classification method is vital in terms of ergonomics of a motorcycle [6]. According to this technique, motorcycles are categorized as RIPOC Type 1: forward lean riding posture, RIPOC Type 2: upright riding posture, RIPOC Type 3: seat back leg forward riding posture, and RIPOC Type 4: double forward riding posture. Lai et al. [7] followed a similar technique for classification of the motorcycle, but the terms used as a cruiser (lean backward with feet forward), sport (forward leaning), and touring. Generally, motorcycles popularly used in India are classified based on design styles and appearance [8]. Many customers are also attracted by the aesthetic look and brand name [9], aerodynamics [10], and engine capacity. The global trend of possessing a motorcycle for style and purpose [11] is also making the customer's mindset.

2 Rationale for the Research

During the conceptualization of motorcycle design, engine capacity and exterior styling get priority, but due importance is not given to various human factor issues like body joint angles and postural comfort/discomfort. This leads to early fatigue [1], joint pain, and sores of the riders. Studies have shown that higher risks are involved in motorcycle riding [12–15] than four-wheeler. Motorcycle has the highest number of road accidents among road users [13]. It is a fact that death due to a motorcycle accident happens once in every hour in India [16].

The specific reasons for road accidents are difficult to identify. However, few primary reasons mentioned by researchers [14, 17, 18] include motorcycling fatigue, lack of training, drunk riding, etc. Motorcycling fatigues are caused due to vibration, bad road condition, poor riding posture, etc. [15]. The adopted riding posture is dependent on the dimension and spatial arrangement of motorcycle components, human anthropometry [2], etc. Body joint angles or the riding postures adopted during riding has to be comfortable to ensure full concentration and presence of mind on the road since motorcycle riding involves firm control and steady traveling [1]. The posture of the motorcyclists has been studied by a few researchers [19–21] using RULA, QEC, WERA, etc. The aforesaid postural evaluations are generally conducted with mock-ups/prototypes. Thus, these are not for the proactive ergonomics evaluation tool for posture evaluation during conceptualization. Although digital human modeling (DHM) based virtual simulation allows posture prediction and posture evaluation in the early developmental stage of the design process, it would be only applicable when the CAD model of the motorcycle is developed.

Hence, it is challenging to assess the posture of the riders on the intended motorcycle design during 2D sketching at the conceptualization stage. Current practice for predicting posture includes superimposing 2D manikin on the sketch of the motorcycle. To facilitate the motorcycle designer/engineer, the current researchers have set the following two objectives.

(a) Proposing ‘rider triangle’ (connecting three points located at the handlebar, seat, and pedal) based motorcycle classification method.
(b) Proposing ‘rider triangle’ based alternative posture determination technique for a standard motorcycle without the direct involvement of 2D manikin.

3 Methodology

The methodology followed to fulfill the aforesaid objectives can be described in two parts: (1) method for classification of motorcycles under study and (2) prediction of motorcyclist’s posture and validation of the prediction.

3.1 *'Rider Triangle' Based Classification of Motorcycles Following Photographic Survey*

- In a photographic study, motorcycle photographs were randomly collected from some popular brands (Bajaj, TVS, Royal Enfield, and Hero), which are available in the Indian market [11]. A total of 31 photographs (right-side-view images) of motorcycles including images of five-Royal Enfield, eight-TVS, nine-Hero, and nine-Bajaj models were collected from the company Web sites of the manufactures. All the collected photographs were visually calibrated to make sure of the availability of perfect side view.
- Following identification of three points of rider-motorcycle interfaces, namely (a) handlebar point, (b) footrest point, and (c) seat index point from the photographs, the interface points for each of the motorcycles were connected to develop so-called rider triangle [22]. The orientation angles of this triangle around the vertical axis (y-axis) drawn through seat index point (SIP) (as shown in Fig. 1) were used to categorize motorcycles in various groups, e.g., cruise, sports, and standard motorcycles and scooters. The two-orientation angles used for this purpose are θ_{SF} (Theta seat-footrest connecting line) and θ_{SH} (Theta seat-handlebar connecting line) (as shown in Fig. 2).

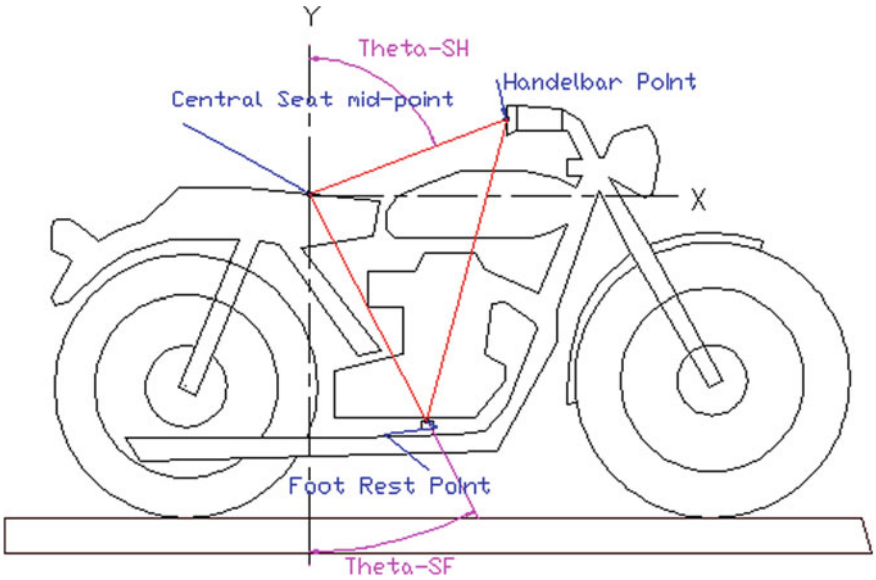

Fig. 1 'Rider triangle' drawn on a typical motorcycle

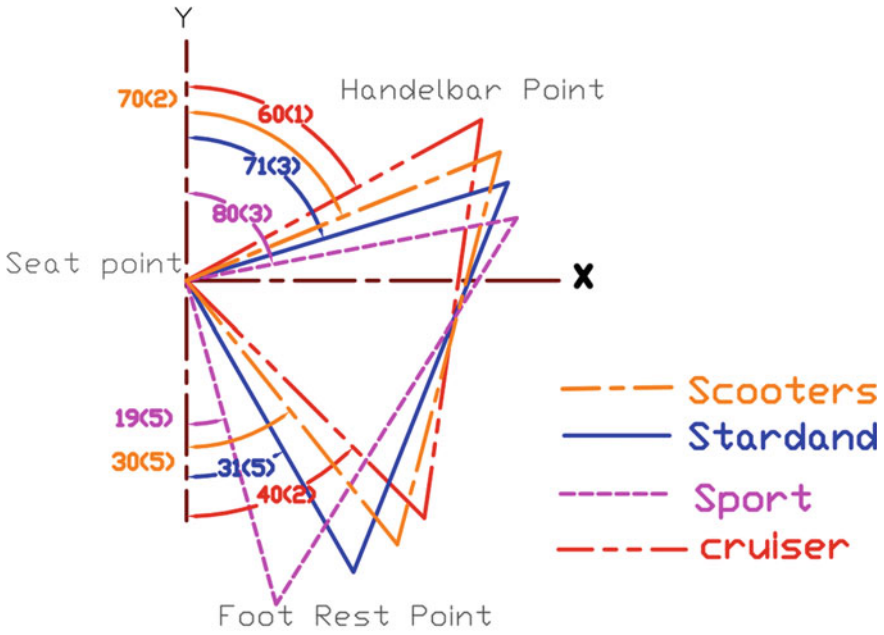

Fig. 2 Orientation angles of 'rider triangle' around a vertical axis for different types of motorcycles

3.2 Developing Regression Equations for the Prediction of Motorcyclist's Posture and Validation of the Predicted Position

- To delimit the current study, out of different types of motorcycles, posture prediction equations were proposed only for standard motorcycles, as these are the most widely used/sold all over the world, particularly in India [23].
- The posture prediction of the riders on standard motorcycles was initiated through the posture study using online software (available from https://cycle-ergo.com) [24], which required photographs of standard motorcycles and side-view image of 2D manikin rider. Different seating positions of the manikins on the seat (center, back, and forward) of the motorcycle images were defined using the aforesaid online software. It also enabled to change the stature of the manikin as per the requirement to define the variation of different percentile values of the stature (e.g., 5th, 50th, and 95th percentiles).
- Among the 31 motorcycles under study, only 14 standard motorcycles with rider positioned at the center of the seat were used for posture evaluation with the help of the previously mentioned software. During this process, the stature of the rider manikin was changed according to the 5th percentiles (5th p), 50th percentiles (50th p), and 95th percentiles (95th p), values as per Indian anthropometric database [25]. Next, the image of each standard motorcycle interfaced with

the 2D manikin of the rider was snipped from the software and saved as image files.

- The saved images were visually calibrated (using AutoCAD) to have a perfect side-view photograph for the measurement of six segmental angles (absolute). The six segments are the trunk, forearm, arm, thigh, leg, and foot. Few segmental aspects, e.g., neck and wrist, were not considered in the current study.
- The measured six segmental angles were tabulated, and mean values were calculated in MS Excel. The mean segmental angles of all percentiles manikins are plotted as the radial graph, as shown in Fig. 3.
- The raw measurements of segmental angle for manikin of different percentiles, $\theta_{SF,}$ and θ_{SH} data were brought to SPSS software for normality test and followed by correlation study and regression modeling. The best regression model was

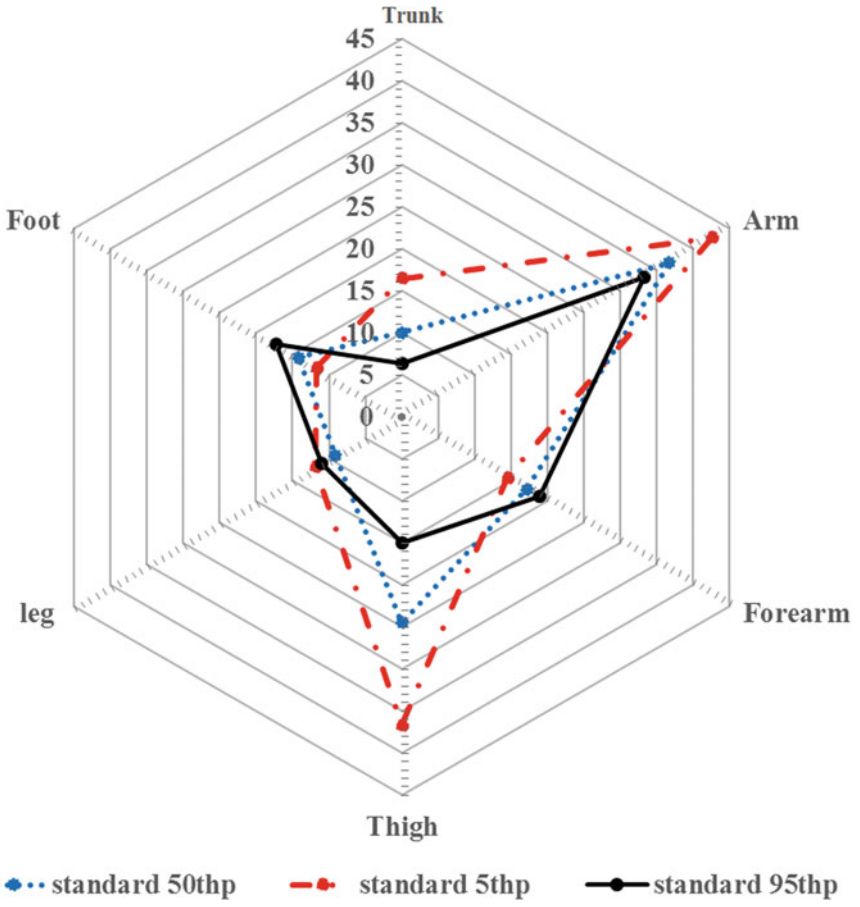

Fig. 3 Segmental angles 2D mankins (with 5th p, 50th p, 95th p stature) positioned on a standard motorcycle

selected based on residual value, level of significance 0.05, and correlation (r) greater than 0.5.

- The selected regression equations for calculating segmental angles were verified with the measured angles from the collected samples of the photograph of real standard motorcycles with real riders (50th p stature). The within-sample verifications were made by providing θ_{SF} and θ_{SH} in the regression equation and measuring the values of segmental absolute angles.

4 Results and Discussion

4.1 Classification Method of Motorcycles

The 31 motorcycles under the current study were categorized as 6 scooters, 3 cruiser motorcycles, 14 standard motorcycles, and 8 sports motorcycles based on the value of orientation angles (θ_{SF} and θ_{SH}) of the 'rider triangle.' The mean and standard deviation (SD) values of θ_{SF} and θ_{SH} for all these motorcycles are presented in Table 1. This classification is corroborating with the widely used nomenclature across different parts of the globe (Europe, Asia, and North America). These terms are also matching with manufacturer's selling tags. 'Bajaj Avenger 220 cruiser' has been grouped under the category of cruiser motorcycles (θ_{SF} and θ_{SH} angle of 40 $\pm$ 2° and 60 $\pm$ 1°, respectively). Sabbah and Bubb [22] proposed a triangle-based motorcycle classification system, but their classification method does not deal with the orientation angles of the triangle, and it is qualitative in nature. They used the terms endure, sports motorcycles and naked motorcycles for classification.

The classification technique described in the present research is based on the limited number of motorcycle samples. Thus, the values of the θ_{SF} and θ_{SH} might be changed slightly if the sample size is different.

4.2 Posture Prediction for the Rider on Standard Motorcycle

The measured mean values of various segmental angles (Table 2) of 5th p, 50th p, and 95th p 2D manikins on all the standard motorcycles under study were plotted as the radial diagram for comparative visual representation (Fig. 3). The radial diagram showed that thigh angles for different percentile manikins varied by an angle of 10°. Similarly, an angle difference at trunk or torso was also found relatively high. The difference among the arm angles of three different percentile manikins was relatively less (about 5°) in comparison with thigh and trunk angles. However, the mean differences at the foot, leg, and forearm angles among manikins of three different percentile manikins were not much. Sabbah and Bubb [22] also observed a similar variation/differences in segmental joint angles [26]. Dutta et al. [26] conducted a

Table 1 Triangle orientation angle for all kind of motorcycles and average/SD for the same

Classified	Company	Model	θ_{SF}	θ_{SH}	Average ± SD	
					θ_{SF}	θ_{SH}
Cruiser motorcycles	Bajaj	Avenger 220	41	60	40 ± 2	60 ± 1
	Royal Enfield	Thunderbird 350	40	61		
	Royal Enfield	Thunderbird 500	38	60		
Scooter	Hero	Duro DZ	33	67	34 ± 3	70 ± 2
	Hero	Maestro	38	68		
	TVS	Neo XR	35	71		
	TVS	Rockz 125	32	70		
	TVS	Scooty pep	35	70		
	TVS	Tormax 150	28	72		
Standard motorcycles	Bajaj	Discover 125	27	66	30 ± 5	71 ± 4
	Bajaj	Pulsar 135 LS	33	74		
	Bajaj	Pulsar 150	30	75		
	Bajaj	Pulsar 180 classic	28	69		
	Bajaj	Pulsar 180 DTS-i	24	74		
	Hero	CBZ Extreme	27	74		
	Hero	Glamor	35	67		
	Hero	Hunk	25	76		
	Hero	Ignitor	27	76		
	Hero	Impulse	28	70		
	Hero	Splendor Pro	31	70		
	TVS	Star city	32	68		
	Royal Enfield	Bullet classic 500	42	70		
	Royal Enfield	Classic 350	39	65		
Sport/racing motorcycles	Bajaj	Pulsar 220	16	75	19 ± 5	80 ± 3
	Bajaj	Pulsar 220 DTS-i	15	77		
	Bajaj	Pulsar 350 NS	10	86		
	Hero	Karizma ZMR	23	77		
	TVS	Apache RTR-160	22	80		
	TVS	Apache RTR-160	25	80		
	TVS	Apache RTR-180	25	80		
	Royal Enfield	Continental GT	17	81		

Table 2 Mean and SD values of various segmental angles

Stature percentiles	Trunk	Arm	Forearm	Thigh	Leg	Foot
	Mean (SD)	Mean (SD)	Mean (SD)	Mean (SD)	Mean (SD)	Mean (SD)
5th p	17 (7)	43 (4)	15 (3)	37 (7)	12 (8)	12 (7)
50th p	10 (6)	37 (5)	17 (4)	24 (5)	9 (8)	14 (10)
95th p	6 (5)	33 (5)	19 (4)	15 (5)	11 (8)	17 (12)

study involving 30 volunteers and three different motorcycles (pulsar, discover, and glamor). In their research, the shoulder angle was measured but not the trunk angle. Sabbah and Bubb [22] measured motorcycling posture for five different posture adjustments using a 3D posture measure instrument (PCMAN) from 39 participants seated on three different motorcycles (endure, sports motorcycles and naked motorcycles or standard motorcycles). The 39 samples were the representative of three different percentile riders, namely 50th p male and 95th p male and 50th p female. It was reported that 50th p female had a higher variation of joint angles during riding compared to 50th p and 95th p male. Specifically, on sports motorcycles, the variation of the trunk and arm angles of shorter personnel was relatively high. A similar result was obtained in the current study for the rider of 5th p stature on standard motorcycles. Moreover, the variations for the different segmental angles were also high while compared among the riders of different percentile values of stature.

Correlation study and regression models. Normality test was carried out for the values of θ_{SF} and θ_{SH} for different standard motorcycles. A Shapiro-Wilk test ($p > 0.05$) [27] and a visual inspection of the histograms and normal Q-Q plots showed that the data were almost normally distributed for both θ_{SF} and θ_{SH}. A skewness of 1.09 (SE = 0.524) and kurtosis of 0.724 (SE = 1.014) were observed for the θ_{SF} while a skewness of 0.448 (SE = 0.52) and a kurtosis of −0.906 (SE = 1.014) were for the θ_{SH}.

The Pearson correlation test was performed for the manikin of all percentiles to identify the correlation strength between joint angles and θ_{SF}/θ_{SH} for each of the 14 standard motorcycles under study. The results of correlation statistics are shown in Tables 3 and 4. The segmental joint angles with orientation angle (θ_{SF} or θ_{SH}) were found highly correlated in the case of the 2D manikin of 50th p stature compared to the manikins of other percentile stature (50th p and 95th p). The correlation coefficient vales were also found significant at $p < 0.05$ level for 50th p manikin.

Among various regression models (linear, logarithmic, inverse, quadratic, and exponential), best-suited models were selected based on three major parameters such as r (correlation coefficient), r^2, residual, and significance level. The best-identified models (either exponential or linear model) for the angular prediction of an individual segment are shown in Table 5.

The predicted/estimated values of joint angles were compared with joint angles measured from the 2D manikin of 50th p stature positioned of 14 different standard motorcycles images using the one-paired t-test. Before conducting the analysis, the assumption of the normal distribution of differences of scores was examined and

Table 3 Correlation of θ_{SH} correlation with body joint angles

Rider's stature	Correlation and significant level	Trunk	Arm	Forearm	Thigh	Leg	Foot
5thpercentiles	Correlation level	0.452	−0.689	0.738	0.029	−0.405	0.399
	of significance	0.105	0.006*	0.003*	0.923	0.151	0.158
50th percentiles	Correlation level	0.532	−0.550	0.670	0.334	0.602	0.839
	of significance	0.050*	0.042*	0.009*	0.243	0.023*	0.000*
95th percentiles	Correlation level	0.631	−0.452	0.703	0.250	0.853	0.857
	of significance	0.016*	0.105	0.005*	0.388	0.000*	0.000*

*Correlation is significant at the 0.05 level (2-tailed)

Table 4 Correlation of θ_{SF} with body joint angles

Rider's stature	Correlation and significant level	Trunk	Arm	Forearm	Thigh	Leg	Foot
5th percentiles	Correlation and significant level	−0.153	0.709	−0.565	−0.443	0.258	−0.210
		0.602	0.004*	0.035*	0.113	0.373	0.470
50th percentiles	Correlation and significant level	−0.229	0.342	−0.771	−0.575	−0.224	−0.601
		0.431	0. 0.231	0.001*	0.032*	0.442	0.023*
95th percentiles	Correlation and significant level	−0.319	0.512	−0.546	−0.661	−0.641	−0.743
		0.266	0.061	0.043*	0.010*	0.014*	0.002*

*Correlation is significant at the 0.05 level (2-tailed)

Table 5 Regression equations for prediction of rider's body joint angles

Model	Regression equation	r	r^2	Residual error	Sig
Linear	$\Theta_{trunk} = 0.865\ \theta_{SH} - 51.991$	0.532	0.283	389.503	0.050*
Linear	$\Theta_{Arm} = -0.761\ \theta_{SH} + 91.347$	0.550	0.302	273.780	0.042*
Exponential	$\Theta_{forearm} = 50.753\ e^{-0.036\theta SF}$	0.792	0.627	0.277	0.001*
Exponential	$\Theta_{thigh} = 49.517\ e^{-0.024\theta SF}$	0.618	0.381	0.325	0.019*
Linear	$\Theta_{leg} = 1.248\ \theta_{SH} - 80.325$	0.602	0.365	560.874	0.023*
Linear	$\Theta_{Foot} = 2.263\ \theta_{SH} - 148.139$	0.839	0.704	440.698	0.000*

* Significant at the $p < 0.01$ level (2-tailed)

found satisfactory as the estimated skewness, and kurtosis level was less than the maximum allowable values for a t-test (i.e., skew < |2.0| and kurtosis < |9.0|; posten 1984). Significant ($p < 0.05$) correlations between the predicted joint angles and measured joint angles were also observed (Table 4).

The measured trunk angles ($M = 10.07$, SD = 6.46) and estimated trunk angles ($M = 10.04$, SD = 3.43) were almost equal. A dependent sample t-test was performed. The skewness and kurtosis level of the estimated trunk angle were noticed as −0.304 (SD = 0.597) and −1.342 (SD = 1.154), respectively. The difference between estimated and measured trunk angles was not statistically significant, $t(0.02) = 13$, $p > 0.05$.

The measured arm angles ($M = 36.79$, SD = 5.494) and estimated arm angles ($M = 36.77$, SD = 3.02) were almost equal. The skewness and kurtosis level of the estimated arm angle were obtained at 0.304(SD = 0.597) and −1.342 (SD = 1.154), respectively. Following a dependent sample *t*-test, it was observed that there was no significant difference between the mean values of estimated and measured arm angles, $t(0.011) = 13$, $p > 0.05$.

The skew and kurtosis level of estimated forearm angles were obtained as −0.647 (SD = 0.597) and −0.236 (SD = 1.154), respectively. Following a dependent sample *t*-test, it was found that the difference between the mean values of measured forearm angles ($M = 17.21$, SD = 3.64) and estimated forearm angles ($M = 17.14$, SD = 2.98) was insignificant, $t(0.101) = 13$, $p > 0.05$.

The skewness and kurtosis level of estimated thigh angles were obtained as 0.759(SD = 0.597) and −0.052 (SD = 1.154), respectively. Following a dependent sample *t*-test, it was found that the difference between the mean values of measured thigh angles ($M = 24.43$, SD = 5.25) and estimated thigh angles ($M = 23.94$, SD = 2.85) was insignificant, $t(0.423) = 13$, $p > 0.05$.

The skewness and kurtosis level of the estimated leg angle were obtained at −0.304 (SD = 0.597) and −1.342 (SD = 1.154), respectively. The measured leg angles ($M = 9.14$, SD = 8.22) and estimated leg angles ($M = 14.14$, SD = 4.95) were almost equal. Following a dependent sample *t*-test, it was observed that the mean values of the estimated leg angles were not significantly different from the measured leg angle, $t\ (-0.18) = 13$, $p > 0.05$.

The measured foot angles ($M = 14.14$, SD = 10.70) and estimated foot angles ($M = 14.15$, SD = 8.98) were almost same. The skewness and kurtosis level of estimated foot angles were obtained as −0.304 (SD = 0.597) and −1.342 (SD = 1.154), respectively. Following a dependent sample *t*-test, it was found that the difference between the mean values of measured foot angles and estimated foot angle was insignificant, $t\ (-0.005) = 13$, $p > 0.05$.

For the final validation of the predicted joint angles of the riders, an experiment was conducted to measure the joint angle values of the real riders on a standard motorcycle during riding and to compare the same with the estimated values. The real participant (with 50th p stature) was instructed to seat on four different standard motorcycles. The photographs were taken for the measurement of joint angles. The measured angles (real human joint angles) from the photographs were compared with estimated joint angles using a non-parametric statistical test. No significant

difference was observed among the joint angles obtained from different techniques (predicted from the regression equation, measured from 2D manikin in riding posture and measured from the photographs of the real rider). Wilcoxon signed-rank test of independence with $p < 0.05$ was used as a criterion for the analysis of significance.

5 Conclusion

The methodology for classification for motorcycles based on the orientation angle of 'rider triangle' has been proposed in the present research, and it has also been compared with the other classification techniques reported by earlier researchers. The proposed methodology is quantitative in nature as it relies on the values of two-orientation angles (θ_{SF} and θ_{SH}), rather than qualitative aspects like design style or rider's posture, engine capacity, the context of use, etc. The regression equations have been developed to predict the average rider's posture (indicated by six body joint angles) at the conceptual stage of motorcycle design. These equations need only the orientation angles (θ_{SF} and θ_{SH}) of the 'rider triangle' as the input. Although there are various limitations of this technique, still it is capable of giving rough estimates of aforesaid six joint angles of the rider of average stature. Thus, it is expected that the automotive designers/engineers can assess the rider's posture just after their 2D sketching of the bike and establishing the 'rider triangle.' The estimated segmental angles from regression equations could further be analyzed for postural comfort using posture evaluation tools or based on the comfort joint angle database for motorcycle riding. This alternative technique for determining the rider's posture during conceptual sketching of the motorcycle would be helpful for the designer/engineers to consider ergonomics proactively in the design process.

References

1. Jamson S, Chorlton K (2009) The changing nature of motorcycling: the patterns of use and rider characteristics. Transp Res Part F 12:335–346
2. Hale A, Pelowski D, Bhise V (2007) Commonality and differences between cruiser, sport, and touring motorcycles: an ergonomics study (No. 2007-01-0438). SAE Technical Paper
3. J213_201409 (2014) Motorcycle classifications. SAE International, United States
4. Teoh ER, Campbell M (2010) Role of motorcycle type in fatal motorcycle crashes. J Saf Res 41(6):507–512
5. Siefert A, Pankoke S, Wölfel HP (2008) Virtual optimisation of car passenger seats: simulation of static and dynamic effects on drivers' seating comfort. Int J Ind Ergon 38(5–6):410–424
6. Ma'arof MIN, Ahmad IN, Abdullah NR, Karim SA (2012) Motorcycling riding issues: understanding the phenomenon and development of ergonomics intervention in improving perceived comfort for prolonged riding. In: International conference on design and concurrent engineering, pp 15–16
7. Lai H-C, Liu J-S, Lee DT, Wang L-S (2003) Design parameters study on the stability and perception of riding comfort of the electrical motorcycles under rider leaning. Mechatronics 13(1):49–76

8. Jeyakumar T, Gandhinathan R (2014) Industrial design of motorcycle with reference to Indian population. In: Applied mechanics and materials, vol 592, pp 2659–2664. Trans Tech Publications
9. Kreuzbaur R, Maiter A (2005) Embodied cognition and new product design: changing product form to influence brand categorization. J Prod Innov Manag 22:165–176
10. Hanna RK (2012) CFD in sport-a retrospective; 1992–2012. Procedia Eng 34:622–627
11. Iyer NV, Badami MG (2007) Two-wheeled motor vehicle technology in India: evolution, prospects, and issues. Energy Policy 35(8):4319–4331
12. Mondal P, Dalela S, Balasubramanian N, Sharma GK, Singh R (2008) Critical analysis of road crashes and a case study of wet road conditions and road crashes in an Indian metropolitan city. SAE paper no. 2008-28-0078
13. Robertson SA, Minter A (1996) A study of some anthropometric characteristics of motorcycle riders. Appl Ergon 27:223–229
14. Karuppiah K, Salit MS, Ismail MY, Ismail N, Tamrin SBM (2012) Evaluation of motorcyclist's discomfort during prolonged riding process with and without lumbar support. Anais Acad Bras Cien 84(4):1169–1188
15. Velagapudi SP, Ray GG (2015) A study on motorcycle usage and comfort in urban India. In: Proceedings 19th triennial congress of the IEA, Melbourne, pp 9–14
16. Government of India (2014) Ministry of Home Affairs, N.C.R.B., Accidental Deaths and Suicides in India, vol 48, pp 1–289. Available at https://ncrb.gov.in.
17. Haworth N, Rowden P (2006) Fatigue in motorcycle crashes. Is there an issue? In: Proceedings Australasian road safety research, policing and education conference, Gold Coast, Queensland, Australia
18. Hurt H, Ouellet J, Thom D (1981) Motorcycle accident cause factors and identification of countermeasures, vol 1. Technical Report. DOT HS-5-01160. NHTSA, U.S. Department of Transportation
19. Ramasamy S, Adalarasu K, Patel TN (2017) Evaluation of driving-related musculoskeletal disorders in motorcycles riders using Quick Exposure Check (QEC). Biomed Res 28(5), pp 1962–1968
20. Stedmon AW (2007) Rula for motorcycles. In: Annual conference of the ergonomics society on contemporary ergonomics 2007, pp 4–6
21. Abd Rahman MN, Abdul Rani MR, Rohani JM (2011) WERA: an observational tool develop to investigate the physical risk factor associated with WMSDs. J Hum Ergol 40(1–2):19–36
22. Sabbah AO, Bubb H (2008) Development of a motorcycle posture model for DHM systems (No. 2008-01-1866). SAE Tech. https://doi.org/10.4271/2008-01-1866
23. Simindia (2019) Society of Indian Automobile Manufacturers, India [Online]. Available from https://www.siamindia.com/statistics.aspx?mpgid=8&pgidtrail=14. Accessed 23 Sept 2019
24. Motorcycle-ergo (2014) Ergo-motorcycles website [Online]. Available: https://cycle-ergo.com. Accessed 26 Feb 2016
25. Chakrabarti D (1997) Indian anthropometric dimensions for ergonomic design practice. National Institute of Design
26. Dutta K, Basu B, Sen D (2014) Identification and quantification of stressors affecting motorized two wheeler riders: an ergonomic attempt. Int J Res 2(1):13–25
27. Shapiro SS, Wilk MB (1965) An analysis of variance test for normality (Complete samples). Biometrika 52(3/4):591–611. https://doi.org/10.2307/2333709

Thermal Engineering

Performance Enhancement of Evaporative Cooling Device Using Silica Gel as an Adsorbent Material

Jasbir Singh, Neeraj Mehla, and Abhit Kumar Sharma

Abstract In this paper, the performance of the evaporative cooler was analysed when coupled with the silica gel. A bed of silica gel is fabricated and attached with the three sides of the evaporative cooler. The performance of system was tested at different flow rates with and without the use of silica gel. Therefore, it was observed that the performance of the system was reliable with the use of silica gel. However, the system is not run continuously because the silica gel gets saturated after 15–20 min. After saturation, there is a need of replacement of the silica bed with regenerated silica gel, which makes it complicated. Hence, in future the silica bed should be replaced by the desiccant bed for continuous operation of the system.

Keywords Direct water-evaporative cooling · Adsorbent material (silica gel) · Experimental analysis

1 Introduction

Evaporative coolers are utilized to remove the waste heat to the surroundings. However, the major drawback of the conventional evaporative cooler is that it is operated in hot and dry season. Hence, to overcome this drawback, in the present manuscript, the conventional evaporative cooler has been coupled with the adsorbent material (silica gel) and then the performance was analysed. Waugaman et al. [10] reviewed the different desiccant-based cooling cycles. As they reported that, the desiccant-based cooling systems have an ability to be operated on low-grade energy. Daou et al. [1] reviewed the operations of desiccant cooling systems. They studied the solid as well as liquid desiccants and reported that the solid desiccants are less corrosive and easy to handle. They also reviewed the performance of the

J. Singh · A. K. Sharma
Department of Mechanical Engineering, Faculty of Engineering & Technology, Gurukula Kangri Vishwavidyalaya, Haridwar, Uttarakhand 249408, India

N. Mehla (✉)
Department of Mechanical Engineering, National Institute of Technology, Kurukshetra, Haryana 136119, India
e-mail: neerajmehla471@gmail.com

L. M. Das et al. (eds.), *Emerging Trends in Mechanical Engineering*, Lecture Notes in Mechanical Engineering, https://doi.org/10.1007/978-981-15-8304-9_11

desiccant wheel (DW) and desiccant bed (DB) and reported that the DW works continuously while DB works periodically. Parmar and Hindoliya [7] studied the performance of the solid desiccant-based evaporative cooler in Indian climate and reported that the performance of the system was high in warm & humid climate. Varkute et al. [9] created a Peltier-based air cooling system. They concluded that to accomplish the target of dehumidification & cooling, a Peltier module-based air cooler combined with a compressor-based dehumidifier was able for indoor cooling. Mehla and Yadav [6] described the performance of the desiccant dehumidifier and studied the performance on different parameters at different rotational speeds of the desiccant wheel. Kashif Shahzad et al. [4] studied the performance of the solid desiccant dehumidifier coupled with the M-cycle-based heat and mass exchanger (MC-DAC). They reported that the COP of the MC-DAC was more efficient than the conventional system. Shamim et al. [8] developed the multi-layered binder free desiccant-based dehumidifier (MFBDD). They utilized silica gel for the dehumidification and combined it with the conventional vapour compression system. They reported that the average dehumidification capacity of the MFBDD was higher than that of a conventional DW. Fong and Lee [2] reported that the desiccant-based cooling system have an ability to work in hot & humid climatic regions. They reported that the performance of the system was more at high regeneration temperature. Wu et al. [11] reviewed the substrate of solid desiccant dehumidification system (SDDS). The performance of the DW depends upon the substrate having high porosity and high thermal conductivity. Kabeel and Abdelgaied [3] investigated the performance of the desiccant-based air conditioning system by using phase change material (PCM). They reported that the energy saving potential of the configuration having solar energy electric air heater & phase changing material is used for the thermal energy source to heat the regeneration air was more as compared to other configurations. Mehla and Yadav [5] also investigated the performance of solid desiccant-based air conditioning system and reported the energy and exergy analysis.

2 Description of the Experimental Setup

2.1 Working Principle

Desiccant-based cooling consists of dehumidifying the incoming air stream by passing it through a silica gel (desiccant material) & then cooling the air to the desired indoor temperature by spraying the water. The air gets heated when it passed through the desiccant material as it undergoes chemical dehumidification in which vapour condenses to liquid giving the heat energy to the air so it should be cooled to the desired indoor conditions. To use the system continuously, water vapour adsorbed by the desiccant material must be regenerated so that it can adsorb water vapour in the next cycle. This can be done by heating the desiccant material to its regeneration

temperature, which depends upon the nature of the desiccant used. In the present study, the regeneration of the silica gel was done by using the solar energy. The silica gel is directly exposed to the sun for regeneration process.

For testing the system, a small room has been taken and the DEC was placed out of the room over a small table and placed in front of the window. Then, all the open space of the room has been closed. The experiments have been taken in the month of March. Firstly, the reading was taken when the water pump off. The cooler switched on and then, we have measured initial temperature and the airflow rate of cooler by anemometer. We read out the initial humidity of room as well as date and time. After running the cooler up to 2–3 h, we noted down the temperature, humidity, and airflow rate after every 15 min interval and replace the saturated silica gel bed with the unsaturated silica gel. Thereafter, we switched on the water pump and reading has been taken after every 15 min for 2 h.

In second condition, we have not made the water pump off. We maintained it on condition. First, we noted down the initial readings such as humidity, temperature, date and time, airflow rate as well and maintain the water cooler running without silica gel. We noted down the alteration of humidity, temperature, and airflow. After that, we attached the silica gel packing with nut and bolts. We placed the hygrometer in the inner side of silica gel to measure the reduction of humidity. The second reading noted down in the month of April. When silica gel absorbs moisture, its colour changes pink from blue. After saturation, we unattached the silica gel packing and placed in the sun. Moisture gets evaporated in the sun and colour changes blue.

2.2 *Design and Construction of the Experimental Set-up*

Figure 1 shows the schematic diagram and experimental set-up of the direct evaporative cooler (DEC). It consists of a simple water cooler of iron casing which contains a simple water pump and fan and the vanes of fan are made of plastic material. The

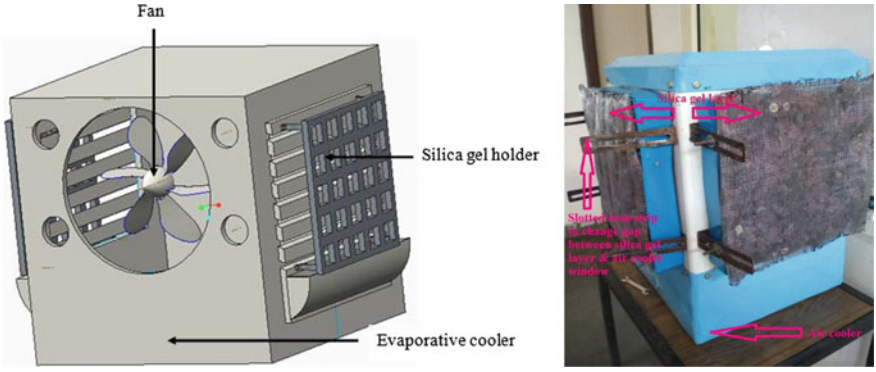

Fig. 1 Schematic diagram and experimental set-up of direct evaporative cooler

Table 1 Specification of the DEC

Specification	Dimensions
Length	40 cm
Width	40 cm
Height	58 cm
Area of window for DEC	35 × 35 cm^2

three sets of silica gel holder are constructed to hold the silica gel. The iron meshes are used to construct the silica gel holder (13 cm × 14 cm). Then, the metal strips are welded with the DEC as show in Fig. 1. It is used to attach or detached the silica gel holder by using nut and bolt arrangement with the DEC whenever required (Table 1).

2.3 Selection of Adsorbent Material (Silica Gel)

To enhance the performance of the DEC, the selection of adsorbent material was most important criteria, which dependence upon the properties of the adsorbent material such as adsorption capacity, rate of adsorption, etc. Hence, in the present study, to achieve the dehumidification process silica gel was chosen as an adsorbent material due to its low cost & satisfactory performance. Silica gel also have good rate of adsorption.

3 Measuring Devices and Instruments

The anemometer (GM816) is used to measure the speed of air having working range from 0 to 30 m/s and the accuracy is ±5% with resolutions of 0.1 m/s. A hygrometer is an instrument used for measuring the water vapour in the atmosphere. The relative humidity (RH) and the temperature of air are recorded by a digital Thermo-Humidity Metre having working range for relative humidity and the temperature's as 10–99% and −10 °C to 50 °C, respectively, whereas the accuracy is ±5% RH and ±1 °C respectively with resolutions of 1% and ±0.1 °C, respectively.

4 Results and Discussion

The experiments were conducted in the month of April 2018. In the manuscript, various cases are studied to find the different results.

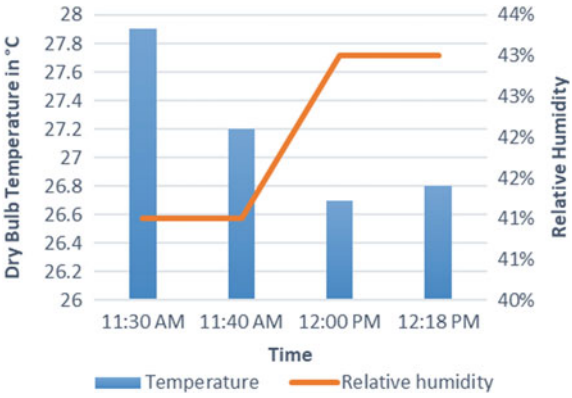

Fig. 2 Variation of temperature and relative humidity with time at an airflow rate of 1.7 m/s

Table 2 Recorded data at an air flow rate of 1.7 m/s

Date	Time	Temperature of outlet air (°C)	Relative humidity (%)	Absolute humidity (in gm/kg)	Air flow rate (m/s)
16/04/18	11:30 am	27.9	41	9.610	1.7
16/04/18	11:40 am	27.2	41	9.219	1.7
16/04/18	12:00 pm	26.7	43	9.392	1.7
16/04/18	12:15 pm	26.8	43	9.447	1.7

4.1 With Silica Gel Layer and Water Pump is Switched On

Figure 2 shows the variation of temperature & relative humidity with time at an air flow rate of 1.7 m/s when water pump is switched on. The minimum temperature of outlet air was recorded 26.7 °C. Table 2 also shows the absolute humidity with time.

4.2 Without Silica Gel Layer and Water Pump is Switched On

Figure 3 shows the variation of temperature & relative humidity with time at an airflow rate of 1.7 m/s when water pump is switched on and silica gel layer is removed. The minimum temperature of outlet air was recorded 26.6 °C. Table 3 also shows the absolute humidity with time.

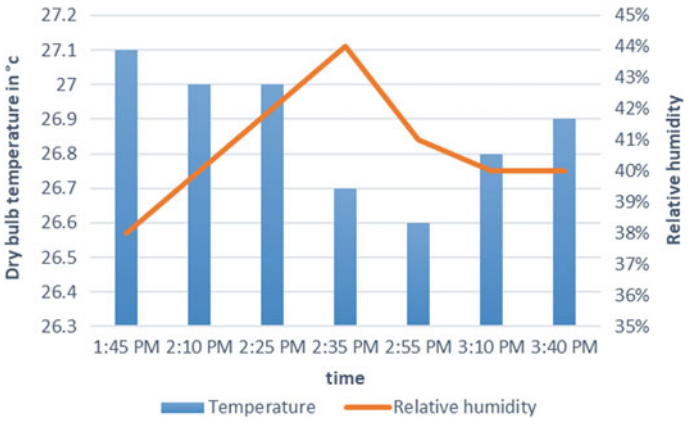

Fig. 3 Variation of temperature and relative humidity with time at an airflow rate of 1.7 m/s

Table 3 Recorded data at an air flow rate of 1.7 m/s

Date	Time (pm)	Temperature (°C)	Relative humidity (%)	Absolute humidity (in gm/kg)	Air flow rate (m/s)
16/04/18	1:45	27.1	38	8.484	1.7
16/04/18	2:10	27.0	40	8.884	1.7
16/04/18	2:25	27.0	42	9.335	1.7
16/04/18	2:35	26.7	44	9.613	1.7
16/04/18	2:55	26.6	41	8.895	1.7
16/04/18	3:10	26.8	40	8.779	1.7
16/04/18	3:40	26.9	40	8.831	1.7

4.3 Without Silica Gel Layer and the Water Pump is Switched On

Figure 4 shows the variation of temperature & relative humidity with time at an air flow rate of 2.4 m/s when water pump is switched on and silica gel layer is removed. The minimum temperature of outlet air was recorded 25.4 °C. Table 4 also shows the absolute humidity with time. In this case, it was observed that the temperature is decreasing with increasing the flow rate. In this case, the performance was not reliable because the humidity is increasing continuously.

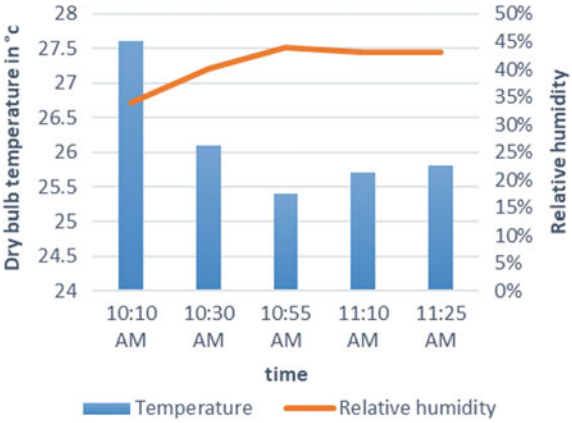

Fig. 4 Variation of temperature and relative humidity with time at an airflow rate of 2.4 m/s

Table 4 Recorded data at an air flow rate of 2.4 m/s

Date	Time (am)	Temperature (°C)	Relative humidity (%)	Absolute humidity (in gm/kg)	Air flow rate (m/s)
17/04/18	10:10	27.6	34	7.808	2.4
17/04/18	10:30	26.1	40	8.419	2.4
17/04/18	10:55	25.4	44	8.891	2.4
17/04/18	11:10	25.7	43	8.845	2.4
17/04/18	11:25	25.8	43	8.898	2.4

4.4 With Silica Gel Layer and the Water Pump is Switched On

Figure 5 shows the variation of temperature & relative humidity with time at an air flow rate of 2.4 m/s when water pump is switched on and silica gel layer has been kept.

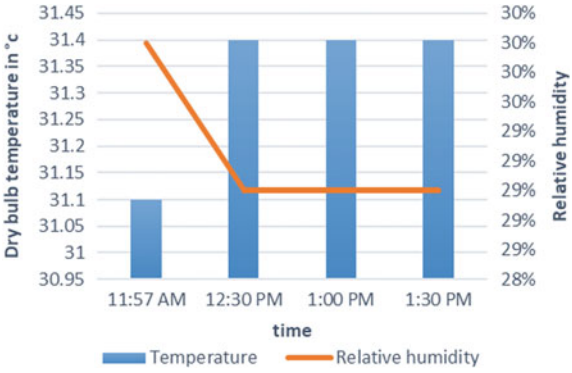

Fig. 5 Variation of temperature and relative humidity with time at an airflow rate of 2.4 m/s

Table 5 Recorded data at an air flow rate of 2.4

Date	Time	Temperature (°C)	Relative humidity (%)	Absolute humidity (in gm/kg)	Air flow rate (m/s)
17/04/18	12:00 am	31.1	30	8.440	2.4
17/04/18	12:30 pm	31.4	29	8.297	2.4
17/04/18	1:00 pm	31.5	29	8.345	2.4
17/04/18	1:30 pm	31.7	29	8.441	2.4

The minimum temperature of outlet air was recorded 31.1 °C. Table 5 also shows the absolute humidity with time. In this case, it was observed that the temperature is slightly increased by using silica gel and absolute humidity first decreased, then increased. The performance of the system was more at high airflow rate with silica gel. Because at low airflow rate, the contact of time between the air and silica gel get increased and rapidly saturated.

5 Conclusions

In this manuscript, the performance evaluation of the direct evaporative cooler based on adsorbent material (silica gel) has been carried out successfully. In this manuscript, five different cases has been studied at two different airflow rates. The relative humidity of air (without silica gel) at higher flow rate increases by 4% while relative humidity of air with silica gel decreases by 1%. Therefore, it was concluded that the performance of system has been improved by using silica gel. At higher airflow rate, average relative humidity of air is 42% while average relative humidity of air at low airflow rate is 30%. Therefore, the saturation of silica gel was more at higher airflow rate as compared to low airflow rate. Whereas with the increase in air flowrate, the silica gels get saturated. It was observed from the results that the use of silica gel is reliable and efficient. However, the major problem faced during the experiment that the silica gel gets saturated after 15–20 min, which interrupts the operation of the cycle. Hence, to overcome this problem, there is a need of desiccant wheel in which both process and regeneration should be taking place simultaneously.

References

1. Daou K, Wang RZ, Xia ZZ (2006) Desiccant cooling air conditioning: a review. Renew Sustain Energy Rev 10:55–77. https://doi.org/10.1016/j.rser.2004.09.010
2. Fong KF, Lee CK (2018) New perspectives in solid desiccant cooling for hot and humid regions. Energy Build 158:1152–1160. https://doi.org/10.1016/j.enbuild.2017.11.016

3. Kabeel AE, Abdelgaied M (2018) Solar energy assisted desiccant air conditioning system with PCM as a thermal storage medium. Renew Energy 122:632–642. https://doi.org/10.1016/j.renene.2018.02.020
4. Kashif Shahzad M, Ali M, Ahmed Sheikh N et al (2018) Experimental evaluation of a solid desiccant system integrated with cross flow Maisotsenko cycle evaporative cooler. Appl Therm Eng 128:1476–1487. https://doi.org/10.1016/j.applthermaleng.2017.09.105
5. Mehla N, Yadav A (2016) Experimental investigation of a desiccant dehumidifier based on evacuated tube solar collector with a PCM storage unit. Drying Technol 35:417–432. https://doi.org/10.1080/07373937.2016.1180300
6. Mehla N, Yadav A (2018) An experimental investigation on solar powered solid desiccant air conditioning (SPSDAC) based on regenerative evaporative cooling system with PCM unit. Int J Ambient Energy, 1–25. https://doi.org/10.1080/01430750.2018.1562969
7. Parmar H, Hindoliya DA (2013) Performance of solid desiccant-based evaporative cooling system under the climatic zones of India. Int J Low-Carbon Technol 8:52–57. https://doi.org/10.1093/ijlct/ctr051
8. Shamim JA, Hsu WL, Kitaoka K et al (2018) Design and performance evaluation of a multi-layer fixed-bed binder-free desiccant dehumidifier for hybrid air-conditioning systems: Part I—experimental. Int J Heat Mass Transf 116:1361–1369. https://doi.org/10.1016/j.ijheatmasstransfer.2017.09.051
9. Varkute N, Chalke A, Ailani D et al (2016) Design and fabrication of a Peltier operated portable air cooling system. Int Res J Eng Technol 03:1801–1805
10. Waugaman DG, Kini A, Kettleborough CF (1993) A review of desiccant cooling systems. J Energy Res Technol 115:1–8. https://doi.org/10.1115/1.2905965
11. Wu XN, Ge TS, Dai YJ, Wang RZ (2018) Review on substrate of solid desiccant dehumidification system. Renew Sustain Energy Rev 82:3236–3249. https://doi.org/10.1016/j.rser.2017.10.021

Design and Analysis of an Air-Purifier Using Cyclone Separator for Industries

R. B. Ananda Krishnan, Sidharth Vijayakumar, K. Hari Krishnan, and S. N. Jyothi

Abstract Controlling air pollution is important for healthy well-being of humans and nature as a whole. The presence of particulate matter in air is a serious matter of concern as it causes several health hazards. One of the most cost effective and efficient methods to separate particulate matter is by using cyclone separator. Cyclone separator is a device without any moving parts having tangential inlet velocity of gas stream transformed into a compact vortex or spiral flow downward between walls of gas discharge outlet and body of cyclone. The centrifugal force resulted by vortex or spiral creation leads to coarse particulate separation of particulate matter (24–30 μm) from the polluted air. This paper presents the design of a 2D-2D cyclone separator using Lapple mathematical model. Tangential inlet velocity and barrel diameter of cyclone separator are some of the important factors which collection efficiency depends on. Optimum barrel diameter and inlet velocity for highest collection efficiency were found by numerical analysis using Lapple model, in which former parameter was made fixed and latter changed and vice versa. The iteration was further carried out on four particles of different densities like manure dust, Arizona test dust, fly ash, and micro-alumina. Collection efficiencies of cyclone separator were determined for the selected particles above mentioned. It was observed that the collection efficiency reached a maximum after a size range (24–40 μm) of particles. The theoretical results obtained were verified with the results obtained in CFD.

R. B. A. Krishnan (✉) · S. Vijayakumar · K. H. Krishnan · S. N. Jyothi
Department of Mechanical Engineering, Amrita Vishwa Vidyapeetham, Amritapuri, India
e-mail: anandakrishnanrb@outlook.com

S. Vijayakumar
e-mail: sidharthvijayakumar7@gmail.com

K. H. Krishnan
e-mail: krishhari1@yahoo.in

S. N. Jyothi
e-mail: jyothisn@am.amrita.edu

L. M. Das et al. (eds.), *Emerging Trends in Mechanical Engineering*, Lecture Notes in Mechanical Engineering, https://doi.org/10.1007/978-981-15-8304-9_12

1 Introduction

Air quality is a concern which requires imperative attention. The scientific methodologies implemented in various industries have led to the rapid increase of dust particles which pose a high threat to air quality. When the level of particulates exceeds a particular range, it is called as pollutants. A range of very different particulates like smoke, soot, mould, etc., can contaminate air. This can cause serious effect in the growth of plants and animals, and in plants, it can lead to impair plant growth and primary productivity (Ulrich 1984); it also causes blockage to stomata which can affect the photosynthetic cycle. This poisoning also puts the lives of people at risk, with diseases like silicosis, pneumoconiosis, asthma, etc., caused by inhaling insoluble dust that lungs cannot remove. To resolve this problem, clean air spots, free from particulate matters need to be created, and cyclone separators should be used effectively.

A cyclone separator is a device for improving air quality by separating solid particulates from gases by using centrifugal force. They have been used for many decades for removing dust from industrial gas as it has low maintenance cost, simple design, low capital, and better adaptivity to any surrounding. It has two parts: upper cylindrical part and lower cone, which are referred to as barrel and cone. Air with particulates is fed to the cyclone separator tangentially and helical flow is set up inside the chamber. Since the particulates have greater inertia compared to air, it will be tight to follow the helical pattern, and as a result, it will hit the wall and collected outside the chamber. As the flow moves to narrow end, the radius of helical flow decreases and velocity increases separating smaller and smaller particulates. Owing to the shape of cyclone separator, the pressure decreases from bottom to top, and as a result, reverse vortex will be formed at a point carrying dust-free air from bottom to top (Fig. 1).

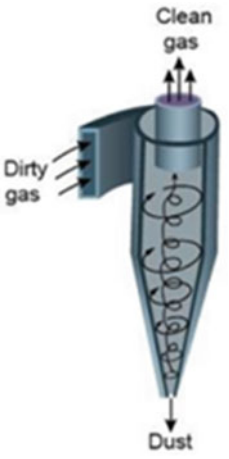

Fig. 1 Path traced by air inside a cyclone separator

Stairmand (1951) had designed a cyclone separator having eight different ratios which can be derived from barrel diameter. Most of the designs were formed on a trial and error basis. 2D2D (Shepherd and Lapple 1939) and 1D3D (Parnell and Davis 1979) are the cyclone separators normally used. The representation of 2D2D means having barrel and cone length 2 times greater than the barrel diameter, whereas 1D3D means barrel and cone length 1 and 3 times greater than barrel diameter. It has been proved that 2D2D and 1D3D cyclone separators are efficient to separate fine particles [1].

The objective of this paper is to design a cyclone separator to separate particulate matters of different materials like manure dust, Arizona dust, fly ash, and micro-alumina from the air with particulates ranging from 2 to 40 μm in size. Lapple's 2D2D mathematical model is used for designing the cyclone separator. To start with the design, the barrel diameter needs to be fixed and other design parameters can be obtained using the barrel diameter. The barrel diameter under consideration is 0.12, 0.18, 0.24, and 0.30 m and the tangential velocities used for calculation ranges from 13 to 16 m/s. The value of barrel diameter and tangential velocity having maximum collection efficiency is taken and the collection efficiency for the above particulates is calculated. The design of cyclone separator was done in SolidWorks. Computational Fluid Dynamics (CFD) was done using Siemens Star-CCM+ software to validate the theoretical analysis. In this section, using particle injection, the collection efficiency of cyclone separator for fly ash ($\rho = 2700$ kg/m^3) and tangential velocity ($V_{\tan} =$ 16 m/s) have been calculated. It was found that the collection efficiency obtained from CFD was greater than the theoretical calculation.

2 Methodology

Cyclones can be designed and optimised based on the level of application. Our design of cyclone is targeted towards removing particulate matter (PM2.5 and PM10) from the workplace and thus to create clean air spots in the industries. They consist of many independent units working together with inlet conditions specified in the design. The publication on optimisation of cyclone separator is less, as there is no single theory predicting their performance with reasonable accuracy. Hence, the optimisation of cyclone is done mostly on the basis of experiment or trial and error basis [2]. It often becomes difficult to conduct experiments by trial and error to find collection efficiency (CE). As a solution, various pre-determined mathematical models can predict the CE with practical variations [3, 4]. In our design, we have used classical cyclone design (CCD), the Lapple model to design the cyclone separator. There are several challenges associated with selection of this model; it was determined by Wang et al. [1] that optimum performance of cyclone depends upon inlet conditions and it does not predict the number of turns required for different cyclones. CCD process can be used only if the design engineer knows (a) Flow conditions (b) Particulate matter and (c) The type of cyclone (2D2D) to be designed. After fixing all necessary parameters, i.e. the particle density (Fly Ash—2700 kg/m^3), inlet tangential velocity

($V_{\tan}$) ($v = 13$ m/s), and by determining cut diameter (C_d) using Lapple model, the CE was determined for barrel diameters (D_c) of 0.12, 0.18, 0.24 and 0.3 m for average particles size ranging 2–40 μm. Since even the smallest particles had more CE than the rest, the D_c was selected to be 0.12 m. The selection of barrel diameter was later followed by optimisation of $V_{\tan}$. The $V_{\tan}$ for maximum CE was similarly determined for average particle sizes.

3 Equations Used

To calculate the number of turn in a cyclone separator

$$N = 1/H_c(L_b + H_c/2) \tag{1}$$

where

N Number of turns in cyclone.
H_c inlet duct height.
L_b height of the barrel.
Z_C height of the cone.

To calculate the cut diameter of the cyclone separator

$$C_d = \sqrt{(9 * \mu * B_c)/\left(2 * \pi * N * V_{\tan}\left(\rho_p - \rho\right)\right)} \tag{2}$$

where

C_d Cut diameter.
μ Absolute viscosity of fluid (Ns/m^2).
B_C Width of the inlet duct.
$V_{\tan}$ Inlet velocity (m/s).
ρ_p Density of the particle (Kg/m^3).
P Density of the fluid (Kg/m^3).

To evaluate the CE of the cyclone separator

$$\eta = 1/\left(1 + \left(C_d/D_p\right)^2\right) \tag{3}$$

where

D_p Average particle size.

4 Design of a Cyclone Separator

Design of cyclone separator plays an integral role, so it is essential to select proper design parameters such that the maximum CE could be attained. Shepherd and Lapple 2D2D model for designing was chosen as a reference. The model was selected because previous work done by Wang [5] suggested that 2D2D cyclones have more CE for particles diameter less than 100 μm. D in 2D2D stands for D_c of the cyclone. If a cyclone is 2D2D, it can be inferred that the height of the barrel and cone will be twice that of D_c. Once we fix the D_c of the cyclone, we can evaluate other design parameters of the 2D2D cyclone from the image given in Fig. 2.

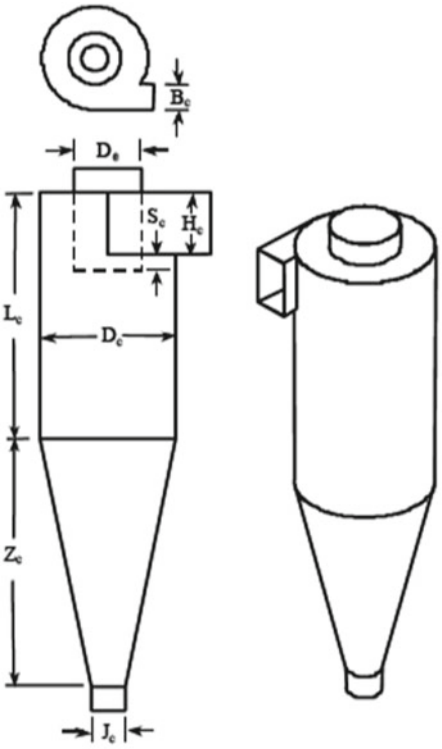

Fig. 2 Design parameter relations of 2D2D cyclone separator (*Source* [6])

2D2D

$B_c = D_c/4$ $J_c = D_c/4$

$D_e = D_c/2$ $S_c = D_c/8$

$H_c = D_c/2$ $L_c = 2 \times D_c$

$Z_c = 2 \times D_c$

Table 1 Parameters used to design cyclone separator

Cyclone dimensions	Abbreviation	Ratio (dim/d_c)	Dimensions (m)
Barrel diameter	d_c	1	0.12
Height of barrel	L_b	2	0.24
Height of cone	Z_c	2	0.24
Inlet height	H_C	0.5	0.06
Inlet width	B_c	0.25	0.03
Outlet length	S_c	0.125	0.015
Gas outlet diameter	D_e	0.5	0.06
Duct outlet diameter	J_s	0.25	0.03

To find out the suitable value of D_c for the cyclone separator, a study was done by [5, 7–9]. D_c's range was found to be 0.12–0.30 m. A study on $V_{\tan}$ for the cyclone was done by [6, 7, 10] and was found to be 5–16 m/s. As we have two unknown quantities, we cannot vary both parameters; hence, it was divided into two steps (a) Constant $V_{\tan}$ with varying D_c. (b) Most efficient D_c was chosen with varying $V_{\tan}$.

Fly ash (2700 kg/m^3) [11] was chosen as the particulate present in the air. Initially, the CE was determined by fixing (1). Number of turns was found to be 6 and by substituting the number of turns in Eq. (2), cut diameter was calculated to be 2.373 E−06. Once we get the value of C_d by Eq. (3), CE of the cyclone was calculated and it was found that CE of 0.6150 was achieved for particle size 3 μm. Similar calculations were repeated for particle size 5, 8, 14, 24, and 40 μm. After performing the above calculations, D_c and $V_{\tan}$, which gave the best efficiency, was chosen and the cyclone was designed. Table 1 has the design parameters used (Fig. 3).

Air can be contaminated by a range of different particles such as dust, smoke, and ash. Particulates can vary in density and size. From a study conducted, the following particles were selected: Arizona test dust [6], fly ash [11], manure dust [11] and micro-alumina [12]. Similar calculations were repeated on these three particles and by using Eqs. (1), (2) and (3), CE was determined for particle size 5, 8, 14, 24, and 40 μm.

5 Computational Fluid Dynamics (CFD)

The theoretical CE obtained for particulates (fly ash) was validated using STAR-CCM + CFD package. The gas inlet conditions at atmospheric pressure were $V_{\tan}$ = 16 (m/s) and density = 2700 (kg/m^3). CFD consisted of the following steps-

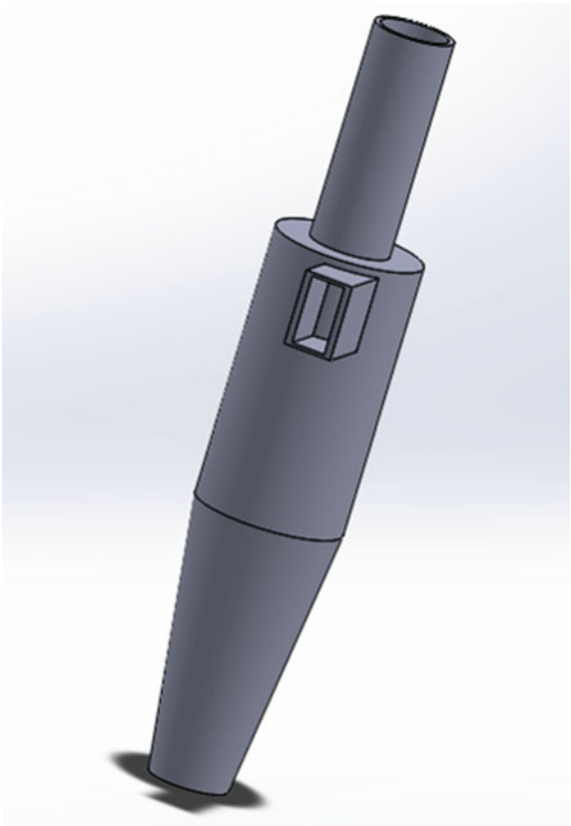

Fig. 3 Designed cyclone separator

5.1 Creation of fluid path from design
5.2 Refined meshing
5.3 Selection of proper physics models to solve
5.4 Iteration
5.5 Results.

5.1 Creation of Fluid Path from Design

Initially, the design is done in SOLIDWORKS and is converted to solid model. This is then imported to STAR-CCM+. It is important to convert all hollow parts in design into solid parts which define fluid path. Then, the boundary interfaces of flow are determined and named to be inlet, outlet 1, and outlet 2 (Fig. 4).

A – Inlet
B – Outlet1
C – Outlet2

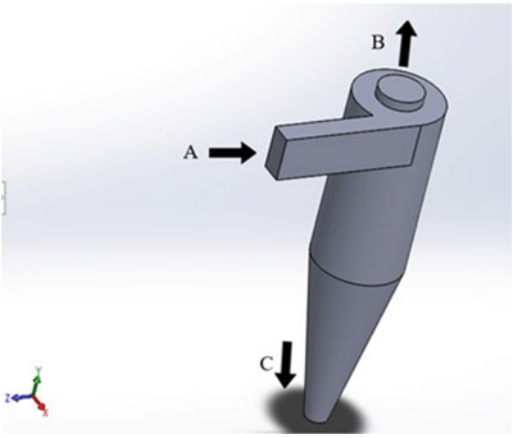

Fig. 4 Creation of flow path

5.2 Refined Meshing

Under OPERATIONS option in STAR-CCM+, we selected appropriate meshes as shown in Fig. 5. The critical areas where the required data like velocity, pressure, and mass flow rate to be determined are further meshed to obtain (Figs. 6, 7, and 8).

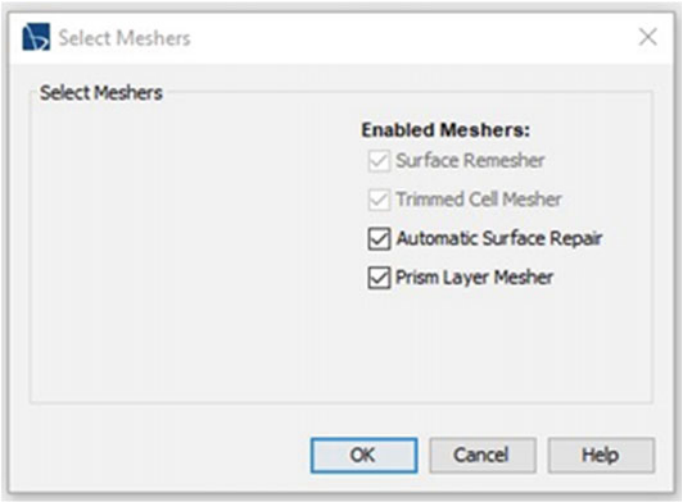

Fig. 5 Selected meshers

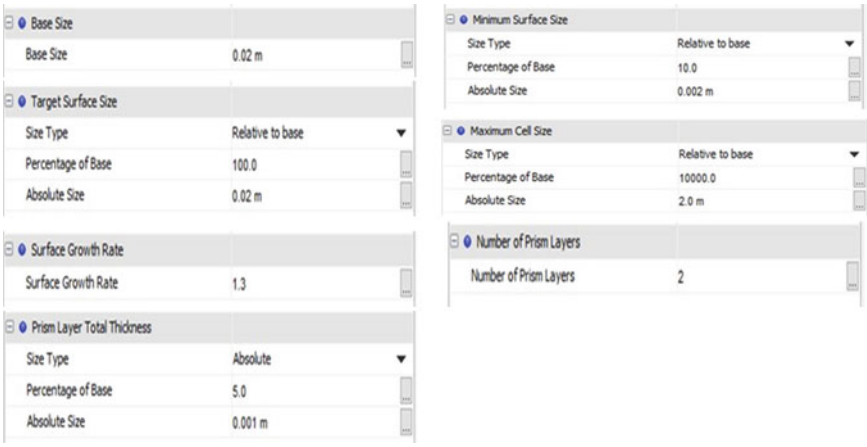

Fig. 6 Mesh parameters

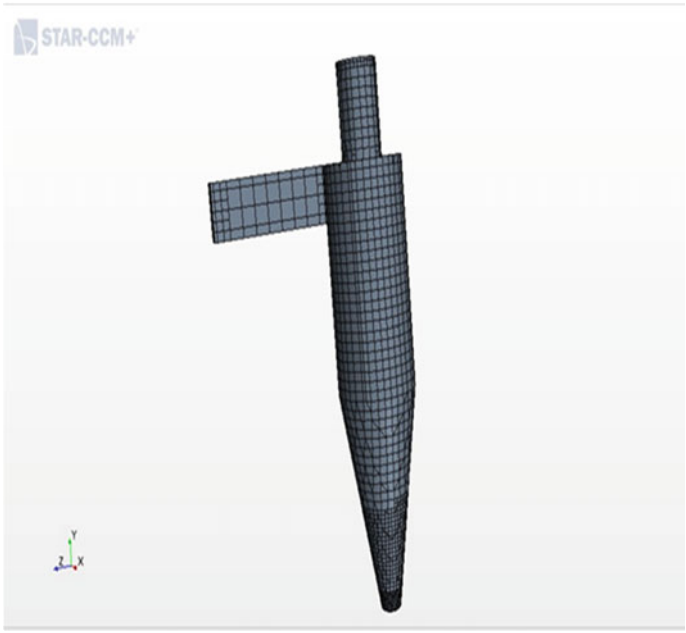

Fig. 7 Meshed cyclone separator

5.3 Selected Physics Models

In analysis, apart from normal velocity and pressure determination along the cyclone, fly ash particles of size and density 4 μm and 2701 kg/are injected and in the end,

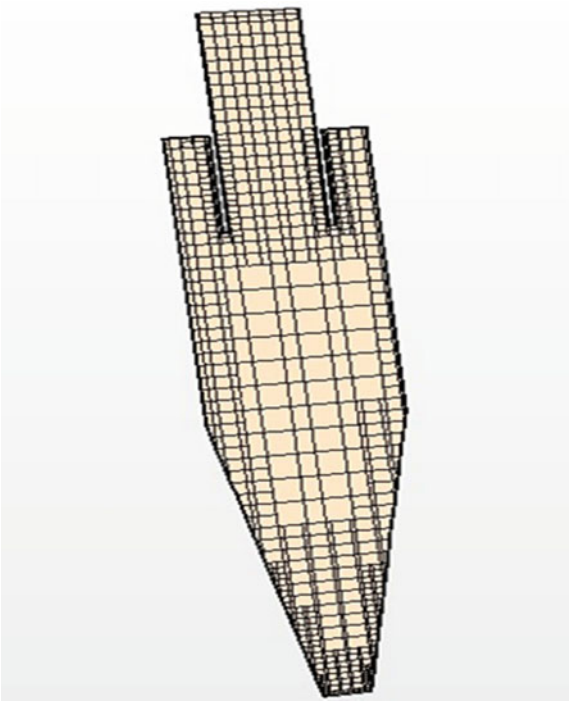

Fig. 8 Volume mesh in a derived cross section

collection efficiency is determined. To obtain results in CFD, numerous models were used. The flow is assumed to be steady three-dimensional flow with mach number less than 0.3 (Segregated flow). The state of flow is turbulent in nature and hence Reynolds averaged Navier Stocks (RANS) model is used. Reynolds stress turbulence model is used since it accounts for direction effects of the Reynold stresses and complex interactions within turbulent flows (Fig. 9).

Lagrangian multiphase model is selected since the inlet medium consisted of two phases, namely air (gas) and dust particles (solid). It accompanies a multiphase interaction between them along the flow in the cyclone separator. All the particles injected are considered to be spherical in shape (Fig. 10).

The Track File node, which has properties, represents the Track File model. This model indicates that the tracks of parcels (parcels are a set of particles) are recorded in a track file and, if so, what variables are recorded. A temporary track file only is created while the simulation runs. It is essential to save the simulation so that this temporary track file is moved to a final file having the same name as the simulation. Boundary sampling model is used to record parcel states when they interact with certain boundary conditions. The residence time model makes particles residence time available as a field function. Erosion modelling predicts the rate of erosion from particle impact on solid walls. Erosion rate is defined as the mass of wall material removed per unit area per unit time. An additional turbulent dispersion force in the phase momentum equations models the effect of turbulence in redistribution of

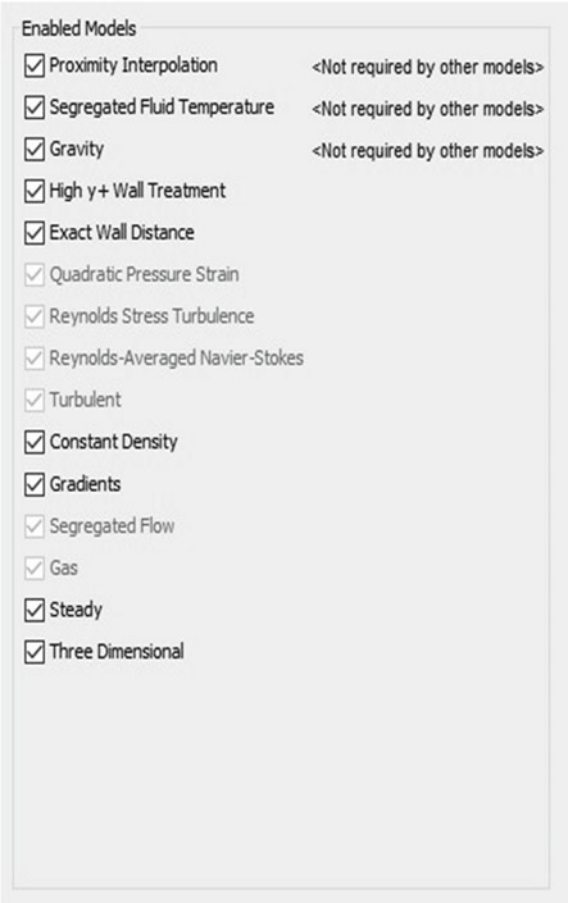

Fig. 9 Selected physics models

non-uniformities in phase concentration. This term arises naturally when Reynolds averaging is applied to the instantaneous drag force. Pressure gradient force model includes the force determination in the cyclone due to the pressure gradient. Figure 11 shows the particle injection in the cyclone.

5.4 Iterations

After fixing all inlet conditions ($V_{\tan} = 16$ m/s, $\rho = 2700$ kg/m^3), categorising inlet, outlet 1, and outlet 2 (as velocity inlets and pressure outlets) and selecting proper physics models, the stopping criteria is set to 3200 iterations. The simulation is then initialised and then run (Fig. 12).

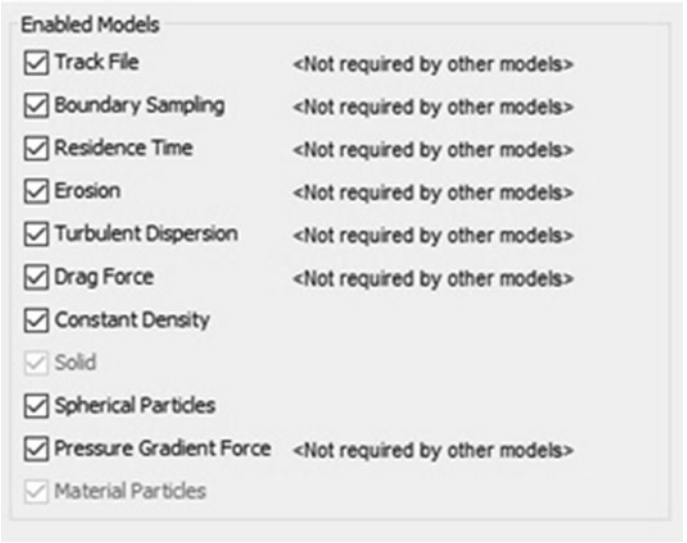

Fig. 10 Selected Lagrangian multiphase models

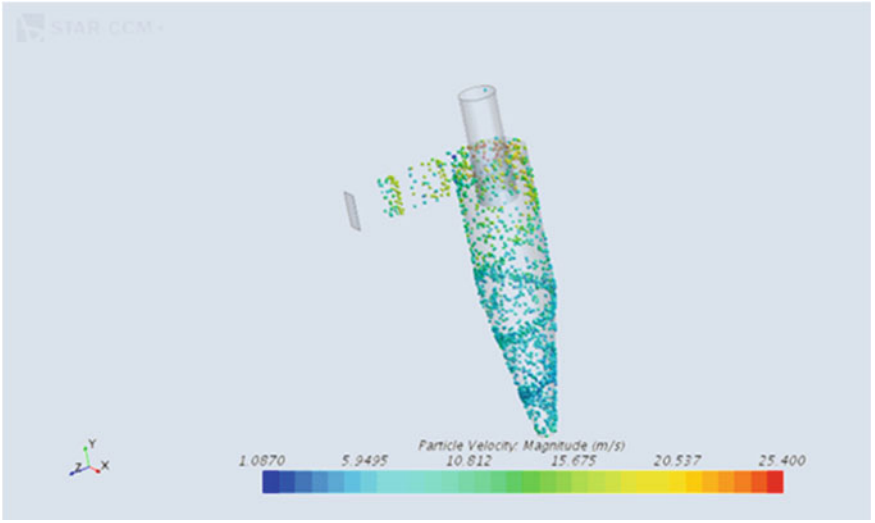

Fig. 11 Above simulation shows the way particles moves inside the cyclone separator after particles are injected along with air. The different colours shows the velocity of particles at a particular instant

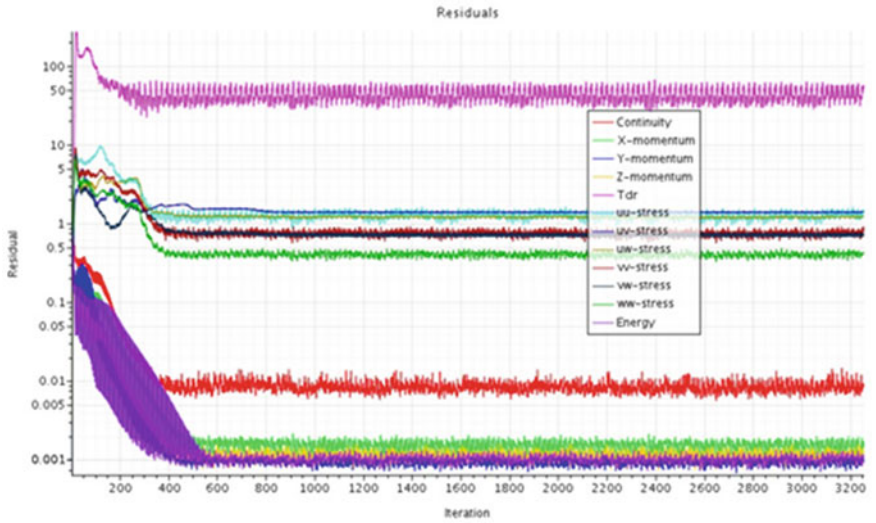

Fig. 12 Iterations

5.5 *Results and Discussions*

It was found from Eqs. (1), (2) and (3), it was found that cyclones which had least barrel diameter gave better efficiency; hence, 0.12 m was selected to be the optimum barrel diameter among 0.12, 0.18, 0.24 and 0.30 m. The graph below shows the decreasing trend of efficiency with increase in D_p (Fig. 13).

Similarly, Eqs. (1), (2) and (3) were used to find optimum $V_{\tan}$ for the selected D_c. It was observed that higher velocity gave higher efficiency for 2D2D cyclones as

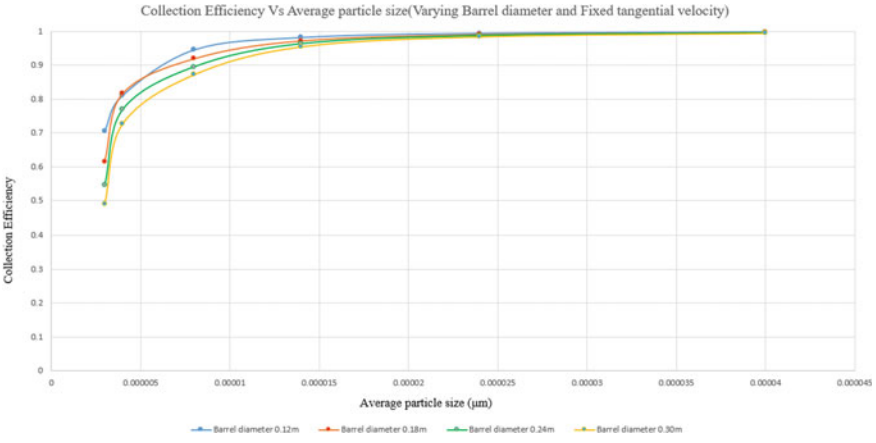

Fig. 13 Variation of collection efficiency with average particle size for different barrel diameter

shown by [9]. Hence, 16 m/s was selected as the optimum $V_{\tan.}$ Graph below shows the increasing trend of efficiency with an increase in $V_{\tan}$ (Fig. 14).

A theoretical study on four different particulates were also done by Eqs. (1), (2) and (3). Table 2 shows this CE results obtained.

From the above tables and Fig. 15, we can infer that it is easier to separate particles which have higher density, i.e. above 1800 kg/m^3 by using a cyclone separator, if low-density particles are used, the efficiency has to be compromised. As settling occurs due to gravity, less dense particle will be difficult to separate by using cyclone separator. For separating less dense particles, methods like magnetic dust separators are used. From Fig. 15, it was also observed that after 24 μm, every particle irrespective of their density had a CE of 99%. This signifies that cyclone can separate particles with larger particle diameter. In this case, particles above 24 μm for all dust particles were separated with very high efficiency irrespective of the density.

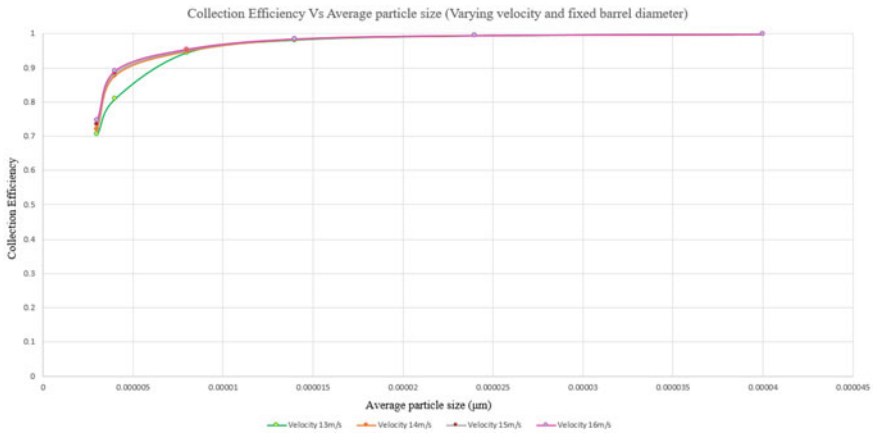

Fig. 14 Variation of collection efficiency versus average particle size for different velocities

Table 2 Collection efficiency for different particles of different density

Average particle size (μm)	Collection efficiency (η)			
	Manure dust $\rho =$ 1800 kg/m^3	Arizona test dust $\rho = 2600$ kg/m^3	Fly ash $\rho = 2700$ kg/m^3	Micro-alumina $\rho = 3900$ kg/m^3
3	0.6482	0.7307	0.7344	0.7998
5	0.8366	0.8829	0.8848	0.9173
8	0.9291	0.9507	0.9516	0.9659
14	0.9756	0.9833	0.9836	0.9886
24	0.9915	0.9942	0.9943	0.9961
40	0.9969	0.9979	0.9979	0.9985

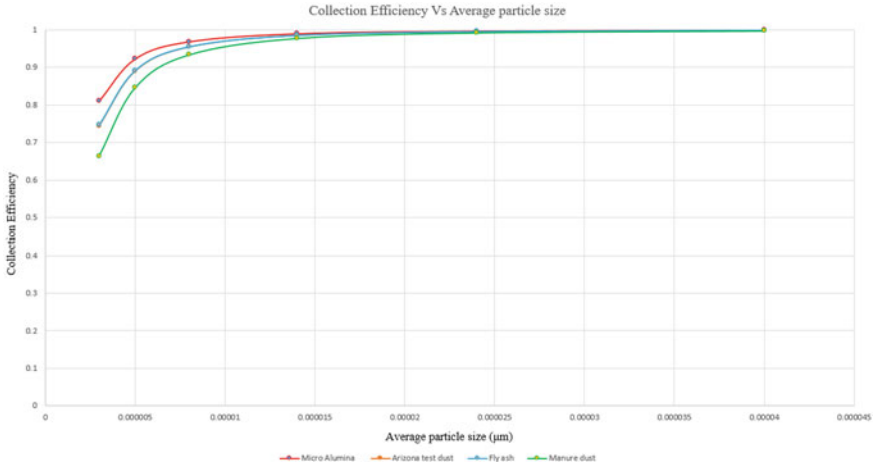

Fig. 15 Collection efficiency versus average particle size for micro-alumina, Arizona test dust, fly ash, and manure dust

5.6 Computational Fluid Dynamics

(a) **Mass flow rates through outlets**

This shows that 75.807% of air coming through inlet is passing by outlet1 which is the gas outlet of a cyclone separator in our design. It happens since there is a generation of pressure gradient along the length of cyclone. The pressure variation causes the cyclone to have a reverse swirl flow. It is due to this oulet1 has more mass flow rate. In Fig. 16, CFD results show that the lowest value of pressure (dark blue region) in near outlet 1. This is the reason why larger amount of air exists along outlet 1 as shown in Table 3. Outlet 2 has light blue colour which implies that pressure is low but not as low as outlet 1, this is the reason why 24.19309% of air is going out thought outlet 2. Highest pressure is observed along the walls of the cyclone separator (red region).

From top to bottom, there is a pressure drop, i.e. light blue in bottom area and dark blue in the upper area. Hence, reverse vortex is formed.

(b) **Streamline of fluid path**

This shows how the air that reaches a certain point starts to experience a reverse swing flow which is caused due to the variation of pressure as shown in Fig. 16. This leads to reverse vortex flow of air and due to the presence of lower pressure at outlet 1, larger amount of air flow through outlet 1. Figure 17 shows the streamline path which air takes inside the cyclone separator.

The dark blue indicates zero velocity and the red indicates high velocity. The flow path of air can be seen with their velocity in different colours.

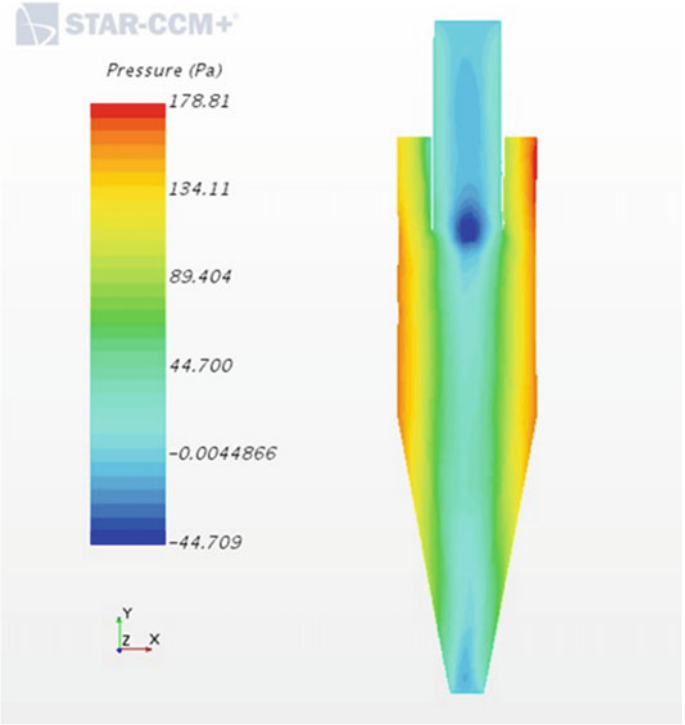

Fig. 16 Pressure gradient along the length of the cyclone

Table 3 Percent of flow rates

Flow region	Flow rate (Kg/s)	Fraction of air(%)
Inlet	3.41E−02	100
Outlet 1	2.59E−02	75.80710
Outlet 2	8.25E−03	24.19309

(c) **Total erosion plot**
Erosion rate is defined as the mass of wall material removed per unit area per unit time (Fig. 18).

(d) **Average collection efficiency**
From the simulation, we obtained the average CE of cyclone separator with fly ash as particulate as 90%. This **validates** the result obtained from theoretical analysis (Fig. 19).

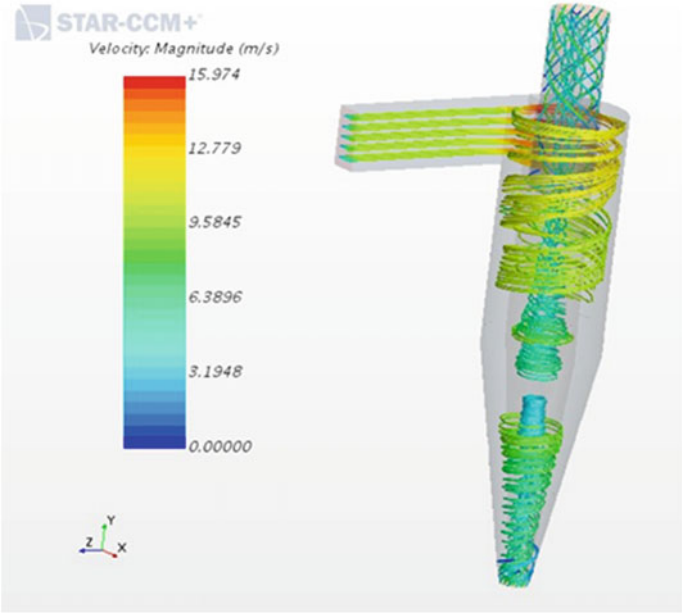

Fig. 17 Streamlines of airflow

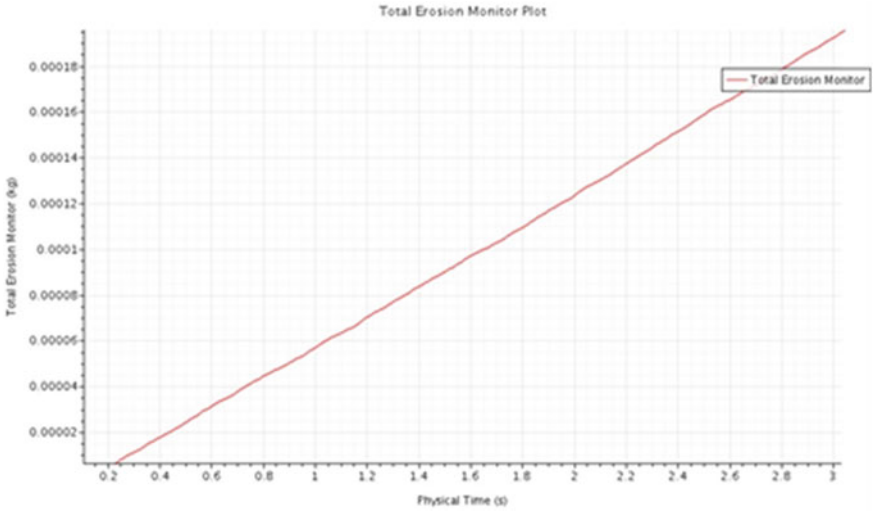

Fig. 18 Total erosion plot versus time

Fig. 19 Collection efficiency plot

Research done by (1) shows that for Lapple 2D2D cyclones has an efficiency of 88% for particulates which has density in the range of 1000–3000 kg/m^3.Velocity and diameter are also comparable hence research done by (1) can validate our results obtained from theoretical and CFD analysis.

6 Conclusion

There are several serious health hazards because of poor air quality. Apart from poor air quality index in metro cities, the employees working in various industries are having serious health threat due to ill-managed particulates in the air. Aggravated cardiovascular and respiratory illness, damaged cells in the respiratory system, asthma, bronchitis, emphysema, and possibly cancer are some of the complicated diseases. Hence, creating good air quality is vital to ensure safe working environment for employees. In most agricultural industries, cyclone separator is used for separating different particles of different density. This property of cyclone separator can be exploited for air purification in industries with very poor air quality. In our work, we have designed a cyclone separator with good collection efficiency. For that, we determined the optimum barrel diameter and tangential inlet velocity for our application using Lapple model. Then, according to standard design procedures, the entire dimensions for the cyclone separator was calculated. After design, theoretical collection efficiency was calculated for different particles like micro-alumina, Arizona test dust, fly ash, and manure dust using Lapple model. The theoretical collection efficiency for fly ash (a random particle) was validated by computational fluid dynamics. This study has proven that CE increases with increase with increase in tangential velocity in particle density and for all particulate matter above 24 μm CE is 99% irrespective of their density. According to theoretical analysis, CE of the cyclone for 4 μm fly ash is found to be 83% and from CFD analysis, it is found to be 90%. Hence, CFD analysis is in agreement with theoretical results. The study

will be extended to design an air purification system. The particulate free air which comes out of the cyclone separator is passed through a series of adsorbent beds which adsorbs and brings down the concentration of toxic gases like CO, SO_2 and NO_2. Adsorption of toxic gases will be done as future work.

References

1. Wang L, Parnell Jr CB, Shaw BW, A study of the cyclone fractional
2. Efficiency Curves. Agric Eng Int: CIGR J
3. Scientific Research and Development (2002) Manuscript BC 02 002, vol 4
4. Liden G, Gudmundsson A (1997) Semi-empirical modelling to generalise the dependence of cyclone collection efficiency on operating conditions and cyclone design. J Aerosol Sci 28(5):853–874. https://doi.org/10.1016/S0021-8502(96)00479-X
5. Dirgo J, Leith, D (2007) Cyclone collection efficiency: comparison of experimental results with theoretical predictions. Aerosol Sci Technol 4:401–415. https://doi.org/10.1080/02786828508959066
6. Taiwo MI, Namad MA, James BM (2016) Design and analysis of cyclone dust separator. Am J Eng Res 5(4):130–134
7. Wang L, Parnell CB, Shaw BW, Lacey RE (2003) Analysis of cyclone collection efficiency. Am Soc Agric Biol Eng. https://doi.org/10.13031/2013.15040
8. Bashir K (2015) Design and fabrication of cyclone separator. Doctoral dissertation, Thesis, China University of Petroleum. https://doi.org/10.13140/RG.2.2.20727.83368
9. Sakura GB, Leung AY Experimental study of particle collection efficiency of cylindrical inlet type cyclone separator. Int J Environ Sci Dev 6(3) (2015). https://doi.org/10.7763/IJESD.2015.V6.581
10. Zhu Z, Na Y, Lu Q (2008) Pressure drop in cyclone separator at high pressure. J Therm Sci 17(3):275–280. https://doi.org/10.1007/s11630-008-0275-7
11. Marinuc M, Rus F (2011) The effect of particle size and input velocity on cyclone separation process. Bulletin of the Transilvania University of Brasov. Forestry, Wood Industry, Agricultural Food Engineering. Series II, vol 4(2), p 117
12. Verma RS, Sen PK, Bohidar SK (2015) Study of design of cyclone separator under collection efficiency and air density effect. Int J Adv Res Sci Eng 4(Special Issue 01)
13. Wang L, Buser MD, Parnell CB, Shaw BW (2003) Effect of air density on cyclone performance and system design. Trans ASAE 46(4):1193–1201. https://doi.org/10.13031/2013.13957
14. Faulkner WB, Buser MD, Whitelock DP, Shaw BW (2007) Effects of cyclone diameter on performance of 1D3D cyclones: collection efficiency. Trans Am Soc Agric Biol Eng 50(3):1053–1059. https://doi.org/10.13031/2013.23146

Development of a Surge Tank Set-up and Its Utilisation in the Diesel Engine for NO_X Emission Reduction

P. Sharma, J. Hira, and P. Anand

Abstract Modern vehicles are the major source of air pollution and diesel engines are the at most pollutant with emission of NOx ranging from 500 to 1000 ppm. NOx is the most harmful pollutant amongst various other emission such as HC, CO_2, CO, PM and soot. In this research work, an experimental investigation has been performed on a single cylinder direct injection compression engine with power capacity 3.5 KW. A surge tank set-up has been developed through which cooled EGR will be utilised for reducing the NO. The results of the engine performance and emission have been investigated at different loading conditions with EGR ranging from 10% to 20%. From the experimental analysis, it has been found out that with 20%, EGR the NO emission level has been reduced by 72% that is from 290 ppm to 83 ppm on full loading conditions.

Keywords EGR · NO emission · Diesel engine · Surge tank

1 Introduction

Reducing pollution is a significant job in developing IC Engines. As the world personality mobility is rising and the transport industry is increasing, it is essential to restrict the effect of vehicles on both the atmosphere and people's health. Concern over global warming and health has made the policy-makers to implement most stringent emission norms and set regulations for automobile industry to introduce cleaner vehicles. Diesel engines have low maintenance cost and greater fuel economy, but most engines

P. Sharma · J. Hira (✉)
Amity University Noida, Noida, India
e-mail: jhira@amity.edu

P. Sharma
e-mail: prakhar.sharma050514@gmail.com

P. Anand
Abdul Kalam Technical University, Lucknow, India
e-mail: prashant88110@gmail.com

L. M. Das et al. (eds.), *Emerging Trends in Mechanical Engineering*, Lecture Notes in Mechanical Engineering, https://doi.org/10.1007/978-981-15-8304-9_13

have higher combustion flame temperature and the reason is presence of O_2 and N_2 [1]. They create nitric acids and associated salts that react with humidity and produce unstable organic compounds in the presence of sunlight, resulting in the creation of ground-level ozone that lastly reaches the earth's surface together with rain or as mist, dew, or dry objects. [2]. To overcome this problem, alternative fuel and pollution reduction techniques come into play. Exhaust gas recirculation (EGR) is one of the established technology that may be effective in heavy-duty diesel engines. In EGR, some part of the exhaust gas is recirculated and transferred to the intake manifold. The exhaust gas gets mix with the fresh charge sucked in by the engine and then flow into the cylinder where they dilute and cool the combusting mixture of gases [3]. The specific heat of the surrounding atmosphere is lower that the EGR. Therefore, the heat capacity of intake charge increases and for the same heat output, the maximum temperature is reduced. Fresh air entering into the chamber is displaced by CO_2 and water vapours present in the exhaust because of which the quantity of oxygen present in the air fuel mixture decreases. Effective air fuel mixture also gets reduced which affects exhaust emission substantially. EGR increases heat capacity of intake mixture, which results in decreasing flame temperature and NOx formation reactions [4]. Based on how the exhaust gases are transferred, there are two EGR techniques, Hot EGR and cooled EGR. When the exhaust gas is recirculated to the intake directly, it is called Hot EGR and when and EGR cooler is used before transferring the exhaust gases it is called cooled EGR. Also, depending on the operating pressure, there are two types of EGR used: low pressure loop EGR and high pressure loop EGR. Nowadays, most diesel engine uses cooled EGR technique to reduce the exhaust gas temperature before sending it into the intake manifold, resulting in higher EGR rates and lower operating temperatures, hence even lower NOx formation [5]. By increasing the portion of low pressure EGR for three operating conditions under steady-state engine operations, resulting in lower pumping losses and intake charge temperature, the relationship between NOx emission and break specific fuel consumption could be improved [6]. By incorporating cooled EGR, the NOx emission decreases from 850 ppm to 310 ppm at 20% EGR rate without significant penalty on brake specific fuel consumption and HC emission [7]. Higher cooling rates result in decreased NOx emission comparably at all loads. The cooling of the combustion chamber reduces the temperature, thus reducing NO_X emissions. Optimum EGR rate is observed at 15% as there is a noticeable increase in thermal efficiency as well as decrease in harmful emission [8]. With the increase in the load, the NO_X reduction is high, and the main reason behind the reduction is the reduced oxygen concentration and also decreased flame temperature in the diesel engine combustion chamber. Oxygen is available in ample amount at part load. But at higher loads, oxygen reduces remarkably, that is why NOx reduced more at higher loads than part loads [9]. At low EGR rates, there is no change in the engine power and torque with fluctuating EGR. But at higher value of EGR rates, both the power and the torque decrease sharply because the combustion gets worse and internal power work increases [10]. The effect of EGR on a variable compression ratio engine is positive as the brake thermal efficiency of the engine is increased at higher loading condition without affecting the volumetric efficiency [11]. This could happen due to reigniting of hydrocarbon in the combustion chamber

sucked in during recirculation [12]. The local NO concentration increases when the residual gas enters following start of combustion to a peak point where burned gases equivalence ratio varies from a rich mixture to a lean mixture [13]. Turbo-charged engine develops less NOx as compared to normal engines and its value ranges 0.4–1.2 kg/hr at 100% load [14]. The NOx emission has been reduced substantially from a value of 662 ppm to 503 ppm, respectively, using karanja biodiesel as fuel with 15% EGR value [15].

From the above literature review, it has been found out that EGR is the most prominent technique for reduction in the NO emission. So keeping in view, our main objective is to design and develop a cooled EGR surge tank set-up for measuring the engine performance and emission characteristics.

2 Experimental Set-up

In this research work, an air-cooled single cylinder marshal diesel engine has been used at a consistent speed of 1500 rpm. The set-up used in this work consists of EGR surge tank, air filter, rotameter, water pump, thermocouple arrangements, control valves and EGR flow pipes. The concept of surge tank is introduced to damp the vibrations and fluctuations caused by the recirculated exhaust gases which in return provides a smooth flow of gases into the intake manifold (Table 1).

Aluminium ranks are used for the development of surge tank set-up. The flow of the exhaust gases recirculated is controlled by the control valves. High temperature exhaust gases are cooled down to a certain limit by the cold water, flowing through the surge tank. An air filter is used to purify the cooled exhaust gases by trapping some of the pollutants and fed the clean air back into the engine. A rotameter is utilised to measure the discharge of recirculated outlet gases. Thermocouples are installed at the two ends to measure the hot gas temperature at the exhaust manifold and cold gas temperature at the inlet manifold. The diesel is fed to the graduated

Table 1 Diesel engine specifications

Sl. No.	Description	Data
1.	Name of engine	Marshal engine
2.	Type of engine	Vertical 4 stroke, CI diesel engine
3.	Number of cylinders	Single cylinder
4.	Bore	80 mm
5.	Stroke	110 mm
6.	Cubic capacity	0.555 L
7.	Compression ratio	16.5:1
8.	Rated power	5 BHP
9.	Type of cooling	Air cooled

cylinder and the volumetric flow was measured using stop watch. The load on the engine is applied with a load bank and multimeters are used to measure current and voltage at the corresponding loads. An AVL DIGAS 444 gas analyser is employed to analyse the concentration emission such as CO, CO_2, HC and NO from the engine. The experiment is conducted at three different loading conditions: no load (0 W), half load (1200 W) and full load (2400 W). The test is performed for 10 min on each load with different EGR percentages regulated by the control valves and the fuel consumption is measured with the help of measuring cylinder for ten minutes. Following steps were performed during the experiment:

1. The engine was made to run on diesel without incorporating EGR, to create the baseline data at different loads.
2. To calculate the performance parameters current and voltage were noted down for the corresponding loads.
3. Emission readings were taken from the gas analyser at each load.
4. EGR set-up was installed and continuous flow of water is provided for the cooling of exhaust gas.
5. All readings were obtained while using EGR set-up.
6. Emission readings and performance parameters were calculated using respective formulae and the results were compared.

Figure 2 shows the developed EGR set-up which has been utilised for the experimentation including performance parameters and emission characteristics. It consists of arrangement including the surge tank and rotameter to measure the flow of exhaust gas inside the combustion chamber (Fig. 1).

3 Development of Surge Tank

Figures 3 and 4 show the designed surge tank set-up. The set-up consists of aluminium tanks and pipes of copper and steel. The smaller tank is of five litres and placed inside the bigger tank of capacity 10 litres. The copper pipe is concentric with the steel pipe and the set-up acts as a concentric tube heat exchanger having the copper pipe inside the steel pipe. The copper pipe goes through the outer tank and is connected to the inner tank while the steel pipe is connected to the outer tank. In the developed heat exchanger set-up, the hot exhaust gases flow through the copper pipe and gets cooled by the water flowing through the steel pipe. The unsteady flow of exhaust gases causes unwanted vibrations in the set-up and, therefore, has to be eliminated. The sudden increase in the flow area helps in maintaining a steady flow, which eliminates the vibrations. Hence, the surge tank set-up is utilised to decrease the vibrations and to provide a continuous flow of the gases.

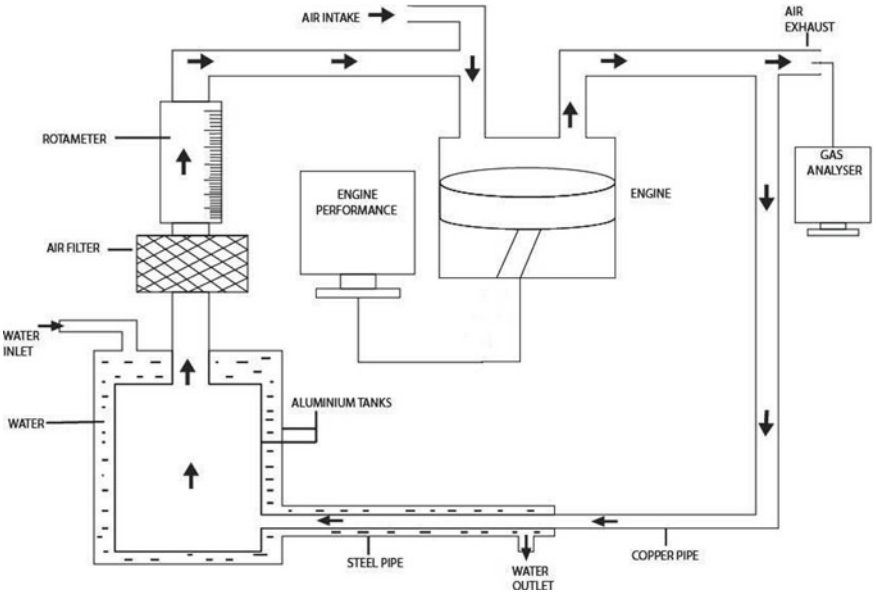

Fig. 1 Schematic diagram of the surge tank set-up

4 Results and Discussions

The diesel engine was being run at various loading conditions, also with varying the EGR % ranging from 0 to 20% for investigating engine performance and emission parameters. The diesel engine performance and emission have been represented graphically for brake thermal efficiency, brake specific fuel consumption, volumetric efficiency, and various emission parameters.

4.1 Performance Parameters

Brake-Specific Fuel Consumption. Figure 4 indicates the variations in break-specific fuel consumption with increasing EGR rate at different loads. As the EGR is increased, there is a notable improvement in fuel usage on high loading conditions. Reduction of pumping work could be the major reason for that effect as the amount of EGR rate is increased. Due to the reduction in pumping work, the entire inlet charge passed the throttle. This has led to increase in the value of break-specific fuel consumption.

Break Thermal Efficiency. The break thermal efficiency for various loads have been shown in Fig. 5. The brake thermal efficiency has been found using the ratio of actual brake work to the diesel fuel inlet as input value. It has been found out that

Fig. 2 Developed set-up with surge tank

with the increase in the EGR% the brake thermal efficiency also increases. The main reason is the induction of exhaust gases in the intake manifold.

Volumetric Efficiency. Volumetric efficiency indicates the breathing capacity of an engine. The power output of the engine totally depends upon the utilisation of the air. Figure 6 shows the variation in volumetric efficiency of the test engine with different EGR rates at different loads. It has been observed from the experimentation that with the increase in EGR rate, volumetric efficiency decreases. Reason behind the reduction in efficiency is the replacement of fresh air charge with the exhaust gases due to the implementation of EGR. The intake air mass flow decreases with the increase in EGR rates.

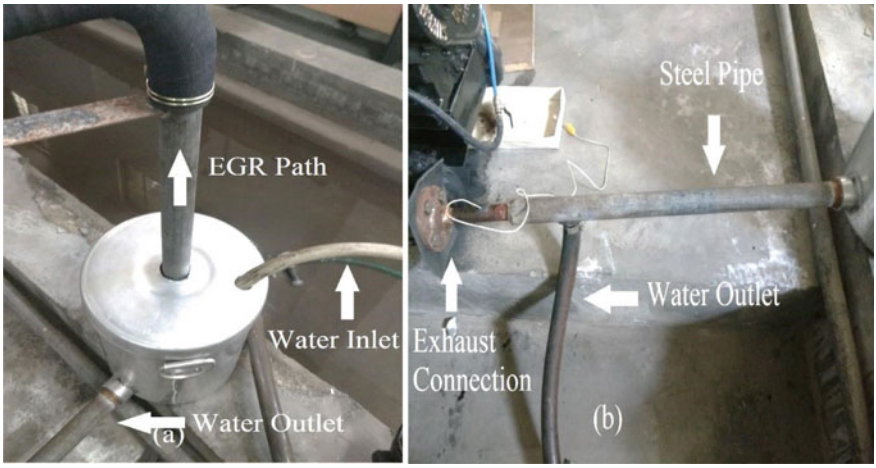

Fig. 3 **a** Pictorial representation of surge tank with inlet and outlet water flow **b** Copper with steel pipe connections transferring EGR and water flow

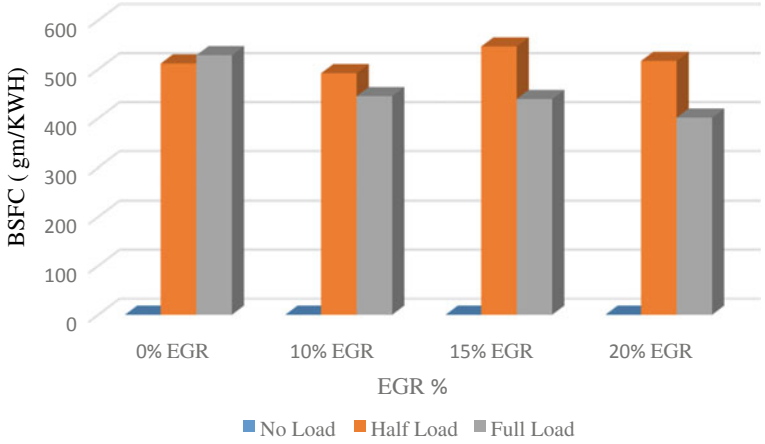

Fig. 4 Variation in BSFC with different EGR rates on different loads

4.2 Emission Parameters

NO Emission. Figure 7 shows the difference in the NO emission values by using EGR and it is has been observed that with increase in the EGR%, the NO emission decreased. The reason behind that could be the reduced flame temperature and oxygen concentration in combustion chamber. Flame temperature is reduced because recirculated exhaust gas helps in increasing the specific heat of the intake air. It is clear that without EGR, NO emission had a maximum value of 290 ppm at full load

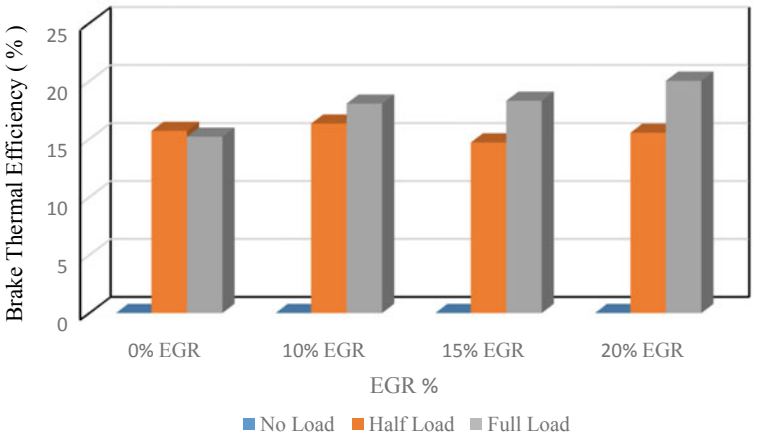

Fig. 5 Variation in BTE with different EGR rates on different loads

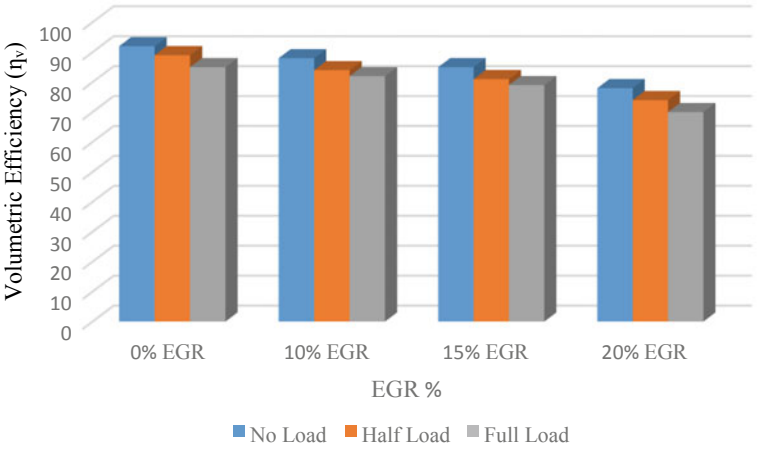

Fig. 6 Variation in volumetric efficiency with different EGR rates at different loads

and after using 20% EGR, it is reduced to 83 ppm. Maximum reduction of 90.18% is observed at 10% EGR on half load.

HC and CO Emission. Figures 8 and 9 shows the variation in HC and CO emission with EGR rates at different loading conditions. It is found that the amount of HC and CO increases with increase in the EGR rate. This could be due to reduction in oxygen concentration which results in rich air fuel mixture at different places inside the combustion chamber. This heterogeneous mixture does not combust completely and results in higher HC and CO emissions.

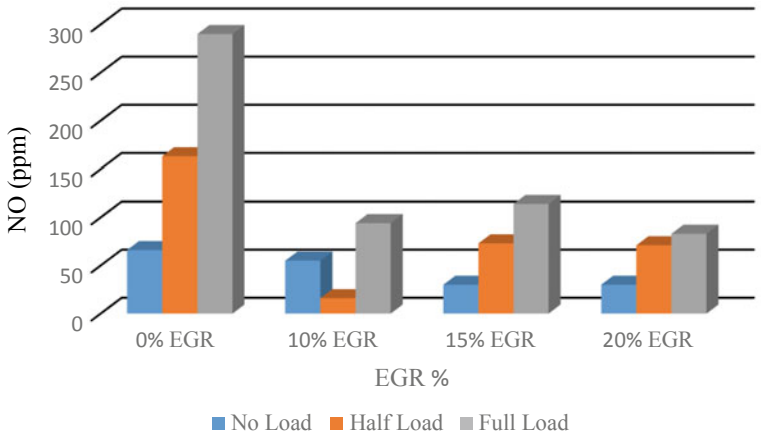

Fig. 7 Variation in NO emission with different EGR rates at different loads

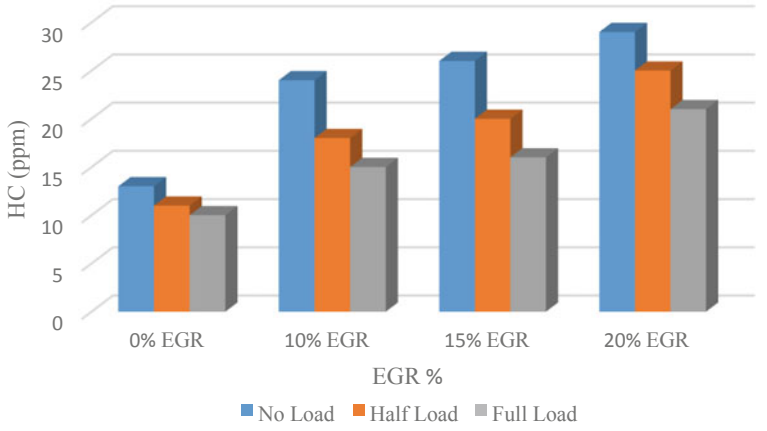

Fig. 8 Variation in HC emission with different EGR rates at different loads

5 Conclusions

The experimental work was carried out on single cylinder diesel-fuelled CI engine at a steady speed of 1500 rpm. The developed cooled EGR set-up was utilised to control the flow of EGR and also reducing the NO emissions. From the experimental investigation, following conclusions are emerged.

- The engine performance parameters (a) BSFC: it increases with increase in the percentage of EGR and is maximum at 15% EGR, i.e. 546.17 gm/KWh, (b) BTE: it also increases with increase in EGR rate and at 20% EGR it is maximum, i.e.

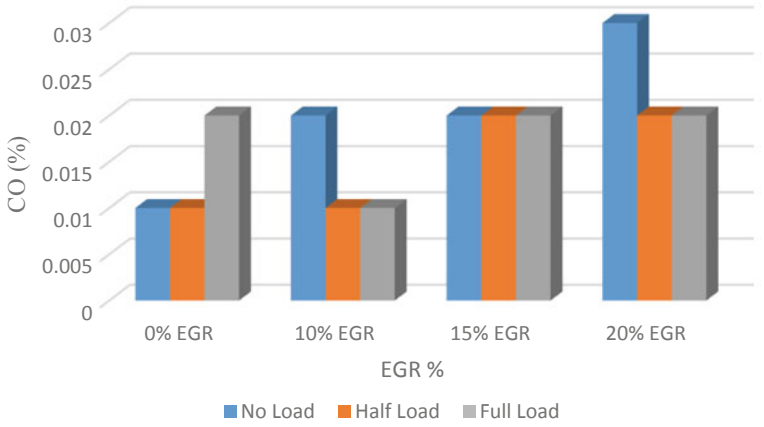

Fig. 9 Variation in HC emission with different EGR rates and different loads

20.03%, (c) VE: Volumetric efficiency decreases with increase in EGR rate and it is minimum at 20% EGR, i.e. 70%.

- The NO emission is significantly reduced through the utilisation of cooled EGR. With 20% EGR, the NO emission was reduced by 71.37% at full load without effecting the performance of the engine.
- The surge tank set-up has with aluminium and copper material has proven to be an effective set-up for transferring the exhaust gases and temperature reduction device for achieving the desired engine temperatures.

References

1. Dangar H, Rathod GP (2013) Combine effect of exhaust gas recirculation (EGR) and varying inlet air pressure on performance and emission of diesel engine. IOSR J Mech Civ Eng (IOSR-JMCE) 6(5):26–33
2. Hebbar GS, Bhat AK (2013) Control of NOx from a DI diesel engine with hot EGR and ethanol fumigation: an experimental investigation. Int J Automot Technol 14(3):333–341
3. Maiwada Badamasi, Muaz Nura, Musa Gali Hurana (2016) Diesel engine modification techniques to minimise its exhaust emission (theoretical survey). Int J Theor Appl Res Mech Eng 5:2319–3182
4. Amritkar AB, Badge N (2016) Effect of exhaust gas recirculation (EGR) in internal combustion engine. Int Res J Eng Technol 3(3):1180–1185
5. Bedar P, Kumar GN (2016) Exhaust gas recirculation (EGR)—Effective way to reduce NOx emission. J Mech Eng Biomech 1(2):69–73
6. Park Y, Bae C (2014) Experimental study on the effects of high/low pressure EGR proportion in a passenger car diesel engine. Appl Energy 133:308–316
7. Wankhade AM, Thakur SB, Sapre PG (2014) Emission and performance characteristics of single cylinder diesel engine using cold EGR. Int J Eng Sci Res Technol 3(12):156–162
8. Sujeeva Raju G, Naresh Babu G (2017) Improve in the emission characteristics of diesel engine using EGR at different cooling rates. Int Res J Eng Technol 4(6):1566–1571

9. Hebbar GS (2014) NOx from diesel engine emission and control strategies-a review. Int J Mech Eng Robot Res 3(4):471–482
10. Cheng W, Li X, Yi X (2017) Influence of exhaust gas recirculation on low-load diesel engine performance. Wuhan Univ J Nat Sci 22(5):443–448
11. Bharat NK (2015) Effect of exhaust gas recirculation on engine performance and emission on variable compression ratio engine. Int J Innov Eng Res Technol ICITDCEME'15 Conference Proceedings, pp 1–5
12. Jagadish MS, Roshan RD, Nikhilesh DB, Amit VP (2016) Case study of exhaust gas recirculation on engine performance. IOSR J Comput Eng Conf Proc, pp 13–17
13. John H (1988) Internal combustion engine fundamentals. Mc Grawhill
14. Domkundwar VN (2017) Internal combustion engines. Dhanpat Rai and Co. (P) Ltd
15. Hira J, Sharma R, Kamboj K, Kumar V, Sharma P (2019) NOx emission in diesel engine through developed cooled EGR setup. In lecture notes in mechanical engineering, advances in interdisciplinary engineering, Springer. pp 1–13

Numerical Study of Swan Neck Rear Wing for Enhancing Stability of Ground Vehicle Bodies

A. Mathur, A. Mahajan, A. Aggarwal, C. Mishra, and A. Roy

Abstract Lift generated on ground vehicles moving at high speeds has always been a major concern for aerodynamicists and designers. A proven way out is to use passive lift mitigating strategies for generating additional downforce on the vehicle for regaining the loss of stability. A rear wing helps in rectifying such trouble of handling cars at high speeds by generating negative downward force which improves overall stability of the vehicle. A new dual wing spoiler is designed for the mentioned purpose in this work. The spoiler is fitted on a generic ground vehicle having slant edge angle of 35°. Innovative swan neck linkage has been used to connect the rear wing with the vehicle. Numerical investigations have been performed on symmetric models of the vehicle with and without the new wing at different length-based Reynold's numbers ranging from 1.98×10^6 to 4.76×10^6 using two-equation realizable k-ε eddy-viscosity turbulence model. The observed data showcased an increment of 20% in drag coefficient on the entire vehicle. At the same time, it was found that there is a drastic decrement in lift coefficient in comparison to the baseline values of the vehicle, albeit it showed a minor increase with increase in Reynold's number.

Keywords Rear wing · Swan neck · Turbulence modeling · S1223 · Ahmed body

A. Mathur · A. Mahajan · A. Aggarwal
Department of Mechanical and Automation Engineering, Maharaja Agrasen Institute of Technology, GGSIP University, Delhi, India

C. Mishra
Trontek Electronics Pvt. Ltd., Delhi, India

A. Roy (✉)
Department of Mechanical Engineering, Indian Institute of Technology, New Delhi, India
e-mail: aditya.roy1510@gmail.com

L. M. Das et al. (eds.), *Emerging Trends in Mechanical Engineering*, Lecture Notes in Mechanical Engineering, https://doi.org/10.1007/978-981-15-8304-9_14

1 Introduction

Safety and stability of vehicles existing in the modern world have been among the most critical design considerations, besides making them more energy efficient. Safety of passengers and driver is further compromised when we deal with the case of vehicles moving at very high cruising speeds. This is primarily because of high amount of lift generated due to flow of air over the vehicles at the considered range of velocities. Numerous cases of accidents have been reported till date in the motorsports industry due to instabilities caused as a result of high speed. Thus, in addition to a judicious need to increase the efficiency and performance of vehicles, attention is warranted by research and studies on active or passive lift prevention mechanisms. The aerodynamic design of a vehicular body is of prime importance as it is directly associated with ameliorating the performance and thus contributing significantly for a greener and safer transportation system. As a majority of the transportation system consists of cars and other ground vehicles, this study focuses on improving the aerodynamic performance of simplified ground vehicle body, in other words, also known as Ahmed Body [1], which consistently replicates the realistic car geometry flow phenomena. Thus, analysis on this body can be generalized for most of the ground vehicle bodies.

Although a decent amount of research has already been done on Ahmed body [2] with flaps for lift mitigation, such as the one done by Beaudoin and Aider, and Katz [3, 4], we perform computational simulations on a novel rear wing design fitted on to an Ahmed body in this study. Downforce generated by any passive method counteracts the effect of lift and contributes to the stability of the body. To generate downforce, there are certain aerodynamic modifications possible on the surface of the vehicle which improve the flow of air over the vehicle. Spoilers are the devices which are installed at the rear of a vehicle, also known as rear wings and they contribute in generating a significant amount of downforce as quoted by Toet [5]. In this work, we analyze the effect of using an innovative swan neck design [6] of rear wing on Ahmed Body [2]. Hamut et al. [7] elucidated that using a spoiler makes flow separation occur further behind the vehicle. Effect of the proposed wing design and its repercussion on flow separation and finding the resulting changes in drag characteristics is one of the primary objectives of the present work. Whenever a rear wing is installed on a ground vehicle for increasing downforce on the same, a certain amount of penalty in the form of drag addition needs to be paid. This is mainly because of two contributing factors, namely frontal area increment and wake region modification. Both, increase in frontal area and inception of vortices resulting alterations in wake zone of the vehicle translate to additional form drag.

Several design decisions on aerodynamics of the rear wing were carefully analyzed, as will be explained in detail in the upcoming section. Numerical simulations have been conducted on baseline as well as modified cases of Ahmed body to carefully study the enhancement of downforce alongside the drag penalty. Slant angle for the Ahmed body has been taken as 35° throughout this study because of the proven ability of turbulence models to accurately capture the flow separation

caused over backlight region [8–11]. Rear wing which is used for spoiler design carries the profile of S1223 airfoil, which was first proposed by Selig and Guglielmo [12]. Inception of vortices emanating from the rear wing and changes in wake region compared to baseline case and its effect on drag has been presented for Reynold's number in the range of 1.98×10^6 and 4.76×10^6, both values included.

2 Design

The design of rear wing under consideration will be explained in this section. For high-speed sports car, a rear wing helps in mitigating lift by creating a downforce component that gives better traction control thus improving handling. A dual element wing is selected for the airfoil. Multi element wings create more downward force as compared to a single element wing and have a better downforce to drag force ratio. For designing the wings of the spoiler, S1223 airfoil is chosen [12], the profile of which is shown in Fig. 1. Since the chosen airfoil is an asymmetric airfoil, it was turned upside down in order to generate negative lift. The width of the upper wing is 0.75 times the width of the lower wing. The upper wing is inclined at 7° angle of attack and the lower wing is at 0° angle of attack. The lower wing has been kept at the mentioned attack angle in order to reduce the risk of excessive induced flow separation at the rear of the car while the upper wing has been inclined at the mentioned angle of attack for generating adequate amount of negative lift. The choice of airfoil promises ample amount of downforce component even at 0° attack angle. Inclining the upper wing at the mentioned attack angle ensures a greater amount of effective surface area for encounter of fluid which further translates to higher amount of lift.

In a transverse sense, span of the dual wings is equal to width of the Ahmed body. As can be seen from Fig. 2, strategically shaped end plates have been provided at the sides of both the wings, keeping in mind certain aerodynamic considerations. In case of rear wings in automotive applications, high-pressure region is generated at the top surface of the wing and a resulting low-pressure region is generated at the lower surface of the wing. Air would always have a tendency to move from a region of high-pressure to a region of low-pressure due to an assumption of incompressibility of fluid. Because of its motion of free flow, air tries to move from the top face towards bottom face from the sides. This results in additional vortices from the sides of the upper and lower wings. Allowing this would further increase the intensity of C-pillar vortices emanating from the vehicle. Although these vortices cannot be completely

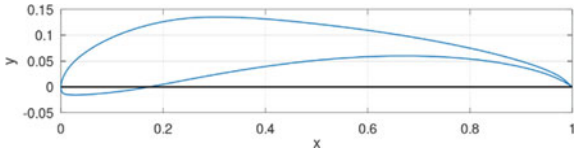

Fig. 1 Profile of S1223 airfoil with chord length of 1 m

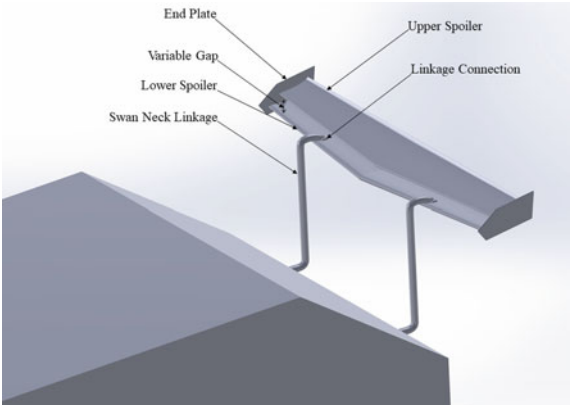

Fig. 2 Design of swan neck rear wing

prevented, employing end plates restricts their formation of some extent, thus further enhancing the downforce to drag force ratio.

The placement of this dual wing on the Ahmed body is done with the help of swan neck linkage. According to classical laws of flow physics, any hindrance in the free path of fluid flow would generate a wake region behind the hindrance body at the considered range of Reynold's number. Thus, it becomes needless to say that the linkages establishing connection between the wing and Ahmed body would themselves produce their own wake region which happens to lie in the wake region of the Ahmed body as a whole. A swan neck linkage reduces the induced drag component by shifting its wake region away from that of the vehicle body. This helps in reducing the adverse pressure gradients developed. As a result, the additional drag penalty is reduced to some extent by using swan neck linkages. This governs our choice of selection of the same in the wing design. The two connections of linkage on the wings was at lower wing where each connection was at one fourth length of the wing from sides. Placement of the spoiler was 30 mm above the roof of Ahmed body.

3 Grid Discretization and Numerical Solution

A cuboidal computational domain was defined around the vehicular body with dimensions set according to literature [13]. In order to avoid the risk of flow recirculations at the domain outlet, domain length behind the Ahmed body was taken as five body lengths (one body length is equal to 1044 mm, which is the total length of the Ahmed body). In the front it was taken as three body lengths whereas extents towards sides and the top were kept as two body lengths. It is necessary to define several smaller regions within the domain according to priority of mesh refinement. These are called bodies of influence. In our analysis, three bodies of influence were used for refining the mesh in regions vicinity of the car and separately focusing on underbody and

wake zone, respectively. Finest mesh sizing was provided to the wake region of influence, followed by underbody and car box regions of influence respectively. Hexahedral structured elements were employed for capturing the boundary layer flow phenomena around the vehicular body whereas unstructured tetrahedral elements were used for discretizing the domain at all locations away from the boundaries of the car. All the tetrahedral elements were converted to polyhedral elements, the usage of which reduced total number of cells in the domain, thus decreasing computational effort. Moreover, polyhedral elements improved the overall mesh quality thus resulting in more accurate solutions and faster convergence. Literature suggests that the eddy-viscosity turbulence models are adequately well equipped in capturing the flow phenomena associated with an Ahmed body having slant angle of 35° [8]. The realizable k-ε model proposed by Shih et al. [14] has been employed in the present work for conducting numerical simulations and modeling the Reynold's stresses according to Boussinesq hypothesis. In this model, while the equation for turbulent kinetic energy (k) remains identical, a new equation for turbulence dissipation rate (ε) and a new formulation for the eddy viscosity was implemented. The eddy-viscosity is no longer a constant but rather variable, depending on mean rate of rotation tensor. This allowed for a better ability of the model to catch separated flow regimes fairly accurately. In addition to the fundamental equations shown by Eqs. (1) and (2), all the other model specific relations can be referred to from the work of Shih et al. [14].

$$\frac{\partial}{\partial t}(\rho k) + \frac{\partial}{\partial x_j}\left(\rho k u_j\right) = \frac{\partial}{\partial x_j}\left[\left(\mu + \frac{\mu_t}{\sigma_k}\right)\frac{\partial k}{\partial x_j}\right] + G_k + G_b - \rho\varepsilon - Y_M + S_k \quad (1)$$

$$\frac{\partial}{\partial t}(\rho \varepsilon) + \frac{\partial}{\partial x_j}\left(\rho \varepsilon u_j\right) = \frac{\partial}{\partial x_j}\left[\left(\mu + \frac{\mu_t}{\sigma_\varepsilon}\right)\frac{\partial \varepsilon}{\partial x_j}\right] + \rho C_1 S_\varepsilon - \rho C_2 \frac{\varepsilon^2}{k + \sqrt{\nu\varepsilon}} + C_{1\varepsilon}\frac{\varepsilon}{k} C_{3\varepsilon} G_b + S_\varepsilon \quad (2)$$

Standard velocity inlet and pressure outlet boundary conditions were specified in the domain. Velocity was varied from 27.78 m/s to 66.67 m/s keeping density, dynamic viscosity and characteristic length identical. Density of air was set as 1.225 kg/m^3 and dynamic viscosity was taken as being equal to 1.79×10^{-5} kg/m-s. No-slip conditions were specified for the walls. Second order discretization on pressure-based coupled solver ensured accuracy in solution, the convergence criterion for which was set as 10^{-4} for continuity equation and 10^{-6} for all the other equations. Grid dependence study was performed on the Ahmed body geometry with rear wing attached using four types of grids having different element sizes. The extra-coarse, coarse, medium and fine meshes consisted of 1.8 million, 2.5 million, 3.4 million and 4.1 million cells respectively. Error percentage between drag coefficients predicted by extra-coarse and coarse meshes was 2.67%, that between coarse and medium meshes was 0.91% whereas that between medium and fine meshes

was a mere 0.16%. Considering the factors of minimal difference between results produced by medium and fine grids and increase in the capacity of computational resources required, the medium grid configuration was chosen for carrying out all the simulations.

4 Results and Discussion

This section discusses the results obtained by implementing a dual rear wing with swan neck linkages on an Ahmed body. Results will be talked about pointing out clear references with suitable contours obtained from CFD simulations. Finally, a note on drag and lift variations will be presented and compared with baseline Ahmed body simulations. As mentioned above, calculations were carried out for eight values of Reynold's number ranging from 1.98×10^6 to 4.76×10^6, both values included. Experimental validation was conducted for baseline case of Ahmed body without spoiler with the work of Meile et al. [15] who conducted experimental as well as numerical investigations a simple Ahmed body having 25° and 35° of slant angle. They carried out experiments in an open test section wind tunnel with closed return. We found a disagreement of 0.43% in value of drag coefficient predict by our numerical model from the reference experimental values, which instilled in us motivation to proceed with our numerical solution setup. It is to be noted that all contours shown in this section are for cases having inlet velocity of 44.44 m/s (160 kmph). This has been done to maintain uniformity and avoid confusions while referring to the figures.

Figure 3 shows velocity contours plotted on the symmetry plane for baseline and new configurations. Velocity contour for the baseline case indicates a fully detached flow forming the wake region behind the vehicle. An important point of difference may be pointed out between Fig. 3a and b. It is evident that the wake region formed in case of Ahmed body having rear wing is significantly bigger than baseline case. This

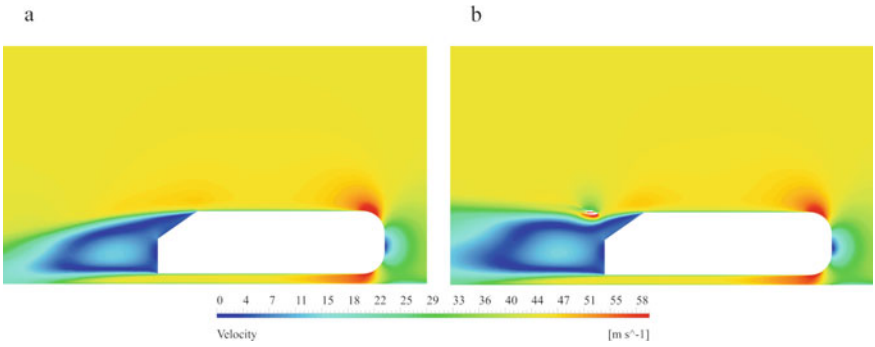

Fig. 3 Velocity contour on symmetry plane at 44.44 m/s velocity for **a** baseline and **b** modified case

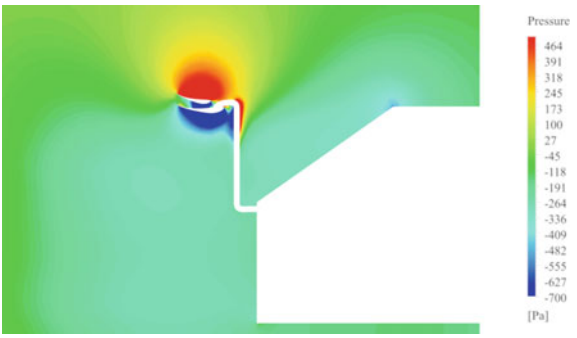

Fig. 4 Pressure contour on a plane passing through center of linkage

is because of a multitude of reasons. Firstly, airstreams follow a diverging path after interacting with the wing and secondly, airfoil theory comes into picture when we consider the aerodynamics introduced by rear wing airfoils. When airstreams hit the leading edge of the wings, some amount of air flows towards the top surface while some turns towards the lower surface. High velocity region can be seen beneath the airfoil and low velocity region can be seen as being existent on the upper surface of both the wings. The lower wing introduces a highly negative low-pressure zone near its lower surface and this explains why an appreciable amount of air is suctioned towards it, thus increasing the size of the wake region. Figure 3b also shows how flow remains attached on the lower surface of the lower wing because of it being inclined at 0° attack angle. On the other hand, relative flow separation can be seen to be taking place on lower surface of the upper wing because of its higher angle of attack. Although this translates to a slight increase in drag component, it is compensated by an even more significant increase in downforce component. Curves showing drag and lift coefficients at various Reynold's numbers will be presented in the upcoming paragraphs. Figure 4 shows pressure contour mapped on a plane passing through one of the linkages. After passing through the backlight region, airflow encounters the linkages prior to coming in contact with dual wings. Stagnation zone is thus formed at the onset of linkages, which is represented here in red colored high-pressure region. A very interesting flow phenomenon taking place here is that while the stagnation zone should be uniform for the whole linkage, we can rather see an uneven distribution of high-pressure zone only towards the top. This is primarily because of the interaction with reversed airstreams approaching the backlight region from back of the vehicle. Proof of this fact can also be seen from the gradually increasing intensity of high-pressure zone as we move up the surface of linkage. In case of simple flow past a cylinder, high-pressure stagnation zone is encountered at the front of the cylinder whereas a low-pressure wake region is realized at the back. The example of a cylinder was taken as reference to explain the flow physics taking place at the back of the linkage. Linkage-contributed wake region can be seen as being proportional to the stagnation zone developed. A reduction in the extent and size of linkage-contributed wake region results in a decrement in drag addition in our case. This itself is the point of advantage of using swan neck linkages for establishing connection between rear

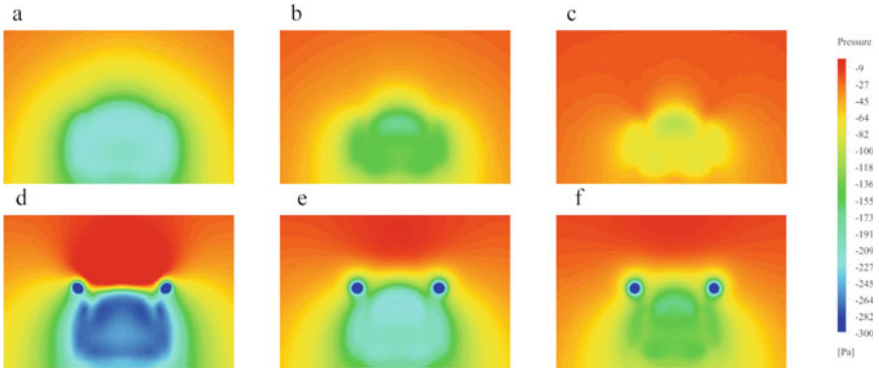

Fig. 5 Pressure contour seen from back of the car at distance of 0.15 m **a**, **d**, 0.25 m **b**, **e** and 0.3 m **c**, **f** for baseline and modified cases

wing and the car. Had the linkage been moved further downstream to be connected to the lower surface of lower wing, the stagnation and wake zones would have been larger thus contributing to a greater addition in drag. Moving towards the wings, we see the formation of a high-pressure zone on top of the upper wing. This is because of the uninterrupted encounter of airstreams onto the top surface of the wing which primarily contributes to downforce addition. In a general sense, the lower wing having a similar airfoil profile must also generate an identical downforce component as a result of pressure distribution but we see that this is not the case. The top surface of the upper wing has a high-pressure region and the lower surface has a low-pressure region which is tantamount to negative lift creation. The effect of low-pressure region of upper wing is translated to the top surface of the lower wing. However, a significant low-pressure region is seen in the vicinity of bottom face of the lower wing. A cumulative effect of high and low-pressure gradients generates a significant amount of downforce as will be evident from lift coefficient plot.

Figure 5 shows pressure contours mapped in the wake region on planes at the back of the vehicle body for both, baseline (Fig. 5a–c) and rear wing (Fig. 5d–f) cases respectively at three distances of 0.15 m, 0.25 m and 0.3 m from the rear face of the car. Although of low intensity pressure gradients, one can see the two C-pillar vortices emanating from two sides of the car at the rear in baseline case. It can be pointed out from modified cases that pressure gradient associated with the wake region in this case is more adverse than baseline case and also that wing vortices can be seen originating from sides of the wings. Both of these factors add up to unavoidable drag increment on employing a rear wing which in our case, has not been excessively high because of the design decisions taken. Effect of wake region dies out as we keep on moving behind the car. It may be said that rear wing case shows its effect till farther back. This kind of critical difference between pressure distribution at the rear of the vehicle points to the reasons behind drag addition as a result of wing implementation.

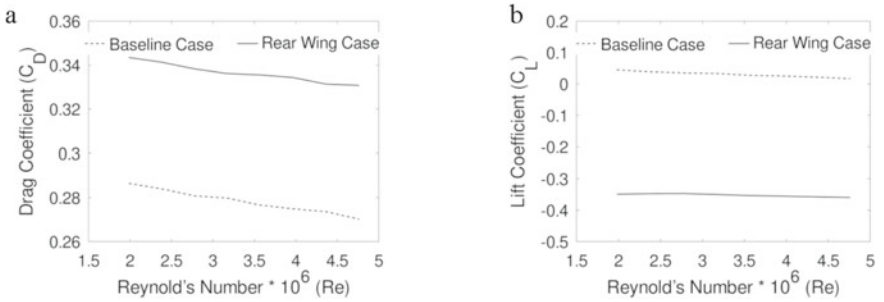

Fig. 6 Plot of **a** C_D versus *Re* and **b** C_L versus *Re* for both cases

Figure 6 shows variations of lift and drag coefficients for both the investigated configurations (black for baseline case and red for rear wing case) at all considered Reynold's numbers. Drag and lift plots follow an almost constant variation along the investigated range of Reynold's numbers and this follows the prescribed trend by Bayraktar et al. [16] for Ahmed body. Mean percentage increase in drag coefficient is found to be 20.87% which is subject to variation based on slant angle of the Ahmed body. While there is some increase in wind resistance due to increment in drag coefficient, there is a demonstrated addition in downforce as can be made out from the negative lift coefficients. Since, the 35° slant angle case is a low-lift configuration, it would be an exaggeration to point out the percentage decrement in lift coefficient. It can be seen that there is a significant decrease from an average value of 0.03 to −0.35. In realistic car geometries, such an extent of lift decrement at high cruising speeds would ensure both safety and stability. This kind of a rear wing design not only helps in improving driving safety in motorsport cars, but also common passenger cars travelling at relatively lower cruising speeds.

5 Conclusion

Design of a dual rear wing with aerodynamically shaped end plates has been proposed in this study which is fitted on to the body of generic ground vehicle with the help of a swan neck linkage. Benchmark simulations have been reported for validation of numerical model used. Effect of changes seen in the wake region compared to baseline case of Ahmed body has been pointed out and carefully studied. While the resulting increase in size of wake region along with the inception of wing vortices translate to an additional drag on the body, placement and design of the linkage help in limiting the linkage-induced drag to some extent, as was seen above. In addition to this, a drastic decrement in lift coefficient was seen which proves the fact that utilizing such a wing design having an S1223 airfoil with the said linkage would

prove to be very useful in enhancing the overall stability of a vehicle moving at high cruising speeds. This study provides basis to car designers for considering the usage of an S1223 airfoil in a dual-wing setup with swan neck linkage for enhancing the downforce characteristics of ground vehicles intended to ply at high speeds.

References

1. Ahmed SR, Ramm G, Faltin G (1984) Some salient features of the time-averaged ground vehicle wake. SAE Trans 93(2):840222—840402, 473–503
2. Ahmed SR (1983) Influence of base slant on the wake structure and drag of road vehicles. J Fluids Eng 105:429
3. Beaudoin JF, Aider JL (2008) Drag and lift reduction of a 3D bluff body using flaps. Exp Fluids 44:491–501
4. Katz J (2005) Aerodynamics of race cars. Annu Rev Fluid Mech 38:27–63
5. Toet W (2013) Aerodynamics and aerodynamic research in Formula 1. Aeronaut J 117:1–26
6. Kurec K, Remer M, Mayer T, Tudruj S, Piechna J (2019) Flow control for a car-mounted rear wing. Int J Mech Sci 152:384–399
7. Hamut HS, El-Emam RS, Aydin M, Dincer I (2014) Effects of rear spoilers on ground vehicle aerodynamic drag. Int J Numer Methods Heat Fluid Flow 24:627–642
8. Guilmineau E (2008) Computational study of flow around a simplified car body. J Wind Eng Ind Aerodyn 96:1207–1217
9. Tunay T, Sahin B, Ozbolat V (2014) Effects of rear slant angles on the flow characteristics of ahmed body. Exp Therm Fluid Sci 57:165–176
10. Rao A, Minelli G, Basara B, Krajnović S (2018) On the two flow states in the wake of a hatchback ahmed body. J Wind Eng Ind Aerodyn 173:262–278
11. Roy A, Dasgupta D (2020) Towards a novel strategy for safety, stability and driving dynamics enhancement during cornering manoeuvres in motorsports applications. Sci Rep 10(1)
12. Selig MS, Guglielmo J (2003) Low reynolds number airfoil design. J Aircr 34:72–79
13. Lanfrit M (2009) Best practice guidelines for handling automotive external aerodynamics with FLUENT 2:412
14. Shih TH, Liou WW, Shabbir A, Yang Z, Zhu J (1995) A new k-ε eddy viscosity model for high reynolds number turbulent flows. Comput Fluids 24:227–238
15. Meile W, Brenn G, Reppenhagen A, Lechner B, Fuchs A (2011) Experiments and numerical simulations on the aerodynamics of the Ahmed body. CFD Lett 3:32–39
16. Bayraktar I, Landman D, Baysal O (2001) Experimental and computational investigation of Ahmed body for ground vehicle aerodynamics. SAE Tech Pap 1

CFD and Thermal Analysis of the Flat Plate Collector—Solar Water Heater Under Steady-State Conditions

A. Bharti, B. Sharma, and M. K. Paswan

Abstract This project involves the study of the outlet water temperature, Nusselt number, heat transfer coefficient and efficiency of a flat plate collector–solar water heater having a straight riser and header set-up. Records of mass flow rate were maintained and its effects on the outlet temperature of the water and the thermal efficiency were observed. ANSYS Fluent was employed for predicting the Nusselt number, heat transfer coefficient, outlet temperature of water and efficiency using the experimental values of solar radiation, ambient temperature and the temperature of the water at the inlet. It was found that the thermal efficiency of the solar water heater increases with mass flow rate of water to achieve a long and stabilized efficiency curve. Nusselt number shows gradual increase with the increasing mass flow rate. The results were validated by the experimental results obtained from the experimental set-up situated on the roof of Mechanical Engineering Department.

Keywords Flat plate collector · Experimental · ANSYS · Efficiency · Nusselt number · Heat transfer coefficient

1 Introduction

Current energy demands are primarily derived from the fossil fuels. The demand for energy has been on the rise since the past decade. Overpopulation has led to overutilization of our natural resources and we now face the danger of depletion of these resources. To progress along the lines of sustainable development, we now have turned to renewable sources of energy; such solar energy can be harnessed using a solar flat plate collector.

A solar water heater was designed by [2] and its cost and thermal efficiency were determined. Studies and research indicated that solar flat plate collector that had metal absorber plates and covers was one of the most effective means of converting solar

A. Bharti (✉) · B. Sharma · M. K. Paswan
Department of Mechanical Engineering, National Institute of Technology Jamshedpur, Jamshedpur 831014, Jharkhand, India
e-mail: anandbharti62@gmail.com

L. M. Das et al. (eds.), *Emerging Trends in Mechanical Engineering*, Lecture Notes in Mechanical Engineering, https://doi.org/10.1007/978-981-15-8304-9_15

energy into heat in a practical and judicious manner without destroying the atmosphere [7, 8]. [9] analysed the effect of various parameters that affect the performance of the system and observed that the performance of the collector majorly depended on the type of collector and the tilt angle of the set-up. Further research by [10] and [12] showed the effect of surface coatings with different properties on the solar radiation that is incident on the collector surface and the resultant heat resistance capacity of the system. [3] employed lumped method for their studies and deduced the expression for the temperature of the working fluid along with the temperature of the absorber plate of the solar collector. [5] typified the performance of the solar collectors by carrying out studies based on the two-dimensional finite element method. [14] optimized the design parameters for obtaining the maximum performance of the solar water heater using TRNSYS.

Sultana et al. [17] used a Computational Fluid Dynamics software to examine the thermal performance of the solar collector by deducing the heat loss, radiation and convective heat transfer coefficient and went on to find the maximum overall thermal efficiency. [13] adopted a numerical method for the analysis of the single glazed flat plate collector and predicted the temperature of the water at the outlet with the help of a Computational Fluid Dynamics software. A fair agreement was obtained between the CFD results and experimental data in case of their studies. [4] employed CFD and showed that the model that was developed was successful in anticipating the performance of the system with minute errors. [11] analysed the polymer solar collectors using CFD software to examine the effect of factors, such as the rate of flow, temperatures, the solar insolation, on the thermal efficiency of the set-up. The experimental and simulation results were shown to agree fairly.

1.1 Flat Plate Collector—Solar Water Heater

A flat plate collector can be defined as a box made up of a metal that has a glazing (glass cover) on top followed by an absorber plate which is usually dark in colour. In order to reduce the heat losses, the surface of the collector (sides and bottom) is insulated. Sunlight enters the flat plate collector–solar water heater through the glass cover and falls on the absorber plate, heating it in the process. Thus, the solar energy is converted into heat energy. This heat energy is passed on to the working fluid flowing within the pipes, attached to the absorber plate. Since surface coatings, such as black paint, capture and preserve heat in an enhanced manner, absorber plates are generally painted with these coatings as shown in Figs. 1 and 2.

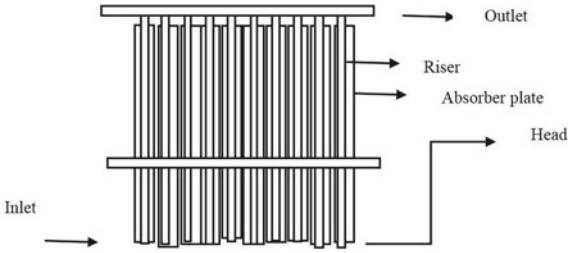

Fig. 1 Schematic of flat plate collector–solar water heater

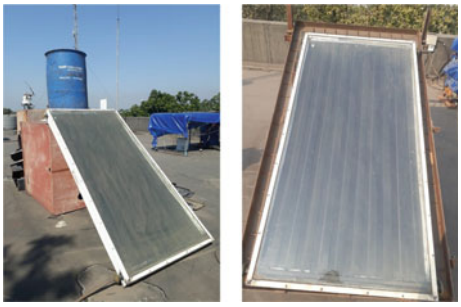

Fig. 2 Experimental set-up of flat plate collector–solar water heater

1.2 Experimental Set-up

As shown in Fig. 2, the experimental set-up consists of the following:

1. Glass plate (glazing)
2. Headers
3. Pipes/Tubes
4. Absorber plate
5. Reflector plate
6. Glass wool
7. MS Cladding
8. Water supply tank

The data in Table 1 was obtained from the experimental set-up situated on the roof of the Mechanical Engineering Department, National Institute of Technology, Jamshedpur.

The water is stored in the overhead tank. Water enters the flat plate collector from the bottom. When the temperature of the water begins to increase, the hot water rises up in the tubes owing to a decrease in its density. The cold and dense water goes down and takes its place. For a tilt angle of around 23°, this natural circulation gives rise to a small mass flow rate of about 0.0051 kg/s and the heated water eventually leaves the flat plate collector from the top at about 60 °C. The experimental data for solar radiation were obtained from SRRA for a span of 15 days from 01.09.2018 to 16.09.2018.

Table 1 Experimental data of flat plate collector–solar water heater

Dimension	Data
Glass plate thickness	10 mm
Header outer Dia.	23.6 mm
Header inner Dia.	23.4 mm
No. of tubes	10
Tube inner Dia.	8 mm
Tube outer Dia.	10 mm
Absorber plate thickness	1 mm
Absorber plate length	1695.6 mm
Absorber plate width	835 mm
Tube length	1715.6 mm
Reflector plate thickness	1 mm
Glass wool thickness	50 mm
MS cladding thickness	3 mm
Water tank height	1.2 m

2 Methodology

For the research work conducted, properties, such as density and thermal conductivity, of the absorber plate, riser tube and water were assumed to be constant. The bottom most wall had been modelled as insulated and water is incompressible in nature.

For Re <2300, the flow has been considered laminar. The number of elements for the entire domain was kept less than 51,000. A constant solar flux is applied on the absorber plate and the heat that the solar plate absorbs can be calculated from the equations suggested by [1, 15, 16]:

$$I_{\text{abs}} = \alpha\, \tau(I) \tag{1}$$

In the above equation,

I = Radiation intensity of collector, W/m^2
α = Absorptivity of the absorber plate
τ = Transmissivity of the absorber plate

Further, the efficiency η is calculated as given in [1] by:

$$\eta = \frac{Q_{\text{useful}}}{Q_{\text{overall}}} \tag{2}$$

where

$$Q_{\text{useful}} = \dot{m} c_p (T_{\text{outlet}} - T_{\text{inlet}}) \tag{3}$$

$$Q_{\text{overall}} = \text{AI} \tag{4}$$

In the above equation,

Q = Heat transfer rate, W
$\dot{m}$= mass flow rate, kg/sec
c_p= Specific heat capacity, J/kg-K
T = Temperature, K
A = Collector area, m^2

The Reynolds number Re values were calculated from the following equation:

$$\text{Re} = \frac{v \times d}{\nu} \tag{5}$$

Here, d is tube diameter in m, v is velocity in m/sec and ν is kinematic viscosity in m^2/sec. Prandtl numbers were taken from the data book. Values of Nusselt number Nu for a range of mass flow rates were obtained and heat transfer coefficients were calculated as follows:

$$\text{Nu} = 0.023\text{Re}^{0.8}\,\text{Pr}^{0.4} \tag{6}$$

Heat transfer coefficient is calculated as,

$$h = \frac{\text{Nu} \times k}{L} \tag{7}$$

Here, L is length of the tube, h is heat transfer coefficient in W/m^2-K and k is thermal conductivity in W/m-K.

3 Results and Discussion

The set-up was modelled in SolidWorks and then imported to ANSYS Fluent for thermal analysis. The number of elements was limited to 51,000 in the ANSYS Fluent (student version), as shown in Fig. 3.

For a tilt angle of 23°, when the flow rate is varied, the efficiency being a function of the mass flow rate and the outlet temperature, gradually begins to increase. But after a certain point in time, the efficiency attains a constant value of 0.47 and undergoes a long period of stabilization. As shown in Fig. 4

The plot of experimental and CFD values of efficiency vs mass flow rate curve for the SWH is shown in Fig. 4. The CFD value of efficiency gradually begins to

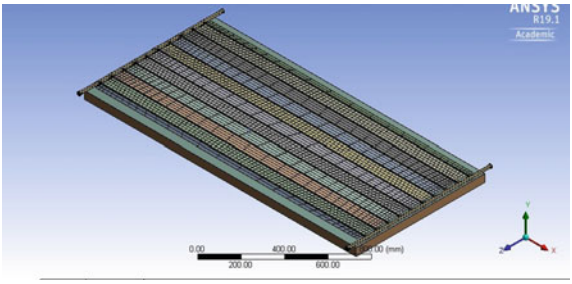

Fig. 3 Solar water heater meshed in ANSYS Fluent

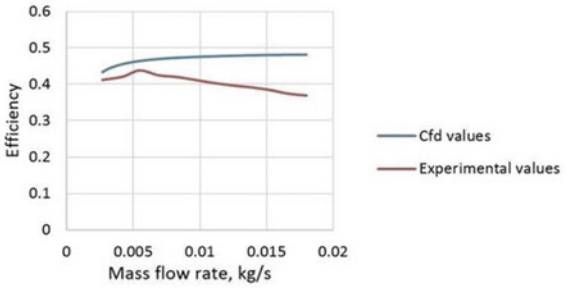

Fig. 4 Efficiency versus mass flow rate curve for the SWH

increase with an increase in mass flow rate and this trend was already reported by [6]. The experimental value of efficiency initially increases with an increase in mass flow rate and attains a peak at a mass flow rate of 0.0058 kg/s and then decreases. Since the CFD analysis was based on the assumption of a perfect contact between the absorber plate and the tube, better heat transfer occurs between the plate and the tube compared to the actual case. Hence, the experimental value of efficiency is lower than that of the CFD value.

Figure 5 shows the plot of experimental and CFD values of outlet temperature vs mass flow rate curve for the SWH. It can be seen clearly from the figure that, the outlet temperature decreases from 358 K to 308 K. With increase in mass flow rate the heat

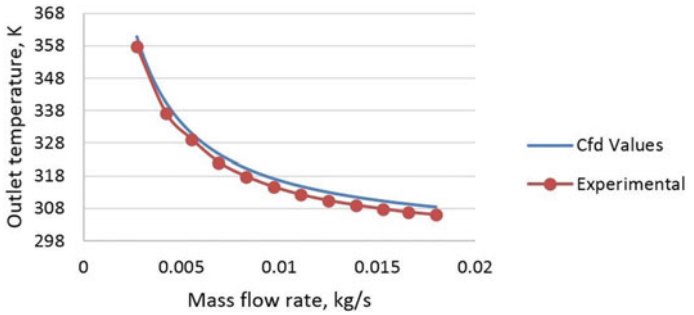

Fig. 5 Outlet temperature versus mass flow rate curve for the SWH

transfer rate increases leading to decrease in the absorber plate temperature. This results in decrease of the outlet temperature. The figure indicates good agreement of experimental and CFD values.

Plot of experimental and CFD values of Nusselt number vs mass flow rate curve for the SWH is shown in Fig. 6. The experimental values of Nusselt number were calculated using Eq. (6), and it shows a good agreement with the CFD values.

Figure 7 shows the plot of experimental and CFD values of heat transfer coefficient vs mass flow rate curve for the SWH. The thermal conductivity varies little within the given range of temperature so the heat transfer coefficient shows a similar trend as Nusselt number. The non-agreement in CFD and experimental values arises due to assumptions considered in the numerical and computational analysis like constant solar radiation, ambient temperature, steady-state analysis, properties such as density and thermal conductivity of the absorber plate, riser tube and water were assumed to be constant. These assumptions are inherently the part of experimental results.

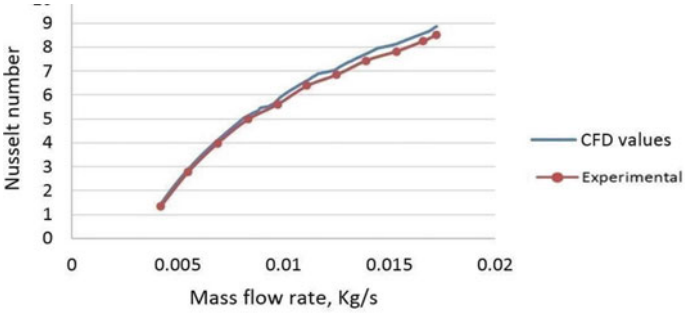

Fig. 6 Nusselt number versus mass flow rate curve for the SWH

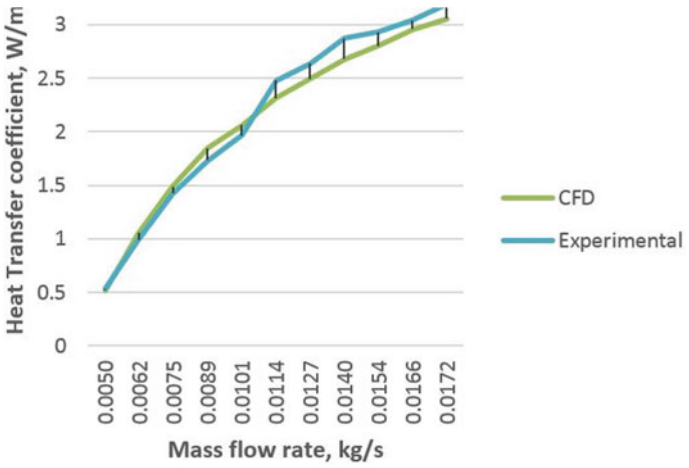

Fig. 7 Heat transfer coefficient versus mass flow rate curve for the SWH

4 Conclusions

1. The variation of efficiency with the mass flow rate for the solar flat collector was obtained at a tilt angle of 23°.
2. For a convenient outlet temperature of around 333 K, a mass flow rate of 0.0051 kg/s should be optimum for the given experimental set-up.
3. The Nusselt number increases gradually with an increase in mass flow rate in case of the solar water heater.
4. Heat transfer coefficient increases gradually with an increase in mass flow rate in case of the solar water heater.
5. The CFD results were validated with experimental results obtained from the solar water heater set-up, situated on the roof of the Department of Mechanical Engineering.
6. This current model could be implemented as a source of renewable energy in areas where sufficient sunlight is available.

References

1. Bhowmik H, Amin R (2017) Efficiency improvement of flat plate solar collector using reflector. Energy Reports 3:119–123
2. Bilgen E, Bakeka B (2008) Solar collector systems to provide hot air in rural applications. Renew Energy 33(7):1461–1468
3. Duffie JA, Beckman WA, Worek W (2013) Solar engineering of thermal processes 3, Wiley Online Library
4. Gertzos K, Pnevmatikakis S, Caouris Y (2008) Experimental and numerical study of heat transfer phenomena, inside a flat-plate integrated collector storage solar water heater (icsswh), with indirect heat withdrawal. Energy Convers Manage 49(11):3104–3115
5. Gorla RSR (1997) Finite element analysis of a flat plate solar collector. Finite Elem Anal Des 24(4):283–290
6. Gunjo DG, Mahanta P, Robi P (2017) Cfd and experimental investigation of flat plate solar water heating system under steady state condition. Renew Energy 106:24–36
7. Janjai S, Esper A, Mu¨hlbauer W (2000) Modelling the performance of a large area plastic solar collector. Renew Energy 21(3–4):363–376
8. Kalogirou S (2009) Thermal performance, economic and environmental life cycle anal- ysis of thermosiphon solar water heaters. Sol Energy 83(1):39–48
9. Kalogirou SA (2014) Flat-plate collector construction and system configuration to op- timize the thermosiphonic effect. Renew Energy 67:202–206
10. Madhukeshwara N, Prakash E (2012) An investigation on the performance characteristics of solar flat plate collector with different selective surface coatings. Int J Energy Environ 3(1)
11. Martinopoulos G, Missirlis D, Tsilingiridis G, Yakinthos K, Kyriakis N (2010) Cfd modeling of a polymer solar collector. Renew Energy 35(7):1499–1508
12. Prakash BJ, Vishnuprasad B, Ramana VV (2013) Performance study on effect of nano coatings on liquid flat plate collector: an experimental approach. Int J Mech Eng Rob Res 2:379–384
13. Selmi M, Al-Khawaja MJ, Marafia A (2008) Validation of cfd simulation for flat plate solar energy collector. Renew Energy 33(3):383–387
14. Shariah A, Shalabi B (1997) Optimal design for a thermosyphon solar water heater. Renewable Energy 11(3):351–361

15. Sivakumar P, Christraj W, Sridharan M, Jayamalathi N (Jan 2012) Performance improvement study of solar water heating system. ARPN J Eng Appl Sciences **7**:45–49
16. Sukhatme SP, Nayak J (2008) Principles of thermal collection and storage. Solar Energy, 3rd edn. Tata McGraw Hill Publishing Company, New Delhi
17. Sultana T, Morrison GL, Rosengarten G (2012) Thermal performance of a novel rooftop solar micro-concentrating collector. Sol Energy 86(7):1992–2000

Performance Comparison of Refrigerants HFO1234yf and HFO1234ze in a Vapour Compression Refrigeration System Operating Under Fouled Conditions

Naveen Solanki, Akhilesh Arora, and Raj Kumar Singh

Abstract In this paper, fouling's effect on performance of a vapour compression refrigeration system is evaluated by changing evaporator and condenser conductances individually, and simultaneously between 0 to 50% and also by variation in $T_{in,cond}$ (i.e. coolant inlet temperature of condenser at 35, 37.5 and 40 °C), for refrigerants HFC134a, HFO1234yf and HFO1234ze, while keeping the $T_{in,evap}$ (i.e. evaporator air inlet temperature at 0 °C) and constant $\eta_{cp,isn}$ (efficiency of compressor, i.e. 65%). A simulation programming is done on EES for computing the results. It is observed that the decrease in COP is more when conductances vary simultaneously in comparison with evaporator and condenser conductances that are varied individually, although fouling of condenser has larger effect on W_{cp}%, as it increases up to 9.12 and 7.41 for refrigerants HFO1234yf and HFO1234ze, whereas for refrigerant HFC134a, its value increases up to 7.38 with varied coolant inlet temperature of condenser ($T_{in,cond}$). It is observed that the second-law efficiency (η_{II}) is decreased and HFC134a can be replaced by refrigerants HFO1234yf and HFO1234ze.

Keywords Vapour compression · Compressor · Evaporator · Fouling · R1234yf · R1234ze · R134a

N. Solanki (✉)
Department of Mechanical and Automation Engineering, Maharaja Agrasen Institute of Technology, PSP Area Sector-22, Rohini Delhi 110086, India
e-mail: naveensolanki1984@gmail.com

A. Arora · R. K. Singh
Department of Mechanical Engineering, Delhi Technological University, Shahbad Daulat Pur, Bawana Road, Delhi 110042, India
e-mail: akhilesharora@dce.ac.in

R. K. Singh
e-mail: rajkumarsingh@dce.ac.in

L. M. Das et al. (eds.), *Emerging Trends in Mechanical Engineering*, Lecture Notes in Mechanical Engineering, https://doi.org/10.1007/978-981-15-8304-9_16

1 Introduction

The harmful effects of global warming and ozone depletion of chlorinated and fluorinated refrigerants, i.e. CFCs, HCFCs and HFCs, have led the scientist to look for alternate refrigerants. Calm [1] addressed future direction for the next generation of refrigerants. Currently, HFO1234yf and HFO1234ze are gaining popularity because of their low GWP values (refer Table 1). Brown et al. [2] valuated thermodynamic properties for eight fluorinated olefins by using the Peng–Robinson equation of state and compared it with R134a. Brown et al. [3] evaluated the potential of HFO1234ze (Z) in high-temperature heat pumping applications. They calculated the COP for R114 and HFO1234ze(Z) is 3.24 and 3.40, respectively, and volumetric heating capacity for R114 and HFO1234ze(Z) is 1667 kWm^{-3} and 1645 kWm^{-3}, respectively. Thus, HFO1234ze(Z) could be a possible replacement for R114. Reasor et al. [4] described R1234yf has a low GWP, and their results showed the comparison between the thermo-physical properties of R1234yf, R134a and R410. Karber et al. [5] reported refrigerants R-1234yf is good replacement for R134a in domestic refrigerators, while R1234ze performs favourable in terms of energy consumption. Devecioğlu and Oruç [6] studied a comparison of low GWP refrigerant like R450A, R513A, R1234yf and R1234ze (E) with R134a, DR-33, L40, DR-7, etc., in

Table 1 Thermophysical and thermodynamic properties of HFC134a, HFO1234yf and HFO1234ze

S. no.	Description	R134a	R1234yf	R1234ze
1	Refrigerant name	Tetraflouro ethane	Tetraflouro Prop-1-ene	Tetraflouro Propene
2	Chemical formula	$C_2H_2F_4$ (CF_3CH_2F)	$C_3F_4H_2$ ($CH_2 = CF\ CF_3$)	$C_3F_4H_2$ ($CHF = CHCF_3$)
3	Ozone depletion potential	0	0	0
4	Global warming potential	1430	4	6
5	Tc (K)	374.21	367.85	382.52
6	Pc (Mpa)	4.06	3.38	3.63
7	Molecular mass (kg/kmol)	102.03	114.04	114.06
8	Liquid density, kg/m^3 (25 °C)	1207	1094	1163
9	Vapour density, kg/m^3 (25 °C)	32.4	37.6	26.4
10	Boiling point (°C)	−26	−29	−19
11	Stability	Single bond makes it stable	Double bond makes it unstable in atm	Double bond makes it unstable in atm
12	Safety group	A1	A1	A1

terms of liquid density and viscosity properties. Their results showed that R444B, HFO1234yf, L40 and DR-5 refrigerants can be good substitute to R22, R134a, R404A and R410A, respectively. Jankovic et al. [7] presented two different analyses (first on equal temperatures of condensation and evaporation and other in condenser's equal cooling medium conditions) of HFO1234yf and HFO1234ze (E) as drop-in replacements for R134a. Miranda et al. [8] experimentally evaluated and compared the performance of HFO1234ze(E), HFO1234yf and R450A as alternatives to R134a in a variable speed compressor and their results showed a diminution in the cooling capacity and COP values obtained with HFO1234ze(E), HFO1234yf and R450A and in comparison with R134a. Sánchez et al. [9] compared alternatives refrigerants (low GWP) R290 with R600a (HCs), R152a (HFCs) with HFO1234yf and HFO1234ze(E) with R134a under the same operating conditions, and their results showed that HFO1234yf and R152a are two potential drop-in alternatives to R134a.

As per literature survey, HFOs are future refrigerants, however their performance need to be evaluated before putting them into commercial use. Table 1 shows the thermophysical and thermodynamic properties of refrigerants (R134a, R1234yf and R1234ze).

Qureshi and Zubair [10] worked on the effect of fouling on the performance of VCRS and their results proved that the performance of R134a is more effective among R410A, R407C and R134a. Also, refrigerant R717 performed better among R404, R290 and R717. Qureshi and Zubair [11] experimentally investigated the fouling effect of condenser on simple VCR system performance, by using HCFC22.

Currently, the performance of system is evaluated by using two approaches, viz. (i) first-law analysis and (ii) exergy analysis (second-law analysis). The second approach helps to quantify the irreversibility of the system components. Many studies in past have been reported which involved exergy analysis of refrigeration systems such as Refs. [12–14]. In one of the notable study, Arora and Kaushik [15] developed a computational model for first-law (energy) analysis and second-law (exergy) analysis under actual VCRS and validated that R507A offers better COP and exergetic efficiency.

Literature survey conveys that the researchers are still focusing on refrigerants having high GWP. However, the two new alternative refrigerants, i.e. HFO1234yf and HFO1234ze, are potential replacements for R134a that have GWP lower than 10, and for these two alternative refrigerants, the performance degradation due to fouling of VCRS has not been studied. Accordingly, in this study, the effect of fouling on refrigeration system using energy and exergy analysis technique has been carried out for refrigerants HFC134a, R1234yf (HFO) and R1234ze (HFO). The effect of variations in evaporator and condenser conductances and $T_{in,cond}$ has been evaluated on VCRS performance, and computed parameters are second-law efficiency (η_{II}), effectiveness, compressor power, change in $\dot{Q}_{evap}$ and COP.

In refrigeration systems, refrigerant HFC134a is commonly used, however its GWP is very high, i.e. 1430 therefore requires replacement. HFO1234yf and HFO1234ze have very low GWP values less than 10 and are used as substitute to HFC134a in VCRS (i.e. MAC system or house hold air-conditioners). In the present

study, the effect of change in conductances due to fouling of condenser and evaporator on the performance of VCR system has been examined. The motivation of this study is the fouling which is a very common phenomenon (happen due to scale formation on condenser and evaporator tubes, offering resistance to heat flow) in VCRS, which results in drop of its performance over a period of time.

2 Description of Model with Its Validation

A VCR system schematic diagram is shown in Figs. 1, and 2 shows T–S diagram of VCR cycle. The system works between two temperatures T_1 and T_2.

By applying the first approach, i.e. first law of thermodynamics to the system, Eq. (1) is obtained

$$\left(\dot{Q}_{\text{cond}} + \dot{Q}_{\text{loss, cond}}\right) - \dot{W}_{cp} - \left(\dot{Q}_{\text{evap}} + \dot{Q}_{\text{loss, evap}}\right) = 0 \tag{1}$$

Evaporator heat transfer rate,

$$\dot{Q}_{\text{evap}} = \dot{m}_{\text{ref}} * (h_3 - h_2) \tag{2}$$

$\dot{Q}_{\text{evap}}$ can be written as in form of effectiveness (ϵ)and minimum heat capacity (C_{min})

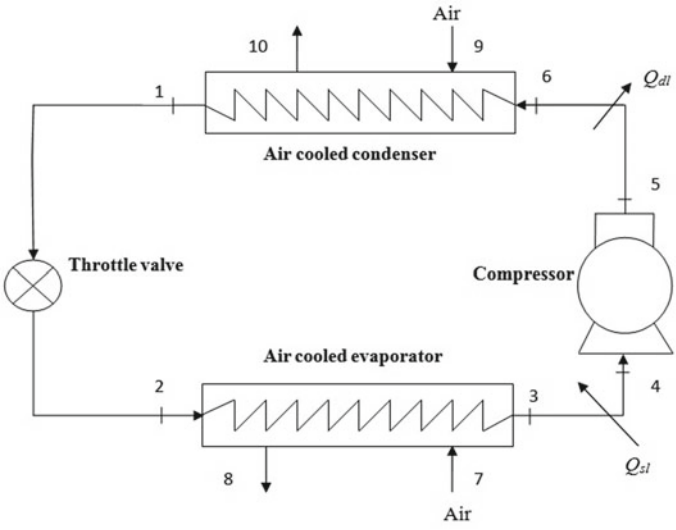

Fig. 1 VCR system diagram

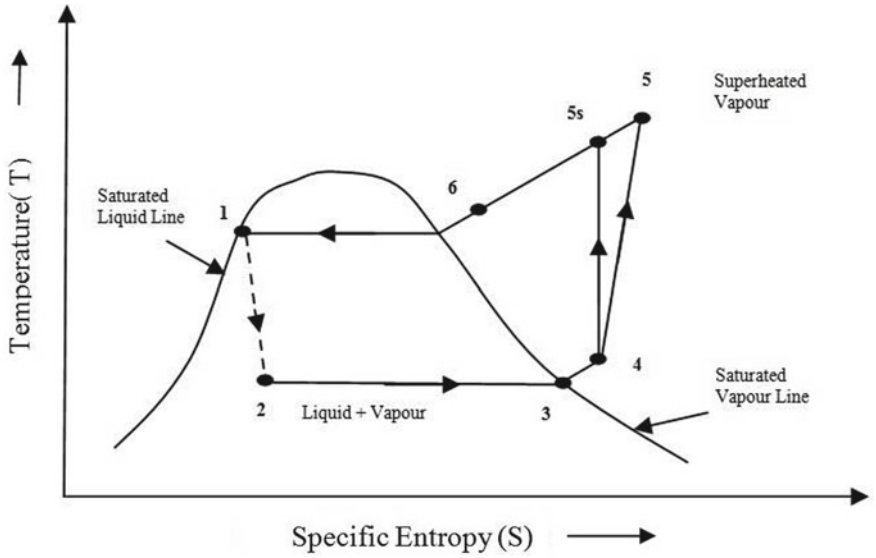

Fig. 2 T–S diagram of VCR cycle

$$\dot{Q}_{evap} = (\epsilon C_{min})_{evap} * (T_7 - T_2) \tag{3}$$

- T_2 = Refrigerant temperature entering to evaporator.
- T_7 = Surrounding temperature entering to evaporator (Air).

Condenser heat transfer rate is given below:

$$\dot{Q}_{cond} = \dot{m}_{ref} * (h_6 - h_1) = (\epsilon C_{min})_{cond} * (T_1 - T_9) \tag{4}$$

- T_1 = Refrigerant temperature exiting from condenser.
- T_9 = Surrounding temperature entering to condenser (Air).

Compressor power:

$$\dot{W}_{cp} = \dot{m}_{\text{ref}} * (h_5 - h_4) = \frac{\dot{m}_{ref}(h_{5s} - h_4)}{\eta_{\text{cp,isn}}} \tag{5}$$

State 5 showing actual condition of superheated vapour refrigerant.
By using SFEE, the work input (compressor) can also be expressed as:

$$\dot{Q}_{\text{cp}} - \dot{W}_{\text{cp}} = \dot{m}_{\text{ref}} * (h_5 - h_4) \tag{6}$$

- $\dot{Q}_{cp}$= Compressor heat transfer to the surrounding.

The suction line heat leaking is

$$\dot{Q}_{sl} = \dot{m}_{\text{ref}} * (h_4 - h_3) \tag{7}$$

The discharge line heat leakage is

$$\dot{Q}_{dl} = \dot{m}_{\text{ref}} * (h_6 - h_5) \tag{8}$$

And

$$COP = \frac{Q_{\text{evap}}}{W_{\text{cp}}} \tag{9}$$

The second-law efficiency:

$$\eta_{\text{II}} = \frac{\text{COP}}{\text{COP}_{\text{rev}}} = \frac{\eta_{\text{I}}}{\eta_{\text{th,rev}}} \tag{10}$$

where

$$\text{COP}_{\text{rev}} = \frac{T_7}{T_9 - T_7}$$

The effectiveness:

$$\epsilon = \frac{\text{Actual heat transfer}}{\text{maximum possible heat transfer}} \tag{11}$$

where

$$\epsilon_{\text{evap}} = \frac{T_7 - T_8}{T_7 - T_2} \quad \text{and} \quad \epsilon_{\text{cond}} = \frac{T_{10} - T_9}{T_6 - T_9}$$

The overall conductance (UA), effectiveness (ϵ)and heat capacity are expressed as (Incropera et al. [16])

$$UA = C_{min} * ln\left(\frac{1}{1-\epsilon}\right) \tag{12}$$

The conductance (in percentage reduction) is given in Eq. (13)

$$UA\% = \left(1 - \frac{UA}{UA_{cl}}\right) * 100 \tag{13}$$

In this paper, EES software program is developed for the above set of Eqs. (1) to (13), where conductance values (in percentage decrease) have been varied individually and simultaneously due to fouling from 0 to 50% in evaporator and condenser heat exchangers. The values of clean condition refer to no fouling, i.e. no percentage

reduction in conductance. Assumptions made for the analysis are as follow (Miranda et al. [8]).

(i) The system operates under steady-state condition.
(ii) The refrigerant leaves the evaporator and condenser in saturated state.
(iii) The expansion process in throttling is isenthalpic.
(iv) The pressure losses in connecting pipe lines and different components of the system are negligible.
(v) In suction line and discharge line, heat leakage is negligible.
(vi) The change in K.E. and P.E. are neglected.

3 Model Validation

The data of ref. [10, 17] have been used for the validation purpose of the current model. Tables 2 and 3 represent the data for model validation.

4 Results and Discussion

Performance of VCRS has been computed using the thermodynamic model presented in above section. The performance is measured with three refrigerants (HFC134a, HFO1234yf and HFO1234ze). The results obtained are discussed below. The input parameters, for computing results, are mentioned in Table 4 [18].

Condenser and evaporator fouling effect on compressor power (*Wcp %*)

Figure 3 represents the effect on $\dot{W}_{cp}$ with variation in T_9 and the combined effect of fouling of condenser and evaporator for refrigerants HFC134a, HFO1234yf and HFO1234ze. It is observed that with decrease in conductance (or increase in fouling), the compressor work decreases.

Tables 5, 6 and 7 at condenser inlet temperatures of 40, 37.5 and 35 °C show the comparison of results of change in compressor power with condenser and evaporator fouling for refrigerants R1234yf, R1234ze and R134a, respectively. It is ascertained that at $T_{in,\,cond} = 35$ oC, refrigerant HFC134a has maximum decrease in the value of change *W*cp%. Refrigerant R1234ze is the second lowest followed by R1234yf.

Condenser and evaporator fouling effect on cooling capacity

Figure 4 represents the effect on cooling capacity with variation in T_9 (condenser coolant temperature) and the combined effect of fouling of condenser and evaporator for refrigerants HFC134a, HFO1234yf and HFO1234ze. It is found that with decrease in conductance (or increase in fouling), the cooling capacity decreases.

Tables 5, 6 and 7 show the comparison of results of change in $\dot{Q}_{evap}$ with condenser and evaporator fouling at T_9 (40, 37.5 and 35 °C) for refrigerants HFO1234yf, HFO1234ze and HFC134a. It is observed that at $T_{in,\,cond} = 40$ °C, refrigerant

Table 2 Performance data comparison between [17] and present work on HCFC22

$T_{in,evap}$(°C)	$\dot{Q}_{cond}$ *(kW)	$\dot{Q}_{cond,mod}$(kW)	Error (%)	$\dot{W}_{cp}$ *(kW)	$\dot{W}_{cp,mod}$(kW)	Error (%)	T_1 *(°C)	$T_{1,mod}$(°C)	Error (%)	COP*(kW)	COP_{mod}(kW)	Error (%)
0	82.16	82.40	0.29	24.92	25.19	1.07	48.75	48.77	0.04	2.30	2.27	−1.32
15	122.0	122.93	0.57	31.45	32.37	2.84	52.99	53.09	0.18	2.88	2.80	−2.77

*Data from [17]—Table 2 depict the maximum encountered error is 2.84

Table 3 Data comparison of condenser and evaporator fouling of refrigerant R134a at $T_e = 0$ °C between Qureshi and Zubair [10] and present model data

Decrease in $UA_{cond,evap}$ (%)	Variation in $\dot{Q}evap$ (%)		Variation in $\dot{W}_{cp}$ (%)		Variation in COP (%)		Error (%) (COP[10])
	Qureshi and Zubair [10]	Current model	Qureshi and Zubair [10]	Current model	Qureshi and Zubair y[10]	Current model	
0	0	0	0	0	0	0	0
10	−2.163	−2.160	−0.247	−0.247	−1.921	−1.918	−0.15
20	−4.823	−4.828	−0.572	−0.586	−4.276	−4.276	0
30	−8.134	−8.120	−1.015	−0.989	−7.193	−7.204	0.15
40	−12.319	−12.320	−1.637	−1.636	−10.860	−10.861	0.009
50	−17.694	−17.690	−2.543	−2.541	−15.547	−15.540	−0.04

*Table 3 depicts that the maximum percentage error (in COP) encountered is <1%

Table 4 Input parameters for result computation

Parameters	Values
Temperature of air entering the evaporator ($T_{in,evap}$ in K)	273
Temperature of air entering the condenser ($T_{in,cond}$ in K)	308–313
Evaporator capacity ($\dot{Q}_{evap}$ in kW)	100
Isentropic efficiency of compressor ($\eta_{cp,isn}$)	0.65
Effectiveness (Є)	0.80
$[(\epsilon * C_{min})_{cond}$, KW/K]	9.39
$[(\epsilon * C_{min})_{evap}$, KW/K] DOS (Degree of superheat) is neglected in suction line	8.2

HFO1234yf has maximum decrease in the cooling capacity (%) value. Refrigerant HFO1234ze shows the minimum decrease in the value of cooling capacity whereas HFC134a lies between the two alternative refrigerants.

Condenser and evaporator fouling effect on COP

Figure 5 represents the effect on COP with variation in T_9 (condenser coolant temperature) and the combined effect of fouling of condenser and evaporator for refrigerants HFC134a, HFO1234yf and HFO1234ze. It is found that with decrease in conductance (or increase in fouling), the COP decreases.

Tables 5, 6 and 7 at T_9 (40, 37.5 and 35 °C) show the comparison of results of change in COP with condenser and evaporator fouling for refrigerants HFO1234yf, HFO1234ze and HFC134a. It is observed that at $T_{in,\,cond} = 40$ °C, refrigerant HFO1234yf shows maximum decrease in the COP (%) value, whereas COP (%)

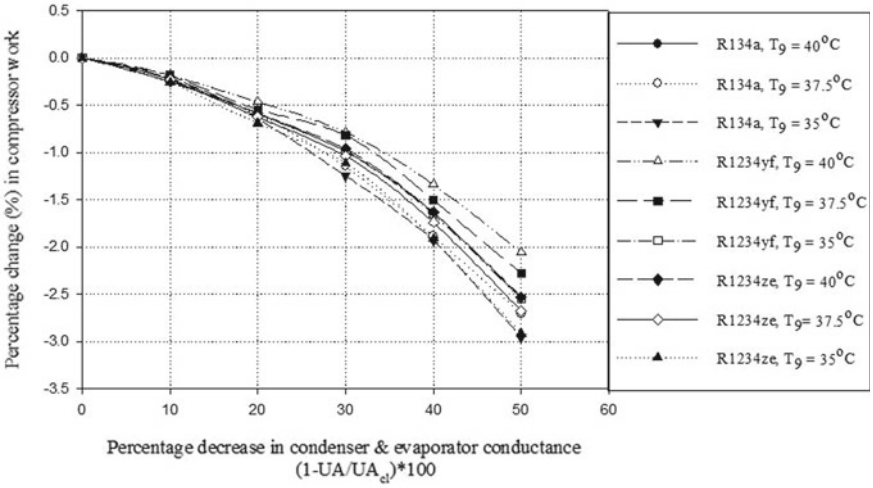

Fig. 3 Percentage decrease in condenser and evaporator conductances versus percentage change in compressor work

Table 5 Results comparison of HFO1234yf, HFO1234ze with HFC134a at $T_{in,\,cond} = 40$ °C

Refrigerant	Variation in $UA_{cond\&evap}$ (%)	Variation in $\dot{W}_{cp}$ (%)	Variation in $\dot{Q}_{evap}$ (%)	Variation in COP (%)
R1234yf	10	−0.18	−2.56	−2.38
	50	−2.05	−20.87	−19.20
R1234ze	10	−0.21	−2.14	−1.93
	50	−2.52	−17.67	−15.54
R134a	10	−0.25	−2.16	−1.92
	50	−2.54	−17.69	−15.54

Values of COP without fouling: R1234yf = 1.338, R1234ze = 1.675 and R134a = 1.664

Table 6 Results comparison of R1234yf, R1234ze with R134a at $T_{in,\,cond} = 37.5$ °C

Refrigerant	Variation in $UA_{cond\&evap}$ (%)	Variation in $\dot{W}_{cp}$ (%)	Variation in $\dot{Q}_{evap}$ (%)	Variation in COP (%)
R1234yf	10	−0.18	−2.44	−2.26
	50	−2.27	−19.97	−18.11
R1234ze	10	−0.23	−2.12	−1.89
	50	−2.67	−17.47	−15.20
R134a	10	−0.25	−2.13	−1.89
	50	−2.70	−17.49	−15.19

Values of COP without fouling: R1234yf = 1.495, R1234ze = 1.808 and R134a = 1.798

Table 7 Results comparison of R1234yf, R1234ze with R134a at $T_{in,\,cond} = 35\ °C$

Refrigerant	Variation in $UA_{cond\&evap}$ (%)	Variation in $\dot{W}_{cp}$ (%)	Variation in $\dot{Q}_{evap}$ (%)	Variation in COP (%)
R1234yf	10	−0.22	−2.37	−2.15
	50	−2.55	−19.36	−17.25
R1234ze	10	−0.26	−2.11	−1.86
	50	−2.91	−17.37	−14.90
R134a	10	−0.25	−2.11	−1.86
	50	−2.95	−17.39	−14.88

Values of system COP without fouling: R1234yf = 1.656, R1234ze = 1.951 and R134a = 1.940

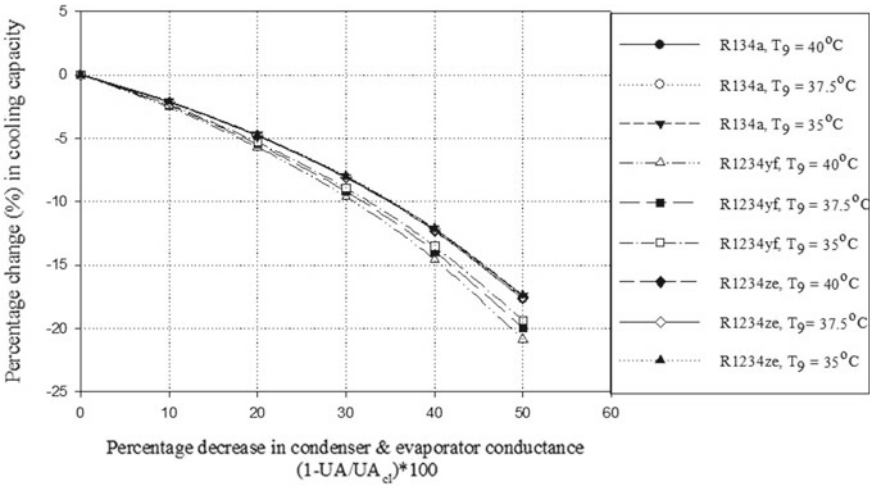

Fig. 4 Percentage decrease in condenser and evaporator conductances versus percentage change in cooling capacity

value change for R134a and R1234ze is nearly same at different values of T_9. One more important point to note here is the values of COP given below Tables 5, 6 and 7. The COP values are for unfouled condition. Under unfouled conditions, HFO1234ze performs better, i.e. its COP is higher than the COP of either of HFC134a and HFO1234yf.

With reference to above results, following points are observed that COP decreases at a higher rate in comparison to the case when either evaporator or condenser fouling is considered. This happens because with the percentage decrease in condenser and evaporator conductances simultaneously, the $\dot{W}_{cp}$(compressor work) decreases at a lower rate and $\dot{Q}_{evap}$ reducing highly as compared to condenser and evaporator fouls individually. Figure 6 represents the p–h diagram of the cycle when (i) there is no fouling (cycle 1–2-3–4) and (ii) when fouling is 50% (cycle 1′-2′-3′-4′). It is observed that as the fouling increases, evaporator pressure drops down whereas

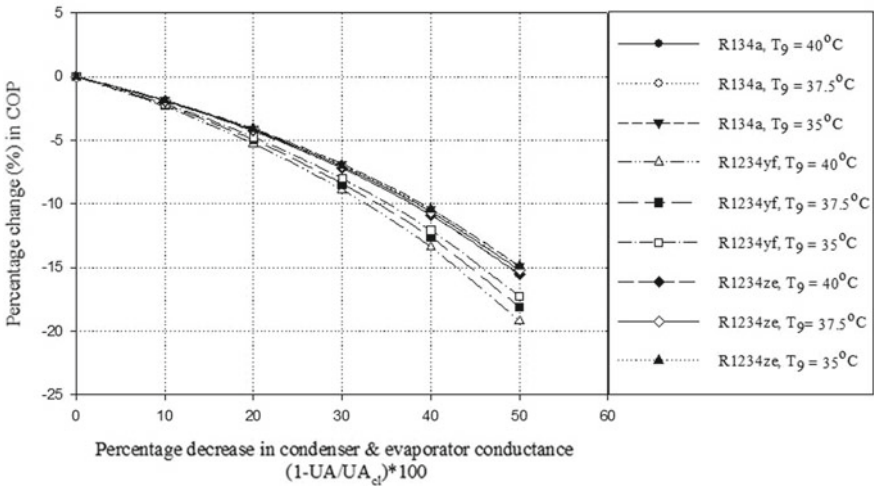

Fig. 5 Percentage change in COP versus percentage decrease in condenser and evaporator conductances

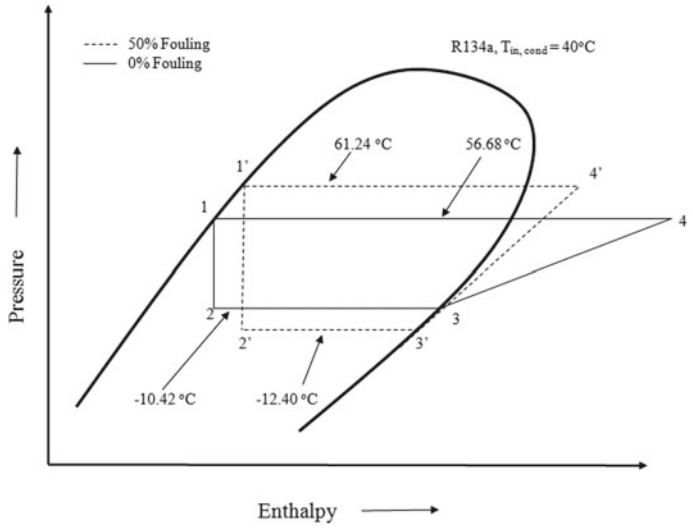

Fig. 6 Pressure—enthalpy diagram of VCRS

condenser pressure increases. The rise in condenser pressure and fall in evaporator pressure will result in drop-in COP which indicates that with an increase in fouling the COP goes down.

Combined effect on effectiveness of condenser and evaporator fouling

Figure 7 represents the effect on effectiveness with variation in T_9 (condenser coolant temperature) and the combined effect of fouling of condenser and evaporator for refrigerants HFC134a, HFO1234yf and HFO1234ze. It is ascertained that with an increase in fouling or decrease in conductance, the maximum decrease in effectiveness is up to 31% of the fouled heat exchanger.

Condenser fouling effect on W_{cp}, Q_{evap} and COP

Tables 8, 9 and 10 at condenser coolant inlet temperatures of 40, 37.5 and 35 °C, shows the comparison of results of compressor power (W_{cp} (%)), cooling capacity (Q_{evap} (%)) and COP (%) value with condenser fouling for refrigerants HFO1234yf, HFO1234ze and HFC134a.

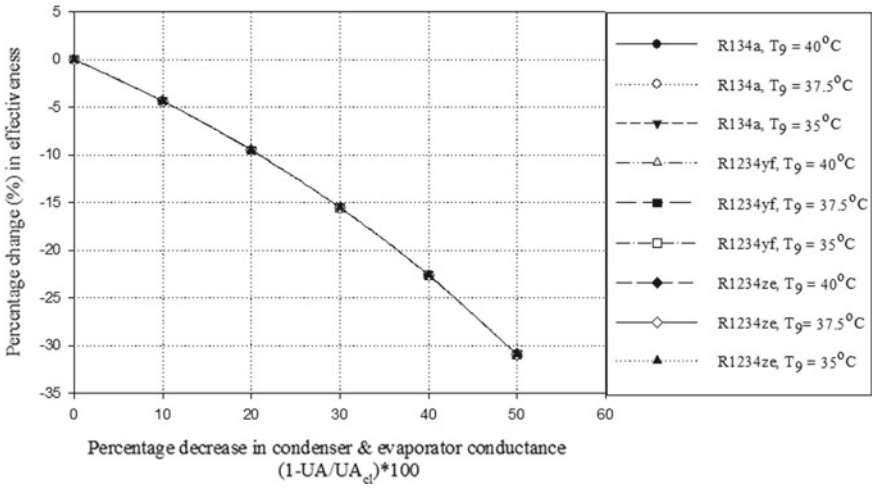

Fig. 7 Percentage change in effectiveness versus percentage decrease in condenser and evaporator conductances

Table 8 Results comparison of R1234yf, R1234ze with R134a at $T_{in,\,cond} = 40$ °C

Refrigerant	Variation in UA_{cond} (%)	Variation in W_{cp} (%)	Variation in COP (%)	Variation in Qevap (%)
R1234yf	10	0.57	−2.01	−1.46
	50	7.48	−19.29	−13.25
R1234ze	10	0.70	−1.59	−0.91
	50	6.83	−14.47	−8.63
R134a	10	0.71	−1.61	−0.91
	50	6.69	−14.49	−8.77

Table 9 Results comparison of R1234yf, R1234ze with R134a at $T_{in,\ cond} = 37.5$ °C

Refrigerant	Variation in UA_{cond} (%)	Variation in W_{cp} (%)	Variation in COP (%)	Variation in Qevap (%)
R1234yf	10	0.68	−1.93	−1.26
	50	8.25	−18.25	−11.51
R1234ze	10	0.80	−1.60	−0.81
	50	7.22	−14.17	−7.98
R134a	10	0.76	−1.58	−0.83
	50	7.08	−14.18	−8.09

Table 10 Results comparison of R1234yf, R1234ze with R134a at $T_{in,\ cond} = 35$ °C

Refrigerant	Variation in UA_{cond} (%)	Variation in W_{cp} (%)	Variation in COP (%)	Variation in Qevap (%)
R1234yf	10	0.74	−1.85	−1.12
	50	9.12	−17.55	−10.06
R1234ze	10	0.87	−1.59	−0.73
	50	7.41	−13.88	−7.50
R134a	10	0.79	−1.56	−0.77
	50	7.38	−13.91	−7.56

From Tables 8, 9 and 10, it is observed that at $T_{in,\ cond} = 35$ °C, HFO1234yf has maximum increase in value of W_{cp} (%) and at $T_{in,\ cond} = 40$ °C has maximum decrease in value of COP (%) and Q_{evap} (%) value.

Evaporator fouling effect on W_{cp}(compressor power), Q_{evap}(cooling capacity) & COP

Tables 11, 12 and 13 at condenser coolant inlet temperatures of 40, 37.5 and 35 °C show the comparison of results of compressor power (W_{cp} (%)), cooling capacity (Qevap (%)) and COP (%) value with evaporator fouling for refrigerants HFO1234yf, HFO1234ze and HFC134a.

Table 11 Results comparison of HFO1234yf, HFO1234ze with HFC134a at $T_{in,\ cond} = 40$ °C

Refrigerant	Variation in UA_{evap} (%)	Variation in W_{cp} (%)	Variation in COP (%)	Variation in Qevap (%)
R1234yf	10	−0.71	−0.41	−1.13
	50	−6.64	−3.59	−9.99
R1234ze	10	−0.96	−0.34	−1.29
	50	−8.45	−3.04	−11.22
R134a	10	−0.96	−0.33	−1.29
	50	−8.41	−2.99	−11.16

Table 12 Results comparison of R1234yf, R1234ze with R134a at $T_{in,\ cond} = 37.5$ °C

Refrigerant	Variation in UA_{evap} (%)	Variation in W_{cp} (%)	Variation in COP (%)	Variation in Qevap (%)
R1234yf	10	−0.79	−0.40	−1.19
	50	−7.49	−3.34	−10.59
R1234ze	10	−1.07	−0.30	−1.37
	50	−9.03	−2.90	−11.67
R134a	10	−1.02	−0.32	−1.34
	50	−8.98	−2.87	−11.60

Table 13 Results comparison of R1234yf, R1234ze with R134a at $T_{in,\ cond} = 35$ °C

Refrigerant	Variation in UA_{evap} (%)	Variation in W_{cp} (%)	Variation in COP (%)	Variation in Qevap (%)
R1234yf	10	−0.86	−0.39	−1.24
	50	−8.31	−3.08	−11.19
R1234ze	10	−1.17	−0.28	−1.44
	50	−9.66	−2.74	−12.13
R134a	10	−1.08	−0.31	−1.39
	50	−9.63	−2.71	−12.08

From Tables 11, 12 and 13, it is observed that at $T_{in,cond} = 35$ °C, HFO1234ze has maximum decrease in compressor power (W_{cp} (%)) value, cooling capacity (Qevap (%)) value and at $T_{in,\ cond} = 40$ °C refrigerant HFO1234yf has maximum decrease in COP (%) value.

At condenser coolant inlet temperatures ($T_{in,\ cond}$) of 40, 37.5 and 35 °C, the comparison of results of η_{II} (second-law efficiency) for unfouled (0%) condition and at 50% decrease in conductance (or increase in fouling condition) is shown in Table 14. It is found that η_{II} decreases most when evaporator and condenser (both) are fouled. However, the effect of evaporator fouling on η_{II} is less in comparison

Table 14 Second-law efficiency comparison between HFO1234yf, HFO1234ze and HFC134a

Refrigerant	Variation in $UA_{cond,\ evap}$ (%)	η_{II} (%) $T_{in,cond} =$ 40 °C	η_{II} (%) $T_{in,cond} =$ 37.5 °C	η_{II} (%) $T_{in,cond} =$ 35 °C
R1234ze	0	24.52	24.83	25.01
	50	20.71	21.06	21.29
R1234yf	0	19.60	20.53	21.23
	50	15.84	16.81	17.57
R134a	0	24.37	24.69	24.88
	50	20.59	20.94	21.17

to condenser fouling (not shown individual effect). In present work, the reduction in η_{II} for R1234yf is lowest followed by R134a and R1234ze. Refrigerant R1234yf shows the minimum change in second-law efficiency at 50% fouling. Even though the decrease in second-law efficiency is more in case of R1234ze, still it is better because (even after reduction of second-law efficiency due to fouling), the absolute value of second-law efficiency of R1234ze is higher than R1234yf (Refer Table 14).

The results presented above substantiate that R1234ze outperforms R1234yf whether the system is operating under unfouled condition or fouled condition. Thus, one can easily conclude that HFO1234ze is better than HFC134a for specified operating conditions, both under unfouled as well as fouled conditions.

5 Conclusions

The effect of condenser and evaporator (both) fouling has been evaluated and the conclusions drawn for refrigerants HFC134a, HFO1234yf and HFO1234ze are as follows:

(a) The maximum decrease in W_{cp}% is observed at $T_{in,condin,cond} = 35$ °C. The value of W_{cp}% decreases up to 2.91% for R1234ze and 2.55% for R1234yf, whereas for R134a, it decreases by 2.95% at T = 35 °C.
(b) The maximum decrease in cooling capacity is observed at $T_{in,cond} = 40$ °C. The value of Qevap% decreases up to 17.67% for R1234ze and 20.87% for R1234yf, whereas for R134a its value decreases up to 17.69% at $T_{in,cond} = 40$ °C.
(c) The maximum decrease in COP is observed at $T_{in,cond} = 40$ °C. The value of COP% decreases up to 15.55% for R1234ze and 19.21% for R1234yf whereas in R134a its value decreases up to 15.54% at $T_{in,cond} = 40$ °C.
(d) The maximum decrease in effectiveness of the fouled heat exchanger is observed up to 31% when its UA% value is halved (i.e. 50%), and the fouled heat exchanger effectiveness decreases equally (for all refrigerants with same percentage).
(e) The second-law efficiency ($\boldsymbol{\eta_{II}}$) obtained for R1234ze is the highest among the refrigerants considered both under fouled and unfouled condition. At $T_{in,cond} = 40$ °C, on the basis of the second-law efficiency ($\boldsymbol{\eta_{II}}$) at 50% decrease in conductance (or increase in fouling), the refrigerants can be arranged as R1234yf (15.84%) < R134a (20.59%) < R1234ze (20.71%).

The decrease in conductance (or increase in fouling), decreases the $W_{cp,}$ Q_{evap}, COP and η_{II} of VCRS, and it is found to be severest for refrigerant HFO1234yf and the results of HFO1234ze and HFC134a are nearly same. Thus, on the basis of results obtained, it is concluded that the refrigerant HFO1234ze performance is better in both fouled as well as unfouled conditions in comparison to HFO1234yf and HFC134a. Hence, it is recommended that HFO1234ze should be used in place of R134a.

Nomenclature

HFO	Hydro-fluoro-olefin
CFCs	Chloro-fluoro-carbons
NBP	Normal boiling point
SFEE	Steady flow energy equation
COP	Coefficient of performance
ODP	Ozone depletion potential
C	Thermal capacitance rate (kWK^{-1}) minimum value
Q	Heat transfer rate (kW)
m	Refrigerant mass flow rate (kg s^{-1})
P	Pressure (MPa)
UA	Overall conductance (kWK^{-1})
η	Efficiency
ϵ	Effectiveness

Subscripts

cl	Clean
cl	Clean
act	Actual
f	Fouled state
c	Critical
in	Entering
isn	Isentropic
min	Minimum
ref	Refrigerant
rev	Reversible cycle
sl	Suction line
th	Thermal
I	First law
II	Second law

References

1. Calm J (2008) The next generation of refrigerants – Historical review, considerations, and outlook. Int J Refrig 31:1123–1133
2. Brown JS, Zilio C, Cavallini A (2010) Thermodynamic properties of eight fluorinated olefins. Int J Refrig 33:235–324
3. Brown JS, Zilio C, Cavallini A (2009) The fluorinated olefin R-1234ze (Z) as a high-temperature heat pumping refrigerant. Int J Refrig 32:1412–1422

4. Reasor P, Aute V, Radermacher R (2010) Refrigerant R1234yf performance comparison investigation. Int Refrig Air Conditioning Conf at Purdue. Paper No. 1085
5. Karber KM, Abdelaziz O, Vineyard EA (2012) Vineyard experimental performance of R-1234yf and R-1234ze as drop-in replacements for R-134a in domestic refrigerators. Int Ref Air Cond Conf Purdue July 16–19, 2241:1–10
6. Devecioğlu AG, Oruç V (2015) Characteristics of some new generation refrigerants with low GWP. The 7th Int Conf Appl Energy 75:1452–1457
7. Jankovic Z, Atienza JS, Suarez JAM (2015) Thermodynamic and heat transfer analyses for R1234yf and R1234ze (E) as drop-in replacements for R134a in a small power refrigerating system. J Appl Thermal Eng 80:42–54
8. Miranda JMM, Babiloni AM, Minguela JJR, Carpio VDM, Rodríguez MC, Esbrí JN, Hernandez CS (2016) Comparative evaluation of R1234yf, R1234ze (E) and R450A as alternatives to R134a in a variable speed reciprocating compressor. J Energy 114:753–766
9. Sánchez D, Cabello R, Llopis R, Arauzo I, Gil JC, Torrella E (2017) Energy performance evaluation of R1234yf, R1234ze(E), R600a, R290 and R152a as low-GWP R134a alternatives. Int J Refrig 74:269–282
10. Qureshi BA, Zubair SM (2011) Performance degradation of vapor compression refrigeration system under fouled conditions. Int J Refrig 34:1016–1027
11. Qureshi BA, Zubair SM (2014) The impact of fouling on the vapour compression refrigeration system: an experimental observation. Int J Refrig 38:260–266
12. Akhilesh A, Arora BB, Pathak BD, Sachdev HL (2007) Exergy analysis of a Vapour Compression Refrigeration system with R-22, R-407C and R-410A. Int J Energy 4:441–454
13. Arora A, Kaushik SC (2008) Theoretical analysis of a vapour compression refrigeration system with R502, R404A and R507A. Int J Refrig 31:998–1005
14. Arora A, Sachdev HL (2009) Thermodynamic analysis of R422 series refrigerants as alternative refrigerants to HCFC22 in a vapour compression refrigeration system. Int J Energy Res 33:753–765
15. Arora A, Kaushik SC (2010) Energy and exergy analyses of a two-stage vapour compression refrigeration system. Int J Energy Res 34(10):907–923
16. Incropera FP, DeWitt DP, Bergman T, Lavine A, (2006) Fundamentals of heat and mass transfer, 6th ed. Wiley
17. Stoecker WF, Jones JW (1982) Refrigeration and air conditioning. McGraw-Hill, New York
18. Khan J, Zubair SM (1999) Design and performance evaluation of reciprocating refrigeration system. Int J Refrig 22:235–243

Computational Model Sensitivity and Study of Joint Bias-Perturbed Grazing Flow Through Perforated Liner

N. K. Jha, Ashutosh Tripathi, and R. N. Hota

Abstract Perforated liners are used to suppress the thermoacoustic instabilities in jet engines. These are perforated cylindrical sheets traversed by bias flow and grazed by grazing flow through the orifices. In this paper, time-domain numerical studies have been conducted to simulate the interaction between sound and joint grazing-bias flow. Effect of propagation of the sound wave is modeled by giving perturbation to the mean flow. For this purpose, sinusoidal perturbation of desired frequency is added to the mean flow by means of user-defined function (UDF) which constitutes mean and perturbation components of the velocity. Turbulence models mainly standard k-ε, SST k-ω, and scale-adaptive simulation (SAS) are compared by assessing their ability to capture the key flow features of these interactions. Velocity power difference for with and without perturbation cases are analyzed. The velocity power difference spectra indicate a relationship between the perturbation energy/acoustic energy loss and creation of additional turbulent fluctuation components. The present results thus support the theory of vortex–sound interaction and subsequent dissipation of sound. On comparison, it is observed that for a transient numerical study of these interactions, the SAS turbulence model is the best among all the models considered.

Keywords Liner · Grazing flow · Bias flow · Perturbation

1 Introduction

Bias flow acoustic liners are passive dampers, applied to suppress thermoacoustic instabilities. These liners, with a mean flow through the perforations, are primarily applied for cooling the combustor wall. Apart from the cooling function, these are also well known for having the ability to suppress thermoacoustic instabilities by providing a substantial amount of acoustic dissipation. The motion of fluid through the liner is a combination of grazing and bias flow. Damping of sound wave is a

N. K. Jha (✉) · A. Tripathi · R. N. Hota
Indian Institute of Technology, Indian School of Mines, Dhanbad 826004, India
e-mail: nandanjha922@gmail.com

L. M. Das et al. (eds.), *Emerging Trends in Mechanical Engineering*, Lecture Notes in Mechanical Engineering, https://doi.org/10.1007/978-981-15-8304-9_17

result of an interaction of the sound wave with grazing and bias flow. According to vortex sound theory [1], damping of sound occurs by the conversion of acoustic energy into hydrodynamic energy of the jet before being dissipated into heat. The sound field can be defined as the unsteady flow part of the total flow field. In some recent numerical studies [2], [3], propagation of sound wave has been modeled by imposing sinusoidal perturbed flow of desired excitation frequencies to the mean flow as boundary conditions. The level of perturbation was chosen as 2% [2] and 1% [3] in the previous studies. Schulz et al. [4] conducted an experimental investigation of realistic bias flow liner. They investigated the energy transfer between acoustics and the flow field at a bias flow liner using spectral analysis of the velocity fluctuations measured by optical techniques in the vicinity of the perforation. Most of the studies in the literature are limited to considering either grazing or bias flow. Only few works have been carried out on joint grazing–bias flow interacting with sound. In the present paper, numerical studies have been conducted on the interaction of sound (as a perturbation in grazing flow) with grazing and bias flow at orifice junctions. Different turbulence models are compared based on their ability to capture key flow features of these interactions. In Sect. 2, the computational domain, generated mesh, and boundary conditions are described. The numerical methodology is described in Sect. 3 along with the grid independence test and validation. Section 4 deals with the implementation of all considered models at a fixed grazing flow of Mach 0.1 and a bias flow jet velocity of 7 m/s. A comparative study is conducted among the turbulence models. This section also presents the studies of cases considering with and without perturbation. Power spectral density (PSD) of rms of velocity fluctuations at different locations in the domain is plotted by acquiring velocity data at certain monitored points all long the domain.

2 Computation Domain

The 2D computational domain along with the boundary conditions is shown in Fig. 1. The domain has the dimensions as used by Heuwinkel et al. [5], $LD = 80$ mm, upstream length $Lu = 1015$ mm, downstream length $Ld = 1015$ mm, liner length $Ll = 60$ mm, thickness $T = 1$ mm, and hole diameter $D = 2.5$ mm.

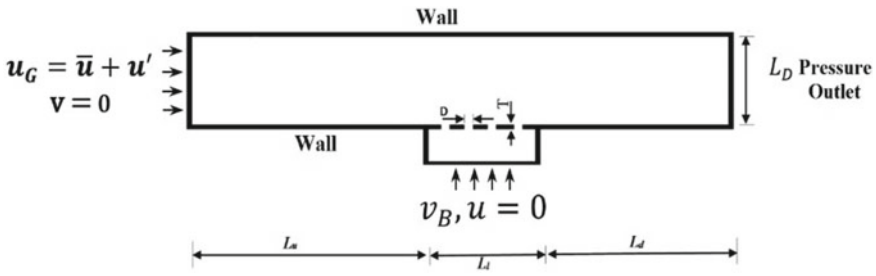

Fig. 1 Computational domain with boundary conditions

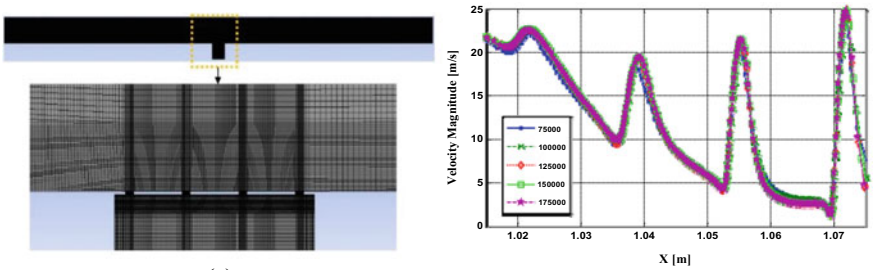

Fig. 2 **a** Grid along the domain and enlarged view around the liner **b** Instantaneous velocity magnitudes over the liner for various number of elements

Inlet is considered as velocity inlet and outlet as pressure outlet as the boundary conditions with rest of the boundaries as wall. Grazing flow with perturbation (acoustically excited grazing flow) enters through one inlet as $u_u = \bar{u} + u$ where $\bar{u} = 34.3$ m/s, $u' = 0.343$*sin $(2\pi\, ft), f = 1122$ Hz, and a bias flow $vB = 7$ m/s through each orifice. Reynolds number based on grazing flow duct dimensions and velocity corresponds is 1,18,000. The grid-sensitivity test presented in Fig. 2b is carried out by changing the number of grid elements. The results obtained with 1,25,000 number of elements is found to be nearly invariant with further grid refinement.

3 Numerical Methodology

The governing equations are solved by a commercial finite volume code, ANSYS Fluent. In aero-acoustics, where the applications like combustion requires the unsteady interaction of the flow with other physical effects like sound, RANS solutions are not adequate, as they are of overly diffusive nature, damping out important flow features. Menter and Erogov [6] introduced SST-SAS, which modifies to the already resolved scales in a dynamic manner and allows the growth of a turbulent spectrum in the detached region by the introduction of SAS source term QSAS in the transport equation for the turbulence eddy frequency. In order to validate the SAS model incorporated in ANSYS Fluent, works of Zhao et.al [7] have been reproduced using SAS model as shown in Fig. 3. Time evolution of pressure oscillations downstream of the orifices were monitored and found in close agreement with the results of SAS.

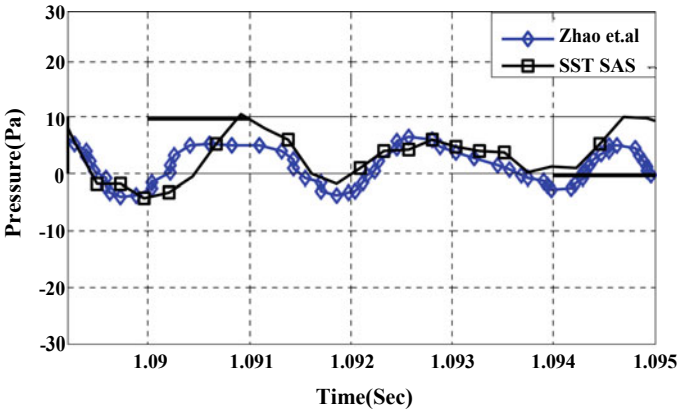

Fig. 3 Pressure (Pa) plotted after convergence

4 Results

4.1 Comparative Study of Different Turbulence Models

The comparison has been done among different turbulent models, viz. standard k-ε, SST k-ω, and SAS. For this purpose, PSDs of rms of velocity fluctuations, transient velocity signal, vorticity magnitude, and wake profiles are plotted for these turbulence models.

Figure 4a reveals that only SAS model captured all the harmonics where the fundamental harmonics correspond to the perturbation frequency. The predicted harmonics correspond to the vorticity production and their decay into smaller and smaller vortices. Only a single peak of lesser strength at the excitation frequency by using SST k-ω model can be observed. The standard k-ε model did not capture any harmonics, suggesting the inability to capture vortex shedding. Figure 4b shows the transient velocity magnitude signal monitored for all the models at a point closer to the downstream of the liner. The signals appear to be periodic in nature after the transition period as the fully developed turbulence. A turbulent flow is featured by unsteady continuous eddies in motion with each other. Further, these eddies produce fluctuations in the flow properties like velocity and pressure. Periodic fluctuations of the velocities are clearly visible using SAS model. The fluctuations produced by the other two models are considerably weaker than SAS. After a certain transition period of time, the fluctuations are completely regular for the SAS model. This regularity is due to the constant generation of vortices downstream of the orifice junctions. The period of oscillation is 0.0009 s, which corresponds to the time taken for one vortex to move from the recirculation region and is same as the time period of excitation. According to the vortex sound theory, vortex should shed so that the conversion of sound energy into the kinetic energy of the flow can take place. For this, the contours

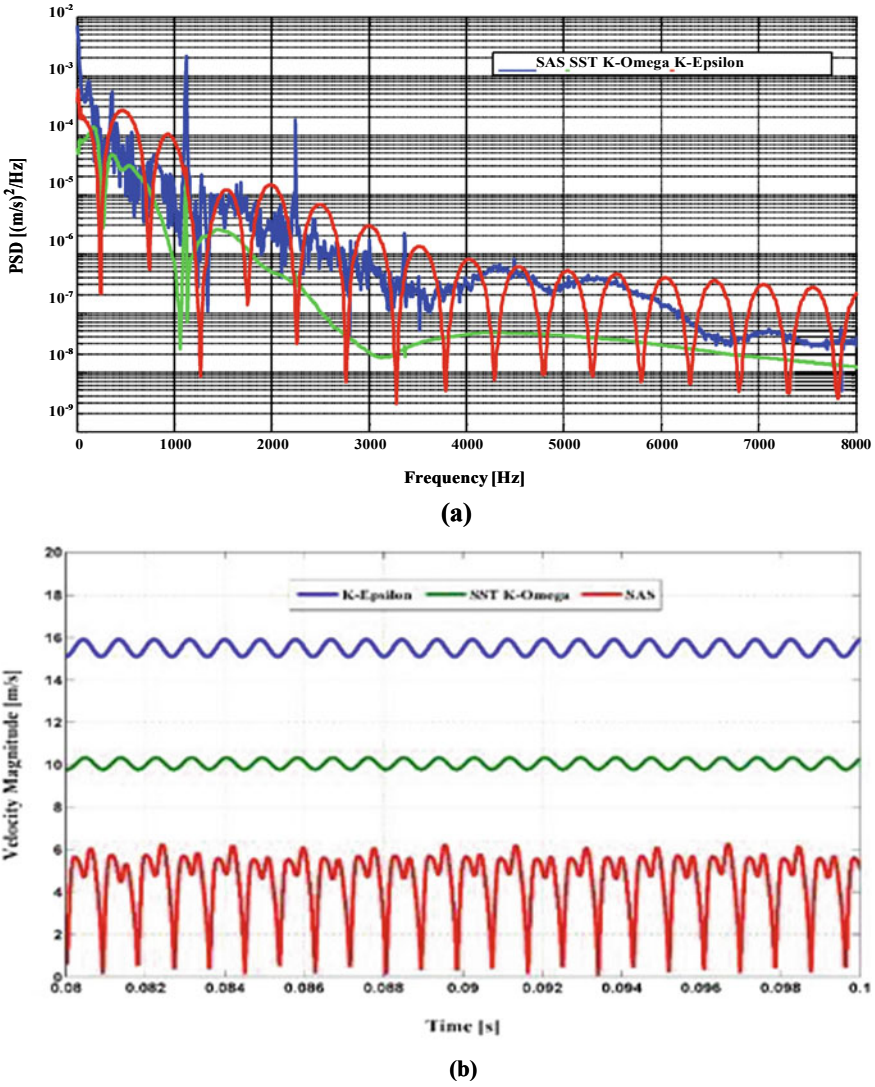

Fig. 4 **a** PSD of rms of velocity fluctuations **b** Transient velocity magnitude profile at a location $x = 1.077$ m and $y = 2$ mm

of vorticity magnitude are shown in Fig. 5 at the same instant, for all the models. It can be seen that turbulence models other than the SAS are not able to resolve the regions of circulation. The comparative vorticity magnitude contours support the argument of Menter and Erogov [5] about the overly diffusive character of RANS model in the detached regions while the ability of SAS model to resolve the unsteady flow fields in the detached regions containing vortices.

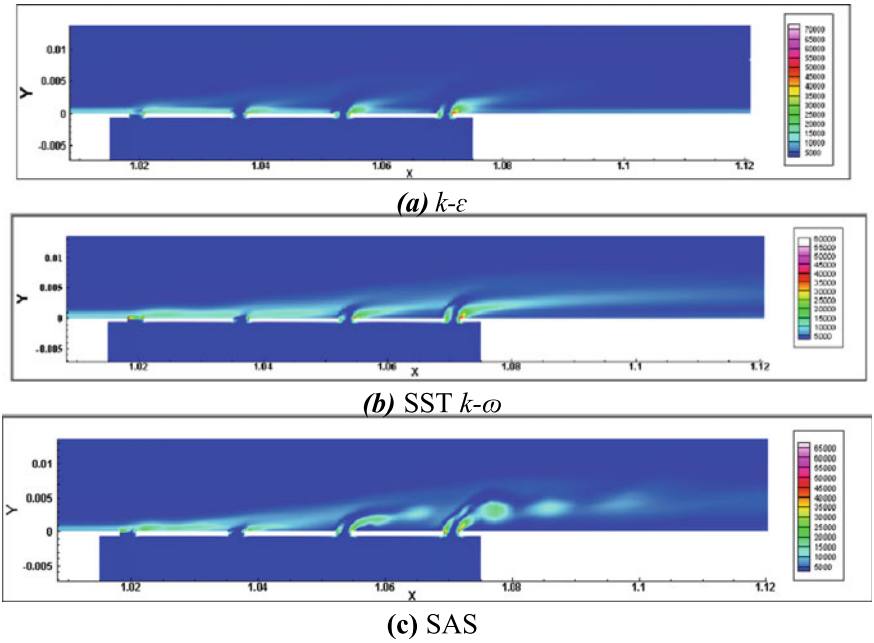

(a) k-ε

(b) SST k-ω

(c) SAS

Fig. 5 Vorticity magnitude contours at T = 0.136971 s

The velocity profiles are investigated by plotting the velocity magnitude at four different cross sections for all the models, as shown in Fig. 6. The flow profile close to the downstream edge has inflexion points and is well captured by the SAS model only. Based on the Rayleigh criterion, this indicates an unstable profile. The profiles are also plotted at four vertical locations above the liner, as shown in Fig. 7. Near the interaction zone, SAS shows the ability to capture the unsteady flow features while far from the interaction region it behaves like other RANS models.

4.2 With and Without Perturbations

To get some insight of the effect of perturbation, profiles of instantaneous velocity magnitude are computed using the SAS model and are plotted for the cases considering with and without perturbation. In far upstream (Fig. 8a) and far downstream (Fig. 8c) of the liner, profiles of velocity magnitude are of the same nature for both the cases. However, in the vicinity of the liner, two inflexion points can be observed for the perturbed case and only one for without perturbation (Fig. 8c). More inflexion points for the perturbation case suggests greater instability or shedding of vortices that can further lead to damping out of the perturbation energy as per the vortex sound theory. In Fig. 9, PSD of the rms of fluctuating velocity for both cases is shown over

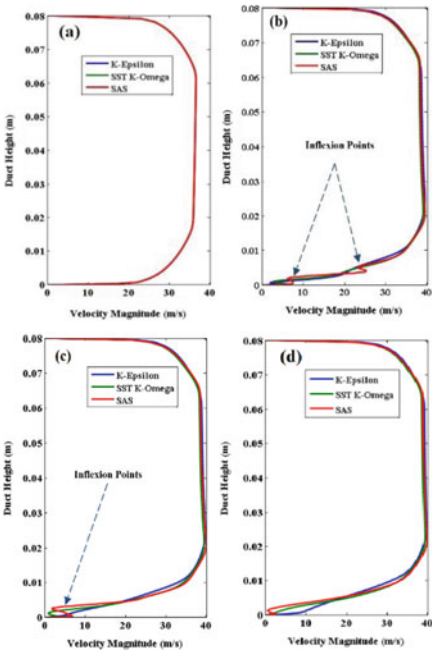

Fig. 6 Velocity magnitude profile plotted at different cross sections for axial positions **a** 0.975 m. **b** 1.075 m. **c** 1.085 m, and **d** 1.185 m

a frequency range upto 6 kHz. For the perturbed case, the frequency of perturbation and the decaying harmonics can be observed. The fundamental harmonics are the same as the excitation frequency, which suggests a maximum production of vortices at the excitation frequency due to the perturbed unsteady flow. For the case without perturbation, no harmonics can be seen. In comparison to the non-perturbed case, gain in energy level with increased turbulence production almost over the entire range of frequency range can be observed.

4.3 Scale-Adaptive Simulation of Flow–Perturbation Interaction

PSDs of rms of velocity fluctuations at different axial locations for the fixed vertical position are computed, plotted and stacked in Fig. 10 to throw some light on the shedding and dissipation of vortices. Eight such locations were considered: two upstream the liner (*a, b*), three above the liner (*c, d, e*), and three downstream of the liner (*f, g, h*). For the locations upstream, no harmonics can be seen as there are no vortices shed in these regions. One harmonic can be seen for the location *c*, indicating the role of bias flow in the formation of the recirculating zone or vortices. For locations after second, third, and fourth orifices, an increment in the number of peaks can be seen. PSD at the downstream location '*g*' shows decay in its strength and

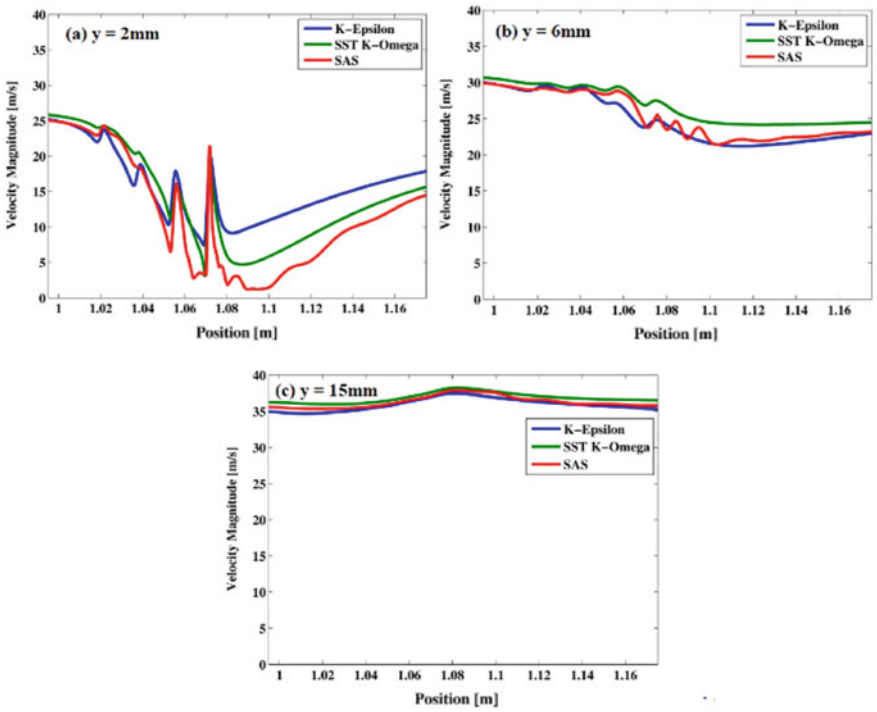

Fig. 7 Velocity magnitude at different locations along vertical directions

at a far downstream location '*h*,' no peaks can be detected, i.e., vortices get dissipated as viscosity dominates in these regions. Further, the power spectra computed from velocity signal for the non-perturbed case were subtracted from the spectra with perturbation at a point, $x = 1.077$ m and $y = 2$ mm, downstream of the orifice. The results are depicted in the third octave bands in Fig. 11. The third-octave band containing the perturbation frequency is the band number 17. This specific band shows a distinct maximum, indicating the production of vortices in this band.

5 Conclusions

In the present work, the problem of sound–flow interaction at a bias flow liner is considered. The effect of propagation of the sound wave is modeled as a perturbation in the mean flow. The inflexion points near the interaction zone are observed for the perturbed case only. Turbulence models have been compared based on their ability to capture unsteady flow features. The results of the SAS model are observed to be very encouraging and show that this model is a better alternative to conventional turbulence models for the sound–flow interaction case. The dynamic behavior of the

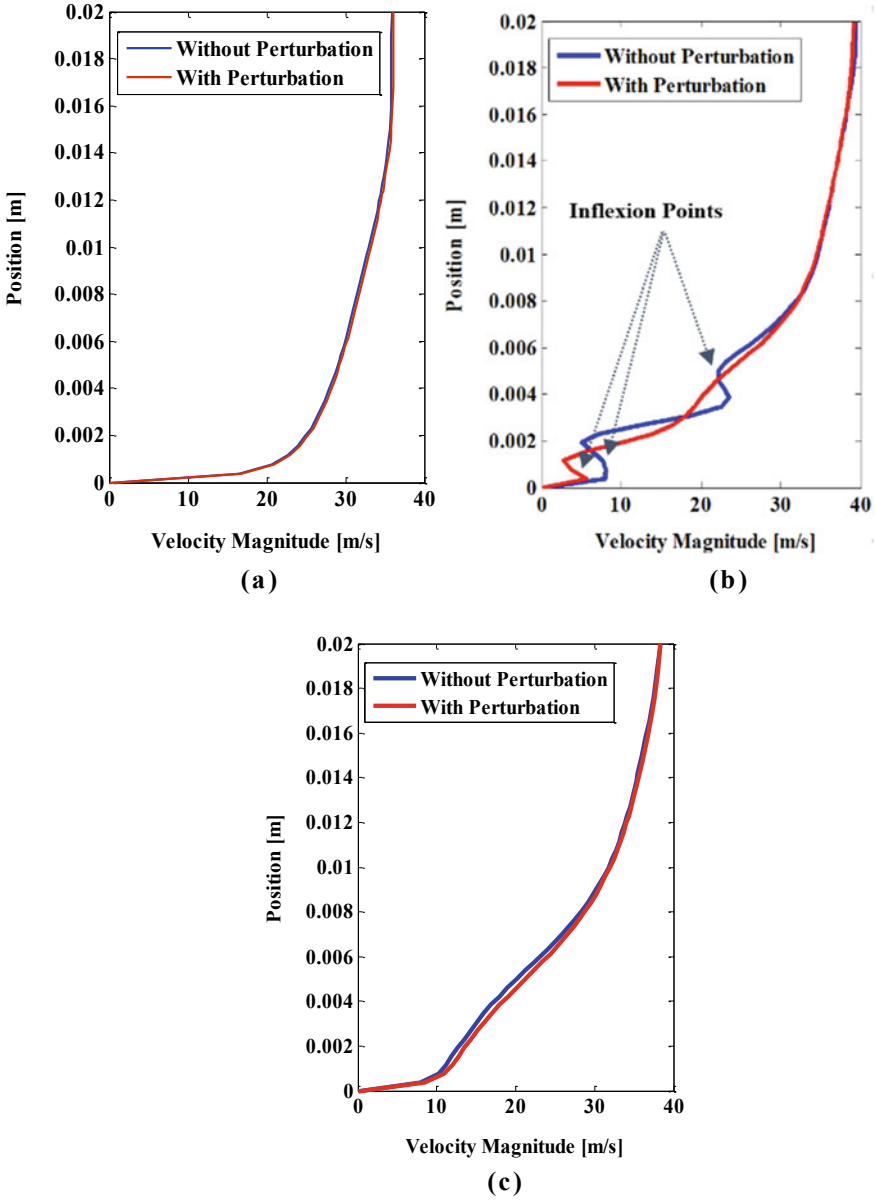

Fig. 8 Velocity magnitude profile at with and without perturbation **a** 1.0 m (before liner) **b** 1.075 m (end of the liner) **c** 1.106 m, far downstream the liner

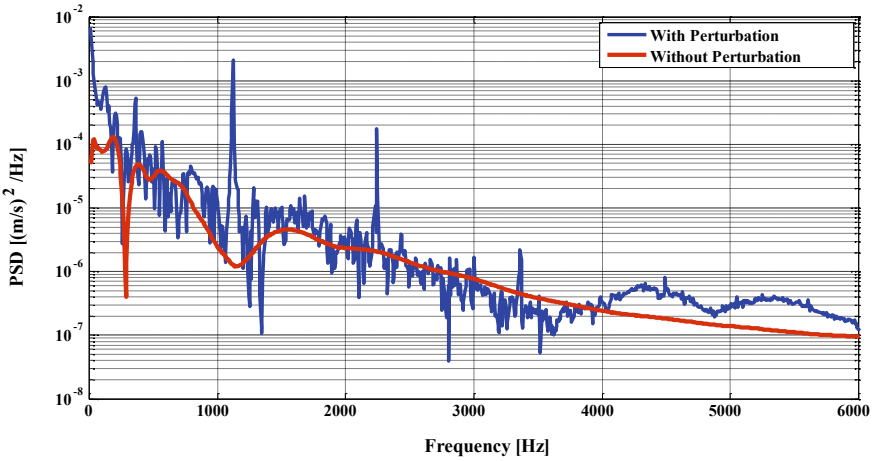

Fig. 9 PSD of rms of velocity fluctuations with and without perturbation at $x = 1.077$ m, $y = 2$ mm

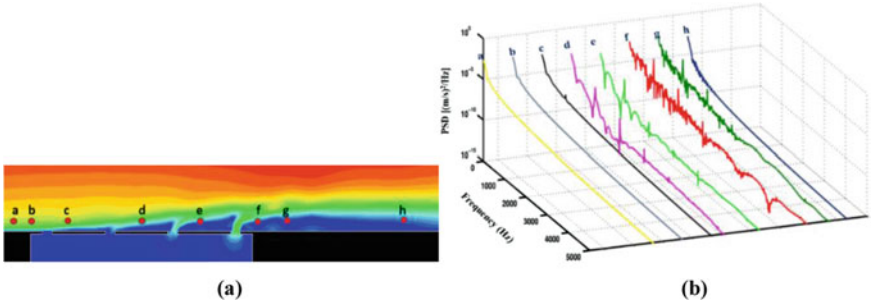

Fig. 10 **a** Stacked PSDs of rms of velocity fluctuations at different monitored locations along the domain **b** velocity magnitude contour depicting different monitored locations

flow has been captured, providing important information on the flow structure like vortex shedding and subsequent dissipations. The observed energy difference in the third octave band supports the assumption of transfer of the perturbation energy into the turbulent fluctuating energy.

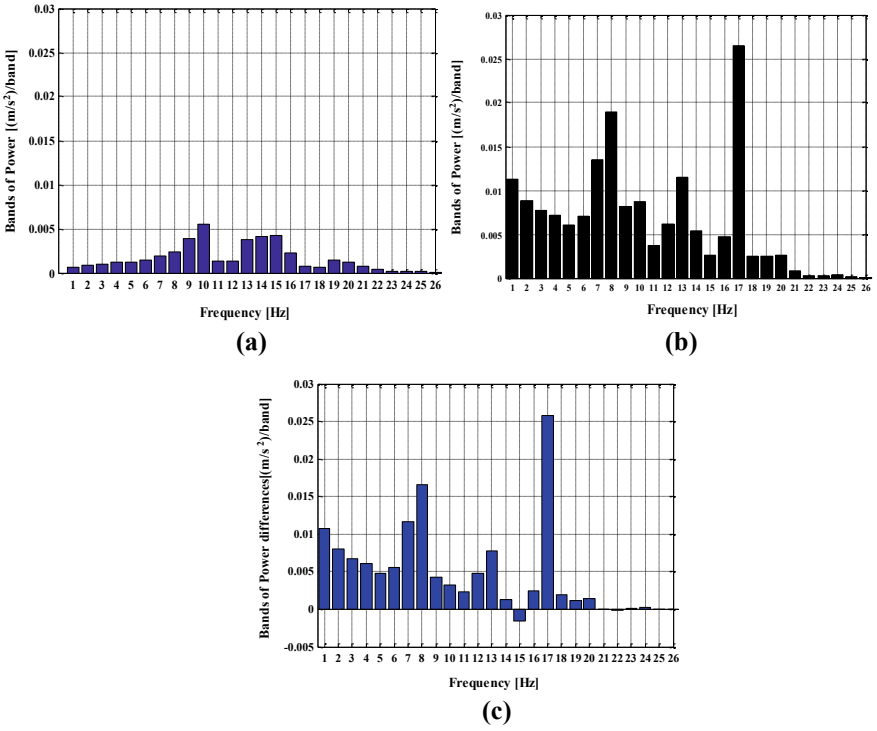

Fig. 11 Third octave band of power **a** without perturbation **b** with perturbation and **c** difference

References

1. Howe MS (2002) Theory of vortex sound. Cambridge University Press, Cambridge
2. Mazdeh A (2012) Damping parameter study of a perforated plate with bias flow. University of Dayton, University of Dayton
3. Ji C, Zhao D (2014) Two-dimensional lattice Boltzmann investigation of sound absorption of perforated orifices with different geometric shapes. Aerosp Sci Technol 39:40–47
4. Schulz A, Haufe D, Czarske J, Fischer A, Bake F, Enghardt L Spectral analysis of velocity fluctuations in the vicinity of a bias flow liner with respect to the damping efficiency. Acta Acustica United Acustica 101(1):24–36
5. Heuwinkel C et al (2010) Characterization of a perforated liner by acoustic and optical measurements. In: 16th AIAA/CEAS Aeroacoustics conference, American institute of aeronautics and astronautics
6. Menter F, Egorov Y (2005) A scale adaptive simulation model using two-equation models. In: 43rd AIAA aerospace sciences meeting and exhibit, American institute of aeronautics and astronautics
7. Ji C, Zhao D (2013) Lattice Boltzmann simulation of sound absorption of an in-duct orifice. Proc Meet Acoust 19(1):30015

Role of Agitator Diameter and Nusselt Number for Finding Heat Transfer Equations in Jacketed Vessel

Pardeep Kumar, Ansar Ali Sk, Sandeep Kumar, and Dinesh Khanduja

Abstract In an agitated vessel for finding heat transfer coefficient, few factors play important role. For properly mixing of different fluids, the method of forced convection is used with the help of agitators. For studying the role of agitator diameter and Nusselt Number, calculations of heat transfer were performed with three different agitators of different diameters. It was observed that the diameter of agitator, D_a predicts the effect in Reynolds number, an approach has been done for fining the connection between the agitator diameter and Nusselt Number. A link between $(N_{uj}/N''_{Pra}{}^{1/3}\ N''_{Rea}{}^{2/3})$ vs D_a/D_T and $(N_{uoc}/N''_{Pra}{}^{1/3}\ N''_{Rea}{}^{2/3})$ vs D_a/D_c in which data of three fluids (1, 2 and 4% CMC-A solutions) have been plotted. Almost negligible effect of D_a/D_T is noticed maybe because of very short variation of D_a/D_T ratio considered in the current work. Nevertheless, an average line between data points gives the implication of D_a/D_T and D_a/D_c equal to 0.1. A comparison has been done between the experimental and calculated Nusselt numbers with standard deviation found to be 8.03%.

Keywords Agitator diameter · Reynolds Number · Prandtl Number · Nusselt Number

P. Kumar (✉) · A. A. Sk · S. Kumar
Department of Mechanical Engineering, MIET, Uttar Pradesh, Meerut, India
e-mail: pardeepkamboj@yahoo.com

A. A. Sk
e-mail: ansnil@gmail.com

S. Kumar
e-mail: sdevnitj@gmail.com

D. Khanduja
Department of Mechanical Engineering, NIT Kurukshetra, Kurukshetra, Haryana, India
e-mail: dineshkhanduja@yahoo.com

L. M. Das et al. (eds.), *Emerging Trends in Mechanical Engineering*, Lecture Notes in Mechanical Engineering, https://doi.org/10.1007/978-981-15-8304-9_18

1 Introduction

In process industry, this is essentially required to do one or various operations in a agitated container to find correlations. These agitated carrier, performance, whether operated ongoing or in a steps have many parameters in common [1]. During these processes, they use negligible amount of energy [2]. All experiments are very rare to perform and take very long time to accomplish [3]. For any type of operations, there is always a standard diameter of the agitator [4].

In process industry, heat exchangers are used and the configuration of exchange of heat in a mechanical vessel using agitator has important attention nowadays. But the investigators found that there is much difference in the heat transfer equations with and without using agitator in heat exchanger [5]. This is because of mainly complications in findings the speed and temperature distribution for the exact mathematical formulation. The other problem of viscosity for Reynolds and Prandt Numbers has constructed problems in getting a favorable equation for Power law fluids. It is noted that the equations delivered for the Power law fluids are constructed from Newtonian fluids equations. Reynolds and Prandtl Number constants are almost same for both types of fluids.

From the previous workers experiments, it is found that the heat transfer equations are not independent on the diameter of agitator. As big numbers of parameters are involved, it is quite difficult to find exact correlation between equations. It is noted that the temperature profile in a mechanical vessel from the surface of the vessel and from the surface of helical coils, based on speed or revolutions and temperature close the surface of wall. The velocity plays a role and which controls the temperature profile on the performance of the system. Many factors like diameter, agitators' type, location of agitator, and rpm affect the correlations. Also tank size, coil diameter, turns, and speed play important role in the same way [6].

2 Literature Review

Carreau et al. [3] conducted experimental work and found heat dissipation and loss in heat had no effect in the heat transfer equation. Local heat transfer coefficient was found with the use of the overall heat equation using a modified Wilson plot. To determine Nusselt Number, Reynolds Number equation was used by them. The Reynolds Number constant was found as 0.66. They suggested the flowing correlations.

$$N_{\mathrm{Nu}} = 3.41\left(N'_{\mathrm{Re}}\right)^{\frac{2}{3}}(N_{\mathrm{Pr}})^{1/3} \tag{1}$$

$$N_{\mathrm{Nu}} = 1.43\left(N'_{\mathrm{Re}}\right)^{\frac{2}{3}}(N_{\mathrm{Pr}})^{1/3} \tag{2}$$

It is interesting to note that they obtained a single equation for heating and cooling experiments.

$$\frac{h_j D_T}{k} = 1.474\left[\left(\frac{D_a^2 N^{2-n}\beta}{K}\right)8\left(\frac{n}{6n+2}\right)^n\right]^{0.70} \times \left(\frac{C_p \mu_{d\infty}}{k}\right)^{0.33}\left(\frac{\mu_{\mathrm{dw}}}{\mu_d}\right)^{-0.24/n} \tag{3}$$

$$\text{For}\frac{D_a}{D_T} = \frac{3}{5}, 0.34 \le n \le 0.63, 100 \le N_{\mathrm{Re}} \le 5000$$

Skelland and Dimmick [5] suggested with mean variations of ±11.3% and ±18.3%, respectively. It is given by.

$$N_{\mathrm{Nu}} = 0.482(N_{\mathrm{Re}})^{\frac{2}{3}}(N_{\mathrm{Pr}})^{1/3}\left(\frac{\mu}{\mu_j}\right)^{0.12} \tag{4}$$

Perarasu et al. [7] conducted experiments and shown that following relation

$$N_u = 0.0877\left(\frac{\rho N D_a^2}{\mu}\right)^{0.64}\left(\frac{C_p \mu}{k}\right)^{0.29}\left(\frac{D_a}{D_T}\right)^{0.1}\left(\frac{D_0}{D_T}\right)^{0.5}\left(\frac{\mu}{\mu_w}\right)^{0.21} \tag{5}$$

Pawar et al. [8] observed that if helix diameter increases, then for constant heat flow coefficient of heat and dimensionless number like Nusselt Number decreases. Mohammad Sharifi [9] showed incremental growth in coefficients and Nu using Power law fluids. The results proved good relationship with the experimental work. Castro1 et. al. [4] proved that the agitator was convenient to agitate and with the mixing results heat transfer enhances.

3 Experimental

Three CMC solutions with concentration of 0.5, 1 and 2% and water were used in the helical coil and 1, 2, and 4% CMC solutions in the test vessel.

The agitator was fitted at the center of the vessel which is used to agitate the fluid in the vessel. The agitator geometry was given power by a 2 H.P. AC motor and speed were controlled by gear box fitted with it. Space was provided at the bottom of the setup to replace different sizes of agitators; for the experiment, three different agitators were used and four blades were provided. Diameters of agitators were 7.5, 12.7, and 18.35 cm^3. and coil tube diameters not changed. The flow constants of the fluids in the vessel varies from 0.69 to 1 and in the helical coil, from 0.79 to 1. Vessel bottom inner surface to agitator height should be 5.5–6.2 cm^2.

4 Result and Discussion

For finding the results of agitator diameter, it is required to measure the heat transfer with three agitator of diameter 7.5 cm, 12.7 cm, and 18.35 cm, respectively. It is noted that the diameter of agitator emits the effect in Reynolds Number; at the same time, it was tried to obtain the result of D_a/D_T on Nu.

Figure 2 helps to find the correlation between ($N_{uj}/N''_{Pra}{}^{1/3}$ $N''_{Rea}{}^{2/3}$) and D_a/D_T in which plot of three different fluids for D_a/D_T of the values 0.166, 0.282, and 0.403 have been graphically shown. It was found that there is no effect of D_a/D_T is observed as little variation of D_a/D_T considered in here. An average for data points explained the index of diameter ratio to be 0.1. Therefore, the overall results of agitator diameter give.

$$h_j \alpha\, D_a^{1.433} \tag{6}$$

In the final stage, $N_{uj}/N''_{Pra}{}^{1/3}$ $(D_a/D_T)^{0.1}$ is graphically plotted with N''_{Rea} in Fig. 3 in which water and 1, 2, and 4% CMC solution were considered. Using least square method, we have.

$$N_{\text{Nuj}} = 0.302 N''^{2/3}_{\text{Rea}} N^{1/3}_{\text{Pra}} \left(\frac{D_a}{D_T}\right)^{0.1} \tag{7}$$

It is quite noticeable that all values of both Newtonian and Power law fluids are in very good agreement with Eq. (2) for $290 < N''_{Rea} < 1.4 \times 10^7$; $4.9 < N''_{Pra} < 850$ and $0.166 < (D_a/D_T) < 0.403$.

Figure 4 shows a comparison of practical Nusselt Numbers with those theoritical from Eq. (2) the standard deviation obtained as 8.03%. Again, $N_{\text{Nuoc}}/N''^{2/3}_{\text{Rea}} N''^{1/3}_{\text{Pra}}$ when graphically represented against (D_a/D_c) as given in Fig. 4, the exponent of (D_a/D_c) obtained 0.10.

C_2 constant in the equation for water, and 1, 2 and 4% CMC solutions for agitators are plotted in Fig. 5 where $N_{Nuoc}/N''^{1/3}_{Pra}(D_a/D_c)^{0.1}$ are graphed against N''_{Rea} (Fig. 6).

$$N_{\text{Nuoc}} = C_2 \left(N''_{\text{Rea}}\right)^{2/3} \left(N''_{\text{Pra}}\right)^{1/3} \left(D_a / D_T\right)^{0.1} \tag{8}$$

$$N_{\text{Nuoc}} = 0.036 \left(N''_{\text{Rea}}\right)^{\frac{2}{3}} \left(N''_{\text{Pra}}\right)^{\frac{1}{3}} \left(D_a / D_T\right)^{0.1} \tag{9}$$

Practical values of Nu are compared with theoretical correlates as for $290 < N''_{\text{Rea}} < 1.4\text{X}10^7$, $4.9 < N''_{\text{Pra}} < 850$ and $0.166 < (D_a/D_c) < 0.403$ with a standard variation of 15.03% (Fig. 7).

Finally, the Nusselt Number equation for vessel surface and inside the helical coil has been established as:

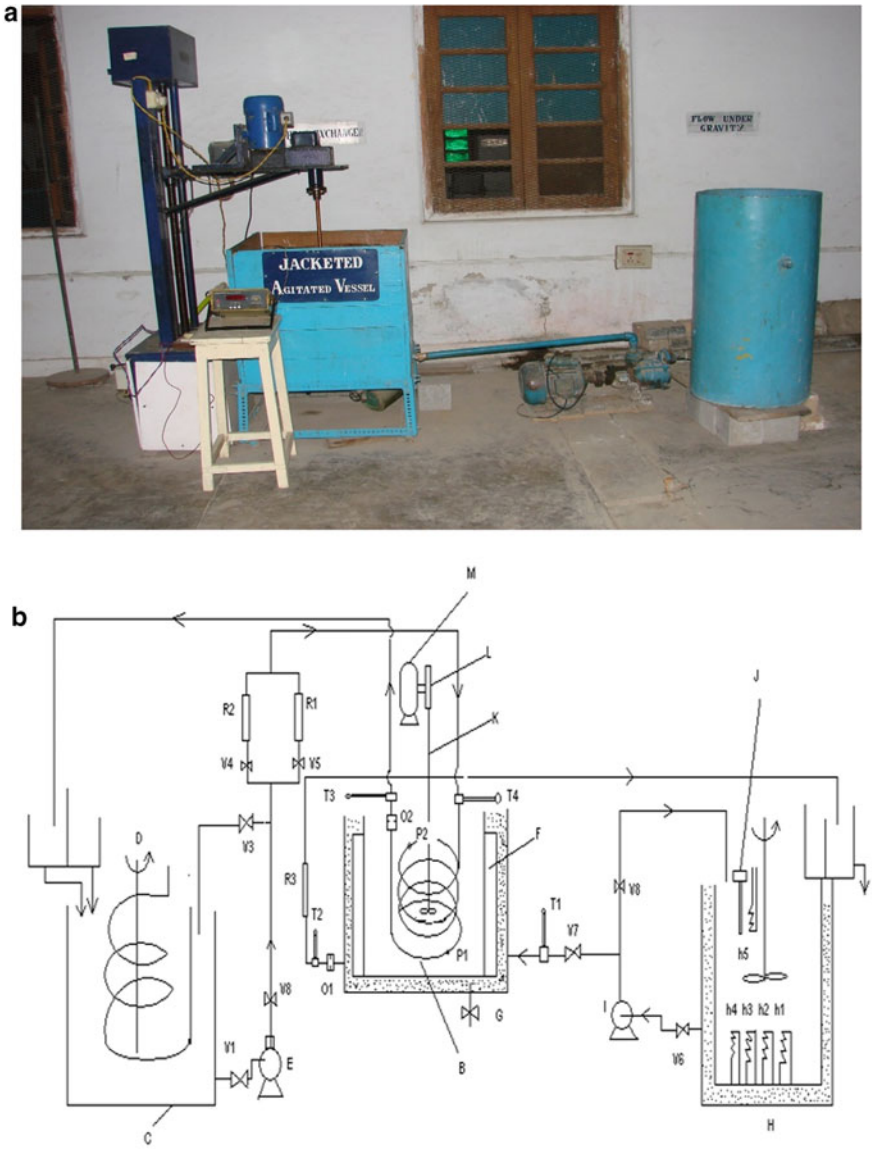

A-main vessel, B-helical coil, C- tank, D- agitator, E- pump, F- insulated jacket, G- tank of wood, I- pump, J- controller of temperature, K- agitator, L- reduction gear box, M- Moto R1-R3- Rota meters, T1-T4- thermometers, V1-V8- regulating valves, h1-h5- heater, p1 and p2- pressure tapings

Fig. 1 A experimental setup b experimental setup schematic diagram

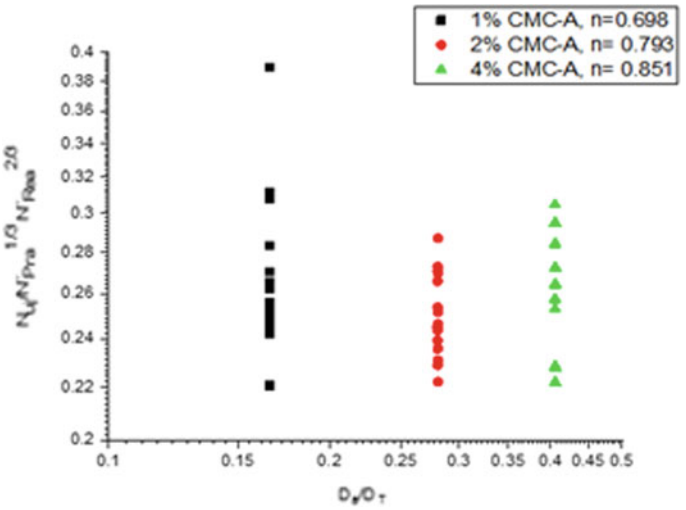

Fig. 2 Heat transfer correlation (effect of diameter)

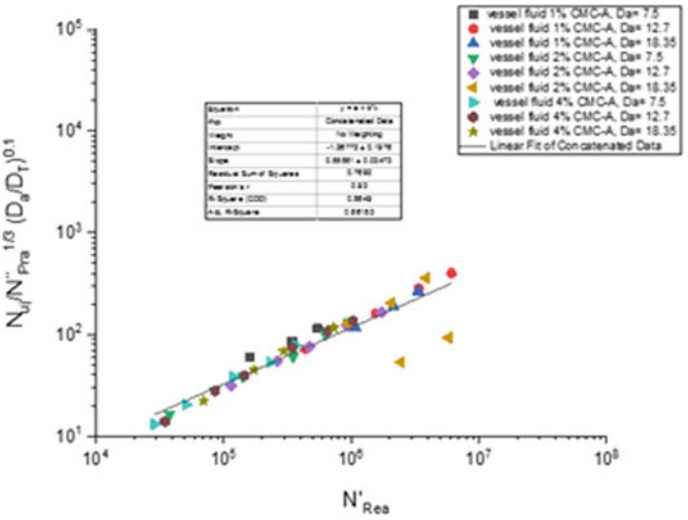

Fig. 3 Effect of Reynold Number on heat transfer (Jacket to Agitated)

For vessel surface: $N_{Nuj} = 0.302 N''^{\frac{2}{3}}_{Rea} N''^{\frac{1}{3}}_{Pra} \left(\frac{D_a}{D_T}\right)^{0.1}$ (Standard variation1 8.03%)

For helical coil: $N_{Nuoc} = 0.036 N''^{\frac{2}{3}}_{Rea} N''^{\frac{1}{3}}_{Pra} \left(\frac{D_a}{D_c}\right)^{0.1}$ (Standard variation1 5.03%)

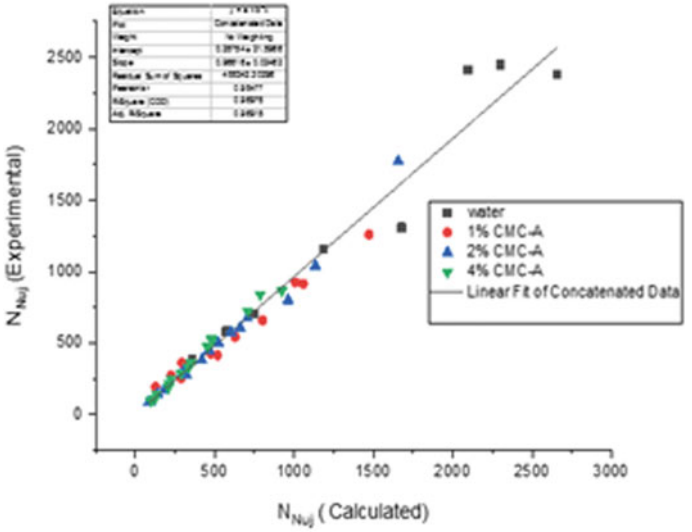

Fig. 4 Comparison between experimental and calculated values of Nusselt Number

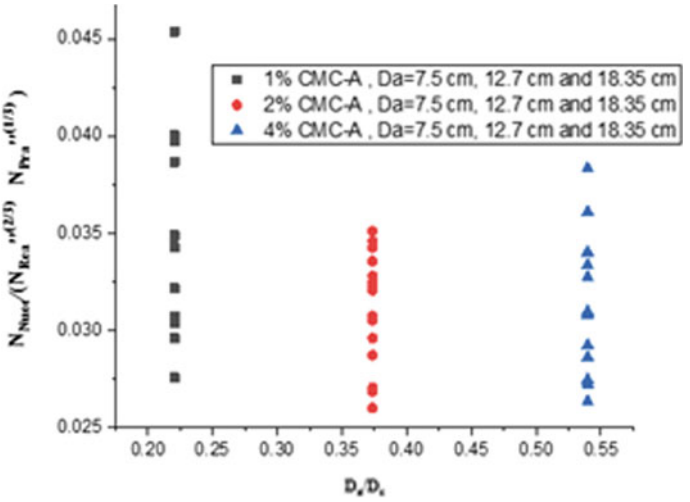

Fig. 5 Effect of agitator diameter on heat transfer (coil to agitated vessel)

$$290 < N''_{\text{Rea}} < 1.4x10^7, 4.9 < N''_{\text{Pra}} < 850 \quad \text{and} \quad 0.166 < \frac{D_a}{D_T} < 0.403$$

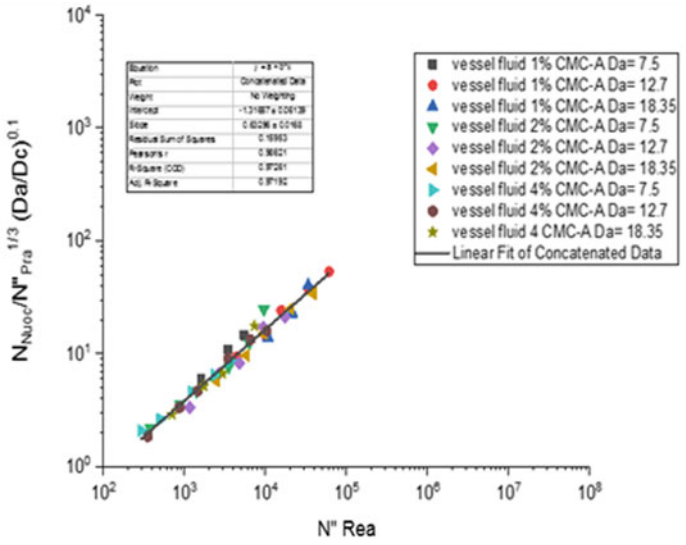

Fig. 6 Heat transfer correlation for Newtonian and non-Newtonian fluids (coil to agitated)

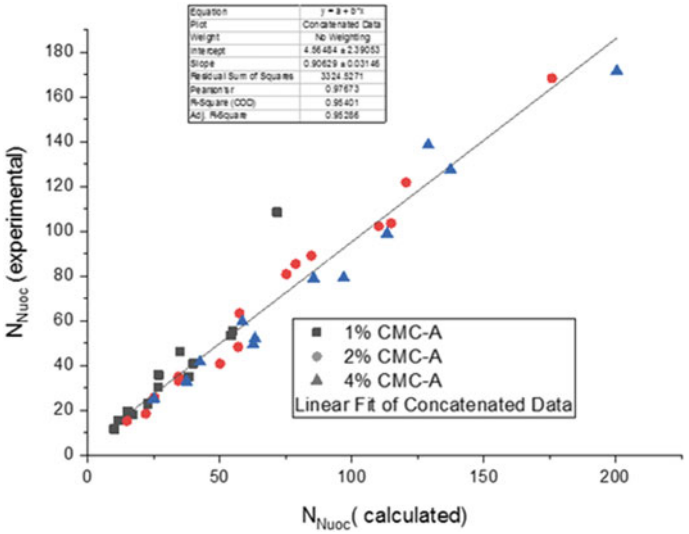

Fig. 7 Comparision between experimental and calculated values of Nusselt Number (coil to agitator)

5 Conclusions

The data for stirred fluids that is Newtonian and Power law of fluid have finally established by considering the viscosity of the liquids found at the agitator notch in a cylinder of radius equal to that of agitator rotating in fluids. Data of 1, 2, and 4% CMC solutions, for different impeller diameters, have been established and it was found that the Nusselt Number equation is applicable for both Newtonian and Non-Newtonian fluid with 8.03% standard deviation(for vessel surface) and 15.03% standard devitation (for helical coil).

With the help of the above results for Reynolds Number (Re) and Prandtl Numbers (Pr), Nusselt Numbers(Nu), and $Da/D_{T,}$ ratio one can correlate the available previous researchers data for other Power law fluids which were obtained with different agitator diameters.

Nomenclature

Da	Agitator diameter
D_c	Coil diameter
D_t	Inside diameter coil tube
D_o	Outside diameter coil tube
D_T	Agitated container diameter
h_j	Coefficient heat transfer for jacketed container wall to fluid, Kcal/hr m^2 °C
h_{oc}	Coil outside heat transfer coefficient, kcal/hr m^2 °C
h_{ic}	Coil inside heat transfer coefficient, kcal/hr m^2 °C
k	Thermal conductivity
n	Flow behavior number
n’	Generalized flow behavior index
N_{Nu}	Nusselt Number, h D/k
N_{Nuj}	Nusselt Number, h_j D_T/k
N_{Nuoc}	Nusselt Number, h_{oc} D_o/k
N_{Nuic}	Nusselt Number, h_{ic} D_t/k
N'_{Re}	Reynolds Number
N_{Pra}	Prandtl Number
N_{pr}	Prandtl Number
N'_{pr}	Prandtl Number

References

1. Ashok Reddy K, Bhavanth Rao M, Ram Reddy P (2012) Experimental estimation of heat transfer coefficients using helical coil in an agitated vessel. Int J Eng Trends Technol 3(2):113–122
2. Pawar SS, Vivek FT, Sunnapwar K (2013a) Experimental studies on heat transfer to newtonian and non-newtonian fluids in helical coils with laminar and turbulent flow. Exp Therm Fluid Sci 44:792–804
3. Carreau P, Charest G, Corneille JL (1966) Heat transfer to agitated non Newtonian fluids. Can Jl Chem Eng 44:1196
4. Fedal Castro N, Chitra B, Pushpalatha R, Sudalai S (2014–2015) Heat transfer effects for two different impellers using newtonian and non-newtonian fluids in an agitated vessel. Int J Chem Tech Res CODEN (USA): IJCRGG 7(6):2802–2808
5. Skelland AHP, Dimmick GR (1969) Heat transfer between coils and non newtonian fluids with propeller agitation. I.E.C. Proc Des Dev 8:267
6. Kato Y, Tada Y, Takeda Y, Hirai Y, Nagatsu Y (2009) Correlation of power consumption for propeller and pfaudler type impellers. J Chem Eng Jpn 42(1):6–9
7. Perarasu VT, Arivazhagan M, Sivashanmugam P (2011) Heat transfer studies in coiled agitated vessel with varying heat input. Int J Food Eng 7(4)
8. Pawar SS, Vivek FT, Sunnapwar K (2013b) Exp Therm Fluid Sci 44:792–804
9. Mohammad Sharif ASL, Davood T, Reza Azimiam A (2014) Numerical investigation on heat transfer coefficient enhancement of non-newtonian nanofluid in the turbulent flow inside a tube. Indian J Sci Res 1(2):363–369
10. Ansar Ali SK, Singh LP, Gupta SN (2015) Laminar forced convection to fluids in coiled pipe submerged in agitated vessel. Int J Mech Eng Robot Res. 4(1). ISSN 2278–0149
11. Ansar Ali SK, Singh LP, Gupta SN (June 2014) Heat transfer to newtonian and non-newtonian fluids in mechanically agitated vessel. Int J Sci Eng Technol Res 3(14):3031–3035
12. Debab A, Chergui N, Bekrentchir K, Bertrand J (2011) An Investigation of heat transfer in a mechanically agitated vessel. J Appl Fluid Mech 4(2–1):43–50
13. Kamei N, Hiraoka S, Kato Y (1995) Power correlation for paddle impellers in spherical and sylindrical agitated vessels. Kagaku Kogaku Ronbunshu 21:41–48
14. Kamei N, Hiraoka S, Kato Y (1996) Effects of impeller and baffle dimensions on power consumption under turbulentflow in an agitated vessel with paddle impeller. Kagaku Kogaku Ronbunshu 22(2):255–256
15. Inoue Y, Hashimoto S (2010) Analysis of mechanism of laminar fluid mixing in 3-D mixing tank based on streakline lobes. Kagaku Kogaku Ronbunshu 36(4):355–365
16. Kato Y, Kamei N, Tada Y et al (2011) Power consumption of anchor impeller over wide range of reynolds number. Kagaku Kogaku Ronbunshu 37:19–21

Performance and Emission Testing of Diesel Engine Using Blends of Biodiesel from Castor Oil and Neem Oil Prepared Using Lithium-Doped CaO Nano-Catalyst

Upender Kumar and Pardeep Gupta

Abstract Biodiesel has been attracting scientist for near about a century, and new revolutionary research and technical improvement had taken place in this field. But the basic problem of cost involved in using the biodiesel in engine in place of conventional diesel fuel is lying as such till date. In the present research work, it was tried to eliminate this problem by using non-edible oils with natural sourced catalyst optimizing certain set of parameters of best biodiesel performance. The biodiesel was produced from castor oil from highmedia and neem oil secured form S.K. Bioenergy Pune and Paritosh Herbals Ltd., Dehradun, Uttarakhand. A new method of preparation of nano-catalyst lithium-doped CaO obtained from Musa balbisiana root has been suggested and used to prepare biodiesel. The characteristics of biodiesel produced were tested according to ASTM standards. Different blends of the biodiesel are produced using castor oil, neem oil and conventional diesel oil. The engine characteristics running on blended fuel were tested on a C.I. Engine. The trials were performed on a four-stroke diesel engine operated utilizing various mixes of oil. Engine speed and load are considered as the parameters of interest. The result is the optimized running condition at which the engine will give best BSFC and least pollutants in emission.

Keywords Biodiesel · Castor oil · Neem oil · Musa balbisiana · Li-CaO catalyst · Performance characteristics · Emission characteristics

U. Kumar (✉) · P. Gupta
Mechanical Engineering Department, S.L.I.E.T., Longowal, Sangrur, Punjab, India
e-mail: udhull2015@kuk.ac.in

P. Gupta
e-mail: pardeepmech@sliet.ac.in

L. M. Das et al. (eds.), *Emerging Trends in Mechanical Engineering*, Lecture Notes in Mechanical Engineering, https://doi.org/10.1007/978-981-15-8304-9_19

1 Introduction

The requirement of energy has increased drastically across the world in few past decades. Many factors such as abrupt change and increasing population, industrial growth and increasing urbanization are the few reasons behind this. According to CIA factbook, approximately 11 tons of fossil fuels are consumed every year [1]. Due to large-scale use of the fossil fuel, results will be very alarming in future as the reserved fossil fuels will be exhausted soon. With (nitrogen oxides), PM (particulate matters) and unburnt hydrocarbons are increasing increase in the demand of conventional fuels has also increased harmful content in environment. Exhaust gases like CO_2 (carbon dioxide), CO (carbon monoxide), NOx are the causes of environmental pollution and greenhouse effect. Estimates of future international energy requirements predicts that the energy requirement in 2030 may be 40–70% higher than it was in 2005 due to population rise and improved living standards [1]. Very high rate of energy consumption leads the world to be confronted with the energy crises. The situation will be much challenging in future due to surge in the number of vehicles around the world, when the supply of fuel will become a challenging issue. It has been anticipated that transportation vitality is with yearly increment of 1.8%, and it is anticipated that rate will definitely go to an even further higher level in future.

Biodiesel is a renewable and easily biodegradable environment-friendly fuel with properties comparable to petro-diesel, with which all these problems can be solved to some extent [2]. Biodiesel is basically a mono-alkyl ester formed through a chemical reaction between some alcohol and various feedstocks like vegetable oil, animal fat, waste cooking oil, microalgae, etc [3, 4]. Currently, biodiesel is mostly sourced from edible vegetable oils. But in a developing country, where large quantities of the edible oil is imported, conversion of biodiesel from edible oils is not really practical. On the other hand, India has a large feedstock availability of non-edible oils, which can be used a low-cost feedstock for producing biodiesel. The vegetable edible oils are costly too, whereas the cheaper non-edible vegetable oils can reduce the overall biodiesel cost. Non-edible feedstocks mainly include jatropha, mahua, karanja, neem oil, castor oil, jojoba, rapeseed oil, etc.

Oil from the seeds of these feedstocks can be extracted using various extraction techniques which include mechanical extraction, solvent extraction, enzymatic extraction. Then this extracted vegetable oil is converted into biodiesel using various conversion techniques like transesterification based on mechanical stirring, ultrasonication, enzymatic conversion or cavitation-based conversion.

1.1 Biodiesel

Biodiesel-based engine was first used in 1885 when Dr. Rudolph Diesel ran the compression ignition engine on a shelled nut oil. The engine built by Dr. Rudolph was displayed in the Paris exhibition of 1900 and astounded everybody when the patented

engine was run on petrol and shelled nut oil. In 1912 Rudolph diesel expressed that the utilization of vegetable oils for Internal Combustion Engine may not appear to be extremely critical right now, yet in future, such oils will have importance as high as non-renewable energy sources [5]. Scientists over a period of time learned that it is possible to bring down the viscosity of vegetable oils using transesterification and that it could work well even in new engines of modern era.

Biodiesel is actually a mix esters of multiple chain lengths along with saturated fatty acids. Biodiesel can be created from renewable sources, for example, virgin vegetable oils, utilized cooking oil, fats, and so on. Based on fatty acid components, they can have different composition [6, 7]. The physical and chemical properties may vary depending on difference in composition, affecting engine performance, fuel miscibility, exhaust emissions, lubricity, etc.

Consequently, it is really important to analyze the behavior of engine performance and emission parameters with the variation in ester group in chemical structure, leading to the development of particular fatty acid distribution linked with a particular biodiesel which in return provides various benefits in the biodiesel used for alcohol–diesel blends. Edible oil is most commonly consumed household item which is already undersupplied in India; therefore, the non-edible oils like rice bran oil, sunflower oil, neem oil, castor oil, karanja, castor, mahua, etc., could be the preferred source for the production of biofuels [8, 9].

1.2 Introduction to Castor Methyl Ester (CME)

Castor is increasingly favored among the all non-food seeds created in India because of the high oil substance and enormous biodiesel yield. It is assessed that the castor seeds contain 40% of the oil that can be effectively removed from it. The vegetable oil such as castor being highly viscous cannot be directly used in C.I. engine that directly prevents the atomization of oil. Prevention of atomization directly ceases the combustion process which may lead to the engine damage. To make it helpful for the compression ignition engine, it is important to decrease the consistency of a similar oil which can be accomplished by the procedure of transesterification.

1.3 Introduction to Neem Butyl Esters

The botanical name of neem is Azadirachta Indica. The plant grows in tropical and sub-tropical regions. India has a suitable environment for the plantation and growth of neem tree. India is the native country of the neem tree, and the neem tree has a long productive life span of over a century. Neem seed oil has several advantages in comparison to other vegetable oils due to its inherent physicochemical properties. The neem seed oil has very small amount of FFA content which in turn gives it a low acidity index of 9 mg/g. Small acidity will require smaller quantity of

Table 1 Properties of diesel, CME and neem oil butyl ester

Properties	Diesel	CME	Neem oil butyl ester
Density	830	880	872
Kinematic viscosity	3.5	6.9	4.50
Calorific value (KJ/Kg)	46,500	38,450	42,600
Flash point (°C)	50	160	164
Cetane no	55	50–55	57

basic solution to neutralize resulting in enhanced productivity in transesterification reaction. It has low water content (<0.05%) which helps in avoiding soap buildup during transesterification and also making separation and water washing easier. It has very high gross calorific value (39.50 MJ/kg), high flash point (227 °C) and very low sulfur content (0.11%) making it very good feedstock for biodiesel extraction. Some of the limitations like high carbon residue content (1.4%) and relatively high viscosity are detrimental to the use of neem oil for its conversion to biodiesel. However, viscosity can be reduced either during transesterification or by dilution with diesel. The physical and chemical properties measured for Castor Methyl esters and Neem Butyl esters compared to diesel are shown in Table 1.

2 Literature Review

Lin et al. [10] used biodiesel in compression ignition engine to analyze performance/emission parameters, and he concluded that the higher engine speed results in higher thermal efficiency, larger specific fuel consumption and higher temperature of exhaust gas while decreasing emission levels of CO_2, CO and other gases.

Zhu et al. [11] worked on the testing of compression ignition engine fueled with ethyl alcohol and diesel blends and concluded that the biodiesel alcohol blend gives lower particulate emission but higher NOx emissions. By adding ethanol along with Biodiesel, the Biodiesel-ethanol blend gives lower NOx and lower particulate emission.

Yoon et al. [12] observed the impact of the multiple fuels on the engine performance and exhaust emissions characteristics which showed that there was shorter ignition delay for biogas–biodiesel compared to ultra-low sulfur diesel due to larger cetane number of biodiesel.

Fazal et al. [13] analyzed the impact of various properties of biodiesel like higher propensity for auto-oxidation, larger polarity, hygroscopic character, electrical ability and solubility in biodiesel in comparison to petro-diesel leads to higher corrosion of metallic parts. It also degrades the quality of rubber components.

Additionally, it has high FFA, and large degree of unsaturation left after refinement can likewise improve erosion rate in car motor parts.

Mohapatra et al. [14] used non-edible castor oil in investigating its ethyl and methyl ester for their performance and exhaust emission in an agricultural diesel engine. They concluded by saying that a 20% blend of both esters yields proximal performances to that of petroleum diesel.

Bevinahalli et al. [15] carried out investigation on a single cylinder C.I. engine fueled with Simboura diesel and biodiesel blends. They prepared four types of blends with 10, 20, 30 and 100% biodiesel in the blend with diesel, and upon studying the results found that BTE of B20 was almost that of pure diesel but of higher percentages of biodiesel decreased BTE and increased BSFC. The least emissions were obtained for neat biodiesel (B100).

Patil and Deng [16] observed that non-edible oils such as jatropha and pangomia can become a real good feedstock for biofuel production. Biodiesel production process was optimized, and both two-step and single-step transesterification processes were applied. The yield obtained varied from 90 to 95% for jatropha biodiesel and 80 to 85% for pangomia oil. The fuel properties were compared with reference to those of ASTM biodiesel standards.

Balat [17] had done an extensive review of past work on biofuel. He observed that mainly biodiesel is being prepared from the traditional edible oils due to which food versus fuel issue comes into consideration. Large usage of edible oil for biodiesel production may lead to the shortage of edible cooking oil. As the availability of non-edible oil is not yet made to the desired level, the cost of these oils is very high in the market. Only when extensive use of non-edible oils will be made for biodiesel production only then the biofuel production will become economically viable for the long term.

3 Methodology

The following procedure was followed while conducting the experiments under present work:

1. Preparation of nano-catalyst lithium-doped CaO.
2. Biodiesel extraction using feedstocks, i.e., castor methyl ester (CME) and neem butyl ester (NBE), from two vegetable oils (castor oil, neem oil) using heterogenous catalyst nanocrystalline lithium-doped CaO.
3. Measurement of physical properties of prepared biodiesel, i.e., density, kinematic viscosity, flash point, fire point, etc.
4. Prepare blends of biodiesel (Table 2).
5. Perform the FTIR test on various blends of biodiesel.
6. Testing of the different blends on I.C. engine.
7. Evaluate and analyze the relationship between parameters such as thermal efficiency, specific fuel consumption, temperature difference, volumetric efficiency, exhaust heat difference, Emissions of different gases and smoke density and opacity levels, etc.

Table 2 Fuel used and blends

Blends	Castor methyl ester (%)	Neem butyl ester (%)	Petroleum diesel (%)
B0	0	0	100
B5	2.5	2.5	95
B10	5	5	90
B15	7.5	7.5	85
B20	10	10	80

8. Extract the conclusion from various observations.

3.1 Nano-catalyst Preparation

Nano-catalyst was prepared using the procedure suggested in past literatures in Sarma et al. [18] and Dinesh et al. [19]. For making MBCUS root ash catalyst, the procedure devised by Sarma et al. [18] was followed.

1. First, the Musa roots were sliced into thin layer samples (dimension 2.0 × 15 cm) and were sun dried for about a fortnight.
2. These dried slices were then burnt in an open atmosphere to make its ash.
3. The ash obtained were further transferred to the laboratory and processed for 2.5 h in a muffle furnace at 600 °C.
4. The dried Musa balbisiana roots were placed in muffle furnace and were calcined at 1100 °C in atmospheric conditions with a heating rate concerning 10◦C/min for 4 h. The solid end result was once beaten and after producing the CaO. During calcination, the remaining composition of ash except the CaO is decomposed, thus subsequently producing CaO. After calcination is complete, the furnace temperature was brought down in steps, and when the temperature of furnace reached 150 °C, the sample was transferred to the vacuumed desiccator for storage to avoid moisture pickup and reaction with atmospheric carbon dioxide from the air before being used [18]
5. Lithium-impregnated CaO (Li–CaO) was prepared by the sol–gel process by method as recommended in past literature by Kumar et al. [19]. The method follows the oven drying and the calcination process used to prepare these catalysts. Lithium nitrate is selected as precursor because it is low cost and it has a higher solubility in water. 7 g of lithium nitrate was dissolved in 5 ml of deionized water, and 10 g of CaO obtained from root ash was uniformly mixed by magnetic stirrer. The solution was dried up at 120 °C for 3 h and later calcined at 550 °C for 3 h. XRD analysis of Lithium doped CaO shows the highly crystalline nature of the prepared specimen (Fig. 1).

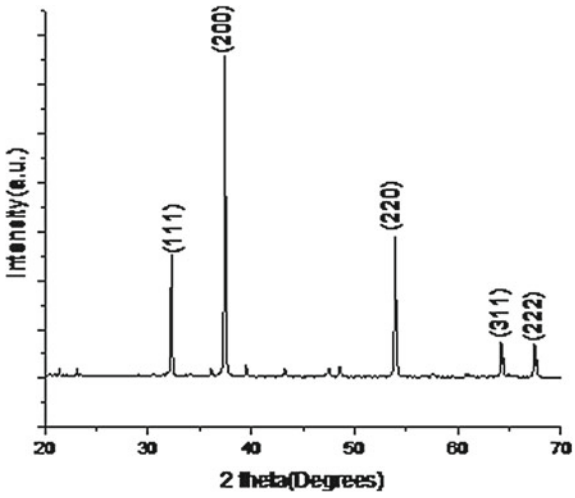

Fig. 1 XRD of nano-catalyst lithium-doped CaO

3.2 Biodiesel Preparation from Castor Oil and Neem Oil

Neem oil butyl esters were prepared from neem oil and n-butanol. Two-step transesterification was carried out [20–22]. Firstly, the high FFA content of oil was lowered to less than one percent by esterification. In the second step, the resulting triglycerides were transesterified using butane-1-ol (6:1 molar ratio) and 1.5% w/w CaO nanocatlyst doped with lithium. 1 L of neem oil was poured in a flask and was heated for about an hour at 1100 C to remove any traces of moisture (or any alcohol) present in it. About 1.8 g of lithium-doped CaO catalyst was added in the absence of moisture. Now, these freshly prepared lithium-doped CaO nano-powder was put into n-butanol in a moisture-free environment [17]. After the catalyst was uniformly mixed in n-Butanol, the mixture so prepared was poured in heated oil with constant stirring. Now the whole mixture was kept in an air-tight vessel with constant stirring initially using magnetic stirrer and then in probe-type ultrasonicator at a temperature of 65 °C for about 2 h (Fig. 2).

The mixture was placed in separating flask to settle overnight for separation of the mixture in two layers to get the ester layer on the top and glycerol on bottom side, ester layer separated as biodiesel. In order to remove the traces of glycerol still present in biodiesel, it was water washed and then heated and died.

Similarly, castor biodiesel was prepared using the similar procedure with only difference is that the ratio of catalyst used was 1% w/w of Li-CaO nanocatlyst with methanol added in the ratio of 6:1 with castor oil. After two-step transesterification, the biodiesel was separated from the glycerol.

Biodiesel thus obtained was separated from the catalyst using filter paper, and then remaining alcohol was separated from biodiesel in the rotary vacuum evaporator to get pure biodiesel. Biodiesel was characterized with FTIR analyser.

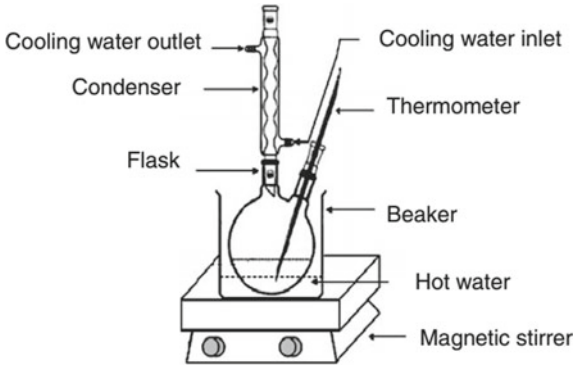

Fig. 2 Experimental setup to produce biodiesel using transesterification

Biodiesel yield ranging from 90 to 94% was obtained in different biodiesel samples.

It is imperative to mention here that the biodiesel yield through probe-type ultrasonicator was higher than with magnetic stirrer probably due to more vigorous mixing of catalyst with alcohol and oil and due to addition effect of ultrasonic cavitation in the solution.

3.3 Testing of Biodiesel Properties and Testing on C.I. Engine

The biodiesel blend samples were prepared using probe-type ultrasonicator using ultrasonic cavitation mechanism, and thereafter, biodiesel quality testing was done for various parameters like density, fash and fire point, viscosity and calorific value. After quality check, the biodiesel blends were prepared and these samples were used for testing of the diesel engine at varying process parameters.

The following instruments have been used for characterization of biodiesel (Table 3).

Table 3 List of instruments used in the present work

S. No	Instrument	Specifications
1	ABB MB 3000 FTIR	Resolution 1 cm^{-1}, Range:450–4000 cm^{-1}
2	Ultrasonic probe-type sonicator	1–150 °C temp., 30 kHz Frequency
3	XRD	Panalytical Xpert-Pro
4	Penskey martens apparatus	Flash point apparatus meant for oils. 50° to 200 °C
5	Density meter	Portable density meter of metler
6	Viscometer	Torsion-type viscometer from ATAGO
7	Calorimeter	Digital automatic bomb calorimeter

4 Result and Discussions

Various fuel quality characteristics of biodiesel blends were analyzed and found to be within ASTM standards for biodiesel.

4.1 Biodiesel Quality Testing

Density: Estimation of density is significant from the many viewpoints. To begin with, it is the significant parameter which will affect the total amount of fuel provided to the ignition chamber and furthermore the nature of fuel consumed in the chamber. Additionally, it influences different properties of fuel like consistency, cetane number, and warming worth. Biodiesel density is additionally significant for the design of the engine, stockpiling of fuel and transportation of the fuel. Because of every one of these reasons, it is imperative to assess the density of the biodiesel [23–25].

Density measurement was done as per ASTM D4052. The principle involved in the measurement of the density involves the technique using oscillating U-tube where the frequency of oscillation is measured electronically, and this is converted into an equivalent value of density. The sample is filled into a vessel with capacity of oscillation. The eigen frequency of the vessel is dependent on the mass of the sample. First, the instrument was switched on and allowed to stand for attaining set temperature 15 °C. Then, the 20 ml sample is taken in a container and the nozzle is dipped in the specimen. As soon as the start button is pressed, the instrument automatically collects the sample and measures the density. After measuring the density, the sample was washed out with the solvent automatically. The properties of Biodiesel blends from 5% to 20% were measured and found to be near to diesel (Table 4).

Kinematic Viscosity: The viscosity of the biodiesel was evaluated as per ASTM D446-12 using viscometer bath. First, the temperature was set at 40 °C. Then, the

Table 4 Various properties of biodiesel blends

	Diesel	B5 blend (2.5% CME and 2.5% NBE)	B10 blend (5% CME and 5% NBE)	B15 blend (7.5% CME and 7.5% NBE)	B20 blend (10% CME and 10% NBE)
Density (Kg/M^3)	830	835	836.75	837.6	837.9
Kinematic viscosity (Cs)	3.7	3.85	3.90	3.96	4.02
Flash point (°C)	76	81	83	83	85
Calorific value (KJ/Kg)	43,600	43,393.27	43,182.05	43,175.2	43,171.5
Fire point (°C)	79	85	87	88	90

half bulb of viscometer tube was filled with a given sample and hold it in the bath for 15–20 min. Then, biodiesel was sucked to smaller tube well above the upper mark.

The time period taken by biodiesel in moving from upper mark and lower mark in seconds multiplied by tube constant gives the measure of viscosity of the biodiesel in centistokes(cSt).

Flash point and Fire point: Flash point and fire points are measured as per ASTM D93-18 standard. The flash point and fire point were measured using a Pensky-Martens closed cup apparatus where the fuel is filled up to the filling mark and heated in a brass cup at a rate of 50 to 60 °C per minute. The sample was stirred at one or two revolutions per second, and when the oil gives out vapor, thereafter the stirring was stopped and the test flame was introduced above the lid and the temperature corresponding to the point where the flash flickering sound was produced was noted down. This is the flash point temperature of the biodiesel. The heating was continued further until the continuous burning of fuel takes place for at least Five seconds, which is the fire point of the biodiesel. The test was repeated with fresh oil samples three times to get the precise average value of the Flash and fire point temperatures.

Calorific value: The calorific value may be defined as the quantity of heat generated by complete combustion per unit mass of fuel with oxygen. Calorific value of the samples was evaluated using automatic digital isothermal microprocessor-based bomb calorimeter.

4.2 FTIR Characterization

In the present work, Fourier transform infrared spectroscopy (FTIR) technique is used to identify the esters in the final products of transesterification. The dominant frequency peaks that are formed with respect to the percentage transmittance are all quantified.

Fig. 3 shows the FTIR spectrum of CME biodiesel, and Fig. 4 shows the FTIR spectrum for NBE biodiesel produced from castor oil and neem oil, respectively. From the FTIR analysis in both cases, significant amount of castor methyl esters and neem butyl esters were confirmed from the corresponding peaks at 1736 and

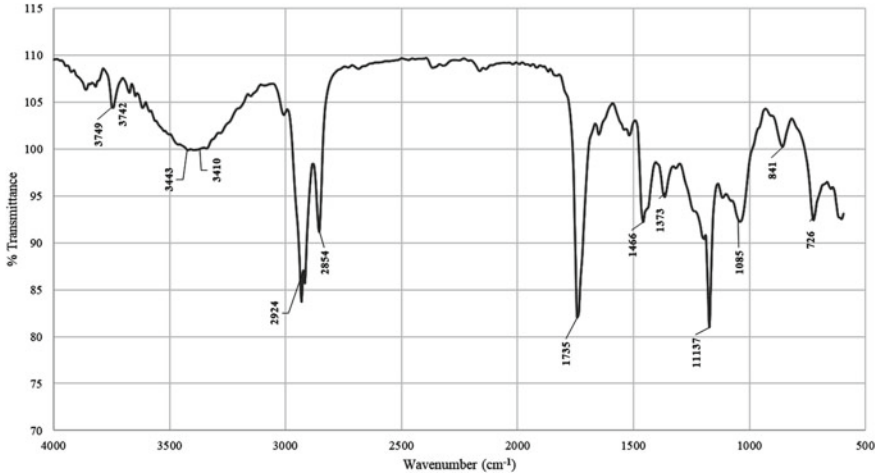

Fig. 3 FTIR spectrum of castor methyl ester

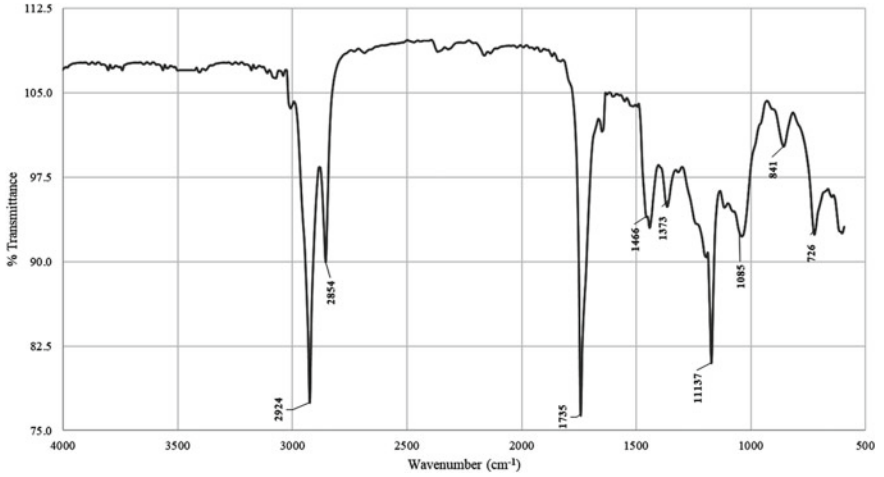

Fig. 4 FTIR spectrum neem butyl ester

1173 cm^{-1} in castor biodiesel and 1744 and 1173 cm^{-1}. Neem and castor oil biodiesel thus can also serve as the very good potential candidate for eco–friendly alternative to diesel fuel.

4.3 Performance Testing on Diesel Engine

The heat balance test on the engine was conducted, and heat balance chart was drawn. Various performance parameters were tested at different loads on pure petro-diesel and blended biodiesel with petro-diesel.

Brake-specific fuel utilization is higher for biodiesel mixes and keeps on in-wrinkling with proportionate ascent of biodiesel amount in the fuel blend. The reason may be the higher oxygen content in biodiesel expands the total burning, lower calorific value and higher viscosity of the biodiesel when contrasted with petro-diesel [3, 4]. For the two mixes and the unadulterated diesel, the BSFC continues diminishing with increment in engine loading (Fig. 5).

Brake thermal efficiency which shows an increasing trend with increasing load, decreases as the blending percentage increases. But, it is bit higher or almost similar to pure diesel for B5. This is probably due to change in cetane number during transesterification in the fuel leading to more efficient combustion of the fuel with increasing load [24, 8, 9] (Fig. 6).

Supplied fuel energy increases with load and blending ratio due to the higher oxygen availability resulting in complete combustion of the fuel leading to higher heat energy (Fig. 7).

Heat lost to cooling water is highest in B20 blend and lowest for diesel. This is due to better promotion of complete combustion process in biodiesel. Due to more efficient combustion, the in-cylinder temperature also rises, resulting in increased pressure and larger heat release rate to the cooling water and lubricant when the engine runs on biodiesel. Another reason might be due to the addition of higher hydrogen content which has lower quenching distance and higher burning flame front velocity of the hydrogen (Fig. 8).

The temperature of exhaust gases can be used to give qualitative inferences about the progress of combustion in the engine [26]. Change in EGT of biodiesel blends with variation in load is shown in Fig. 9. As the load is increased, the exhaust gas

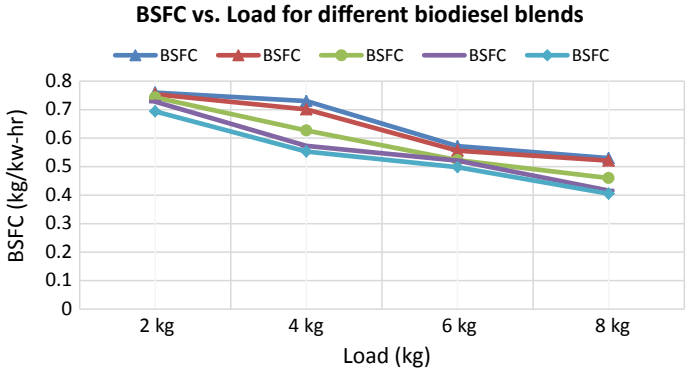

Fig. 5 Load versus brake-specific fuel consumption

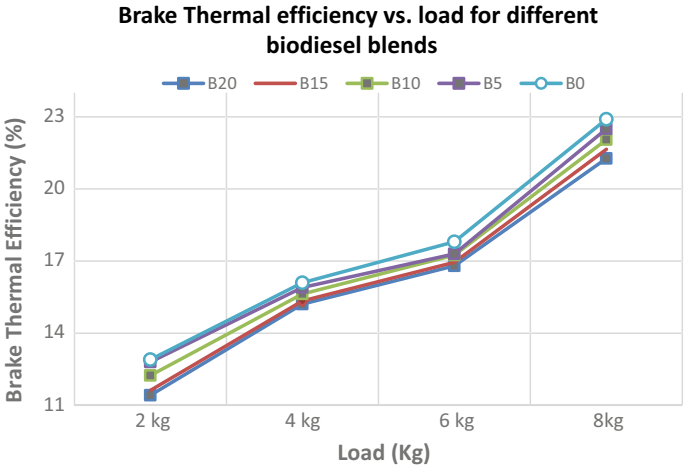

Fig. 6 Load versus brake thermal efficiency

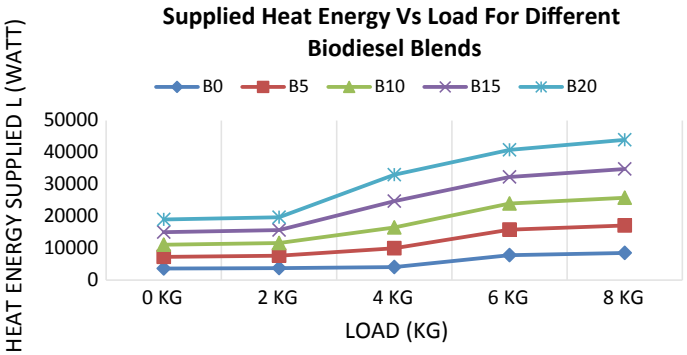

Fig. 7 Variation of supplied fuel energy with load

temperature also rises. Petro-diesel has the least temperature of the exhaust, and B20 has the highest. The reason behind higher EGT in biodiesel blends is the availability of more oxygen atoms in biodiesel and lower thermal efficiency of the biodiesel-based engine. At a lower thermal efficiency, lesser fuel energy is utilized to do work and most of the heat content is passed to the exhaust system. Also, NME has some components of higher boiling points than that of the diesel, in addition to oxygen. This may also lead to higher temperature of exhaust. More fuel is burnt as the load is increased resulting in more fuel is burnt, which results in further increasing EGT as the load is increased.

The volumetric efficiency can be described as the breathing ability of an engine. Volumetric efficiency is the relation between actual and theoretical amount of mixture sucked inside the engine. Volumetric efficiency reduces as the load is increased due

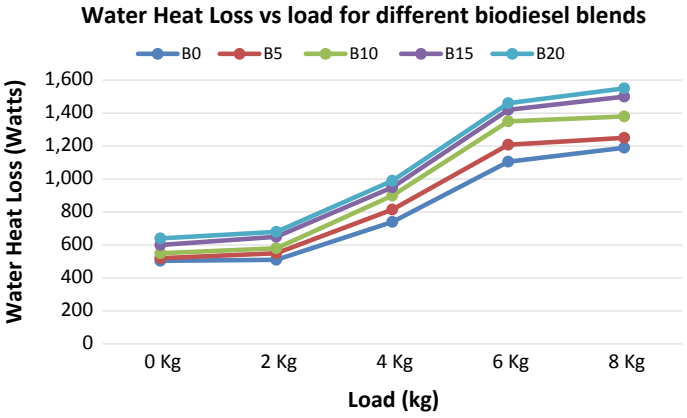

Fig. 8 Variation of cooling water heat loss with load

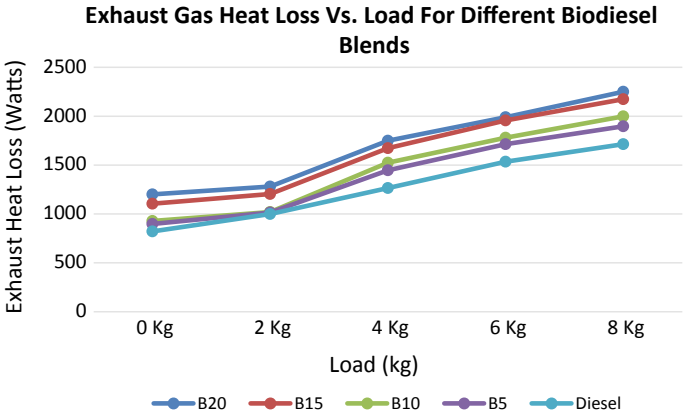

Fig. 9 Exhaust gas temperature difference versus load

to less suction at high speed in small time interval available for it. Due to higher heating value of the mineral diesel, it has got the highest volumetric efficiency and biodiesel blends have a lower volumetric efficiency due to the lower heating capacity of biofuel as it transfers heat to the cylinder walls and thereby to intake valve which reduces air density leading less volume of air going in the cylinder (Fig. 10).

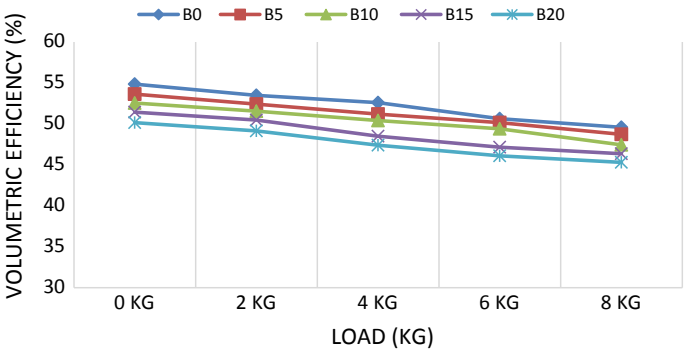

Fig. 10 Volumetric efficiency at different loads of various biodiesel blends

4.4 Emission Testing

Emission analyses were done using Indus smoke meter and AVL Digas 5 Gas Anlyser.

Smoke meter is an instrument for measuring smoke density and opacity of the exhaust fumes from the engine. The smoke opacity increases with load and decreases with increase in the biodiesel percentage in the blend due to relatively better combustion (Fig. 11).

The Indus smoke meter has a 4 m long hose pipe with three different-sized probe. It has the capacity to measure smoke density between 0 to 99.9 HSU and resolution of 0.1%. Accuracy achievable in the instrument is up to $\pm$ 0.1 m^{-1}. For smoke density measurement, the probe was inserted inside the exhaust pipe. A continuous sample was passed through a pipe with light source at one end and a photocell at the other end. The principal of light attenuation was used in the smoke meter to measure the

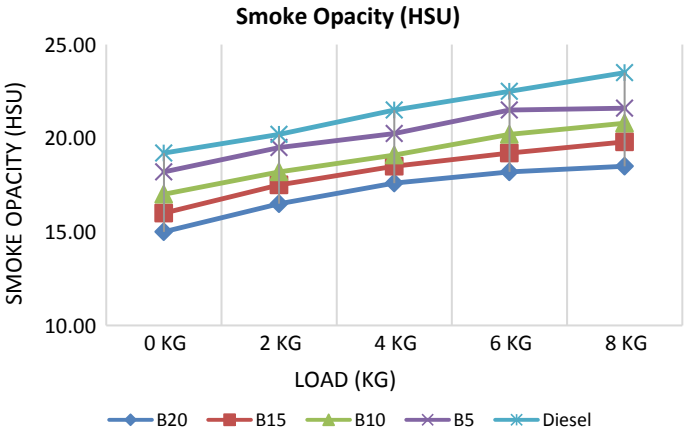

Fig. 11 Smoke opacity at different loads of various biodiesel blends

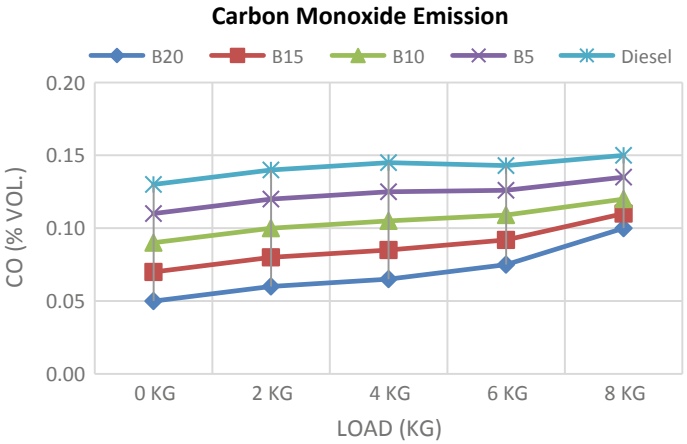

Fig. 12 CO Emission at different loads of various biodiesel blends

smoke density in Hartridge Smoke Unit (HSU). It has been observed that the smoke density is highest in diesel and least in a B20 biodiesel blend with petro-diesel. This is due to effective combustion in the biodiesel and presence of lesser quantity of unburnt fuel particles and soot particulates in the biodiesel in comparison with pure diesel. AVL DIGAS 444 Gas Analyser is used for analyses of various gaseous exhaust emission during the diesel engine testing.

Carbon Monoxide Emission (CO)
The carbon monoxide is emitted in diesel engine due to incomplete combustion of fuel which may be due to the lesser oxygen content in the fuel or lesser time available for completing combustion for oxidation of CO to CO_2. Biodiesel blends have lower CO emission as the blending ratio increases and the pure mineral diesel has the highest emission of CO due to less oxygen content and incomplete combustion in diesel (Fig. 12).

Carbon Dioxide Emission (CO_2)
The emission of carbon dioxide is higher in diesel in comparison to diesel due to more efficient combustion in the biodiesel due to the more oxygen content and proportionately lower quantity of arbon in it (Fig. 13).

Unburnt Hydrocarbons Emission (HC)
In biodiesel due to high content of oxygen, complete and effective combustion of fuel takes place due to which the unburnt hydrocarbon emission is lower in biodiesel and higher in pure mineral diesel (Fig. 14).

Nitrogen Oxide Emission (NOx)
NOx emission increases in biodiesel blends with increasing load and increasing the blending ratio due to higher cylinder peak temperature. As the combustion process

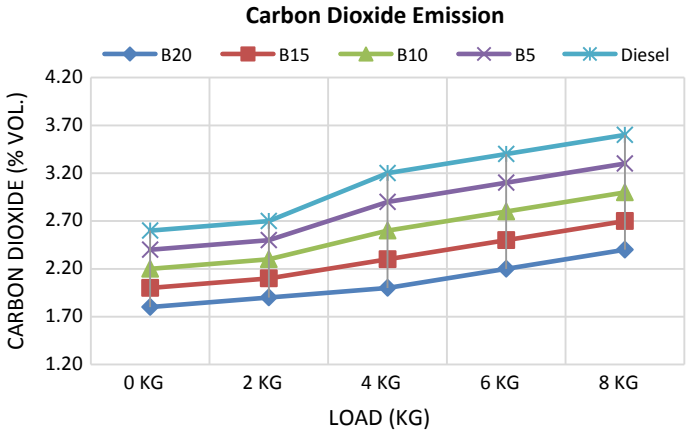

Fig. 13 CO_2 emission at different loads of various biodiesel blends

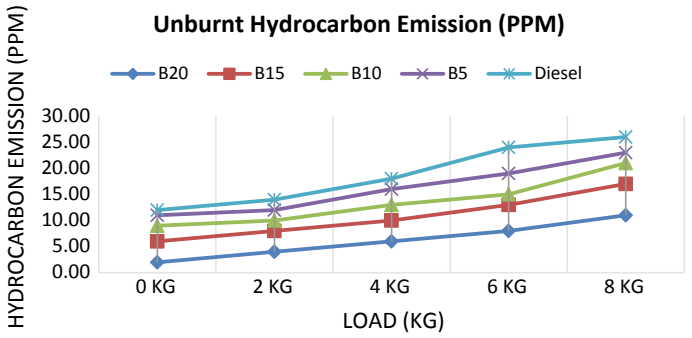

Fig. 14 Unburnt hydrocarbon emission at different loads of various biodiesel blends

is more efficient and fuel burns completely in bodiesel, the total temperature inside the combustion chamber is higher in NOx in biodiesel than in diesel (Fig. 15).

5 Conclusion

In this current work, experiments were performed using castor methyl ester and neem butyl ester blended with petro-diesel and the following results have been concluded from the experimental analysis.

- The BSFC of the blend is higher than diesel fuel because the calorific value of blends is less so more fuel is consumed to generate the same power. The results are in correspondence with the result produced by some other authors in the past [27–29]. BSFC up to 5% blend ratio is almost equivalent to diesel.

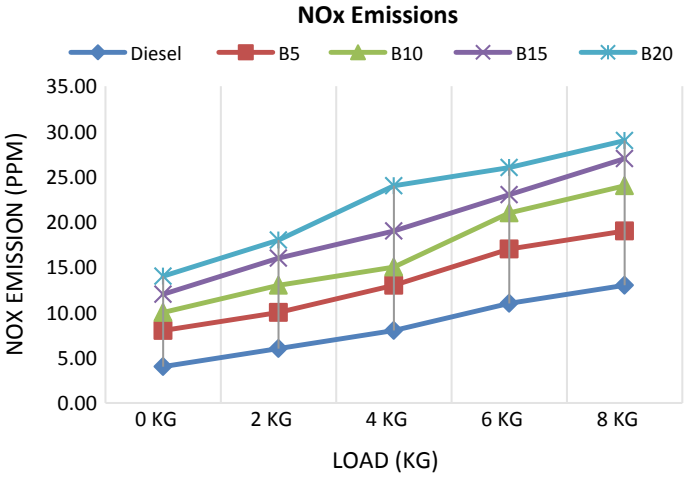

Fig. 15 NOx emission at different loads of various biodiesel blends

- As the load and brake power is raised, the thermal efficiency of diesel, CME and NBE blends also increases. Heat generated inside cylinder rises as soon as the brake power is raised, and therefore, the thermal efficiency of the engine is also enhanced.
- There is not much effect of blending on brake thermal efficiency (BTE) as the BTE of blended fuel is almost same as that of diesel up to 10% blend ratio and reduces marginally after 10% as compared to petro-diesel as a fuel.
- Biodiesel mixing builds the temperature of fumes and the mineral diesel has the least exhaust gas temperature (EGT). It ascends with engine loading. Diesel has minimal temperature of fumes. Lower heat efficiency and higher boiling point constituents of NBE are the principle explanation for the ascent in the exhaust temperature with biodiesel mixing.
- The brake-specific energy consumption (BSEC) will be a more precise measure of performance when multiple fuels of different densities and heating values are blended together. As the power is raised, the BSEC is reduced. Due to lower calorific value of biodiesel blends in comparison to petro-diesel for the same power output, the fuel consumption of an engine will be more with the CME and NBE blends than with the diesel.
- The brake-specific energy consumption of blended fuel is lower up to 10% blend ratio after that it increases because specific fuel consumption for blends is increased as compared to diesel.
- The emission of hydrocarbons, CO_2, CO is much lesser in biodiesel blends, and it is higher in pure mineral diesel. Also, smoke opacity is lesser in biodiesel than in pure diesel. The results are matching with the findings of the investigation of past authors [4, 8, 29].

- NOx emission is more in biodiesel in comparison to pure mineral diesel due to higher peak temperature level due to more efficient burning of biodiesel.

The experimental results concluded that the natural nano-catalyst lithium-doped CaO can be effectively used to prepare biodiesel and will result in the lowering of the overall cost of production. Prepared CME and NBE blends show a good alternate of the conventional diesel oil as the results show the similar or better performance as that of diesel.

References

1. The CIA World Factbook 2018–2019 (2018) Skyhorse Publications, New York, USA
2. Zhang J, Chen S, Yang R (2010) Biodiesel production from vegetable oil using heterogeneous acid and alkali catalyst. Fuel 89:2939–2944
3. Agarwal D, Agarwal AK (2007) Performance and emissions characteristics of jatropha oil (preheated and blends) in a direct injection compression ignition engine. Appl Therm Eng 27:2314–2323
4. Basha SA et al (2009) A review on biodiesel production, combustion, emissions and performance. Renew Sustain Energ Rev 13:1628–1634
5. Robert Nitske W, Wilson CM, Diesel R (1965) Pioneer of the age of power. University of Oklahoma Press, USA
6. Wang Y, Ou S, Liu P, Xue F, Tang S (2006) Comparison of two different processes to synthesize biodiesel by waste cooking oil. J Mol Catal American Chem 252:107–112
7. Singh SP, Singh D (2010) Biodiesel production through the use of different sources and characterization of oils and their esters as substitute of diesel: a review. 14(1):200–216
8. Ghobadian B, Rahimi H, Nikbakht AM, Najafi N, Yusaf TF (2009) Diesel engine performance and exhaust emission analysis using waste cooking biodiesel fuel with an artificial neural network. Renew Energ 34:976–982
9. Enweremadu CC et al (2010) Combustion, emission and engine performance characteristics of used cooking oil biodiesel—a review. Sci Dir Renew Sustain Energ Rev 14:2863–2873
10. Lin C-Y et al (2006) Diesel engine performance and emission characteristics of biodiesel produced by the peroxidation process. Fuel 85:298–305
11. Zhu L et al (2011) Combustion, performance and emission characteristics of a DI diesel engine fueled with ethanol–biodiesel blends. Fuel 1743–1750
12. Yoon SH et al (2011) Experimental investigation on the combustion and exhaust emission characteristics of biogas–biodiesel dual-fuel combustion in a CI engine. Fuel Process Technol 92:992–1000
13. Fazal MA et al (2011) Biodiesel feasibility study: an evaluation of material compatibility; performance; emission and engine durability. Renew Sustain Energy Rev 15:1314–1322
14. Mohapatra SB et al (2016) Non-edible castor oil—an esoteric potential foliage of methyl and ethyl ester, a sustainable additive package for agricultural diesel engines. Res J Recent Sci 5(11):8–16
15. Bevinahalli SN, Sasi MB et al (2016) Performance, emission and combustion test on CI engine by using simarouba biodiesel and diesel blends. Int Res J Eng Technol 03(06):2091–2096
16. Patil PD, Deng S (2009) Optimization of biodiesel production from edible and nonedible vegetable oils. Fuel 88:1302–1306
17. Balat M (2011) Potential alternatives to edible oils for biodiesel production- a review of current work. Energ Convers Manage 52:1479–1492
18. Sarma AK, Aslam M et al (2014) Preparation and characterization of musa balbisiana colla underground stem nano-material for biodiesel production under elevated conditions. Catal Lett

19. Kumar D, Ali A (2010) Nanocrystalline lithium ion impregnated calcium oxide as heterogeneous catalyst for transesterification of high moisture containing cotton seed oil. Energ Fuels 24:2091–2097
20. Gnanaprakasam A, Sivakumar VM, Sunrendhar A, Thirumarimurugan M, kannadasn T (2013) Recent strategy of biodiesel production from waste cooking oil and process influencing parameters: a review. Hindawi Publishing Corporation. J Energ 22
21. Lam MK, Lee KT, Mohamed AR (2010) Homogeneous, heterogeneous and enzymatic catalysis for transesterification of high free fatty acid oil (waste cooking oil) to biodiesel: a review. Biotechnol Adv 28:500–518
22. Charoenchaitrakool M, Thienmethangkoon J (2011) Statistical optimization for biodiesel production from waste frying oil through two-step catalyzed process. Fuel Process Technol 92:112–118
23. Singh A, Thompson J, Gerpen VJ (2006) Process optimization of biodiesel production using alkaline catalysts, American society of agricultural and biological engineers. Appl Eng Agric 22(4):597–600
24. Masjuki HH, Kalam MA et al (2006) Experimental evaluation of an unmodified diesel engine using biodiesel with fuel additive. Oct 18–Oct 20
25. Berchmans JH, Hirata S (2008) Biodiesel production from jatropha oil (Jatropha curcas) with high free fatty acids. Bioresour Technol 99:1716–172
26. Ryu K, Oh Y (2004) Combustion characteristics of an agriculture diesel engine using biodiesel fuel. KSME Int J 18(4):709–771
27. Liquat AM, Kalam MM et al (2011) Engine performance and Emission analysis using Envodiesel and coconut biodiesel blend fuel. Altern Fuels
28. Chalatonal V, Roy MM, Dutta A et al (2011) Jatropha oil production and an experimental investigation of its use as an alternative fuel in diesel engine 2011. J Petrol Eng Fuels 2(5):76–85
29. Muralidharan K et al (2011) Performance, emission and combustion characteristics of biodiesel fuelled variable compression ratio engine. Energy 36:5385–5393

Analysis of the Aerodynamic Characteristics of NREL S823 and DU 06-W-200 Airfoils at Various Reynolds Numbers Using QBlade

Kanthala Uma Reddy, Bachu Deb, and Bidesh Roy

Abstract Most of the fixed pitched wind turbines, which are used for the small-scale power generation, typically, are operated at low Reynolds numbers where the aerodynamic performance of an airfoil can change considerably with Reynolds number. So that the study of aerodynamics performance of airfoil at various low Reynolds number is much important. In this paper, such an attempt has been made through simulating the selected airfoils, says National Renewable Energy Laboratory (NREL) S823 and DU 06-W-200, using QBlade open-source software. QBlade software habits the double multiple stream tube (DMS) algorithms for evaluating the performance of vertical axis wind turbines (VAWTs) blade element method (BEM) for the evaluation of horizontal axis wind turbines (HAWTs). The viscous-inviscid coupled panel process code XFOIL is integrated within the graphical user interface (GUI) of QBlade for the calculation of lift and drag coefficient of an airfoil at any angle of attack (AoA). The simulation is carried out at various Reynolds numbers in the range of 1×10^5 to 3×10^5 for both selected airfoil and compared to each other. The results show that for every applied Reynolds number, S823 airfoil obtains higher lift coefficient up to 10° AoA after that DU 06-W-200 airfoil exhibits higher values and also the same pattern followed for lift-to-drag ratio. Finally, the simulation results are compared with the identified experimental data for validation purpose, and that displays good agreement between the QBlade simulation result and experimental data.

Keywords Reynolds number · Airfoil · QBlade · NREL S823 · DU 06-W-200

1 Introduction

Majority of the people around the world are realizing the benefits of renewable energy sources. Several renewable energy sources are being audited, with one of the more renowned sources being wind. Wind turbines are used to generate power from the

K. U. Reddy · B. Deb (✉) · B. Roy
National Institute Technology, Mizoram 796012, India
e-mail: bdebnitmz@gmail.com

L. M. Das et al. (eds.), *Emerging Trends in Mechanical Engineering*, Lecture Notes in Mechanical Engineering, https://doi.org/10.1007/978-981-15-8304-9_20

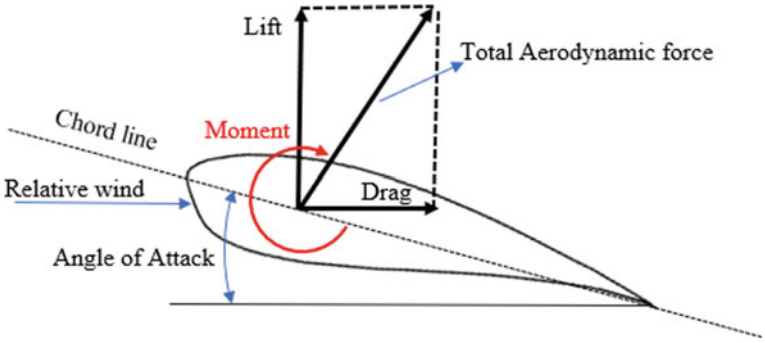

Fig. 1 Aerodynamic characteristics of an airfoil

kinetic energy of the wind. Large-scale wind turbines and small-scale wind turbines are becoming viable solutions for the power generation. Particularly small-scale wind turbines are intended for the application of low average wind speed region. Small-scale wind turbines are presently not as efficient as large-scale wind turbines [1]. Subsequently, these wind turbines are subjected to low wind velocity due to that these turbines produce less than optimum flow conditions and the main cause is that low Reynolds number flow through airfoil of the turbine. Aerodynamic characteristic of an airfoil (Fig. 1) like lift, drag, moment, pressure coefficient, and pitch angle transition of an airfoil is highly dependent on Reynolds number. Liu et al. [2] numerically investigated the effect of Reynolds number on the performance of supercritical airfoil and concluded that lower surface pressure distribution is not vulnerable with variable Reynolds number but upper surface pressure distribution and trailing edge pressure distribution are changing with variation in Reynolds numbers. Kim and Chang [3] examined the influence of Reynolds number ($20{,}000 < Re < 50{,}000$) on aerodynamic characteristics of the NACA0012 airfoil through flow visualization setup and they observed that mushroom structure and verities of airfoil trailing edge highly depended on the Reynolds number. Geng et al. [4] carried out comparison between experimental and 2D unsteady Reynolds averaged Navier–stokes (URANS) results to study the flow in the vicinity of a pitching NACA0012 symmetrical airfoil at a Reynolds number of 1.35×10^5. They determined that CFD and experimental result of lift and drag coefficient values of the particular airfoil at low angle of attack (AoA) almost lie in the same line but at high AoA considerably deviated. Morgado et al. [5] also conducted the comparison between performance prediction software, such as XFOIL and CFD, and experimental studies for E387 airfoil and S1223 airfoil. From the results comparison, they concluded that XFOIL remains the best design and analysis tool for airfoil. Alaskari et al. [6] conducted blade element momentum (BEM) simulation for SG6043 airfoil using open source QBlade software. They concluded that maximum value of lift-to-drag ratio is obtained at an AoA 2°. They also recommended the QBlade software to design and optimize the rotors and blades for a variety of wind turbines. Other researchers [7–9] also used QBlade software for different wind turbine projects. On the basis of that, this paper attempts to analyze

the effect of various Reynolds numbers on the aerodynamic characteristics of on selected airfoils using QBlade software.

1.1 Theoretical Formulation

Reynolds number (Re) is a measure of viscous behavior of air, and it can be defined for quite a few different conditions where a fluid is in relative motion to a surface. These definitions usually comprise the fluid properties of viscosity, density (ρ), velocity (u), and a characteristic dimension. The mathematical expression of Reynolds number (Eq. 1) defines it is the ratio of viscous force to inertia force [10].

$$Re = \frac{\rho u l}{\mu} = \frac{u l}{\vartheta} \tag{1}$$

Here l is the characteristic length, μ and ϑ are the dynamic and kinematic viscosity of the fluid, respectively.

Fluid flow is passing through any kind of surface of the body and it exerts a force on that body [6]. Lift and drag forces are perpendicular and parallel components of this force in the flow direction.

Theoretical formulation for lift (L) and drag (D) of airfoil can be written as following.

$$L = \frac{1}{2} C_L \rho A v^2 \tag{2}$$

$$D = \frac{1}{2} C_D \rho A v^2 \tag{3}$$

2 Airfoils Selection

In the period of 1984 to 1993, the NREL has designed and developed 7 families of airfoil, which consist of 23 verities, suitable for the various rotor diameter. From the 23 verities of airfoils, NREL S823 airfoil (Fig. 2) was selected on the basis obtainability of experimental data [11]. The S823 is especially designed for low wind speed and used for 2 to 10 meter diameter wind turbine and this was compared with another selected airfoil DU 06-W-200 (Fig. 2), which was laminar and unsymmetrical airfoil, especially designed for VAWTs at Delft University of Technology in 2006 [12]. The geometrical characteristics of selected airfoil are shown in Table 1.

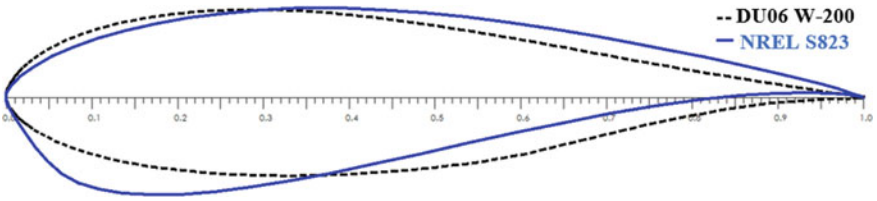

Fig. 2 Geometry of NREL S823 and DU 06-W-200 airfoils

Table 1 Geometrical characteristics of selected airfoils [13]

Airfoil	Maximum thickness (%)	Position (% chord)	Maximum camber (%)	Position (% chord)
NREL S823	21.2	24.3	2.4	70.5
DU 06-W-200	19.8	31.1	0.5	84.6

3 QBlade Software and Methodology

The QBlade software is an open-source software developed by a team at the Technical University of Berlin, Germany, for design and simulate the wind turbines. Many researchers [6–9] have been used the QBlade software for different wind turbine projects and its parametric investigations. Moreover, several educational institutes and universities have encompassed QBlade as a perceptive tool to understand the basic aerodynamic concept of a wind turbine [8]. The functionality of QBlade Software includes different modules shown in Fig. 3.

The NREL S823, DU 06-W-200 airfoil coordinates taken from the airfoil tools Web site [13] and saved in a dat file format. Saved dat file is imported into open-source QBlade software and analyzed several times at various Reynolds numbers. While doing simulation, the following assumption was defined in the QBlade Direct Analysis module.

1. Mach number (Ma) = 0 for inviscid flow simulation (Mach number is ratio of speed of the body/object to speed of the sound in the surrounding medium)
2. The standard and typically used Ncrit value, i.e., Ncrit 9. (Commonly the Ncrit determines the turbulence level, if it is '1′ means lots of disturbance existing in the flow).

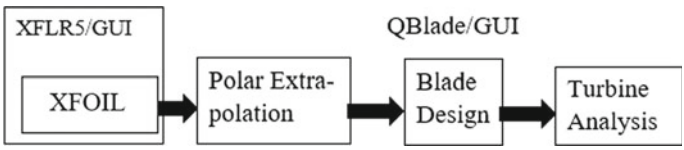

Fig. 3 Different modules in QBlade software [8]

Finally, the result obtained from the simulation was compared with the available experimental data which were taken from literature.

4 Results and Discussion

The public domain numerical simulation QBlade software version 0.96 was used to predict the performance of NREL S823 and DU 06-W-200 airfoils. The following graphs illustrate the variation C_L, C_L/C_D values of a selected airfoil with AoA at different Reynolds numbers. Comparison has been made between the C_L versus AoA, C_L/C_D versus AoA values of NREL S823 and DU 06-W-200 airfoils for the Reynolds numbers 100,000 (Fig. 4a), 150,000 (Fig. 4b), 200,000 (Fig. 4c), 250,000 (Fig. 4d), and 300,000 (Fig. 4e). For Reynolds number 100,000, the significant drop in C_L occurs between 15° and 20° AoA for NREL S823, 10° to 15° AoA for DU06 W-200 airfoil. This will happen due to flow separation or enlarged separation bubble which cannot be predicted in QBlade.

Lift and the ratio of lift to drag curves were plotted against AoA from −5° to 20° for both the selected airfoils, and the lift curves display S823 having high coefficient of lift up to less than 10° and more than 10° AoA DU06 W-200 airfoil show more C_L value. This was happened due to camber present in the airfoil geometries. For the Reynolds number 200,000 to 300,000, DU06 W-200 airfoil exhibits constant maximum C_L value, i.e., 1.41. Whereas maximum C_L value of NREL S823 airfoil increases with increasing Reynolds number. Lift-to-drag ratio also follows the same pattern like lift curves, but maximum C_L/C_D value of NREL S823 airfoil at Reynolds numbers 100,000, 150,000, 200,000, 250,000, 300,000 are 40.73 (at AoA 10°), 53.62 (at AoA 9°), 62.47 (at AoA 8°), 68.94 (at AoA 8°), 73.80 (at AoA 8°), respectively, whereas but maximum C_L/C_D value of DU06 W-200 airfoil at Reynolds numbers 100,000, 150,000, 200,000, 250,000, 300,000 are 33.11 (at AoA 11°), 42.57 (at AoA 10°), 48.69 (at AoA 10°), 52.09 (at AoA 8°), 57.94 (at AoA 9°), respectively.

Generally, the airfoil which has high C_L/C_D value is preferred for designing the blades of the wind turbine.

After analyzing both airfoil, it is clear that C_L, L/D values of both the airfoil design AoA are reliant on Reynolds number. Modern wind turbine design must consider this variant of airfoil performance.

4.1 Validation

To explanation for software confines, a standing airfoil with identified performance is created in QBlade simulation software to allow for assessment between theoretical and experimental data. For that justification, one standing airfoil (NREL S823) and one Reynolds number ($Re = 200{,}000$) were chosen to validate against the Burdett

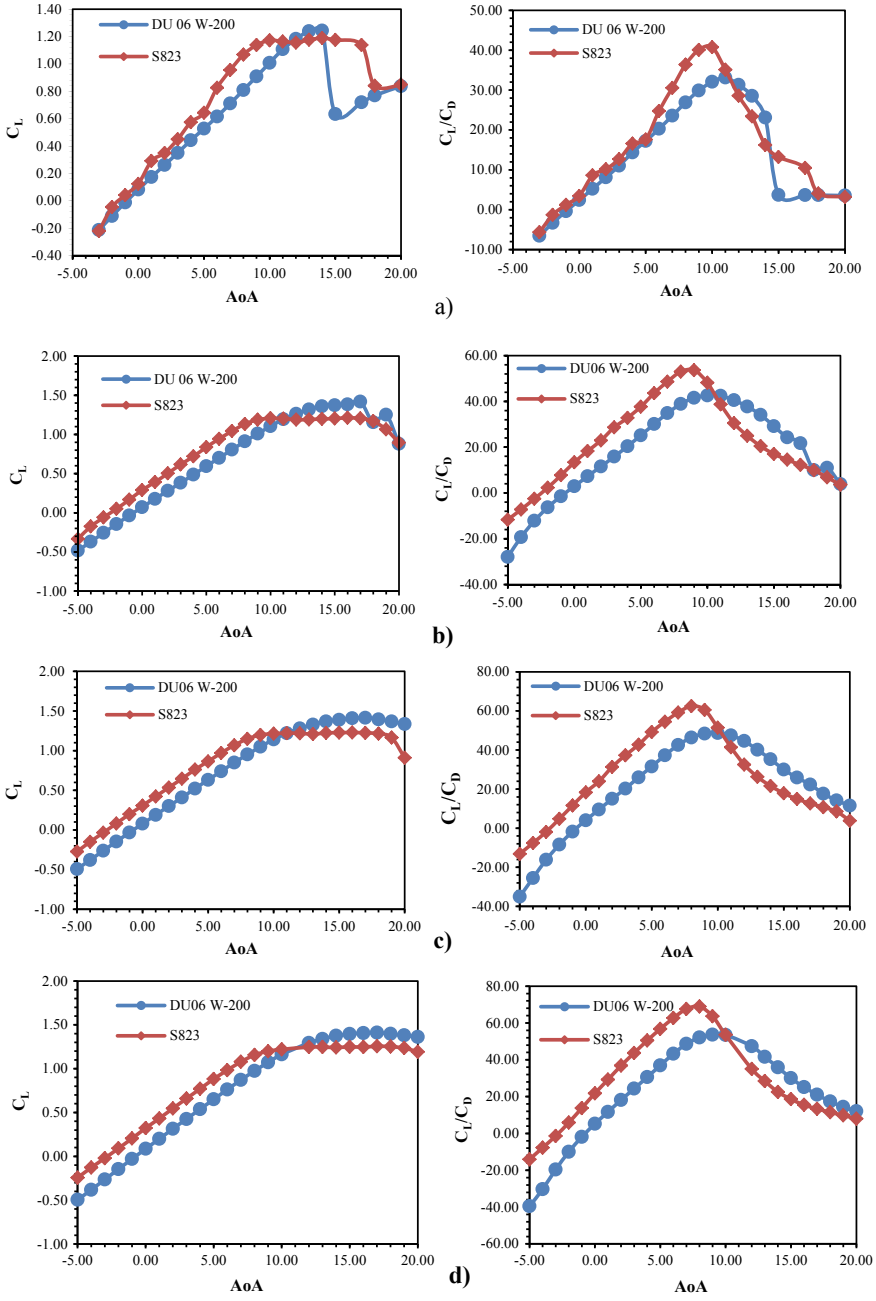

Fig. 4 C_L versus AoA and C_L/C_D versus AoA Graphs **a** $Re = 100{,}000$, **b** $Re = 150{,}000$, **c** $Re = 200{,}000$ **d** $Re = 250{,}000$, **e** $Re = 300{,}000$

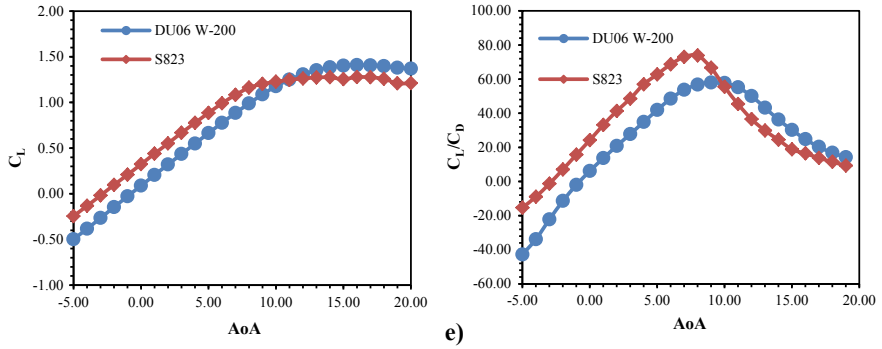

Fig. 4 (continued)

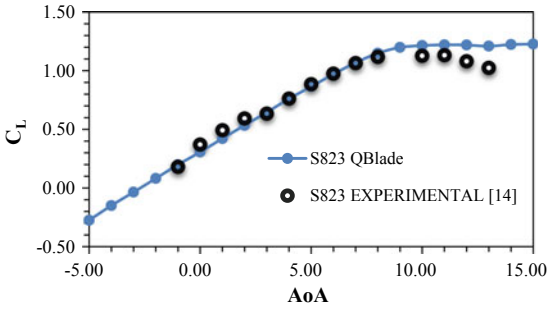

Fig. 5 NREL S823 airfoil QBlade simulation Validation: C_L versus AoA curve ($Re = 200{,}000$)

et al. [14] experimental data. The result comparison displays decent conformity between the simulation result and experimental data are shown in Fig. 5.

5 Conclusion

The NREL S823 and DU06 W-200 airfoil were selected and studied the effect of the Reynolds number on the lift coefficient and lift-to-drag ratio with the help of QBlade open-source software. With the comparison of both airfoil performance in the basis of lift coefficient (C_L) values and the lift-to-drag ratio (C_L/C_D) values following conclusion were drawn.

- NREL S823 airfoil shows higher lift coefficient values for all applied Reynolds number says 100,000, 150,000, 200,000, 250,000, 300,000 up to AoA 10° after that DU 06-W-200 exhibits higher coefficient values.
- C_L values of NREL S823 airfoil increase with increasing Reynolds number whereas DU 06-W-200 airfoil shows highest C_L value (1.41) for Reynolds numbers 200,000, 250,000, 300,000.

- Maximum lift-to-drag ratio value is 73.80 for NREL S823 airfoil which was obtained with respect to Reynolds number 300000 at AoA 8°, and the maximum lift-to-drag ratio value of DU 06-W-200 airfoil is 57.94 obtained at same Reynolds number at AoA 9°.

From the conclusion, it is recommended that both airfoils (NREL S823 and DU 06-W-200) are best suitable for small-scale power generation wind turbines. For less than 10° AoA NREL S823 is suitable for the VAWTs and HAWTs.

References

1. Morsi WG, El-Hawary ME (2009) A wavelet packet transform-based approach for evaluating the performance of a wind farm subject to voltage sag according to IEEE Standard 1459–2000. In: IEEE/PES power systems conference and exposition. IEEE, Seattle, WA, pp 1–7
2. Liu D, Wang Y, Chen D, Peng X, Xu X (2012) Numerical investigation on the Reynolds number effects of supercritical airfoil. In: International conference on advances in computational modeling and simulation. Procedia Engineering, pp 103–109
3. Kim DH, Chang JW (2014) Low-reynolds-number effect on the aerodynamic characteristics of a pitching NACA0012 airfoil. Aerosp Sci Technol 32:162–168
4. Geng F, Kalkman I, Suiker ASJ, Blocken B (2018) Sensitivity analysis of airfoil aerodynamics during pitching motion at a Reynolds number of 1.35 × 105. J Wind Eng Ind Aerodyn 183:315–332
5. Morgado J, Vizinho R, Silvestre MAR, Páscoa JC (2016) XFOIL versus CFD performance predictions for high lift low Reynolds number airfoils. Aerosp Sci Technol 52:207–214
6. Alaskari M, Abdullah O, Majeed HM (2019) Analysis of wind turbine using QBlade software. In: IOP conference series: materials science and engineering, vol 518
7. Mueller-Vahl H, Pechlivanoglou G, Nayeri CN, Paschereit CO (2012) Vortex generators for wind turbine blades: a combined wind tunnel and wind turbine parametric study. In: Proceedings of the ASME turbo expo. Denmark
8. Marten D, Wendler J, Pechlivanoglou G, Nayeri1 CN, Paschereit CO (2013) QBlade: an open source tool for design and simulation of horizontal and vertical axis wind turbines. Int J Emerg Technol Adv Eng 3:264–269
9. Pechlivanoglou G, Nayeri CN, Paschereit CO (2013) Ertragserhöhung einer 1,5 MW WEA durch starre Vorflügel—Die Projektion von Forschungsergebnissen auf reale Anlagen. Available online at: www.windenergietage.de/20F3271230TU.pdf
10. Amin Khana A, Lia W, Zhang J, Shihc TIP (2017) Local vibrations and lift performance of low Reynolds number airfoil. Propul Power Res 6(2):79–90
11. Tangler JL, Somers DM (1995) NREL airfoil families for HAWTs; January 1995 NRELfTP-442–7109. Available online at https://wind.nrel.gov/airfoils/Documents/S822,S823 design pdf
12. Claessens MC (2006) The design and testing of airfoils for application in small vertical axis wind turbines, Master of Science Thesis, Faculty of Aerospace Engineering, Delft University of Technology, 9th Nov 2006
13. Airfoil tools (2019) https://airfoiltools.com/airfoil/index. Access on 03 July 2019
14. Burdett T, Gregg J, Treuren KV (2011) An examination of the effect of Reynolds number on airfoil performance. In: Proceedings of the ASME 5th international conference on energy sustainability AUG 7–10,2011, Washington, DC, USA

Design and Simulation of Wind Tunnel Using CFD Analysis

Ganpati C. Arjune and Shivaji Vithal Bhivsane

Abstract The wind tunnel is proper functioning platform for accurate aerodynamic research which helps to provides adequate environment condition around scaled model to the compatible dimension. Wind tunnel data is part of design process that used to design their model. For correcting wind tunnel data of wall and mounting effects, very careful techniques are used. But it shows limitation for linear flow approximation. This research paper proposed first part of the project, i.e., design calculation and simulation, i.e., flow in wind tunnel and checking incompressible flow in test section over an airfoil using CFD software. Test section has 0.3 * 0.3 m^2 cross-sectional area with 0.5 m length design for proposed wind tunnel. Contraction cone has contraction ratios 7 and cross-sectional area 0.7 * 0.7 m^2 in rectangular shape. Diffuser outer diameter is 0.4 m and length is 1.5 m and diffusion angle 5°. The design philosophy is discussed along method for wind tunnel calculation is outlined. Simulation of wind tunnel using CFD shows no separation of flow along wind tunnel at 25 m\s speed of air. The proposed wind tunnel is conformed to design and can be used for different test in the field of aerodynamics. Wind tunnel design to achieve 40 speed of air with expected low intensity turbulence level. It has available for education and researching in area such as low speed aerodynamics and fundamental research in fluid mechanics.

Keywords Subsonic wind tunnel · Aerodynamics · Fluid dynamics · CFD simulation

1 Introduction

To study the effect of air moving past solid object, wind tunnel is used as a significant research apparatus in aerodynamic investigation such as aerodynamic force and pressure distribution to simulate with actual condition [1]. For aerodynamic research,

G. C. Arjune (✉) · S. V. Bhivsane
Assistant Professor, Department of Mechanical Engineering, Maharashtra Institute of Technology, Aurangabad, Maharashtra 431010, India
e-mail: arjungc163@gmail.com

L. M. Das et al. (eds.), *Emerging Trends in Mechanical Engineering*, Lecture Notes in Mechanical Engineering, https://doi.org/10.1007/978-981-15-8304-9_21

fast, economical and correct way offer by wind tunnel, the most important aspect of wind tunnel is their ability to accurate recreate the full complexity of full fluid flow. For solving aerodynamic problems, experimental information required which obtain in different way like water tunnel test, wind tunnel test, drop test, flight test, shock tube test, flying scale model, ballistic range, whirling arms rocket sleds. Each way is best in its sphere of superiority. Among them wind tunnel seems absolute to solve aerodynamic problems, but still basis and complex aerodynamic problem need to solve using wind tunnel even though society use computer and high technology in wind tunnel testing [2].

Flow visualization in wind tunnel is unique which can find critical problem and solution not seen in the pure numbers but computer provides mostly quantitative data [3]. Essential lift, drag and efficiency can calculate using complex equation. One of the important parts of the aerodynamic research is versatility and tangibility which help to continue to promote wind tunnel testing. All aerodynamic problem could not solve in one single wind tunnel; hence, wind tunnel needs to classified as: (a) on the basic of circuit, i.e., open and closed circuit wind tunnel, (b) based on structure, (c) based on structure material, (d) based on shape of inlet section, (e) based on location, (f) based on speed of air velocity, i.e., subsonic, supersonic, transonic and hypersonic wind tunnel, (g) based on anemometer placement [2].

Major parts of wind tunnel are test section, diffuser, contraction, settling chamber and driving unit say electric motor [8]. Uniform flow within the test section is the main goal of wind tunnel. Test section dimension design based on size of model and type of test to be performed and defined rest of wind tunnel dimension. Test section is key factor in construction and running cost of wind tunnel [8]. Overall length of the construction can be controlled by optimization the design. The optimum length is achieved CR only then is the dynamic load and boundary layer growth at their minimum list value [4]. The power of computing machines and the computer languages necessary to program the foundational mathematics started increasing exponentially. To develop such system was decreased in an equally trend. The condition was met for an economical study of fluid flow prediction to evolve into the field known as computational fluid dynamics. With the help of CFD software and its complimentary CAD graphic interface, one can accurately design and evaluate the flow regimes of a highly capable wind tunnel device [1, 3].

2 Design of Wind Tunnel

Wind tunnel design starts with test section on the basis of accessibility and installation of test model as well as instrumentation. Test section length should be in range of 0.5–3 times of its hydraulic diameter and keep small as possible as for low pressure loss coefficient. Blockage has negligible effect on test result when it about 10%. Test section set 0.5 m length, i.e., 1.67 of its hydraulic diameters [1, 3, 10].

Flow accelerates into the test section by contraction. Design criterion of contraction for desired application that separation is avoided and the exit non-uniformity is

equal to or less than the maximum tolerable level in shortest possible length [10]. Contraction cones design starts with selection of contraction ratio which should be in range of 6–9 for small wind tunnel and also length of contraction should be 0.15–1 times of its inlet section hydraulic diameter. Flow separation avoid if contraction is too large, i.e., pressure drop coefficient decreasing with increase in contraction ratio. 1.05 m contraction length takes to avoid flow separation. Straight contraction shape uses for easier and cheaper contraction. Internal section of nozzle is identical to the test section [1, 2, 4].

To decrease velocity flow in shortest distance, diffuser is used which help to reduce load on drive system [1, 8]. Area ratio, diffuser angle wall contour and diffuser cross-sectional shapes are key factor of diffuser flow. For controlling flow separation, area ratio should be less than 2.5 and diffuser angle 5°–7°. Here, diffusion angle considers as 5°. Calculated length found as 1.15 m, but here considering length is 1.5 m for better flow quality and area ratio 1.78 [2, 9].

Settling chamber used to place honeycomb and screen which help to reduce flow turbulence before move into the contraction [9]. Settling chamber cross section is same as contraction and length took as 0.5 times of the hydraulic diameter of inlet of settling chamber area, i.e., 0.35 [2, 3].

Primary purpose of honeycomb is to reduce swirl and produce well-conditional flow which means reduce in variation in mean and transverse velocity without losing its flexural rigidity under forces during operation. Ratio of length to cell hydraulic diameter ($L\backslash D$) and porosity (flow area/total area) is the primary design parameter for honeycomb [9]. $L\backslash D$ took as 6–8 and porosity as 0.97. Square cross section has edge 5 mm, 0.075 mm thickness and length 12 mm [1].

Screen located inside settling chamber helps to reduce upcoming air turbulence level, i.e., breaks large eddies into small-scale turbulent eddies [9]. Porosity above 0.8 has no control on turbulence and below 0.58 lead to flow instability. Hence, it should be in range of 0.58–8 [2]. Finest screen shows better control over turbulence. Clearance between screens should be 0.2 times of settling chamber hydraulic diameter. Screen dimensions considered as 2 mm thick wire, cell height 8.9 mm, hence 0.6 porosity and 0.14 m distance from contraction inlet. Another one is 3 mm thick wire and cell width 10.5 mm, porosity 0.65 placed from first screen. The drive system chooses which has optimum efficiency, RPM and required power to produce 25 m\s mass flow [1, 10] (Fig. 1 and Table 1).

3 Pressure Losses in Wind Tunnel

At any point in the wind tunnel, the energy loss depends on the cubic velocity at that point. In diffuser, velocity decreases with minimum loss and higher back pressure without boundary layer separation. The total losses occurring in the flow through wind tunnel are equal to the power required to maintain steady flow through the wind tunnel. Pressure loss for each component of wind tunnel determined to conducting numerical simulation in order to comprehends the functionality of the circuit [5]. The

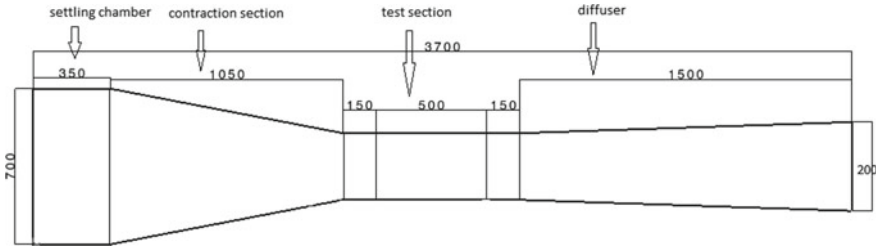

Fig. 1 Wind tunnel design (all dimension in mm)

Table 1 Wind tunnel component dimension

Component of wind tunnel	Cross-sectional area (mm^2)	Length(mm)
Test section	300 * 300	$L_{\text{ts}} = D_{\text{ts}} * 1.5 = 500$
Contraction cone	700 * 700	$L_{\text{cs}} = D_{\text{cs}} * 1.5 = 1050$
Diffuser	400 * 400	$D_{DO} =$ $D_{ts} + \{(2 * (L_{\text{d}} * \tan\theta/2)\} L_d = 1500$
Settling chamber	700 * 700	$L_{sc} = \frac{D_{\text{cs}}}{2} = 350$
Honeycomb	30 * 30	= 12 (inside settling chamber)

total pressure loss coefficient (k_i) which is sum of each section and head losses (h_1) is calculated for upstream and downstream wind tunnel section. Such total pressure loss is then subtracted from the pressure at the exit of the diffuser, establishing the pressure at the exit recovery required by the fluid pump. The pressure recovery required by the fluid pump is calculated on the total pressure loss. The pressure drops coefficient represent as dimensionless form of the energy loss of each section.

Head loss calculated as:

$$h_1 = k\frac{v^2}{2g} = \frac{\Delta p}{\rho g} \tag{1}$$

where V, ρ and k are average fluid velocity in working section, density of fluid, loss coefficient, respectively.

3.1 Test Section

Design of test section purpose is to maintain approximately constant static pressure with list change in Mach number throughout the test section. Test section has constant

height. Its upper and lower wall are deflected to prevent boundary layer growth. The design provides good view to user. Only friction losses find inside test section and k is function of fraction factor which is calculated as [6].

$$k_{\text{ts}} = \frac{L_{\text{ts}}}{D_{\text{ts}}} f_{\text{ts}} \tag{2}$$

where k_{ts}, L_{ts}, D_{ts} and f_{ts} are loss coefficient, length, hydraulic diameter and friction factor of the test section, i.e., working section. The friction factor calculated as following Colebrook equation:

$$\frac{1}{\sqrt{f_{\text{ts}}}} = -2\log_{10}\left[\frac{\varepsilon/D_{\text{ts}}}{3\cdot 7} + \frac{2.51}{\text{Re}\sqrt{f_{\text{ts}}}}\right] \tag{3}$$

ε is roughness and consider as zero in working section.

3.2 Diffuser

The purpose of diffuser is to reduce the power losses due to high flow velocity, i.e., decrease in velocity with distance without separation of boundary layer at walls [8]. Vibration of fan causes change in velocity at test section; hence, separation may occur. Divergence is important aspect for design of diffuser keep small as possible to ensure separation of boundary layer at wall of diffuser. It means long diffuser for high aspect ratio and may be costly inefficient [6]. The pressure losses in diffuser due to skin friction and expansion loss. Equivalent conical expansion angle (θ) and area ratio, i.e., ratio of outlet and inlet cross-sectional area of diffuser are main parameters. Loss coefficient for diffuser (k_{d}) is sum of these two loss factors [1].

$$k_{\text{d}} = k_{\text{f}} + k_{\text{ex}} \tag{4}$$

where k_{f} and k_{ex} are skin friction and expansion lass factors. They are calculated as:

$$k_{\text{f}} = \left(1 + \frac{1}{AR^2}\right)\frac{f_{\text{ws}}}{8\sin\theta} \tag{5}$$

Expansion angle (θ) may calculated as:

$$\theta = \tan^{-1}\left(\frac{R_2 - R_1}{L}\right) = \tan^{-1}\left(\frac{1}{2}\frac{\sqrt{AR}-1}{\frac{L_{\text{n}}}{D_{\text{ws}}}}\right) \tag{6}$$

$$k_{\text{ex}} = k_{\text{e}}(\theta)\left(\frac{AR-1}{AR}\right)^2 \tag{7}$$

For an expansion angle $1.5° \leq \theta \leq 5° k_e(\theta)$ calculated as:

$$k_e(\theta) = 0.1709 - 0.1170(\theta) + 0.03260(\theta)^2 + 0.001078(\theta)^3 - 0.00090760(\theta)^4 - 0.00001331(\theta)^5 + 0.000001345(\theta)^6 \quad (8)$$

3.3 Contraction Cone

Only, skin friction loss considers in a contraction cone and it may be calculated as follows [1, 3]:

$$k_{cs} = \frac{f}{4} \frac{L_{CS}}{D_{CS} - D_{TS}} \left(1 - \frac{D_{TS}^4)}{D_{CS}^4}\right) \quad (9)$$

where L_{CS}, D_{CS}, D_{TS} and f are length of cc, inlet hydraulic diameter of cc, test section hydraulic diameter and skin friction coefficient, respectively [1].

3.4 Settling Chamber

Honey comb and screen are two sections which used to decrease the turbulence in flow and make it straight. To decrease the pressure loss in wind tunnel, velocity at honeycomb and screen section must be low as possible [10]. Screen and honeycomb reduce axial and lateral turbulence, respectively. Screen has a relatively large pressure drop in the flow direction but honeycomb has small pressure drop. Loss in honeycomb calculated as [1]:

$$k_h = \lambda_h \left(\frac{L_h}{D_h} + 3\right)\left(\frac{1}{\beta_n}\right)^2 + \left(\frac{1}{\beta_n} - 1\right)^2 \quad (10)$$

$$\text{Where, } \lambda_h = 0.375\left(\frac{\Delta}{D_h}\right)^{0.4} R_{e\Delta}^{-0.1} \quad \text{Re} < 275 \quad (11)$$

$$\lambda_h = 0.214\left(\frac{\Delta}{D_h}\right)^{0.4} \quad \text{Re} > 275 \quad (12)$$

Screen loss coefficient can be calculated as:

$$k_m = k_{mesh} k_{Rn} \sigma_S + \left(\frac{\sigma_S^2}{\beta_S^2}\right) \quad (13)$$

Table 2 Loss coefficient in wind tunnel section

Wind tunnel component	Loss coefficient
Test section	0.0188
Contraction cone	0.0048
Diffuser	0.04271
Honeycomb	0.00049
Screen 1	0.6399
Screen 2	0.7787
Straight section	0.0111
Total	$\sum k_i = 1.4965$

where σ_S and β_S are screen solidity and screen porosity. k mesh is mesh factor, 1 for new metal wire, 1.3 for average circular metal wire, k_{Rn} is calculated as [1] (Table 2):

$$k_{Rn} = 0.785 + \left(1 - \frac{Re_{ws}}{354}\right) + 1.01 \quad 0 \leq Re_{ws} \leq 400 \tag{14}$$

$$k_{Rn} = 1 \quad Re_{ws} \geq 400 \tag{15}$$

Total pressure loss calculated as power loss in each section of wind tunnel and fan:

$$\Delta P_t = \frac{1}{2}\rho V^2 \sum k_i + \frac{1}{2}\rho V_{fan}^2 \tag{16}$$

Take 25% safety factor, i.e.,

$$\sum k_i = 1.4854 + 0.37135 = 1.871. \tag{17}$$

Dimension of fan is same as diffuser outer diameter. Hence, velocity of fan is calculated as:

$$A_{fan} V_{fan} = A_{ts} V_{ts} \tag{18}$$

where $A_{fan} = A_{ds} = 0.16$, $A_{ts} = 0.09$, $V_{ts} = 25$ m\s, hence. $V_{fan} = 14.0625$ m\s therefore;

$$\Delta P_t = 806.47\text{Pa} \tag{19}$$

3.5 Power Requirement

To maintain steady flow inside test section, power is required that power is equal to losses by kinetic energy dissipated phenomenon, i.e., vortices and turbulence [1]. Design of fan may be on the basis of required velocity at test section and to resist

the decrease in pressure along the wind tunnel. Sum of the pressure drop coefficient (Ki) in each section of wind tunnel equal to required power for given section size and flow condition [6].

$$\eta P = \frac{1}{2}\rho A V^2 \Sigma k_1 \tag{20}$$

Power required is sum of total pressure loss in all section of wind tunnel and fan:
-

$$P_{\text{req}} = Q = A_{\text{fan}} V_{\text{fan}} \Delta P_t = 1814.55W \tag{21}$$

Power in H_{p} is 2.42
For BHP (brake horse power) = 60% approximately;

$$\text{Then, EFF} = \frac{\text{Power in HP}}{\text{BHP}} = \frac{P(Hp)}{BHP} = 4.03(hp) \tag{22}$$

Power (4.03 hp) is more than Preq. So, velocity can increase upto 40 m/s in the test section.

4 CFD Simulation

4.1 Wind Tunnel Simulation

To visualize flow in side wind tunnel or any complex configuration to find a mechanical and flow properties, Ansys use like a tool to represent it. First step is to model wind tunnel and apply proper boundary condition which are calculated using design [6]. Steps involve in Ansys are preprocessing, i.e., modeling, boundary condition

Table 3 CFD model boundary condition summary

Parameter	Input values
Discretization scheme	Second-order upwind
Algorithm	SIMPLEC
Inlet velocity	4.76 m/s
Pressure outlet	105779.4035 Pa
Air density (at 25 °C)	1.18 kg/m^3
Gas constant	287 J/kg-K
Kinematic viscosity	1.51×10^{-5} kg/ms
Time	Steady state

(Table 3) and meshing, solution, i.e., fluent as a solver, and for post-processing, CFX may use.

Total element and node use to simulate wind tunnel are 391,368 and 381,808, respectively. Ansys solution (fluent) shows constant velocity(25 m\s) along test section that means good result which indicates prepared design has no separation at all and no thickening of boundary layer at that region which may face an error in measurement.

4.2 Airfoil Simulation in Test Section

Flow must be adequate for simulation. Such, flow quality is good in test section. Model can simulate in the test section of wind tunnel. 2D airfoil model use for it. 3D model provides same result as per study. 2D model helps to minimise mesh as well as simulation time. To analyze the aerodynamic characteristics (lift and drag) of 2D airfoil, use input variable such as experimental measurement (wind tunnel test data) result and airfoil coordinate. The understanding problem statement that is flow is external aerodynamic flow so we need to fix the outer airflow boundary, i.e., airflow. Airfoil and stream condition (flight speed\ air speed) are required to carry out the analysis. NACA 2412 airfoil coordinates take from UIUC airfoil database.

4.2.1 Flow Consideration

Flow is incompressible and turbulent, i.e., density and viscosity are constant. Only mass and momentum equation need to be solved. Appropriate pressure velocity coupling scheme and turbulence model need to be selected. Here, only steady state analysis is sufficient [5]. Flow is external, as per industry practice, fluid domain around airfoil can be taken as 15–20 times the chord length. Modeling of boundary layer is challenging task for flow around airfoil because of severe stalling effect in the stalling region [8]. Analysis can be fine turned with multiple modeling approaches by comparing the CFD analysis results with experimental results (wind tunnel test data). The flow is incompressible and compressibility effects are negligible; therefore, there will not a shock wave [7, 8].

4.2.2 CFD Analysis Procedure

The first step is to scale the mesh to SI (length in meter) units after importing the mesh to CFD analysis software which include structured mesh with 45,888 quad elements and 46,440 nodes. In this problem, there is need to scale mesh, because airfoil coordinates are normalized to one-unit chord length for test section analysis model scale as 1:10. Pressure-based CFD solver, i.e., Ansys fluent, is used as solver, since there are no severe compressible effects like shock waves. Energy equation and model

density as a function of pressure, temperature and viscosity selected for analysis. Reference pressure is as sea level 101,325 pa which needs to consider for environmental flow. We fix the far field boundary condition, wall boundary condition and solver setting. For test section model inlet velocity is sufficient. For far field boundary condition, we need provide gauge pressure, flow Mach number, i.e., flow is turbulent say velocity as 40 m\s and flow direction cosine along with turbulence boundary condition. X-direction of flow is given by cos (α) and Y—direction flow is sin (α). Wall boundary condition assigns with no slip, adiabatic boundary condition. Need to create fluid properties like density, viscosity, thermal conductivity, specific heat as an air fluid property to all 2D volume elements (quad element). Solver setting depends on governing equation discretization scheme, i.e., second-order upwind scheme which was selected. SIMPLE algorithm is used for pressure–velocity coupling algorithms. Under relaxation factor can set solution control. We take residual value like 1e-10 or 1e-20. Because we know that getting converged solution up to this value is impossible, but it is a technique to keep the analysis running till we stop based on our technical judgment. Once the fluctuation stops, we can declare that solution is converged. Monitor lift and drag coefficient on the curve of airfoil. Very fine mesh use for turbulence flow. Y plus value between 30 to 300 called as inertia dominant region. Inertia dominant region use for simulation. This region depend on mesh. To gain this region we need to check and repeat mesh by changing number of element untill solution becomes grid independent.

4.3 Post-Processing Result

Velocity profile inside test section need to constant when solving mass conservation equation. Such Fig. 2 shows more accurate profile for design data.

Stalling angle of attack of NACA2412 is nearly equal to all result with constant Mach number and Reynold number. It shows that all flow properties at test section, i.e., wind tunnel are accurately design.

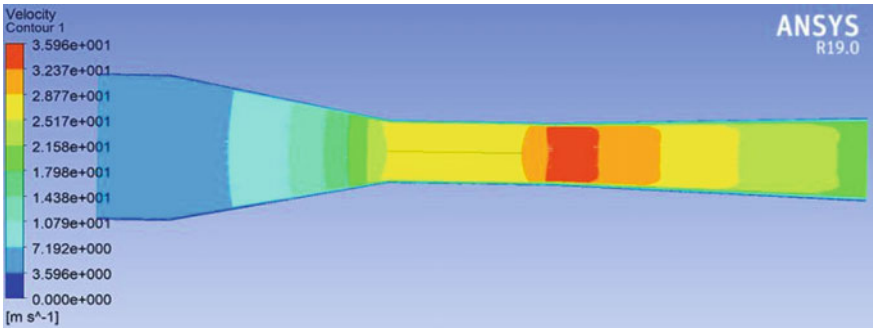

Fig. 2 Velocity profile in complete wind tunnel

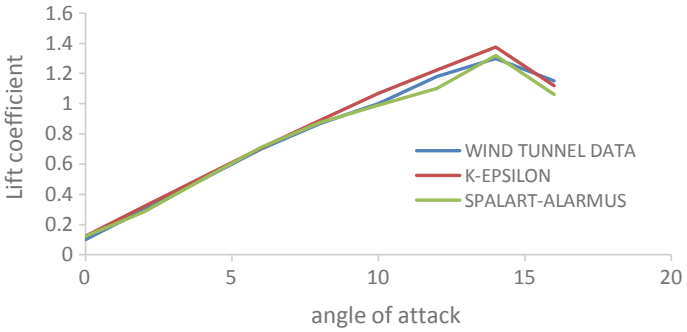

Fig. 3 Lift coefficient versus angle of attack at different model of simulation compare with wind tunnel data

5 Conclusion

- To obtain velocity up to 40 m/s at test section (0.3 * 0.3) m^2, an open-circuit wind tunnel has been designed and simulated. Power loss in wind tunnel is nearly 0.2 with respect to dynamic pressure at test section and 1 Hp motor may sufficient to produce 25 m/s velocity at test section. Construction, test work and calibration will be done in next paper.
- The wind tunnel (Fig. 1) length is 3.7 m and free stream velocity about 25 m/s which is very much smaller and probably not found anywhere.
- CFD using FLUENT to predict flow around airfoil has been achieved; it is clear from the result that lift coefficient on airfoil is increase due to angle of attack increase (Fig. 3) as well as it is noticed that lift coefficient in CFD simulation comparably accurate as wind tunnel data. The 1:10 scaled model of NACA2412 airfoil shows good result in CFD simulation for flow pattern and force coefficient.
- To avoid traditional approach of wind tunnel experiment which costly and time consuming, pre-experimental CFD study helps to reduce repetitive experiment.
- Critical study like turbulence intensities where it is important to resort to wind tunnel experiment.

References

1. Panda MK, Samanta AK (2016) Design of low cost open circuit wind tunnel—a case stud. Indian J Sci Technol 9(30). https://doi.org/10.17484/ijst/2016/v9i30/99195
2. Arifuzzaman M, Mashud M. Design construction and performance test of a low cost subsonic wind tunnel. IOSR J Eng (IOSRJEN) e-ISSN: 2250-3021, p-ISSN: 2278-8719
3. Singh M, Singh N, Yadav SK, Ramswaroop S (2013) Review of design and construction of an open circuit low speed wind tunnel. Glob J Res 13(5) version 1.0 year 2013
4. Bell JH, Mehata RD (1988) Contraction design for small low speed wind tunnel. JIAA report TR-84. Department of Aeronautics, Standard University, NASA CR-177488 (Apr 1988)

5. Pop, Harper JJ (1986) Low speed wind tunnel testing. McGraw-Hill
6. Hussain IY, Mjeed MH, Ali AH, Saesam WS (2011) Design, construction and testing of LSWT with its measurement and inspection and inspection devices. J Eng (6) 17 Dec 2011
7. Joglekar B, Mourya RM (2014) Design, construction and testing open circuit low speed wind tunnel. Int J Eng Res Rev 2(4):1–9 Oct–Dec 2014. ISSN 2348-697X (Online). Available at: www.researchpublish.com Page
8. Anderson JD Jr (2011) Fundamental of aerodynamics, 5th edn. McGraw-Hill, New York
9. Calautit JK, Chaudhary HN, Hughes BR, Sim LF (2014) A validated design methodology for closed-loop subsonic wind tunnel. J Wind Eng Ind Aerodyn 125:180–194. ISSN 016-6105
10. Libbi JN (2011) Wind tunnel in engineering education. Wind tunnel and experimental fluid dynamics research. In: Lerner JC (ed). InTech. ISBN: 978-953-307-6232. (http://www.intechopen.com/books/windtunnel-and-experimental-fluid-dyanamics-research/wind-tunnels-in-engineering-education)

Exergy Analysis of Cogenerative Steam Power Plant

Satpal C. Babre and Kumudini S. Gharge

Abstract In this study, exergy analysis of Sahyadry Sugar Factory (Steam power plant) located in a karad, Maharashtra, has been done. The data is collected from power plant and each component present in a power plant has been analyzed separately based on exergy. In this analysis, it is observed that the maximum amount of exergy destructed in boiler; nearly, 199.29 MW exergy is destructed within a boiler which is 89.4% of fuel exergy input. The second source of major exergy destruction is condenser where 9.88 MW exergy is destructed which is 4.4% of fuel exergy input. The exergetic efficiency of each component and whole cycle has been calculated. The exergetic efficiency of power plant is 7.3% which is very less.

Keywords Exergy · Exergy destruction rate · Exergy efficiency

1 Introduction

Exergy is a maximum theoretical work that can be obtained from system, when its state brings in equilibrium with the reference environment. It is also considered as maximum work potential that can be obtained from a system [1]. Power generation system analysis is usually done for its better performance and for increasing its efficiency. The numbers of methods are available to do so, but exergy gives qualitative improvement in performance and efficiency. This analysis is important for design of new or existing system, maintenance of equipment or system.

Nowadays, the resources of fossil fuels are drastically decreased and energy prices are increasing highly. Due to this reason, optimum steps toward energy generation, energy application and its optimum consumption management methods are

S. C. Babre (✉) · K. S. Gharge (✉)
Government College of Engineering, Karad, Maharshatra, India
e-mail: babresatpal@gmail.com

K. S. Gharge
e-mail: kumudgharge@gmail.com

L. M. Das et al. (eds.), *Emerging Trends in Mechanical Engineering*, Lecture Notes in Mechanical Engineering, https://doi.org/10.1007/978-981-15-8304-9_22

important. For optimal design and optimization purposes of thermal system, accurate thermodynamic analysis required. Two tools are widely used for analysis of thermal system, first is energy analysis as per first law of thermodynamic and second is exergy analysis as per second law of thermodynamics [2]. As exergy analysis follows first and second law of thermodynamics, it is a powerful tool to analyze the system to reveal inefficient thermodynamic processes; it has become key source for the better understanding of processes [3]. Many researchers have suggested that exergy analysis can be used for the making decisions about allocation of resources such as research and development efforts, capital, materials, optimization, life-cycle analysis. [4]. Exergy analysis identifies the locations, type and true value of exergy destruction. Therefore, it can effectively help in planning and gives guidelines for more efficient use of energy in existing power plants [5, 6].

The objective of this work is to evaluate exergy, exergy destruction rate at inlet and outlet of each component of steam power plant present in a Sahyadry Sugar Factory.

2 Plant Description

The power plant uses five boilers of different capacities, in which B1 and B2 of 25 T/h each, B3 of 35 T/h, B4 and B5 of 50 T/h each. Power house consists of 12 turbines, in which T5, T6 and T12 these three are used for power generation, while others for running crushing mills.

2.1 Working of Plant

The steam produced in boiler B1 to B5 is super heated in super heater SH1 to SH5. This super heated steam is collected in a single duct; this collected steam is supplied to the turbine which are split into two groups, namely T1 to T4 and T5 and T6 as shown in Fig. 1. The steam produced in boiler B4 and B5 is super heated in super heaters SH4 and SH5. Again this steam is collected at single duct as shown in Fig. 3.1. This generated steam is again split into two groups of turbine namely T7 to T11 and T12. The turbine T1 to T4 and turbine T7 to T11 used to run crushing mills. The turbine T5, T6 and T12 is used to generate power. The outlet of the turbine is passed to the single condenser. The condensate is collected in a tank. This condensate is drawn by a feed water pumps P1 to P5 and supplied to the boiler through economizer E1 to E5. The fuel used in a boiler is sugarcane bagasse. The bagasse contains 50% moisture. When the fresh sugarcane is crushed, the bagasse generated is dried 50% and supplied directly to the furnace of a boilers.

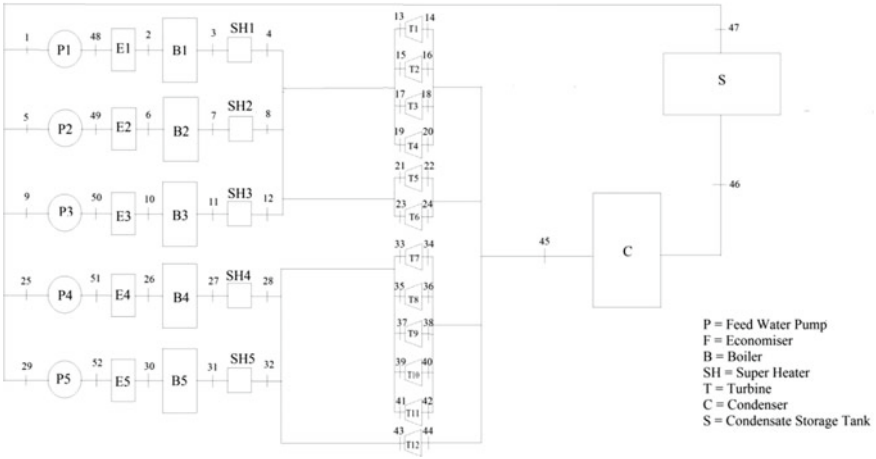

Fig. 1 Plant layout

3 Exergy Analysis Procedure

If the kinetic, potential and chemical exergy are considered to be negligible, the specific exergy is defined as by equation [3].

$$e = h - h_0 - T_0(s - s_0) \tag{1}$$

Total exergy rate of the system is [3],

$$\dot{E} = \dot{m}\,[(h - h_0) - T_0(s - s_0)] \tag{2}$$

To carry out exergy analysis of steam power plant, following assumptions are considered [4, 6]

1. The process is carried out at steady state.
2. Changes in potential and kinetic energies are neglected.
3. There are no heat losses over the surface of the components.
4. Cycle and cooling water are treated as pure.
5. There are no changes of the specific chemical exergies in the cycle.

3.1 Exergy of Fuel (Sugarcane Bagasse)

The ratio (ϕ) of chemical exergy (e) of dry solid fuels to the net calorific value of fuel (NCV), with mass ratio of oxygen to carbon (O/C) varies from 0.667 to 2.67 in general and in particular for bagasse is given by Kotas [7],

Table 1 Formulae being used for calculation

Component	Exergy destruction rate	Eq.	Exergy efficiency	Eq.
Boiler	$\dot{I}_{\text{boiler}} = \dot{E}_{\text{fuel}} + \dot{E}_{\text{in}} - \dot{E}_{\text{out}}$	05	$\eta_{\text{exB}} = \frac{\dot{E}_{\text{out}} - \dot{E}_{\text{in}}}{\dot{E}_{\text{f}}}$	11
Pump	$\dot{I}_{\text{pump}} = \dot{E}_{\text{out}} - \dot{E}_{\text{in}} + W_{\text{p}}$	06	$\eta_{\text{exP}} = \frac{\dot{E}_{\text{out}} - \dot{E}_{\text{in}}}{W_{\text{p}}}$	12
Heater	$\dot{I}_{\text{heater}} = \dot{E}_{\text{out}} - \dot{E}_{\text{in}}$	07	$\eta_{\text{exSH}} = 1 - \frac{\dot{I}_{\text{heater}}}{\dot{E}_{\text{in}}}$	13
Turbine	$\dot{I}_{\text{turbine}} = \dot{E}_{\text{in}} - \dot{E}_{\text{out}} - W_{\text{T}}$	08	$\eta_{\text{exT}} = \frac{\dot{W}_{\text{T}}}{\dot{E}_{\text{in}} - \dot{E}_{\text{out}}}$	14
Condenser	$\dot{I}c = \dot{E}_{\text{in}} + \dot{E}_{\text{out}}$	09	$\eta_{\text{exC}} = \frac{\dot{E}_{\text{out}}}{\dot{E}_{\text{in}}}$	15
Cycle	$\dot{I}_{\text{cycle}} = \sum \dot{I}_{\text{allcomponent}}$.	10	$\eta_{\text{exCycle}} = \frac{W\text{net}}{\dot{E}_{\text{f}}}$	16

$$\phi_{\text{dry}} = \frac{1.0438 + 1.0882\left(\frac{h}{c}\right) - 0.2509[1 + 0.7256\left(\frac{h}{c}\right) + 0.0383\left(\frac{n}{c}\right)}{1 - 0.3035\left(\frac{\text{O}}{\text{C}}\right)} \tag{3}$$

If moisture (W) of the fuel is considered, the chemical exergy $\dot{E}$ of wet bagasse is

$$\dot{E} = \left[\text{NCV} + \text{Wh}_{\text{fg}}\right]\phi_{\text{dry}} \tag{4}$$

The properties of sugarcane bagasse are as follow (Table 1),

$$W = 0.5;\ NCV = 7130\,\text{KJ/Kg} : c = 22.04;\ h = 2.72;\ n = 0.15;\ S = 0.02;\ O = 21.07$$

4 Result and Discussion

At reference environment $P_0 = 101.325\,\text{kPa}$ and $T_0 = 298.15\,\text{K}$, using exergy analysis procedure, following results are obtained (Table 2):

4.1 Exergy Destruction Rate of Cycle

Figure 2 represents exergy destruction rate of a steam power plant cycle. It can be observed that boiler destroying major amount of exergy followed by condenser. Exergy destruction rate of a pump is negligible compared to the other plant components. Exergy destruction rate of condenser is also significant, whereas exergy destruction rate of superheater is moderate. The exergy destruction is mainly caused due to irriversibity in a plant.

Table 2 Results obtained through analysis

Sr. No.	Pressure (bar)	Temperature (°C)	$\dot{m}$ (kg/s)	h (kJ/kg)	s (kJ/kg^{o}C)	E (kJ/kg)	$\dot{E}$ (MW)
1	0.72815	91	9.72	382.1	1.204	27.78	0.27
2	34.34	139	9.72	585.86	1.7285	75.16	0.73
3	20.6	272	5.8	2949.7	6.6322	976.96	5.67
4	31.39	317	5.8	3032.15	6.5583	1081.44	6.27
5	0.70109	90	9.72	376.9	1.193	25.86	0.25
6	34.339	101	9.72	425.32	1.314	38.20	0.37
7	20.6	265	5.83	2938.4	6.6014	974.84	5.68
8	31.39	321	5.83	3042.8	6.6049	1078.19	6.29
9	0.70109	90	9.72	376.9	1.193	25.86	0.25
10	34.39	108	9.72	454.87	1.396	43.30	0.42
11	20.6	280	8.097	2973.75	6.6685	990.19	8.02
12	31.39	341	8.097	3091.45	6.6856	1102.79	8.93
13	18.62	279	3.82	2974.89	6.6913	984.53	3.76
14	0.9	96.71	3.82	2669.56	7.3944	469.57	1.79
15	19.65	285	3.82	2989.77	6.7169	991.78	3.79
16	0.8	93.15	3.82	2665.4	7.442	451.22	1.72
17	20.601	280	2.8	2974.85	6.6645	992.48	2.78
18	0.9	96.71	2.8	2668.23	7.3942	468.29	1.31
19	20.601	290	2.8	2998.69	6.7112	1002.39	2.81
20	0.7	89.96	2.8	2658.1	7.4791	432.86	1.21
21	20.601	330	3.82	3090.86	6.8789	1044.57	3.99
22	0.8	93.15	3.82	2665.4	7.4998	433.98	1.66
23	20.601	328	2.8	3086.24	6.8631	1044.66	2.93
24	0.9	96.71	2.8	2670.1	7.3954	469.81	1.32
25	0.72815	91	25	382.7095	1.2028	28.74	0.72
26	34.339	110	25	463.69	1.4161	46.13	1.15
27	31.39	334	12.197	3074.5	6.6675	1091.22	13.31
28	31.39	383	12.197	3188.79	6.8409	1153.83	14.07
29	0.75606	92	25	385.4	1.217	27.20	0.68
30	34.339	112	25	455.29	1.3926	44.74	1.12
31	31.41	297	12.65	2981.91	6.5112	1045.25	13.22
32	31.39	380	12.65	3183.2	6.8303	1151.39	14.57
33	31.39	370	3.82	3164.2	6.8114	1138.03	4.35
34	0.9	96.71	3.82	2669.69	7.3985	468.48	1.79
35	31.39	368	3.82	3155.2	6.7981	1132.99	4.33

(continued)

Table 2 (continued)

Sr. No.	Pressure (bar)	Temperature (°C)	ṁ (kg/s)	h (kJ/kg)	s (kJ/kg°C)	E (kJ/kg)	Ė (MW)
36	1	99.63	3.82	2674.64	7.3647	483.51	1.85
37	31.39	371	2.8	3161.93	6.7854	1143.51	3.20
38	0.8	93.15	2.8	2664.78	7.5432	420.43	1.18
39	31.39	370	2.8	3160	6.7842	1141.94	3.19
40	0.9	96.71	2.8	2669.69	7.3944	469.71	1.32
41	30.41	371	5.24	3164.1	6.8951	1112.98	5.83
42	1	99.63	5.24	2674.89	7.3598	485.22	2.54
43	31.39	372	3.82	3164.3	6.8215	1135.12	4.34
44	0.8	93.15	3.82	2665.4	7.442	341.68	0.002
45	10.027	180	42.16	2776.2	6.582	818.43	34.50
46	1.9854	120	42.16	2704.88	7.1294	583.89	24.62
47	0.72815	91	79.16	381.1	1.243	15.15	1.19
48	29.43	96	9.72	404.4	1.2594	33.56	0.33
49	29.43	94	9.72	395.9953	1.2366	31.95	0.31
50	34.34	95	9.72	400.5737	1.2477	33.22	0.32
51	47.1	97	25	409.9506	1.2695	36.09	0.90
52	47.1	96	25	405.75	1.2581	35.29	0.88

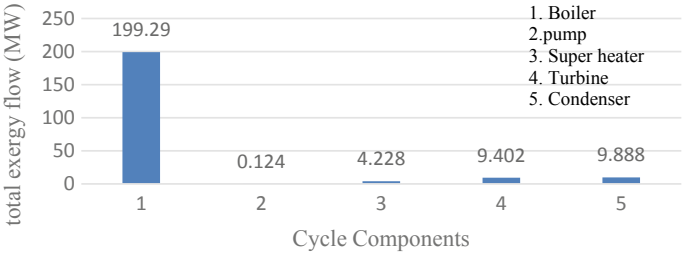

Fig. 2 Exergy destruction rate of cycle

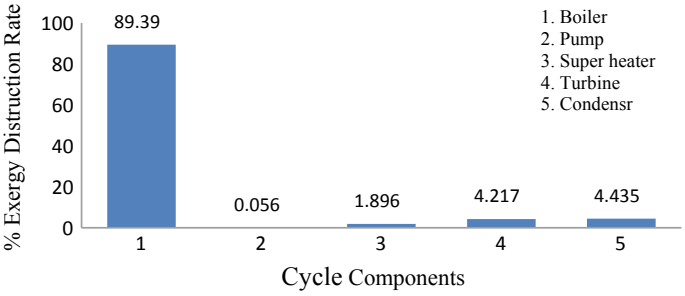

Fig. 3 Percentage exergy destruction rate

Table 3 Exergy efficiency of boiler

Boiler	Exergy efficiency (%)
B1	15.1
B2	16.2
B3	16.6
B4	18.6
B5	18.6

Figure 3 represents exergy destruction rate in terms of percentage. It can be observed that out of total exergy 89.4% of exergy is destroyed in a boiler which indicates that boiler is much poor to utilize available energy and there is need to improve the performance of a boiler. As a boiler is major source of exergy destruction, there is scope of improvement of a boiler.

4.2 Exergy Efficiency of Boilers

Table 3 represents exergy efficiency of boiler which ranges in between 15 and 18%. These efficiencies are low because of entropy generation and high irreversibilities present in a boiler. The irreversibilities are due to uncontrolled combustion, chemical reaction, heat transfer through conduction from the wall of boiler.

4.3 Exergy Efficiency of Turbine

The exergy efficiency of turbine is in between 59 and 75% as represented in Table 4. The decrease in exergetic efficiency is due to friction in turbine, friction is reduced by increasing temperature in a turbine within, metallurgical limit.

4.4 Exergy Efficiency of Super Heaters

See Table 5.

4.5 Discussion

The power plant was analyzed using exergy analysis procedure; the environment reference temperature and pressure are 298.15 K and 101.3 kPa, respectively. The exergetic efficiency measures ideality of process or deviation of process from ideality.

Table 4 Exergy efficiency of turbine

Turbine	Exergy efficiency (%)
T1	59.3
T2	60.0
T3	58.5
T4	59.7
T5	69.7
T6	72.4
T7	73.8
T8	73.8
T9	68.8
T10	72.9
T11	75.0
T12	72.3

Table 5 Exergy efficiency of super heaters

Super Heaters	Exergy efficiency (%)
SH1	89.3
SH2	88.8
SH3	88.6
SH4	94.3
SH5	89.8

Exergy and exergy destruction rate is calculated as presented in a table. It is observed that the exergy destruction rate of the boiler is maximum compared to other components in a power plant. It measures alone 89.4% of losses in the plant, followed by condenser. The exergy destruction rate of the condenser is 4.4%. If we consider first law, major losses are occurred in a condenser; in reality, it happens in a boiler where major amount of entropy is generated. This implies that significant improvements should be done in a boiler instead of condenser. The exergetic efficiency of the power cycle is 7.3%, which is very low. This indicates that tremendous opportunities are available for improvement, redesign and for optimization of the processes. However, this irreversibilities cannot be avoided because of physical, technological and economic constraint.

Irreversibilities can occur in a plant due to many reasons but irreversibility due to chemical reaction is significant. It mainly occurred in boiler due to which major amount of exergy is destructed within a combustion chamber. There is also a significant effect of air to fuel ratio; if it is not controlled or maintained properly, uncontrolled combustion takes place which destroys maximum useful energy in a combustion chamber itself [8]. Heat transfer to finite temperature difference, friction between atoms in a chemical reaction, heat conduction through wall of a boiler also cause irre-

versibility. In a turbine, exergy is destructed due to friction; friction is maximum when temperature inside turbine is low. If the temperature inside the turbine is maintained within metallurgical limits, exergy destruction rate can be minimized [9].

5 Conclusion

In this study, exergy-based analysis is carried out. This analysis shows that energy lost in a condenser device is very less and insignificant compared to the boiler as the quality of energy in condenser is low. The summation of exergy destruction rate in all boilers is about 199.29 MW; in terms of percentage, it is 89.4% of the fuel exergy input to the cycle which is very high. Next to it was the condenser where 9.88 MW of exergy is destroyed; this represents 4.4% of the total exergy. 4.2% exergy is destroyed in a turbine and 2% exergy is destroyed in all heaters and pumps. Exergetic efficiency of power plant is 7.3% which is very low. It means that lot of scope is present to modify the plant or redesign the components. As the chemical reaction is most significant source of exergy destruction, most part of exergy is destroyed in a boiler. Excess air fraction and inlet air temperature are significant to exergy destruction in combustion chamber. The main source of exergy destruction in turbine is friction; it can be reduced by increasing temperature in a turbine within metallurgical limits.

Nomenclature

$\dot{m}$	Mass flow rate (kg/s)
e	Specific exergy rate (KW)
$\dot{E}$	Total exergy rate (KW)
h	Specific enthalpy (J/kg)
s	Specific entropy (J/kg K)
T	Temperature (K)
P	Pressure (bar)
NCV	Net calorific value
Ø	Mass fraction
İ	Exergy destruction rate (KW)
η_{ex}	Exergetic efficiency
o	Dead state conditions
i	Inlet
e	Exit

References

1. Cengel YA, Boles MA (2006) Thermodynamics—an engineering approach, 5th edn. McGrow Hill
2. Mitrovíic D, Zivkovi'c D, Lakovíc MS (2010) Energy and exergy analysis of a 348.5 MW steam power plant. Energy Sour Part A 32:1016–1027 (Taylor & Francis Group, LLC)
3. Isam H (2009) Aljund: energy and exergy analysis of a steam power plant in Jordan. Appl Therm Eng 29:324–328 Elsevier Ltd.
4. Bejan Adrian (2002) Fundamentals of exergy analysis, entropy generation minimization, and the generation of flow architecture. Int J Energy Res 26:545–565
5. Ray TK, Ganguly R, Ekbote P, Gupta A (2010) Second-law analysis in a steam power plant for minimization of avoidable exergy destruction. In: 4th international conference on energy sustainability, ES2010-90144, Proceedings of the ASME May 17–22, Phoenix, Arizona, USA
6. Rosen MA, Dincer I (2003) Survey of thermodynamic methods to improve the efficiency of coal-fired electricity generation. Proc. Instn Mech. Engrs Vol 217 Part A: J. Power and Energy, 63–73
7. Kotas TJ (1995) The Exergy method of thermal plant analysis. Krieger Publishing Company Malabar, Florida
8. Bejan A, Tsatsaronis G, Moran M (1995) Thermal design and optimization. Wiley
9. Eke MN, Onyejekwe DC, Iloeje OC, Ezekwe CI, Akpan PU (2018) Energy and exergy evaluation of A 220 mw thermal power plant. Nigerian J Technol 37(1):115–123